Ultrasound Based Soft Tissue Elastic Modulus and Strain Measurement

Safeer Hyder

Ultrasound Group
School of Electronic and Electrical Engineering

University of Leeds

Submitted in accordance with the requirements for the degree of

Doctor of Philosophy

April 2017

Chapter 2 contains materials from Hyder *et al.* (2014).

Chapter 5 contains materials from Hyder *et al.* (2016).

The candidate confirms that the work submitted is his own, except where work which has formed part of jointly authored publications has been included. The contribution of the candidate and the other authors to this work has been explicitly indicated below. The candidate confirms that appropriate credit has been given within the thesis where reference has been made to the work of others.

Earnestly dedicated to my Parents, Siblings and Mary

Acknowledgements

I should first thank my supervisors Professor Steven Freear and Dr. Sevan Harput for their help during my PhD for their generous academic and moral support throughout this research.

I want to acknowledge my seniors Dr. David M. J. Cowell and Dr. James R. McLaughlan regarding Ultrasound system and another laboratory related assistance. I also want to thank my colleague Ms. Zainab Ramay for her technical guidance regarding beamforming.

I recognise the financial support from the Sukkur IBA and Higher Education Commission, Pakistan.

I would also like to praise Anna de Jong for her secretarial assistance.

I want to thank again all the people of Ultrasound Group for their friendly fellowship, in particular, Professor Steven Freear, Dr. Sevan Harput, Dr. James R. McLaughlan. Dr. David M. J. Cowell, Ms. Zainab Ramay, Mr. Robert Ingham, Mr. Christopher Adams, Mr. Luzhen Nie, Mr. Asraf Moubark, Mr. Oscar Knights and anybody else I may have forgotten to mention their names.

Finally, I would like to extend utmost sincere thanks and appreciation to my family for their loving encouragement, patience, and support during the academy journey.

Abstract

Conventional B-mode ultrasound provides information on the anatomical features using acoustic impedance differences in the tissues. Ultrasound elastography uses a variety of techniques to map soft tissue elasticity. Tissue stiffness is a novel indicator of the tissue health, as many pathologies can alter the tissue stiffness such as cancer and fibrosis. Accurate and early detection of tissue elasticity can guide towards reliable diagnosis, and prognosis of diseases. The objectives of the research reported in this thesis are to implement strain and shear wave elastography techniques on the locally developed ultrasound systems, along with identifying current challenges in elastography and proposing solutions to develop ultrasound elastography as an accurate, and reliable clinical tool.

In the first study, strain elastography was implemented and novel strain estimation quality assessment approach was proposed to discard noisy strain images. The second study proposed a shear wave generation method, called Dual Push Beam (DPB) to address challenges of the current shear wave elastography techniques, such as to reduce data acquisition events and to improve imaging depth.

Further, the thesis includes the study which introduced a new angle-aligned shear wave tracking method, which improved displacement estimation quality for shear compounding. Final study designed seven different elastography schemes and investigated variations in elasticity estimation across the image by changing shear waves generation beam parameters such as aperture size and focal depth and its implication for liver fibrosis and breast cancer diagnosis.

Research contributions

The objectives of this research were to realise strain and various shear wave elastography methods on an in-house developed research ultrasound systems UARP I and UARP II, and to propose solutions for existing challenges of ultrasound elastography. During research work, the emphasis was to exploit the locally designed ultrasound machine which enabled broad control over system hardware and firmware to address research challenges in elastography. The following research contributions were made during the study:

- Strain elastography was realised on UARP I ultrasound system.
- Novel strain estimation quality assessment method was proposed to discard noisy strain images in strain elastography.
- Current shear wave elastography schemes including SSI, U-CUSE, and F-CUSE were realised on UARP II ultrasound system.
- A new shear wave elastography method called DPB was proposed to address limitations on existing techniques including SSI, U-CUSE, and F-CUSE.
- To improve steered shear wave motion detection for shear compounding, a novel method using angle-aligned tracking beams was proposed.
- Seven different elastography schemes were designed for UARP II and performance of each was analysed with respect to liver fibrosis and breast elastography imaging application.

Journal Publications (In Process)

- Hyder, Safeer, Sevan Harput, David MJ Cowell, and Steven Freear. "Dual Push Beam (DPB) Shear Wave Elastography ", *Ultrasound in Medicine & Biology, 2017.*

- Hyder, Safeer, Sevan Harput, David MJ Cowell, and Steven Freear. "Bias and Variability Observations for Different Shear Wave Elastography Methods", *Ultrasound in Medicine & Biology, 2017.*

Conference Publications

- Hyder, Safeer, Sevan Harput, Zainab Alomari, and Steven Freear. "Two-way Quality Assessment Approach for Tumour Detection Using Free-hand Strain Imaging", *In Ultrasonics Symposium (IUS), 2014 IEEE International, pp. 1853-1856. IEEE, 2014.*

- Hyder, Safeer, Sevan Harput, Zainab Alomari, David MJ Cowell, James McLaughlan, and Steven Freear. "Improved Shear Wave-front Reconstruction Method by Aligning Imaging Beam Angles with Shear-wave Polarization: Applied for Shear Compounding Application.," *In Ultrasonics Symposium (IUS), 2016 IEEE International, pp. 1-4. IEEE, 2016.*

Co-authored Conference Publications

- Alomari, Zainab, Sevan Harput, Safeer Hyder, and Steven Freear. "Selecting the Number and Values of the CPWI Steering Angles and the Effect of that on Imaging Quality.," *In Ultrasonics Symposium (IUS), 2014 IEEE International, pp. 1191-1194. IEEE, 2014.*

- Alomari, Zainab, Sevan Harput, Safeer Hyder, and Steven Freear. "The Effect of the Transducer Parameters on Spatial Resolution in Plane-wave Imaging.," *In Ultrasonics Symposium (IUS), 2015 IEEE International, pp. 1-4. IEEE, 2015.*

Contents

List of Figures

List of Tables

Abbreviations

CNR	contrast to tissue ratio
SNR	signal to noise ratio
DPB	dual push beam
FFT	the fast Fourier transform
FT	the Fourier transform
UARP	ultrasound array research platform
SWEI	shear wave elasticity imaging
SSI	supersonic shear imaging
U-CUSE	unfocused comb-push shear ultrasound elastography
F-CUSE	focused comb-push shear ultrasound elastography
ARF	acoustic radiation force
ARFI	acoustic radiation force imaging
1D	one dimensional
2D	two dimensional
3D	three dimensional
SDVU	shear-wave dispersion ultrasound vibrometry
FOV	field-of-view
LPF	low pass filter
TGC	time gain compensation
LNA	low noise amplifier
PGA	programmable gain amplifier
RL	right-to-left
LR	left-to-right
NCC	normalised cross correlation
std.	standard deviation
PRF	pulse repetition frequency

Abbreviations

NHS	national health service
CT	computed tomography
CAT	computed axial tomography
MRI	magnetic resonance imaging
MRE	magnetic resonance elastography
TDE	time delay estimation
RF	radio frequency
SDVU	shearwave dispersion ultrasound vibrometry
LDVU	lambwave dispersion ultrasound vibrometry
SMURF	spatially modulated ultrasound radiation force
NMA	noise masked area
QIBA	quantitative imaging biomarker alliance
WFUMB	world federation for ultrasound in medicine and biology
BIRADS	breast imaging-reporting and data system
RTE	real time elastography
PRI	pulse repetition interval
HRPWM	harmonic reduction pulse width modulation
PWM	pulse width modulation
ADC	analog to digital converter
TX	transmission
RX	reception
FPGA	field programmable gate array
TM	tissue mimicking
dB	decibel
N	nominal
mm	millimetre

List of Symbols

C_s	shear wave speed
C_l	longitudinal speed
G	shear modulus
K	bulk modulus
E	Young's (elastic) modulus
ρ	density of the medium
Z	acoustic impedance
f	frequency
f_s	sampling frequency
f_c	centre frequency
$\hat{\rho}$	correlation coefficient
M	mega
k	kilo
μ	micro
ε	strain
σ	stress
ν	poisson's ratio
$\hat{k}$	wave number
ω	angular frequency
$\bar{s}$	mean strain
ψ	shear wave displacement
Δt	arrival time delay

Chapter 1

Introduction

1.1 Medical ultrasound

Ultrasound imaging is a well-established and widely utilised technique. In England, a total of 40.7 million imaging procedures were reported by the National Health Service (NHS) in the year 2015/16, where ultrasound scans were counted up to 8.92 million and this was second to the 22.6 million X-ray scans, while Computed Tomography (CT) and Magnetic Resonance Imaging (MRI) scans were nearly 4.46 and 3.08 million, respectively. In 2015/2016, the ultrasound images have the second largest share with 22% of the total scans after standard X-ray which are 55.5%, while CT and MRI scans contributed 11% and 7.5% of the total scanning procedures (NHS, 2016).

Ultrasound's strength relative to MRI and CT is its abilities to visualise subtle changes in anatomical structures, providing blood flow velocity, mapping tissue stiffness in real-time, and non-invasiveness. Furthermore, ultrasound scanners are small, portable and economic (Szabo, 2004). The drawbacks of ultrasound are its inability to image bone like structures due to huge acoustic impedance mis-match between bone and soft tissue, accessing deep tissues due to ultrasound shadowing, also mandatory requirement of probe and skin contact along with requirement of substantial training for acquisition and interpretation (Brstad, 2011; Naumova *et al.*, 2014).

Traditional ultrasound is capable of imaging soft tissue anatomy, measuring blood flow parameters and tissue motion, in addition to this, mapping tissue stiffness are emerging features of contemporary ultrasound. The basic principle of ultrasound contrast is based on characteristic acoustic impedance (Z) difference in the tissues, which is defined as the product of acoustic speed and density of the medium (Hoskins *et al.*, 2010). The ultrasound pulses are transmitted using a transducer, then propagate through the tissues, and are reflected back from tissues of different characteristic acoustic impedance and these varying amplitude reflections help to differentiate various tissues. Axial resolution in ultrasound imaging is a function of wavelength and is reciprocal of bandwidth of the transducer. Lateral resolution is determined by ultrasound beam width, which depends on the size of the active aperture and focal depth, and spatially varies as beam width tends to widen away from the focal point (Hoskins *et al.*, 2010; Szabo, 2014). In plane wave imaging, beam width is comparable to transducer element width and uniform along the depth (Montaldo *et al.*, 2009). Ultrasound waves during propagation incur depth and frequency dependent attenuation, the later also deteriorates spatial resolution, whereas SNR is deteriorated for both types of attenuations, specifically severely in plane wave imaging due to unfocused transmissions (Cobbold, 2006; Montaldo *et al.*, 2009).

Ultrasound elastography is an emerging technique and the only competitive modality closer to ultrasound elastography is magnetic resonance elastography (MRE). The disadvantage of MRE is its high cost, lack of equipment portability, and inconvenient process of scanning from the patient's perspective, with advantage of high penetration depth and easy image acquisition and interpretation. In comparison to MRE, ultrasound based elasticity and strain estimation is relatively fast, comparably accurate, economical, and convenient for both patients and practitioners with a disadvantage of limited imaging depth (Mariappan *et al.*, 2010).

1.2 Palpation as a diagnostic tool

Manual palpation is an essential part of the contemporary routine physical examination of patients. In this process, a practitioner applies manual pressure at the patient's skin and senses the information about position, hardness, mobility, and pulsation of structures within the body. In ancient Egyptian medicine, the palpation of pulses was considered to be very important, as quoted from Ebers papyrus [1], which dates back to about 1550 BC, and other sources (Raddin, 1964; Wells & Liang, 2011):

> "If thou examinest a man suffering from a resistance in his cardia (viscera), and thou findest that it goes and comes under thy fingers like oil in a leather bag... then thou shalt examine him lying extended on his back. If thou findest his belly warm and a resistance in his cardia, thou shalt say to him: it is a liver case. Thou shalt prepare the secret herbal remedy which is made by the physician...(Raddin, 1964)"

In 400 BC, Hippocrates identified a relationship between stiffness of tissues and its health, as quoted from 'The Book of Prognostics' (Hippocrates, 2009; Song, 2014):

> "...then, as are painful, hard, and large, indicate danger of speedy death; but such as are soft, free of pain, and yield when pressed with the finger, are more chronic than these...(Hippocrates, 2009)"

Similarly, palpation is also found in traditional Chinese medicine, where the tactile sense of the radial arteries was used for diagnosis of diseases, which dates back to about 500 BC (Wells & Liang, 2011). Modern advancement in biological sciences have found that tissue stiffness altered by certain diseases is caused by exudation of fluid from the vessel system into the extra- and intra-cellular space and, that results in increased interstitial pressure and eventually changing of the tissue stiffness. A scientific reason for tissue elasticity change in liver fibrosis is associated with the replacement of diseased tissues with a stiffer collagen-based matrix (Greenleaf *et al.*, 2003). Disease such as breast cancer tumours can increase the stiffness up to 90 times of the healthy state (Greenleaf *et al.*, 2003). In pathological investigations, various diseases have been found to alter the stiffness of tissues such as breast, prostate and testicular cancer, liver fibrosis, and heart

[1] It is said to have been found between the legs of a mummy in the Assassif district of the Theban necropolis.

failure (Barr *et al.*, 2015; Denis *et al.*, 2015b; Ferraioli *et al.*, 2015; Sarvazyan *et al.*, 2011).

Though palpation is a very useful tool for assessment of superficial arteries such as radial, and carotid artery, nevertheless, in the abdomen, utility of palpation is limited to large size abnormalities and which have significant stiffness difference compared to its surrounding. Another limitation of palpation is the subjective nature of diagnosis which is always prone to human errors. This builds the aspiration to have a technique which can provide quantitative elasticity information of tissues, to detect small, deep and low contrast abnormalities in the human body (Song, 2014). Ultrasound elastography also aims to reduce unnecessary invasive and discomforting biopsy procedures (Athanasiou *et al.*, 2010a; Cho *et al.*, 2014).

1.3 Theory of elasticity

Materials change their shape and size when compressed or stretched. The materials with a tendency to return to their original size and shape after being subjected to the deforming force, are called elastic materials. The fluids resist change only in the volume, while solids resist both size and shape deformations. This indicates fluids possess volume elasticity while solids have both volume and shear elasticity (Callister & Rethwisch, 2011). This change in shape and size is called strain (ε), which is defined as the change in length per unit length (Hoskins *et al.*, 2010).

$$\varepsilon = \frac{\text{length (deformed) - length (original)}}{\text{length (original)}} = \frac{\Delta \mathrm{L}}{\mathrm{L}} \tag{1.1}$$

The strain is a reaction to applied force per unit area on the material and it is called stress (σ) (Hoskins *et al.*, 2010).

$$\sigma = \frac{\text{force}}{\text{area}} \tag{1.2}$$

Materials which have same property independent of the directions are called isotropic materials, and when a property is the same at every point, they are known as homogeneous materials. For homogeneous, isotropic solids, the ratio of stress over strain is constant, is called elastic modulus (E) and measured in the units of Nm^{-1} or Pascal and is derived from Hooke's law (Hoskins *et al.*, 2010).

$$E = \frac{\text{stress}}{\text{strain}} = \frac{\sigma}{\varepsilon} \tag{1.3}$$

It is observed that, when elastic materials are stretched in one dimension, they tend to contract in the other directions and vice versa. This property of elastic materials is measured using Poisson's ratio (ν), which is defined as transverse contraction strain to longitudinal extension strain along the direction of stretching force (Wells & Liang, 2011). There are three common moduli to explain material's elasticity; longitudinal elasticity (E) is the ratio of longitudinal strain in response to longitudinal stress, also called Young's modulus. Shear modulus (G) is defined as a ratio of shear stress to shear strain, and it is also called modulus of rigidity. Bulk modulus (K) refers to a measurement of compressibility of materials. Shear modulus determines the tendency of materials to preserve shape, while bulk modulus defines material property to resist change in volume. Three linear elastic constituent equations describe the relationship between these four constants (Wells & Liang, 2011).

$$G = \frac{E}{2(1+\nu)} \tag{1.4}$$

$$K = \frac{E}{1-2\nu} \tag{1.5}$$

$$\nu = \frac{E}{2G} - 1 \tag{1.6}$$

There are four principle modes of wave propagation in the elastic materials and each is differentiated by the motion of the particles during wave propagation. When particles in solids are displaced in the direction of the travelling wave, the waves are called longitudinal, or compressional waves (Callister & Rethwisch, 2011). Compressional waves have been in use for the medical ultrasound for more than 60 years, while shear waves were explored about 20 years ago (Sarvazyan *et al.*, 2013). For shear wave propagation, particle motion is orthogonal to the direction of wave propagation. Surface and plate waves are other two types of waves. The speed of longitudinal and shear waves in materials is governed by the corresponding modulus, expressed by the following expressions (Callister & Rethwisch, 2011).

$$C_l = \sqrt{\frac{K}{\rho}} \tag{1.7}$$

$$C_s = \sqrt{\frac{G}{\rho}} \tag{1.8}$$

where C_l denotes longitudinal wave, while C_s indicates shear wave speed.

Assuming soft tissues are incompressible with the Poisson's ratio between 0.49 and 0.499 (Wells & Liang, 2011), shear and elastic modulus can be measured from shear wave speed using following equation:

$$E \approx 3G \approx 3\rho C_s^2 \tag{1.9}$$

where ρ is mass density.

As elastography is based on measuring subtle differences in shear elasticity of tissues, conventional B-mode imaging is based on acoustic impedance (Z) differences between tissues, which can be expressed in terms of density (ρ) and Bulk modulus (K) (Hoskins *et al.*, 2010).

$$Z = \sqrt{\rho K} \tag{1.10}$$

1.4 Biological tissues and elasticity

Bulk modulus and acoustic impedance properties of a material are governed by molecular composition of the materials (Sarvazyan *et al.*, 2013) and water makes the major molecular constituent (70% to 75%) of biological tissues like in liver, kidney, heart, and skeletal muscle, which are major ultrasound imaging tissues, therefore, compressional wave speed lies within the ±10% range of water (Duck, 2013). In contrast to bulk modulus, shear modulus in soft tissues is governed by tissue architecture and structural makeup and this architecture greatly vary among different organs and state of the disease (Sarvazyan *et al.*, 2013). According to studies, the shear modulus in tissues offers a broader dynamic range than the bulk modulus, spread over seven orders of magnitude (Hoskins *et al.*, 2010; Sarvazyan *et al.*, 1998). This gives great potential to characterise and identify different kinds of normal tissues. A healthy liver and breast are largely isotropic and homogeneous, whereas, skeletal muscles are transversely anisotropic, where measurements along the fibres and perpendicular to fibre are found to be different. The characterization of muscle tissues along different directions may provide valuable diagnostic information (Gennisson *et al.*, 2010).

Biological tissues have demonstrated both elastic and viscous properties, therefore soft tissues can be characterised as viscoelastic solids. The viscous component of elasticity changes the deformation response of the tissues as applied stress frequency is changed. In terms of shear wave speed, viscosity adds dispersion, the resulting shear wave speed varies at different shear wave frequencies (Chen *et al.*, 2009). Measurement of viscosity of tissues using shear waves offers a new insight into soft tissue imaging. In viscoelastic materials, shear elasticity has both elastic and viscous components and shear modulus is a complex quantity (Sarvazyan *et al.*, 2013).

Various diseases are known to have increased shear elasticity of soft tissues in a larger percentage than the bulk elasticity, this gives shear modulus imaging an advantage over the conventional compressional wave imaging. Effects of pathological conditions change the compressional wave speed, but a comparative difference is higher in shear wave speed measurements (Sarvazyan *et al.*, 2013). This concludes that, the development of shear wave elasticity measurement using ultrasound enables to characterise normal and pathologic tissues in terms of elasticity, viscosity and anisotropy will bring greater insight into the tissues.

1.5 Ultrasound elastography

Ultrasound elastography is the name used for the collection of techniques to measure the stiffness of soft tissues. Elastography methods can be categorised in the way excitations are generated. Elastography has been rigorously investigated and plenty of techniques are designed to measure both tissue elasticity and viscosity.

In this study, the focus is on two major techniques of ultrasound elastography. First is strain estimation based elastography called quasi-static strain imaging, where stress is applied externally and corresponding tissue deformation is measured using ultrasound. The second family of methods generate shear waves in tissues, and track corresponding propagating speed to measure stiffness of the imaged tissues. The shear wave based techniques provide quantitative values of elasticity in Young's modulus while static imaging is a semi-quantitative method.

1.5.1 Quasi-static strain elastography

The strain imaging method dates back to ground-breaking research work by the Professor Jonathan Ophir and followed by series of studies which improved the technique (Ophir *et al.*, 1991). The method aspired to produce 2D Young's modulus *in vivo* images by solving inverse problem equations, however to date, it only offers 2D strain images called elastograms. Small compressions are applied to deform tissues and then measures corresponding strain distribution to characterise the stiffness, as softer tissue experiences higher strain relative to stiffer tissue. The strain imaging requires two RF ultrasound images, first pre-compression and then post-compression RF data image is acquired and processed to produce a single strain image. As compression is usually low frequency or static therefore technique is named as quasi-static strain imaging. In the ideal case of measurements, if both local stress and strain values are known, Young's modulus can be measured using Equation. 1.3. However, in real anatomical and pathologic scenario, imaging tissue geometrics are complex and mathematical models are required to correlate observed strain and stress field with the underlying Young's modulus (E) values. The measured strain and applied local stress depends on both internal and external boundary conditions along with stiffness distribution in the tissue (O'Donnell *et al.*, 1994), therefore, elastic modulus can not be reconstructed accurately using only strain values. However, for low modulus contrast and simplified geometrical boundary conditions, the stiffness distribution may be a relatively good representation of the underlying modulus distribution (Kallel *et al.*, 1998). The tissue stiffness map is produced in the form of strain values and is superimposed on B-mode image and presented along with the original B-mode image where each offers distinct property of soft tissues (Chen *et al.*, 2014).

What is strain?

The objective of the strain imaging is to map local elastic variations in the soft tissues. Soft tissues exhibit both elasticity and viscosity behaviours, since in strain imaging nature of the compression is low frequency therefore viscous term can not be measured.

To understand strain estimation problem in a simplified way, a 1D cross section of the homogeneous tissue medium can be modelled by series of elastic springs (Fig. 1.1a). Assuming, all three springs are of same stiffness and each having a length equal to L. If an axial force is applied at the top by a decompresser, in result overall length of the system is reduced by $3\ \Delta L$, and is reduced to $L - \Delta L$ (Fig. 1.1b). As elasticity is uniform along the compression axis, therefore displacement decreases as the depth increases such as bottom spring displaces less than the top spring, as shown in the displacement profile (Fig. 1.1c). As axial strain is the ratio of total axial deformation over initial axial dimension of an elastic object, therefore each spring experiences local strain (shrink) equal to $\Delta L/L$. The strain experienced for each spring is constant as displayed in the corresponding strain profile (Fig. 1.1d). In an alternative way, the strain profile can be calculated by applying gradient operation on the displacement profile. The straight strain plot indicates that stiffness is constant along the compression dimension, assuming stress is uniform along the same axis.

For heterogeneous medium representation, a modified spring model is shown in Fig. 1.2a, where the elasticity of the central spring is set such that the spring is incompressible (elasticity $\simeq \infty$). In this case, applied displacement is shared by only two springs as shown in Fig. 1.2b, and thus the strain experienced by both above and top springs is increased from ΔL to $3\ \Delta L/2$ as indicated by the strain profile of Fig. 1.2d. From observations of these models it can be concluded that, the local strain experienced by each spring is not only a function of the spring elasticity but also depends on the stiffness of other springs placed in the same compression axis. It is important to note that, both models assumed that when

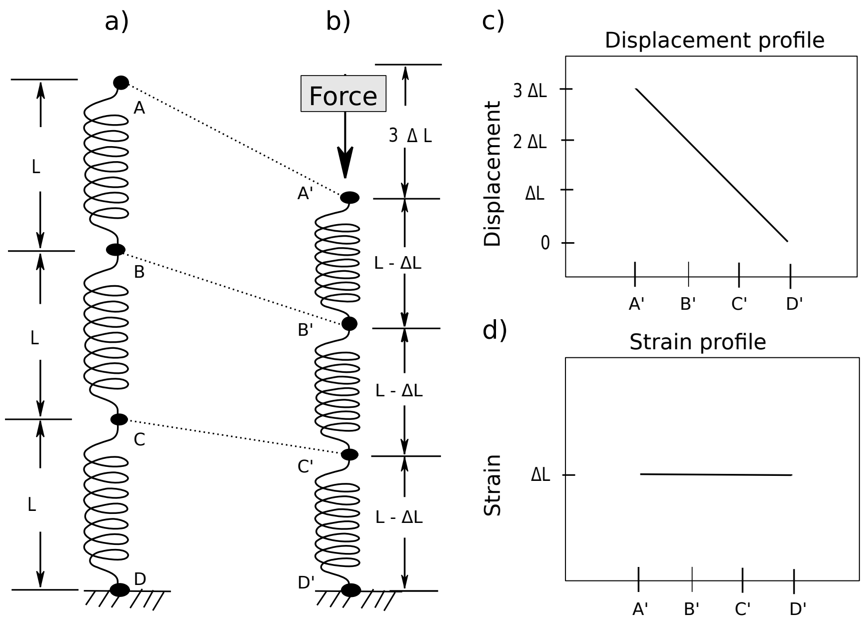

Figure 1.1: Spring model showing reference and compressed homogeneous elastic medium including displacement and strain profiles to demonstrate depth dependent displacement and strain relationship. a) Three springs each of equal length L are connected in series having same elasticity. b) A compression of 3 ΔL is applied, assuming stress along the compression axis is uniform, total applied compression 3 ΔL is equally shared by all springs that is ΔL and each spring shrinks in length from original length L to deformed length $L - \Delta L$. c) The displacement profile indicates linear function of the depth, where the spring closer to compressor displaces higher than the bottom spring. d) Strain profile is a straight line indicating that all springs experience equal strain, and concluding that all spring posses same elastic modulus. The diagram idea is adapted from (Ophir *et al.*, 1991).

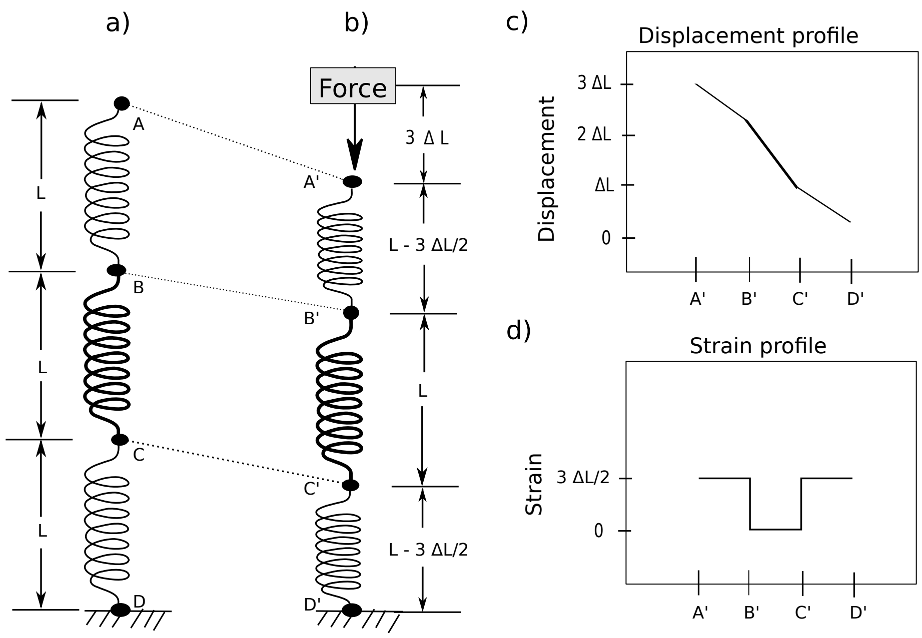

Figure 1.2: Equivalent spring model mimicking heterogeneous elastic medium with inclusion and axial displacement and strain profiles are drawn. a) In this scenario, the central spring stiffness is changed to high elasticity while top and bottom springs have equal spring constants. b) After compression of 3 ΔL is applied using compressor, only top and bottom springs share the applied compression, and both experience same amount of strain equal to 3 $\Delta L/2$, while central spring only translates down without being compressed, as rate of change of displacement along the central spring is lower than the top and bottom springs. c) The displacement profile indicates central spring is only displaced not compressed. d) Strain profile indicates that upper and lower springs have equal strain value while central spring is not compressed and strain is zero. The diagram idea is adapted from (Ophir *et al.*, 1991).

compression is applied, the stress distribution flow along the axis is uniform and pushing force is constant at each spring. In real situations, this assumption is not valid and stress usually have non-uniform profile along the axis. Therefore, local strain estimates in the strain images can only be truly attributed to the local elastic modulus, when the true stress profile is know because calculating stress profile is very challenging in realsitc clinical scenarios due to 3D tissue geometry. (Céspedes & Ophir, 1993; Ophir *et al.*, 1991).

Strain estimation noise

When tissue is compressed, the strains are produced in three dimensions, while generally, axial displacements and strains are calculated. The lateral displacement estimation is challenging due to coarse resolution in the corresponding dimension, whereas, there is no elevational deformation data available in 2D ultrasound methods. Time delay (or displacement) estimation is a fundamental step for strain computation techniques. Using cross correlation for displacement estimation, an axial 1D kernel is selected from pre- and post-compressed beamformed RF frames as shown in Fig. 1.3 and argument of correlation function peak gives amount of spatial shift tissue has incurred and mapped to the spatial centre of the kernal (Pinton *et al.*, 2006; Viola & Walker, 2003). Axial strain at each point in the 2D image is calculated indirectly by the gradient of local displacement (Ophir *et al.*, 1991) or directly using stretching (de-compression) factor used to maximise correlation coefficient in an iterative process (Alam *et al.*, 1998; Varghese & Ophir, 1996).

In the strain imaging case, there are three sources of the strain estimation variance, which are ultrasound system electronic noise, axial sampling quantization noise, and decorrelation noise. The variance due to electronic noise can be reduced by taking the average of ultrasound frames (Varghese *et al.*, 1996). The second type of noise occurs due to finite axial sample frequency. As an example of the current study, 50 MHz sampling frequency and acoustic speed of 1500 m/s, spatial sampling period is 15 μm. When displacement is estimated using cross-correlation, true displacement may fall in between 0 and 15 μm or between multiples of 15, therefore due to course sampling estimated displacements are

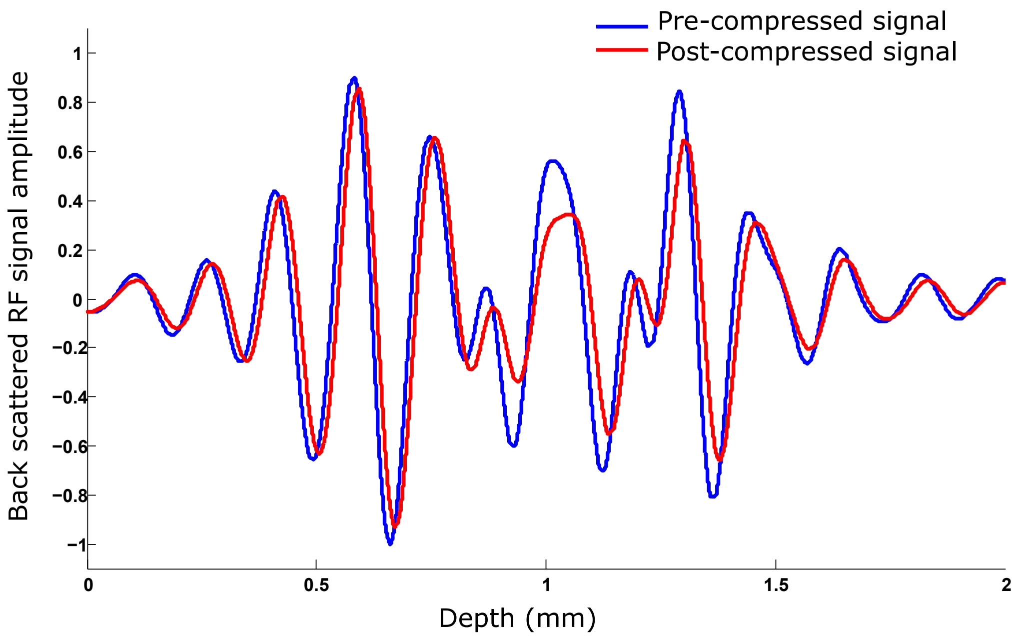

Figure 1.3: A sample kernel of 2 mm ($\sim 6\lambda$) of both pre- and post-compressed signals are shown here. It can be observed that, post-compressed signal (red) is shifted in position from pre-compressed signal (blue) within the kernel location. Actual amplitude of reflected RF data is normalised to unity. This speckle tracking step is repeated along the both axial and lateral dimensions to form 2D axial displacement image.

rounded towards true closer values. This limitation results in the quantization of the displacement estimates and adding to the strain estimation variance (errors) and can be resolved by the over-sampling of the RF data (Varghese *et al.*, 1996).

Dominating noise is decorrelation noise and is caused by the tissue compression. When the compression is applied, scatters moves closer to the each other (scaling), changing the scatterer distribution significantly relative to pre-compressed distribution. The reduced spacing between the scatterers causes mis-alignment between the peaks of the echo signals, and reducing coherence between the pre- and post-compressed signals. The intensity of the decorrelation is proportional to the applied compression, and it can be observed in Fig. 1.4, where correlation functions for gated A-lines selected from three different applied strains are presented. The blue plot shows the autocorrelation function for pre-compressed signal, which is used as benchmark for comparison, while red, green and cyan plots are produced using 0.22% (200 μm), 0.44% (400 μm), and 0.67% (600 μm) applied strain values. It can be noticed, as the applied strain is increasing, the correlation peaks are reducing, as for 0.67% applied strain, correlation peak falls below the 0.6, which indicates poor coherence. To minimise the decorrelation noise in the axial dimension, temporal stretching was proposed by the (Varghese *et al.*, 1996). Temporal stretching is an electronic attempt to increase the coherence by applying a reverse time-scaling operation and is implemented by upsampling using interpolation where the interpolation factor is the function of applied strain (Alam *et al.*, 1998). Impact of temporal stretching can be observed in Fig. 1.5. In Fig. 1.5a, gated 4 mm signals for pre-compressed and 0.89% strain are plotted, where mis-alignment between the echo peaks can be noticed. The post-compressed signal is temporally stretched and plotted in the Fig. 1.5b, where temporal stretching has minimised decorrelation and aligned the echo peaks. The improvement in the coherence due to temporal stretching has improved and correlation peak amplitude is increased from 0.56 to 0.78 and alternatively quality of the strain estimation as correlation coefficient is the measure of coherence between correlated signals (see Fig. 1.5c).

In an attempt to minimise noise contamination in the signals, various methods were proposed. As an example, the sonographic SNR can be improved by averaging multiple events of RF data acquisitions, the noise due to course axial sampling can be minimised by interpolating between the RF data samples, the multi-compression averaging (MA) (Alam & Ophir, 1997) and 3D companding (Chaturvedi *et al.*, 1998) was used to reduce lateral and elevational noise contributions, and axial temporal stretching can be used for recovering signals distorted by the axial tissue compression. This phenomenon was investigated in detail by (Srinivasan *et al.*, 2002) using a simulation study, and concluded that TDE based bias could result in elastogram measured elastographic SNR higher than the theoretically calculated elastographic SNR (alternatively called theoretical upper bound on elastographic SNR). This study used correlation coefficient measured from the elastogram to calculate theoretical upper bound calculations for consistent strain estimation quality measurements.

Limitation of strain elastography Generally, multiple deformation images are acquired using various small increments of displacements. The final image can be selected from produced strain images, either image with the best quality or multiple good quality images can be averaged to produce final low-noise elastogram. For good strain image quality, an intermediate applied strains are preferred as higher values are favourable in terms of displacement SNR but in parallel higher strains lead to noisy estimations (Wells & Liang, 2011). Nevertheless, there is need to develop robust quality metrics which ensure selection of reliable strain image among multiple compression images for accurate clinical diagnosis. Strain elastography is implemented on various ultrasound machines as listed in Table. 1.1 and in some systems it is called Real Time Elastography (RTE).

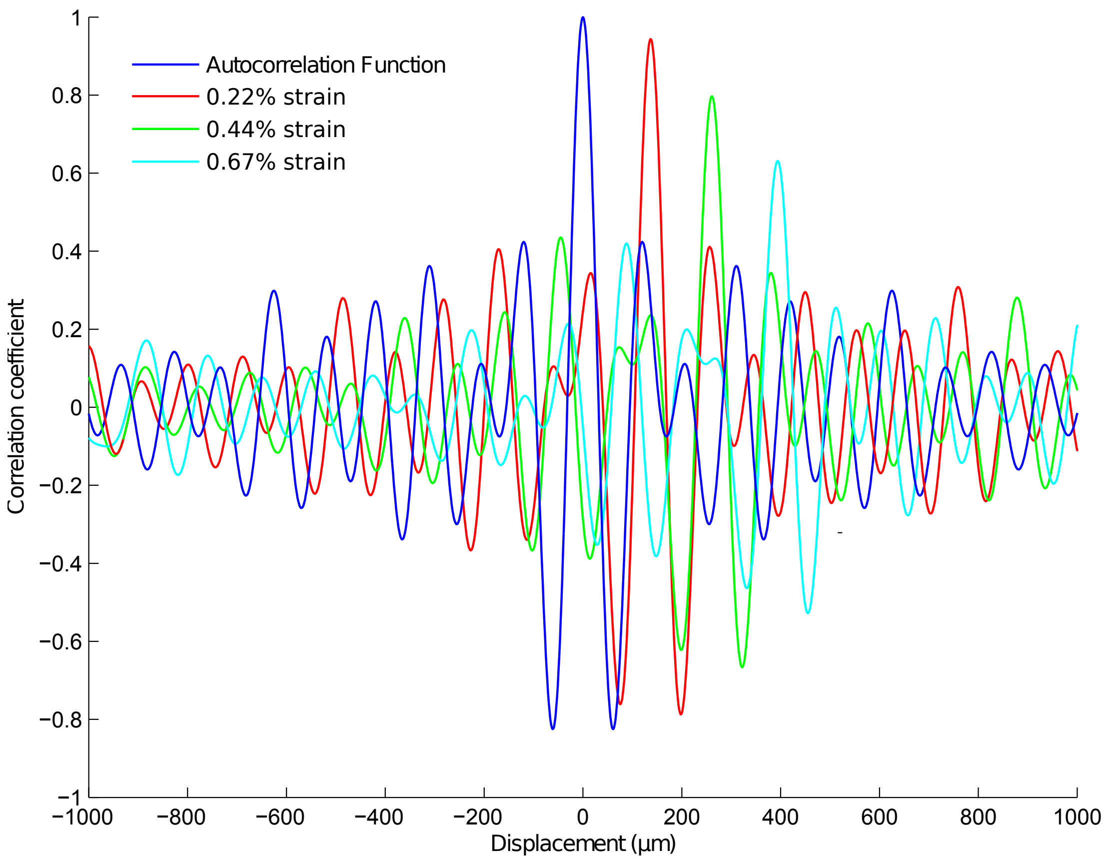

Figure 1.4: Decorrelation noise increased as the applied strain is increased and in result correlation peak reduces. The blue colour shows an autocorrelation functions of the pre-compressed signal, which is used as a benchmark for comparing cross correlation plots of compressed A-line signals. The cross correlation functions are plotted for 0.22% (200 μm), 0.44% (400 μm), and 0.67% (600 μm) applied strain using ultrasound probe. The moving correlation peaks indicate increasing time delay between pre- and post-compressed signal. As the applied strain is increasing, correlation peak amplitude is reducing, indicates coherence is decreasing for higher compressions. Key parameters for these acquired signals are centre frequency (f_c) = 5.5 MHz, bandwidth = 5 MHz, correlation window length = 5 mm.

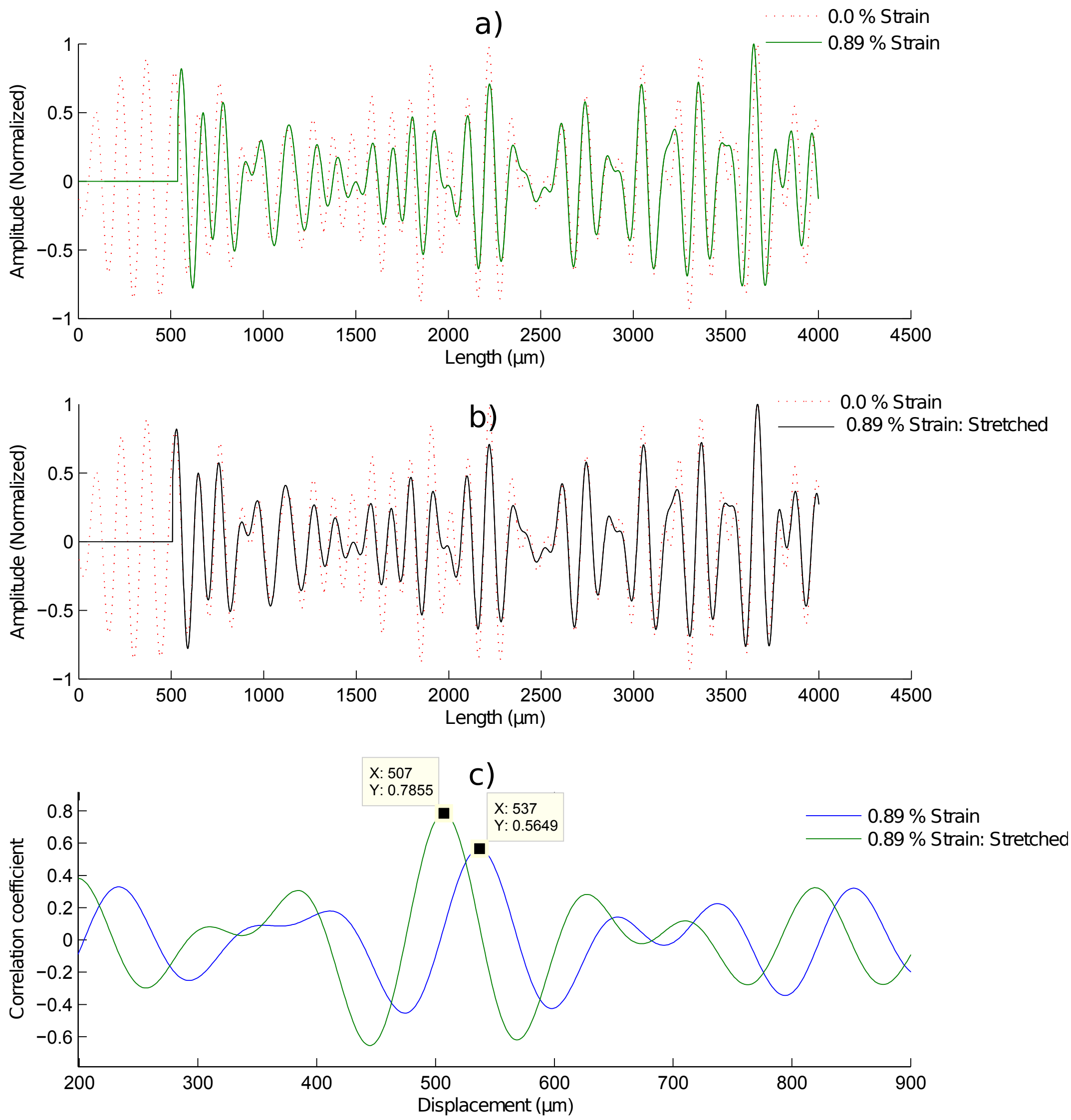

Figure 1.5: Effect of the temporal stretching on coherence improvement is presented using cross correlation functions of un-stretched and stretched signals. a) A 5 mm segments of pre-compressed and 0.89% compressed A-line signals. b) The 0.89% compressed signal is temporally stretched by a factor of 0.89%, and similarity between two compressed signals is relatively improved. c) Correlation functions for both un-stretched and stretched 0.89% data using normalized cross correlation are plotted. Data stickers indicate both displacement (x) and correlation coefficient (y) information. It can be noticed that, temporal stretching has improved correlation coefficient magnitude, and eventually coherence. Key parameters are centre frequency (f_c) = 5.5 MHz, bandwidth = 5 MHz, correlation window length = 5 mm.

Table 1.1: Strain elastography available on commercial systems

Company	System name
Siemens Healthcare	ACUSON S2000™ eSie Touch™
GE Healthcare	LOGIQ S8 and E9
Phillips Healthcare	iU22 and EPIQ
Toshiba	Aplio XG
Samsung Medison	HS40 ElastoScan™
Hitachi	HI VISION Avius™
Esoate	MyLab™Eight

1.5.2 Shear wave elastography theory

Strain elastography is based measurement of on stress and strain to recover elasticity of soft tissues, which is limited to provide relative and semi-quantitative information about stiffness due to highly challenging stress measurement requirements. An alternative method is to generate shear waves in tissues and measure Young's modulus by calculating the speed of propagating shear waves. In 1968, Professor Sarvazyan initiated the concept of using shear waves for soft tissue elasticity (Sarvazyan *et al.*, 1968), followed by series of research publications, and eventually lead to first successful implementation published in 1998 (Sarvazyan *et al.*, 1998), named as shear wave elasticity imaging (SWEI) and methodology. The SWEI used acoustic radiation force (ARF) to generate shear waves and tracking shear strain (displacement) using conventional speckle tracking methods. The relationship between shear wave propagation speed and elasticity of the tissues can be determined by the wave equation, which for a given medium is purely elastic, locally homogeneous, incompressible, and isotropic is expressed as (Manduca *et al.*, 2001; Sarvazyan *et al.*, 2013; Song, 2014):

$$G\nabla^2\psi + (K + G)\nabla(\nabla.\psi) = \rho\frac{\partial^2\psi}{\partial t^2} \tag{1.11}$$

where G denotes shear modulus, ψ is shear wave displacement, K is bulk modulus, ρ is the mass density and t is the time. Assuming there is pure shear wave propagation in the tissues, diverging vector fields are zero, thus $\nabla.\psi = 0$. The equation 1.11 can be simplified after replacing divergence part equal with zero:

$$G\nabla^2\psi = \rho\frac{\partial^2\psi}{\partial t^2} \tag{1.12}$$

This above equation is called the Helmholtz equation (Manduca *et al.*, 2001) and it can be re-arranged as:

$$G = \frac{\rho\frac{\partial^2\psi}{\partial t^2}}{\nabla^2\psi} \tag{1.13}$$

This above equation can simply be explained in terms of equation 1.3 for elastic modulus: the left side in both equations represent a mechanical property, which is related to each other using equation 1.9. The right side in equation 1.3 represents ratio of stress to strain, while in equation 1.13, the numerator denotes stress, while denominator represents strain. Eventually, both equations are reaching to similar objective using different phenomenon (Song, 2014).

One category of mathematical methods use equation 1.13 to reconstruct elastic modulus are called algebraic direct inversion methods. However, this method is not recommended for ultrasound based elastography methods because the noise level in the ultrasound signals can be further amplified after by double differentiation operation and specially the denominator term requires double differentiation in the spatial domain, which is relatively more contaminated with the noise than the displacement time profile (Bercoff *et al.*, 2004b; Manduca *et al.*, 2001; Song *et al.*, 2011). In magnetic resonance elastography (MRE), an algebraic direct inversion method is preferred to solve equation 1.13, due to low noise levels in tracking data specifically in the spatial dimension (Manduca *et al.*, 2001; Oliphant *et al.*, 2001). In an alternative way, shear modulus (G) can be calculated by measuring shear wave propagation speed (C_s) by tracking the shear wave front, using equation 1.9, where mass density does not vary significantly and is assumed uniform throughout the estimation region. equation 1.9 is the fundamental equation for calculating 2D elasticity maps for all shear wave based elastography techniques (Song *et al.*, 2011, 2012, 2013a, 2014). It is important to note that, equation 1.9

assumes that viscous component is equal to zero, and tissue is purely elastic, local homogeneous, incompressible and isotropic. Research suggests that, tissue assumptions of isotropy, incompressibility, and local homogeneity are valid for many kinds of imaging conditions, while viscosity varies among different organs and the degree of disease (Song, 2014). In this thesis, all studies conducted using shear wave elastography are focused on measurement of only elasticity component (Shear modulus or Young's modulus) of tissues, because measuring Young's modulus has been linked to having high clinical value and strong correlation with tissue pathology.

1.5.3 Ultrasound shear wave generation and detection

ARF based shear wave elastography methods use single transducer to generate and track shear waves, which offers similar conventional ultrasound clinical set up, which is convenient for patients and sonographers. In comparison to mechanical excitation, ARF based methods are relatively accurate due to absence of vibrator motion artefact and less out of imaging plane waves induced bias. Also, ARF induced shear waves are transient, and broadband which provides advantage for correlation analysis for shear wave speed detection, and dispersion analysis. Elastography approaches based on intrinsic excitations lack consistency, and reproducibility, also imaging is subjected to only physiological motion regions, relative to ARF based shear wave elastography methods (Song, 2014). ARF based shear wave techniques use long duration ($\sim 600\ \mu s$) 'push' pulses to apply a force called ARF on tissues. The exerted force (F) is a function of acoustic intensity (I) carried by compressional wave and tissue frequency-dependant attenuation (absorption and scattering) and acoustic speed (C_l), as expressed by the equation (Song, 2014):

$$F = \frac{2\alpha I}{C_l} \tag{1.14}$$

After shear wave generation, succeeding tissue motion detection or tracking is key part of shear wave elastography. In ARF-based methods, shear waves induce peak axial displacements on the order of tens of micrometers. Ultrasound B-mode imaging mode based tracking beams gather speckle tissue information at ultra-fast frame rate ($\sim$ 3-10 kHz) before and after shear wave generation for duration subjected to shear wave attenuation. Once B-image dataset for before (reference) and after shear wave generation (shifted) is obtained, ultrasound based time delay estimation can be used to produce 2D images of localised tissue motion. Time shift in speckle positions between frame t_1 and frame t_2 can be detected by performing normalised cross correlation on consecutive B-mode A-line gated RF reference (f_r) and shifted (f_s) signals, expressed as (Pinton *et al.*, 2006; Song, 2014):

$$\delta t = \arg(c(j)) = \frac{\sum_{i=-M/2}^{M/2} \left[f_r(i) - \bar{f}_r\right] \left[f_s(i+j) - \bar{f}_s(j)\right]}{\sqrt{\sum_{i=-M/2}^{M/2} \left[f_r(i) - \bar{f}_r\right]^2 \sum_{i=-M/2}^{M/2} \left[f_s(i+j) - \bar{f}_s(j)\right]^2}} \tag{1.15}$$

where $\bar{f}_r$ and $\bar{f}_s$ mean reference and shifted signals and M in samples is the size of gated RF data segments. The sample index where peak of the correlation function $c(j)$ occurs indicates time shift where two signals are highly similar to each other and thus can be used to measure local time shift δt between successive B-mode frames. Provided speckle shift in time is obtained, amount of shift into space (axial displacement) can be converted using following expression (Song, 2014):

$$\Delta s = \frac{C_l \delta t}{2} \tag{1.16}$$

Once shear wave spatial and temporal displacement dataset images are obtained, time of flight methods can be applied laterally on shear wave motion temporal profiles to detect shear wave speed and eventually shear modulus (McLaughlin & Renzi, 2006; Tanter *et al.*, 2008).

1.5.4 Shear wave elastography methods

Shear wave elastography can be categorised based on shear wave generation, which can be mechanically generated using vibrators (shakers), using acoustic radiation force, or by exploiting physiological tissue motion. Diagram of contemporary shear wave elastography schemes showing three different categories is presented in Fig. 1.6. Magnetic resonance elastography (MRE) generates shear waves externally using a shaker which vibrates at a fixed frequency ($\sim 50-200$ Hz) and tracks corresponding 3D tissue motion dataset using magnetic resonance imaging. MRE have an advantage of high quality tissue motion measurement, however, acquisition time, space, and cost limits clinical scope of the technique (Muthupillai *et al.*, 1996; Sack *et al.*, 2001; Sinkus *et al.*, 2000; Yin *et al.*, 2007). In Sonoelastography, two mechanical vibrators produce two shear waves at slightly distinct frequencies and resultant interference pattern generates crawling waves which were used to measure mechanical properties of tissues (Wu *et al.*, 2004, 2006). Researchers have also investigated the role of physiological motion induced shear waves to extract mechanical properties of tissues. For cardiac stiffness imaging, pulsive waves in the myocardium that are produced using systole were exploited by (Kanai, 2005, 2009). Another method tracked heart activation by measuring transient strains occurring in response to cardiac electrical activation and the technique was called electromechanical wave imaging (EWI) (Konofagou *et al.*, 2011; Pernot *et al.*, 2007; Provost *et al.*, 2011a,b; Vappou *et al.*, 2010). In another study, blood vessel pulsations induced motion was tracked to reconstruct mechanical properties of the brain (Weaver *et al.*, 2012).

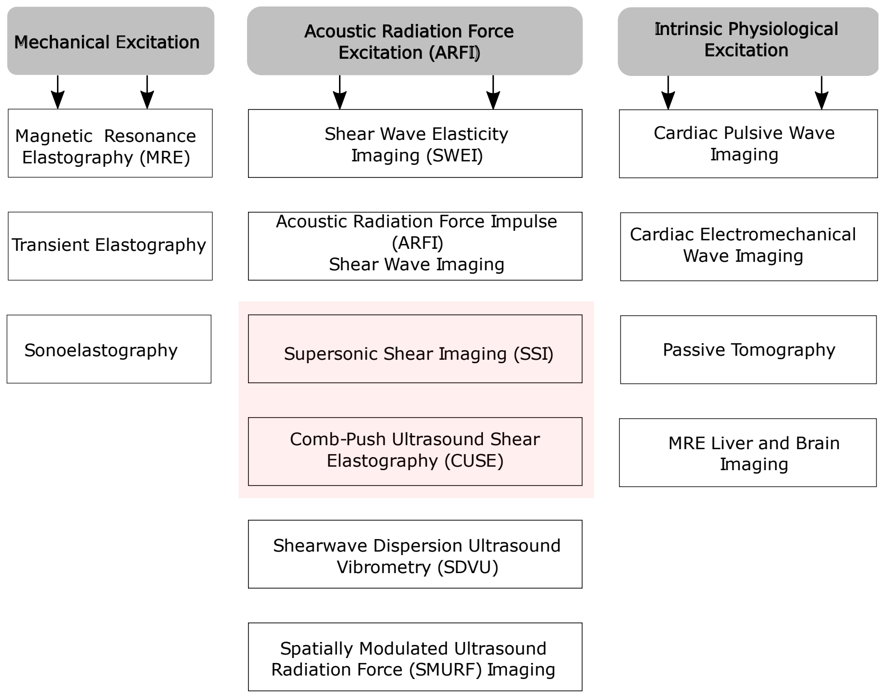

Figure 1.6: Contemporary shear wave elastography technqiues used to measure shear modulus of soft tissues are presented in this diagram. Here techniques are categorised based on method of generating shear waves such as (left) mechanically generating using a vibrator, (middle) using ultrasound probe inducing acoustic radiation force, and (right) using internal phsysiological excitations such as pulsation, cardiac contraction and expansion, and respiratory motion. In this chapter, SSI and CUSE techniques are reviewed in detail.

The first mathematical and experimental basis for shear acoustic waves remotely generated by radiation force was provided by (Sarvazyan *et al.*, 1998), named as Shear wave elasticity imaging (SWEI). The key objective of technique was to produce localised stress and strain, in contrast to strain elastography (Ophir *et al.*, 1991) (where stress was applied externally) and updated elastography from a semi-quantitative to a quantitative method, as presented using diagram in Fig. 1.7a. As a pilot study, shear wave generation was obtained using ultrasound focused beams generated by the therapeutic transducer, while MRI and optical systems were employed for tracking shear wave induced displacements, and shear wave speed was calculated by tracking shear wave front peaks along the lateral direction (Sarvazyan *et al.*, 1998). Finally, shear wave speed was used to calculated the shear and Young's modulus parameters (Sarvazyan *et al.*, 1998).

Professor Nightingale proposed the concept of localised remote palpation using acoustic radiation force generated by focused ultrasound beams and to measure dynamic displacement profiles to characterise tissue viscoelasticity (Nightingale *et al.*, 2001). The idea aimed to avoid unknown boundary condition issues by generating localised displacements which are less vulnerable to boundary conditions such as decorrelation noise in static elastography. The method used a single ultrasound diagnostic transducer to generate both localised displacements and tracked these displacements dynamically, and the method was called Acoustic Radiation Force Impulse (ARFI) imaging, as presented using diagram in Fig. 1.7a. This method provides semi-quantitative stiffness information because uniform radiation force can not be generated across the whole imaging region, as radiation force intensity is the function of beam geometry, tissue attenuation and elastic heterogeneities (Bercoff *et al.*, 2004b). ARFI forms a 2D stiffness image by repeating push and detect sequence for every point in the image, causing tissue heating problems which were analysed later to be within safe recommended levels (Palmeri & Nightingale, 2004). The method is commercially implemented by the Siemens (Siemens Healthcare, Erlangen, Germany) and named as Virtual Touch™tissue quantification. A research study compared static elastography and ARFI methods and results suggested relatively high performance for ARFI produced images for both homogeneous and heterogeneous conditions (Melodelima

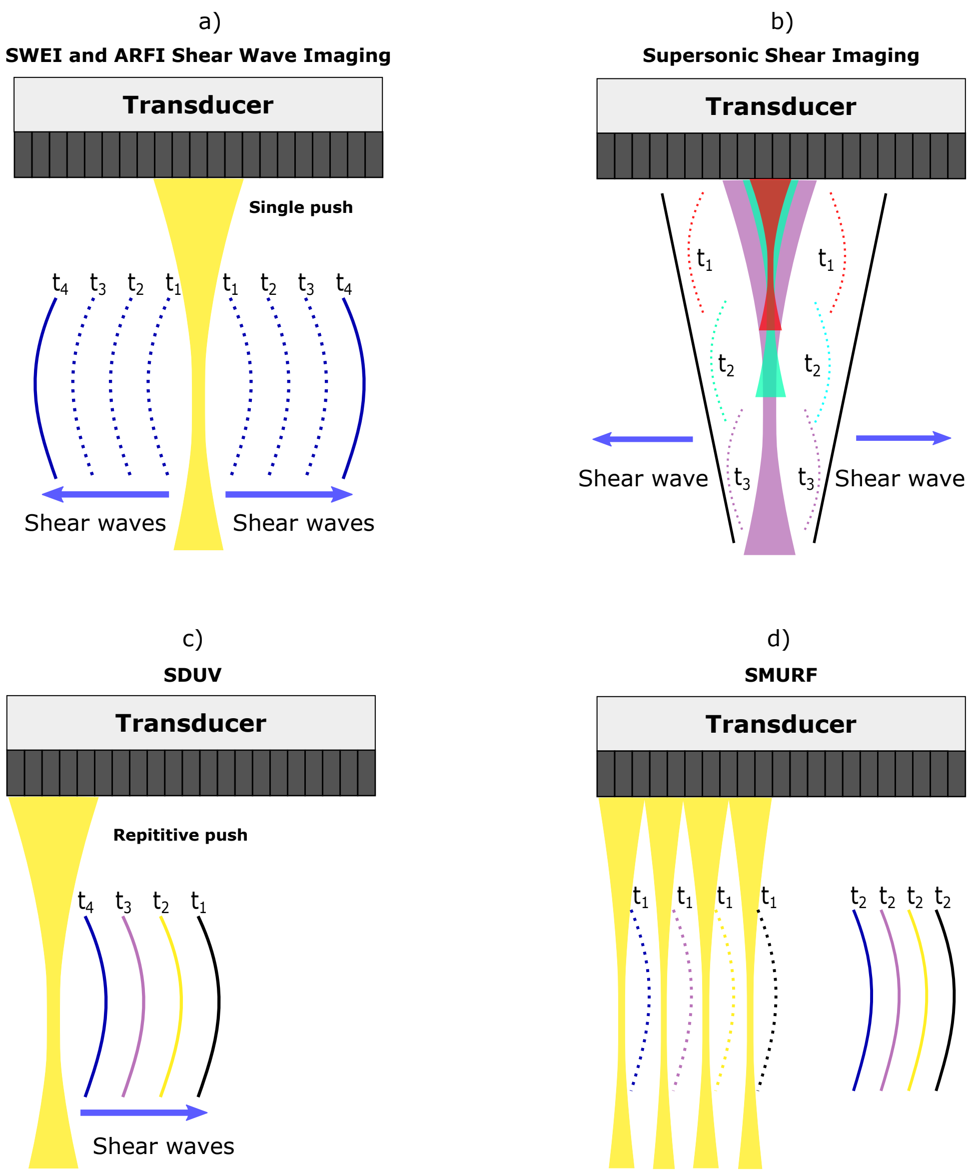

Figure 1.7: Schematic diagrams of shear wave elastography technqiues. a) SWEI and ARFI techniques both use focused single push beam to generate shear waves travelling away from the beam in both directions. Shear wave speed is estimated by measuring shear wavefront arrival time at different lateral locations. b) Supersonic shear imaging generates sequentially multiple push beams focused at increasing or decreasing depths to generate Mach cone shaped quasi-planner beam. shear wave speed estimation method is similar to SWEI and ARFI. c) SDVU method uses single focused push beam applied repetitively to generates harmonic shear waves and measures shear wave speed at multiple frequencies using Voigt model. d) SMURF places multiple focused push beams at known lateral locations and uses single A-line tracking beam to measure shear wave speed.

et al., 2007). In an extension of the work, a same group proposed single ultrasound diagnostic transducer based shear wave generation and tracking and used direct inversion method to extract local shear modulus using dynamic displacement profiles (Nightingale *et al.*, 2003).

Transient elastography (FibroScan®, Echosens, Paris, France) was proposed and used for grading liver fibrosis for hepatitis C virus (HCV) patients, which used a piston-like 50 Hz vibrator for shear wave generation, connected with a 5 MHz single element transducer, used for measuring induced displacement (Sandrin *et al.*, 2003). The measured hepatic stiffness (shear modulus) in this technique was an averaged value over sample size of 20 mm by 20 mm. The technique was specifically designed for liver fibrosis staging, a non-invasive, convenient, and efficient alternative to liver biopsy and prospective update of the technique into 2D was discussed and subjected to ultrafast ultrasonic imaging systems (Sandrin *et al.*, 2003). The subsequent research (Castéra *et al.*, 2005; Foucher *et al.*, 2006; Fraquelli *et al.*, 2007; Friedrich-Rust *et al.*, 2008) compared performance of the technique with other clinical biomarkers and resulted similar performance. The method has the disadvantage of using heavy and bulky external vibrators and subjected to spatial directivity pattern biases (Bercoff *et al.*, 2004b).

In the aspiration to design a quantitative technique which can measure both elasticity and viscosity using conventional low frame-rate ultrasound scanners, Professor Greenleaf group developed a Shearwave dispersion ultrasound vibrometry (SDVU) technique which divides transducer aperture into two parts and uses each as ‘push’ and ‘detect’ beam sub-apertures, as presented using diagram in Fig. 1.7c (Chen *et al.*, 2004). The push sub-aperture part transmits a continuous amplitude modulated (AM) ultrasound beam to generate harmonic shear waves with frequency on the order of hundreds of Hertz, while simultaneously detect beam is placed along the propagation path at known location and shear wave speed is measured by tracking phase change using homogeneous Voigt medium (Chen *et al.*, 2004). The shear wave at various frequencies can be generated by controlling modulating frequency of AM ultrasound and dispersion can be extracted (Amador *et al.*, 2011; Chen *et al.*, 2009). Another technique developed by the Mcleavey *et al.* generated shear waves of known spatial frequency (inverse of wavelength) and measured shear wave temporal frequency using standard A-line tracking beams (McAleavey *et al.*, 2007). The final shear wave speed was calculated using assumed mass density, known spatial frequency and measured temporal frequency, and the technique was named as spatially modulated ultrasound radiation force (SMURF), as presented using diagram in Fig. 1.7d (McAleavey *et al.*, 2009, 2007).

Among ARF techniques, SSI and CUSE based techniques have been relatively efficient and convenient to achieve 2D non-invasive elasticity image in clinical conditions. The next section presents a detailed insight into both the techniques and understands working principles, advantages, pitfalls, challenges and clinical utility of each technique.

Supersonic Shear Imaging (SSI)

Acoustic radiation based shear wave generation, and ultra-fast plane wave imaging based shear wave tracking was first demonstrated by (Bercoff *et al.*, 2004b) to produce a 2D Young's modulus maps of phantoms and *in vivo* breast investigation, which was preceded by preliminary studies (Bercoff *et al.*, 2002, 2004a). The method used five focused radiation force beams called push beams, placed at different axial locations, to fill the imaging region with high amplitude shear waves, as presented using diagram in Fig. 1.7b. The push beam (shear wave source) speed is configured relative to assumed tissue shear modulus in a way that, constructive and destructive interference of shear wave from each push beam produces a Mach cone, as produced by supersonic aircraft, and the technique was named as Supersonic Shear Imaging (SSI). Advantage of placing multiple push beams at successive depth was to enhance amplitude of shear waves, and improve axial extension of shear wave generation. The Mach cone angle is function of pushin beam speed, and speed of generated shear waves, and push beam speed higher than the shear wave speed creates Mach numbers greater than one. Mach numbers greater than six generate plane shear wave beam and can be varied between one and six for various push beam geometries, where each can travel at different angle. Shear wave tracking in the whole 2D imaging region was made possible by exciting all the transducer elements simultaneously with plane waves and acquiring RF data at frame rates of up to 6000 frames/sec. Before shear wave generation, a sequence of reference frames are acquired using plane wave imaging mode. Shear wave generation uses multiple high-intensity focused beams, followed by shear wave tracking using unfocused plane aperture beams for typical duration of 15 to 25 ms. Shear wave speed were measured using inversion algorithm and local displacement temporal data generated by shear waves outside the focused beam region, while shear elasticity inside the radiation force beam area could not be recovered as the shear term is extremely weak, and the region is called 'dead zone'. In the same study, compounding multiple angle B-mode images was proposed to reduce elasticity estimation errors, and was named as shear compounding. Using this technique, quantitative 2D estimates of tissue elasticity were obtained for homogeneous, inclusion-based phantom, and *in vivo* healthy breast study, while ultrasound exposure maintained under the Food and Drugs Organization (FDA) recommendations such as mechanical index (MI) and thermal index (TI). The technique have also reduced operator dependency, as experienced by static elastography (Bercoff *et al.*, 2004b).

Limitation of SSI Two limitations are observed for the SSI based shear wave elastography scheme. One of the limitation is SSI used shear wave beams placed at single location along the FOV, this results in poor shear wave SNR at left and right edges of the imaging region. Further, conventional SSI could not reconstruct shear wave speed where push beams are placed called 'dead zone'. To resolve this, three SSI events were used to produce full FOV elasticity map, which eventually increased ultrasound exposure, signal processing, and acquisition time (Muller *et al.*, 2009; Tanter *et al.*, 2008). Another limitation is related with shear wave compounding, where shear waves are generated at multiple angles while tracking beams remain as zero-angle plane waves. This results in the mis-alignment between shear wave induced displacement direction and tracking beams, and eventually errors in estimated displacement.

Comb-Push Ultrasound Shear Elastography (CUSE)

Shigao *et al.* evaluated feasibility of unfocused beams for shear wave generation and produced elasticity maps over relatively good axial extent (10-40 mm for linear array and 15-60 mm for curved array). The shear wave speeds were cross-validated using MRE, 1D transient elastography and calibrated commercial CIRS (CIRS, Inc. Norfolk, VA) phantoms. Shear wave peak axial displacements up to 30 μm were generated were produced using unfocused beams, and travelled up to 10 mm before being attenuated completely. Observed shear waves speeds were consistent along the depth, in contrast to focused beams where depth-dependent bias was observed for linear arrays (Zhao *et al.*, 2011b). Depth-dependent bias for curved linear array was observed and it enhanced as push beam aperture was increased. However, axial extent of the imaging was limited due to poor shear wave energy at deeper regions, and lateral extent due to high shear wave attenuation (Chen *et al.*, 2011; Zhao *et al.*, 2012). Later, four unfocused push beams called comb-push pattern (where each push beam was treated as teeth of a comb) were used for Spatially modulated ultrasound radiation force (SMURF) technique which uses single A-line for shear wave tracking (Zhao *et al.*, 2011a).

Song *et al.* combined unfocused comb-push pattern based shear wave generation and ultrafast ultrasound imaging capacity and developed a new technique called unfocused Comb-push Ultrasound Shear wave Elastography (U-CUSE). The shear wave field travelled laterally in both the left and right directions, generating constructive and destructive interference patterns which were separated using directional filters (Deffieux *et al.*, 2011) and elasticity maps were produced for both left-travelling and right-travelling shear waves (Song *et al.*, 2012). The final 2D Young's modulus map was obtained by concatenating left-travelling and right-travelling shear wave field maps (Song *et al.*, 2012). The CUSE successfully reconstructed 2D elasticity map for full FOV in a single shear wave generation and tracking sequence, also called push-detect event. The CUSE addressed both shear wave attenuation limitation and multiple push-detect event requirement faced by the SSI based elastography technique (Song *et al.*, 2012). The method increased imaging area where sufficient shear wave energy is available by placing shear wave sources at five lateral locations in comb-push pattern. After one year, the same research group investigated other two shear wave generation beams in a comb-push pattern, named as Focused CUSE (F-CUSE) and Marching CUSE (M-CUSE). F-CUSE used four focused push-beams generated simultaneously along lateral dimension, while M-CUSE applied four focused push-beams sequentially along lateral direction to fill the whole FOV with shear wave energy. Results suggested that, both techniques increased penetration depth of shear waves relative to U-CUSE method, while F-CUSE was found superior to M-CUSE, because transducer is more vulnerable to heating in M-CUSE method (Song *et al.*, 2013a).

In an attempt to spread shear wave sources across the imaging region equally and enable shear wave energy at every pixel in the image, in 2014 Nabavizadeh *et al.* proposed steered push beam (SPB) technique. The SPB technique used multiple intersecting steered and unfocused push beams placed along the lateral image plane to generate shear wave field. The study conducted using homogeneous and inclusion-based phantoms produced elasticity maps of comparable performance or better in some cases relative to U-CUSE and F-CUSE techniques. It was observed that, shear wave SNR was slightly less than produced by F-CUSE due to use of unfocused beams (Nabavizadeh *et al.*, 2014, 2015). To improve shear wave elasticity estimation accuracy, Song *et al.* presented shear compounding where multiple angle shear wave field elasticity maps were produced in a single push-detect event and final averaged elasticity map demonstrated reduced estimation variance and improved inclusion reconstruction (Song *et al.*, 2014).

ARF based SWE techniques are currently implemented on medical ultrasound machines such as SSI is implemented on Aixplorer (Supersonic Imagine, Aix-en-Province, France), ARFI SWE is implemented on ACUSON S2000 and S3000 ultrasound systems (Siemens Healthcare, Erlangen, Germany), commercially named as Virtual Touch^{TM} quantification and on EPIQ 5 (Phillips, Medical Systems, Best, Netherlands) and LOGIQ E9 (GE Healthcare, UK) scanner is also equipped with ARF based shear wave elastography method.

1.5.5 Clinical application of shear wave elastography

Shear wave elastography techniques are clinically experimented for various diseases, of which breast cancer and liver cirrhosis are major targets. Some of the clinical research is detailed in following paragraphs.

Breast cancer Breast cancer is the most common cause of the mortality among women and in 2012 around 1.7 million cases were recorded globally (Ferlay J, 2014). Carcinoma is the most common type of breast cancer which starts in the epithelial tissue cells, while another type of breast cancer is sarcomas which start in the cells of fat, muscle and connective tissue (World Cancer Research Fund, 2017). Breast cancer which are spread into surrounding breast tissues are called invasive while those which do not spread into the surroundings are known as in-situ cancers (World Cancer Research Fund, 2017). Breast carcinoma progresses over time and can be prevented by early detection. Shear wave elastography has incepted as complementary tool for diagnosis, and therapy management of breast cancer tissues. In 2008, a preliminary *in vivo* clinical investigation of breast cancer diagnosis using SSI was conducted, SSI results were compared with cytological and histological diagnosis as a reference method. The study diagnosed 15 patients, where 11 with benign and 4 with malignant lesions and Breast Imaging Recording and Data System (BI-RADS) was used for staging each lesion. It was observed that, elasticity maps provided good delineation between breast fatty tissues ($E \sim 5$ kPa), parenchyma ($E \sim 40$ kPa) and lesions ($E > 100$ kPa) and also lesion size detection was comparable with the size measurement using pathology. It was found that, benign solid lesion cases' mean elasticity was detected between Young's modulus of 45-80 kPa where malignant lesions demonstrated elasticity higher than 100 kPa and in some cases above 180 kPa. Results suggested that, in fluid-filled cysts regions, shear wave data was absent (in agreement with the shear wave theory), can be used to detect cysts like structure in breast (Tanter *et al.*, 2008). In order to develop elasticity cut-off values to differentiate beign and malignant lesions, a large-scale multi-center study was conducted (Berg *et al.*, 2012). The study suggested lesion stiffness greater than 160 kPa and B-mode BI-RADS score of 3 for biopsy, while BI-RADS 4a masses with elasticity less than 80 kPa for follow-up (Berg *et al.*, 2012). These cut-off values were also suggested by the two other independent studies (Athanasiou *et al.*, 2010b; Chang *et al.*, 2011). The clinical feasibility feasibility of U-CUSE was also evaluated for breast cancer (Denis *et al.*, 2015a,b) and promising results were observed.

Liver cirrhosis Liver fibrosis is natural healing response of the liver chronic injury such as viral infection, alcohoholic and non-alcoholic steatohepatitis and develop scary despositions slowly to cirrhosis and then Hepatocellular carcinoma

(HCC) (Pellicoro *et al.*, 2014). HCC is the second most leading cause of cancer-related deaths globally (Mohammed *et al.*, 2017). Bioposy is the 'gold standard' for fibrosis assessment and staging however non-invasive ultrasound elastography methods are intensely investigated as biopsy have drawbacks of invasiveness, very small specimen size, and interobserver variability (Albrecht *et al.*, 2017). The cut-off values for fibrosis varies among different shear wave elastography methods and are also system-specific (Albrecht *et al.*, 2017). TE is the most widely used technique, however accuracy of SSI method is comparable to the TE results (Cassinotto *et al.*, 2014). A feasibility study of SSI technique for quantitative viscoelastic characterization of liver was conducted on 15 healthy volunteers through intercostal window (Muller *et al.*, 2009). The results indicated clear delineation between Young's modulus values of intercostal muscle ($E \sim 100$ kPa) and healthy liver tissues ($E < 10$ kPa) (Muller *et al.*, 2009). Another clinical study for hepatic fibrosis in 113 patients was conducted and values were compared with transient elastography (FibroScan). A mean offset of 2.4 kPa was observed between SSI and FibroScan (FS) based measurements, and that difference was associated with distinct shear wave spectrum (SSI = 60 - 600 Hz and FS = 50 Hz) between these two techniques. SSI was credited to be superior to FS in accuracy having broadband shear wave signal and large imaging area (Bavu *et al.*, 2011). There are various cut-off values proposed for diagnosis and staging of liver disease while etiology and medical history factors are suggested to use for accurate diagnosis (Bavu *et al.*, 2011; Ferraioli *et al.*, 2015).

For shear wave elastography methods, there is a variability in elastic modulus estimation among techniques, ultrasound machines, transducers, and measurement depths (Dillman *et al.*, 2015; Hall *et al.*, 2013; Palmeri *et al.*, 2015; Shin *et al.*, 2016; Zhao *et al.*, 2011b). Therefore, it is highy challenging to set standard cut-off values for liver fibrosis staging as the range of values between two fibrosis stages (F2-F3) are on the order of 2-3 kPa, and a small shift in the values will change the result from one stage to another stage (Piscaglia *et al.*, 2016). Current research problem for shear wave elastography techniques is to understand the physical reasons of elasticity estimation variability and provide corrections to achieve standard cut-off values specially for liver fibrosis diagnosis and staging. Although, this problem poses a bigger challenges for liver elastography but resolving this issue is equally important for all tissue types.

1.6 Aim of the thesis

Aim of thesis is to identify and resolve challenges of current elastography schemes. During the literature review, four different challenges were observed. The aim of the thesis was achieved using five objectives. First objective was to design both strain and shear wave elastography transmit and receive signal processing flow and implement on the locally developed ultrasound machines. The other four objectives were to resolve and/or understand problems with the current shear wave elastography schemes as briefly presented in Sections. 1.5.1, 1.5.4 and 1.5.5.

1.7 Organisation of chapters

The thesis is organised in a way to explain how aim of the thesis is fulfilled. The Chapter 1 contain literature about the scope of ultrasound imaging, introduction to general ultrasound elastography, review of strain and shear wave elastography. The Chapter 2 explains and addresses limitation of strain elastography scheme. The Chapter 3 is allocated for understanding details of shear wave elastography implementation. The Chapter 4, 5 are allocated to address challenges briefly explained in the Section 1.5.4 while Chapter 6 is dedicated to identifying problems related to the challenge given in Section 1.5.5. Finally Chapter 7 summarises all the conducted research work along with presenting related future directions, and a list of publications. References for all chapters is listed at the end of this thesis. Here, each chapter is summarised in the following paragraphs.

Chapter 1 The first chapter presents an overview of ultrasound imaging followed by palpation and its relationship with the inception of ultrasound elastography. Fundamentals of general elasticity and specifically biological soft tissue elasticity is also covered in this chapter. Following this, a brief review of static strain elastography is presented.

Chapter 2 This chapter presents a novel quality evaluation method for strain elastography which guides to select accurate strain map among multiple compression images. The study also implemented strain elastography on the UARP I ultrasound system and applied the proposed method to two different size inclusion phantom studies.

Chapter 3 This chapter focuses on the basics of shear wave elastography, followed by a brief review of current shear wave elastography method. A detailed review of two commercially implemented shear wave elastography techniques SSI and CUSE is given. Finally, implementation details of shear wave elastography schemes implemented on the recently developed ultrasound system UARP II are presented.

Chapter 4 This chapter presents a novel shear wave generation scheme based on two lateral shear wave beams applied simultaneously, called Dual Push Beam (DPB) shear wave elastography. This method addressed the limitation of conventional shear wave elastography methods such as SSI and formed 2D whole field of view elasticity map non-invasively in a single acquisition event. The DPB also improved shear wave generation depth in compression to other shear wave methods such as U-CUSE and F-CUSE.

Chapter 5 Chapter 5 presents a novel shear wave tracking method for steered shear wave propagation. A Phantom based experimental study suggested that the proposed method is able to suppress displacement direction artefacts and improve shear wave displacement amplitude in comparison to the conventional method of shear wave detection.

Chapter 6 This chapter presents a study which investigated the variability of shear wave speed across the elasticity map when push beam aperture and focal depth are changed. The results indicated small variability across elasticity image for medium size push beam apertures, and high for variability for large size apertures, which may lead to errors in diagnosis of liver fibrosis.

Chapter 7 This chapter summarises and concludes all the research work presented in this thesis, and directions of future work are also proposed.

Chapter 2

Two-way Approach for Quality Evaluation of Elastograms

2.1 Introduction

In strain elastography, it is well-established that there is a band-pass characteristic relationship between applied strain and quality of the images (Varghese & Ophir, 1997a). The strain images produced from the very low and very high applied strain fields are highly noisy and intermediate strains generate optimal elastograms. Therefore, in both experimental and clinical conditions, different deformations are applied and multiple strain images are produced. For final diagnosis, there is a need to select accurate and reliable elastogram among multiple produced images. This study aims to deal with the tracking quality of the strain images to select reliable strain map among images produced using multiple deformations and presents a novel method which addresses the limitations of previous methods.

Conventionally, elastographic signal to noise ratio (SNR) for homogeneous medium, and elastographic contrast to noise (CNR) ratio for heterogeneous medium are used as quality metrics, mathematically expressed as (Alam *et al.*, 1998).

$$\mathrm{SNR} = \frac{\bar{s}}{std(s)} \tag{2.1}$$

$$\text{CNR} = \frac{2(\bar{s}_i - \bar{s}_b)}{std(s_i) + std(s_b)} \tag{2.2}$$

The $\bar{s}_i$ and $\bar{s}_b$ are mean strain for inclusion and background, while $std(s_i)$ and $std(s_b)$ are strain standard deviation for inclusion and background portions respectively (Alam *et al.*, 1998).

For inclusion based phantoms, lesion detectability performance is assessed by measuring image contrast between the inclusion and surrounding tissues. In the elastographic research literature, while characterising the quality for lesion detectability only CNR is used as a quality metric and strain images producing higher CNR values are considered high quality estimation (Alam *et al.*, 1998; Bilgen, 1999). In this research it is observed that, optimal elstograms selection based on only CNR is often misleading because higher contrast does not guarantee accurate estimation as higher CNR may result from the inaccurate estimations due to high noise present in the RF signals. The higher CNR can only be relied when adequate level of strain estimation accuracy is maintained and signals used for tissue motion preserve significant coherence. This observation also has been made in the simulation study by (Srinivasan *et al.*, 2002), where correlation coefficient measured from the elastograms included in the upper bound on strain SNR expressions. The strain estimation accuracy is determined by the amount of coherence between pre- and post-compressed signals, and can be measured using cross correlation coefficient.

Quality of the strain imaging relies on the faithful matching between signals and that is represented by correlation coefficient. In 2010, Cambridge research group proposed a method to track quality of strain estimation at pixel level used amplitude of the ultrasound signal and red-masked the pixels of low quality (Chen *et al.*, 2010; Lindop *et al.*, 2008). However, using amplitude to measure strain estimation accuracy is very weak metric as accuracy partially depends on the ultrasound signal SNR, while other factors such as tissue, applied deformation, and transmission signal parameters also contribute to the overall accuracy of the strain images (Lindop *et al.*, 2008). For medical use, in order to improve the diagnostic confidence of the strain imaging technique, images need to be as accurate and reliable as possible. This requirement necessitates another quality metric along with CNR which increases the diagnostic accuracy and helps to scrutinise the optimal strain image. There is currently no method which quantifies the accuracy of strain estimation at the pixel level which ensures that there is an adequate level of contrast between inclusion and background and also confirms that there is significant coherence of signals which is required for the accurate strain estimation.

In this study, a novel metric based on correlation coefficient named the noise masked area (NMA) percentage is introduced along with CNR. The NMA percentage calculates and locates the area of the strain image where strain calculation correlation coefficient ($\hat{\rho}$) falls below a -3 dB level ($i.e$ $\hat{\rho} < 0.7$). Three phantoms studies are conducted and the proposed method is applied for inclusion based phantoms.

2.2 Materials and methods

In this section, tissue mimicking phantom preparation details are presented. Further it includes RF data acquisition details, signal processing flow and algorithms used to produce 2D strain image.

2.2.1 Tissue-mimicking phantom preparation

Tissue-mimicking (TM) phantoms are prepared to accurately mimic acoustical propagation ($i.e$ speed, attenuation), and stiffness of tissue of interest and/or to replicate pathological conditions such as lesion with properties such as stiffness, shape and size. For strain imaging experiments, only contrast ratio between inclusion and background is needed which can be achieved by the varying the proportions of the materials during preparation (Madsen *et al.*, 2005).

An agar (Science Lab, Inc.) and gelatin (Science Lab, Inc.) based formula was used for the preparation of homogeneous and heterogeneous phantoms (Madsen *et al.*, 2005). Three different phantoms were fabricated in the laboratory, one without inclusion and two with 10 mm and 5 mm cylindrical inclusions. Homogeneous phantom (see Fig. 2.1c) is prepared to validate strain estimation performance for phantoms without inclusions. Two heterogeneous phantoms are

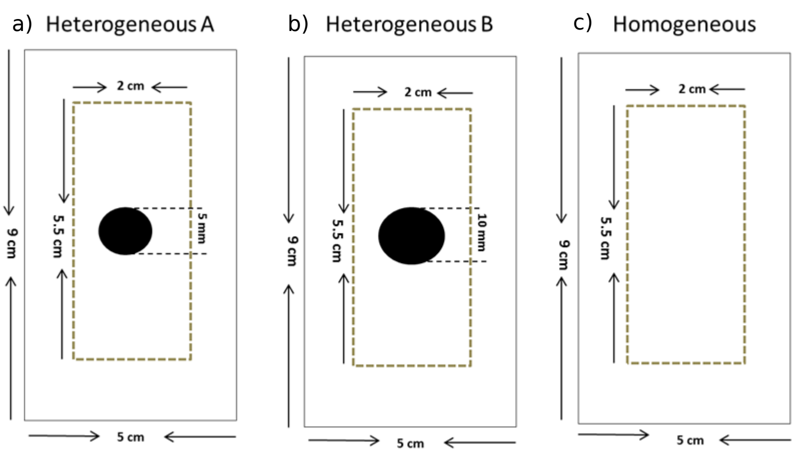

Figure 2.1: Geometry of all three phantoms, while inner dashed rectangles indicate imaging region. a) Heterogeneous phantom with 5 mm inclusion. b) Heterogeneous phantom with 10 mm inclusion. c) Homogeneous Phantom.

fabricated with less stiff background medium and 5 mm and 10 mm cylindrical inclusions with three times stiffer than the surrounding material (see Fig. 2.1a and Fig. 2.1b). Heterogeneous phantoms are used to assess strain imaging capacity to detect different size stiffer targets embedded in the softer background.

Heterogeneous phantoms preparation in two steps. First, background part is prepared and inclusion mixture is poured into the cylindrical holes. For homogeneous phantom, only background material is prepared. The process involved first preparing solutions of agar and gelatin separately with added glass bead scatters, then mixing together. After the mixture was cooled down, it was poured into the container. To avoid bacterial infections, a preservative germall® plus (ISP chemicals, LLC) was added in the phantom solution. In the heterogeneous phantom preparation, the procedure was similar to homogeneous, only the agar percentage for the inclusion were varied to achieve higher stiffness. In the phantom preparation, amount of agar determines stiffness in the phantom, therefore agar portion in the inclusion is three three times higher than the background, while gelatin percentage was uniform both in the background and the inclusion preparation (see Table. 2.1). For speckle generation, soda-lime glass beads (mo.sci, corp) with average diameter of 20 μm were used, where glass wet percentage for inclusion was higher than the background to achieve B-mode contrast. Acoustic speed of both parts of the phantom was measured equal to 1540 ± 5 m/s using pulse-catch method.

Table 2.1: Phantom preparation material in weight percentage

Material	Agar	Gelatin	Glass beads	Germall plus	Distilled water
Background	1.17	3.60	4.60	1.45	89.18
Inclusion	3.53	3.60	5.60	1.45	85.82

2.2.2 RF data acquisition

RF data acquisition was obtained using a custom-built 96 channel ultrasound system named as Ultrasound Array Research Platform I (UARP I) developed by the Ultrasound Group, University of Leeds (Smith *et al.*, 2012). The UARP I was connected with 128 element L3-8/40EP medical probe (Prosonic.co, Ltd), excited by a Gaussian pulse with a -6 dB bandwidth of 5 MHz, and centred at 5.5 MHz. The transmit beams were focused at 55 mm depth and in the receive mode, delay and sum beamformer was applied to produce each scan line. The 32 element sub-aperture for each scan line was used and total 65 lines were combined to form full B-mode mode image. The lateral width of the image was equal to 20 mm. All the backscattered echoes were received at 50 MHz sampling frequency. The RF data acquisition parameters are listed in Table. 2.2. After data acquisition, un-beamformed RF data were bandpass filtered, beamformed, amplified for frequency and depth dependant attenuations. A sample of three B-mode images formed using all three phantoms is shown in Fig. 2.2. These images clearly indicate that conventional ultrasound imaging is indifferent to the elasticity variations along the tissues, and elasticity change do not necessarily alter the echogenecity of the tissues, therefore B-mode images conveyed no elasticity information about the tissues.

Table 2.2: Ultrasound array transducer and RF data acquisition parameters

Parameter	Value
Transducer Name	Prosonic L3-8/40EP
Transducer Elements	128
Transducer Centre Frequency	4.79 MHz
Transducer Fractional Bandwidth (-6 dB)	57.2 %
Transducer Element Pitch	0.3048 mm
Transducer Elevation Focus	20 mm
Transducer Elevation Aperture Size	6 mm
Transducer Field of View	38.71 mm
UARP I Transmit Sampling Frequency	80 MHz
UARP I Receive Sampling Frequency (f_s)	50 MHz
UARP I channels	96
Excitation Pulse Centre Frequency (f_c)	5.5 MHz
Imaging Plane (Axial and Lateral)	20-75 mm and 20 mm
Focal Depth	55 mm
Beam Aperture Size	32 Elements
Lateral Lines	65

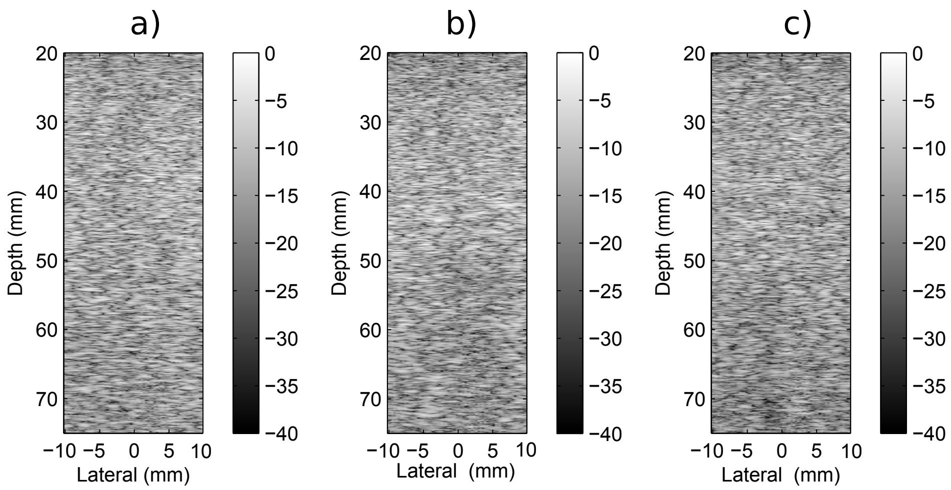

Figure 2.2: A sample of the B-mode Images for all three phantoms is shown where it can be clearly seen that B-mode images are not able to detecte elastic targets. a) Homogeneous phantom. b) 10 mm inclusion phantom. c) 5 mm inclusion phantom. These images were produced using 0.44% applied strain data frames.

2.2.3 Strain estimation

In this chapter, to achieve robust strain estimation, adaptive temporal stretching method was used, which uses local stretching factor to directly calculate local strain and it is designed as an iterative scheme, which iteratively applies possible range of stretching factors on the gated signals until the maximum correlation coefficient is obtained and search is exhausted Alam1998. To reduce displacement quantization errors due to sub-sample delays, before performing strain estimation operation, RF data is interpolated using spline interpolation and sampling frequency is up-sampled 5 times to achieve 250 MHz. Interpolation factors between 2 and 20 with an increment of 1 were investigated and it was found that quality of the elasticity image is saturated after 5 times, thus 5 times up-sampling was chosen for all the experiments.To select optimal data window and overlap for cross correlation analysis, various length windows were investigated and 4 mm data window with separation of 0.5 mm between two consecutive windows was found optimal. The lower size windows increases the axial resolution of the strain images, but reduce the quality of correlation analysis (Varghese & Ophir, 1997b).

Finally, a 3 x 3 median filter was applied on the strain images to remove strain estimation outliers. All parameters are summarised in Table. 2.3.

Table 2.3: Signal processing parameters displacement estimation

Parameter	Value
Acoustic speed (c)	1500 m/s
Correlation Window length (T)	4 mm
Correlation window separation (ΔT)	0.5 mm
Up-sampling	5 times
Median Filtering	3 $\times$ 3 filter

2.2.4 Elastogram quality estimation approach

In this study, a two-way quality estimation approach is proposed combining conventional metric CNR with the correlation coefficient based metric, called noise masked area (NMA) percentage. The NMA percentage is defined as percentage of the strain correlation coefficient $\hat{\rho}$ value lower than 0.7 (-3 dB cut-off point), where correlation coefficient equal to 1 indicates perfect coherence between signals and is expressed as;

$$\text{NMA}(\%) = \frac{\hat{\rho} < 0.7}{\text{total } \hat{\rho}} \times 100 \tag{2.3}$$

In order to calculate the quality of a strain image with an inclusion, first region-of-interest (ROI) are placed inside and outside the inclusion. It is recommended that, ROI for background is selected at the same depth as of the inclusion to ensure that stress field is same for both inclusion and background. In strain elastography, the area closer to transducer may be noisy therefore ROI needs to placed where consistent uniform strain values are achieved in most of the strain images. In the second step, elastographic CNR between lesion and background is calculated using equation 2.2 and normalised by the maximum value for all images. All the normalized CNR values which are greater than the 0.7 (-3 dB value) threshold level are regarded as possessing the significant level of CNR and are selected for the third step. In the third step, NMA percentage is calculated using equation 2.3 for all images and out of the elastograms which are above CNR threshold, one possessing the lowest value of NMA percentage is selected as relatively accurate strain image. In the fifth step, for clinical diagnostic use, only strain image with the optimal quality is displayed, whereas noisy pixels of the strain image are masked by the grey colour, to further localise image pixels with poor strain quality.

To evaluate the proposed concept, three different experimental studies are conducted, including a homogeneous study and two heterogeneous studies. The strain images are produced for all three different phantoms, in each study strain estimation quality is analysed and most reliable strain images are selected.

2.2.5 Homogeneous phantom study

The objective of the homogeneous phantom study is to validate implementation of the strain imaging using the UARP I ultrasound system and to evaluate performance of the strain estimation. This subsection includes details of the experimental setup, and quality metrics such as strain SNR and NMA are summarised and presented.

Experimental setup

In this study, a homogeneous phantom was used for acquiring RF data, where the medical probe is placed at the surface of the phantom (see Fig. 2.3). Between transducer and the phantom surface, ultrasound gel was used to avoid back reflections due to impedance mismatch. The probe with translation stage (Thorlabs, Inc, USA) to regulate the required applied compression. First, RF image was collected without compressing the phantom surface using ultrasound acquisition parameters detailed in Table. 2.2, and this image is used as a reference image to measure strain for subsequent compressed RF data acquisitions. After a reference RF speckle image is obtained, the probe was moved 200 μm in the axial direction to produce a strain field in the phantom and another RF image with displaced speckles was captured keeping all other parameters intact. The axial phantom dimension was equal to 90 mm, and the applied displacement of 200 μm which converts to strain percentage equal to 0.22 %. Following the similar acquisition method, a total of 16 compressed RF images were acquired with incremental strain of 0.22 % for each image up to maximum strain of 3.5 %. The axial imaging region spans from 20 mm to 75 mm, while transmit beams were focused at 45 mm, and total RF data of 55 mm were acquired for each compression.

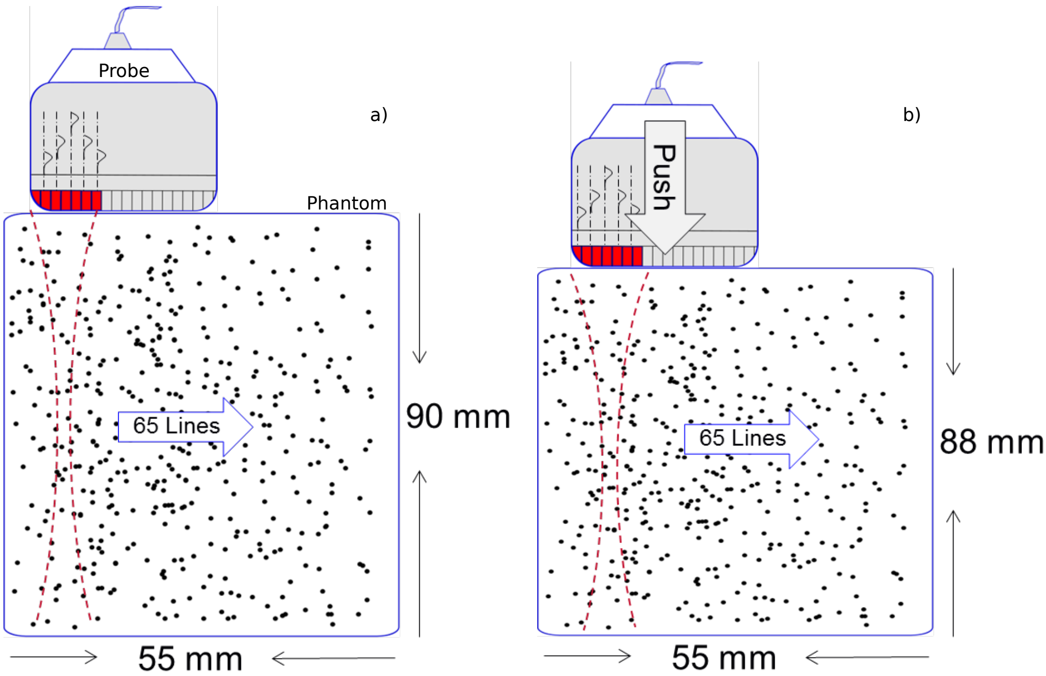

Figure 2.3: The experimental setup for the strain imaging using focused transmit and receive beams. Each beam is produced using 32 elements and is focused at the axial centre (45 mm) of the phantom. Each RF image is composed of 65 ultrasound scan lines. Imaging region is 75 mm x 20 mm (axial x lateral). a) First, a reference RF data image is collected without applying compression, this image gives pre-deformed state of the speckles in the phantom. b) The compression is applied using probe and applied displacement is controlled by a manual motion control apparatus. A sample of the axial compression of 2 mm is visualised.

2.2.6 Heterogeneous phantom study I and II

The objective of this study is to use the proposed method for the 10 mm and 5 mm inclusion based phantom and select a reliable strain image based on contrast and estimation coherence measurement among the multiple deformation produced images. This subsection also presents and discusses strain SNR and NMA percentage plots.

Experimental setup

In this experiment, phantoms with a 10 mm and 5 mm cylindrical inclusion which are three times stiffer than the surrounding medium is used. The details of the experiment are same as used in the homogeneous phantom study (see Section 2.2.5) and phantom diagram for 10 mm and 5 mm inclusion are shown in Fig. 2.1.

2.3 Results

Homogeneous phantom experiment results

The strain images were produced for 16 distinct applied deformations and are presented in Fig. 2.5. It can be observed that, strain images with applied strain values between 0.89% and 2.67% have produced (D to L images) indicate that elastograms are produced successfully where local strain is close to the range of applied strain values, consistently in all these images. Subjectively analysing, images with intermediate level strain produced smooth elastograms, while higher and lower applied compression images are noisy. This bandpass pattern in the applied strain domain is consistent with the theoretical framework of strain imaging called strain filter (Varghese & Ophir, 1997b).

In these images, measured strain values are smoother in the different regions, as three distinct regions of estimated strain can be observed in the elastograms, and in the decreasing order along the depth. This can be attributed to the fact that, stress along the compression axis is uniform when the dimensions of the compressor are greater than the phantom dimensions (Ophir *et al.*, 1991). Therefore, possible reason of higher measured strain values close to the surface of the transducer is non-uniform stress profile. Another important observation can be made that, strain values close to the transducer are slightly higher than the applied values, whereas, theoretically, local strain values can not be higher than applied global strain value. The possible reason for this is that, the axial

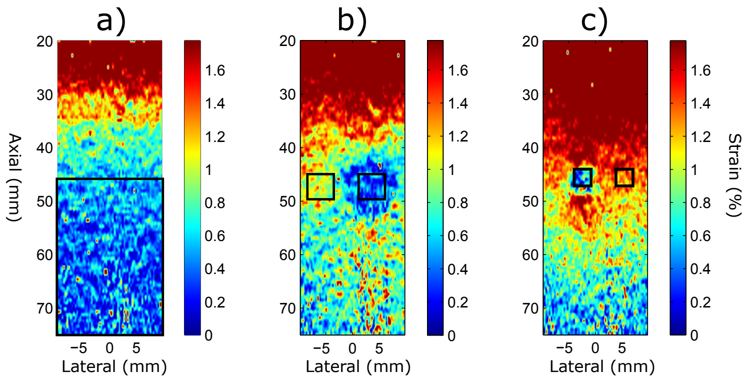

Figure 2.4: ROIs used for calculating quality estimation parameters for homogeneous, heterogeneous I, and heterogeneous II strain images. a) For homogeneous elastograms, the elastogram area where uniform strain estimations are produced is used as indicated by the rectangular box and that is selected from 45 mm to 75 mm for whole lateral dimension of the image. b) For 10 mm inclusion elastograms, a 5 mm square box ROI was placed inside and outside the inclusion at the same depth to calculate CNR. c) For 5 mm inclusion elastograms, a 3 mm square box ROI was placed inside and outside the inclusion at the same depth.

dimension of the phantom along the probe are underestimated and eventually the applied strain is also underestimated.

The SNR measurements are achieved in the ROI selected from larger smoother region as drawn in the Fig. 2.4a and presented in the Fig. 2.6. The ROI starts from 45 mm to 75 mm in depth and 10 mm in the lateral direction. It can be observed that, the SNR response for applied strain values is bandpass shaped, where lower and higher strain values produce lower SNR and intermediate strains possess higher SNR values. The SNR curve along the applied strain does not completely conform the bandpass shape where SNR values for lower strains such as 0.22% and 0.44% produce higher values than the theoretically expected values. Investigating reason for minor discrepancy is subject of the future investigations and can be determined by performing multiple events of the experiment.

Heterogeneous phantom study I results

The strain images are produced for all the applied deformations and are presented in the Fig. 2.8. The quality of the strain images varies for different applied

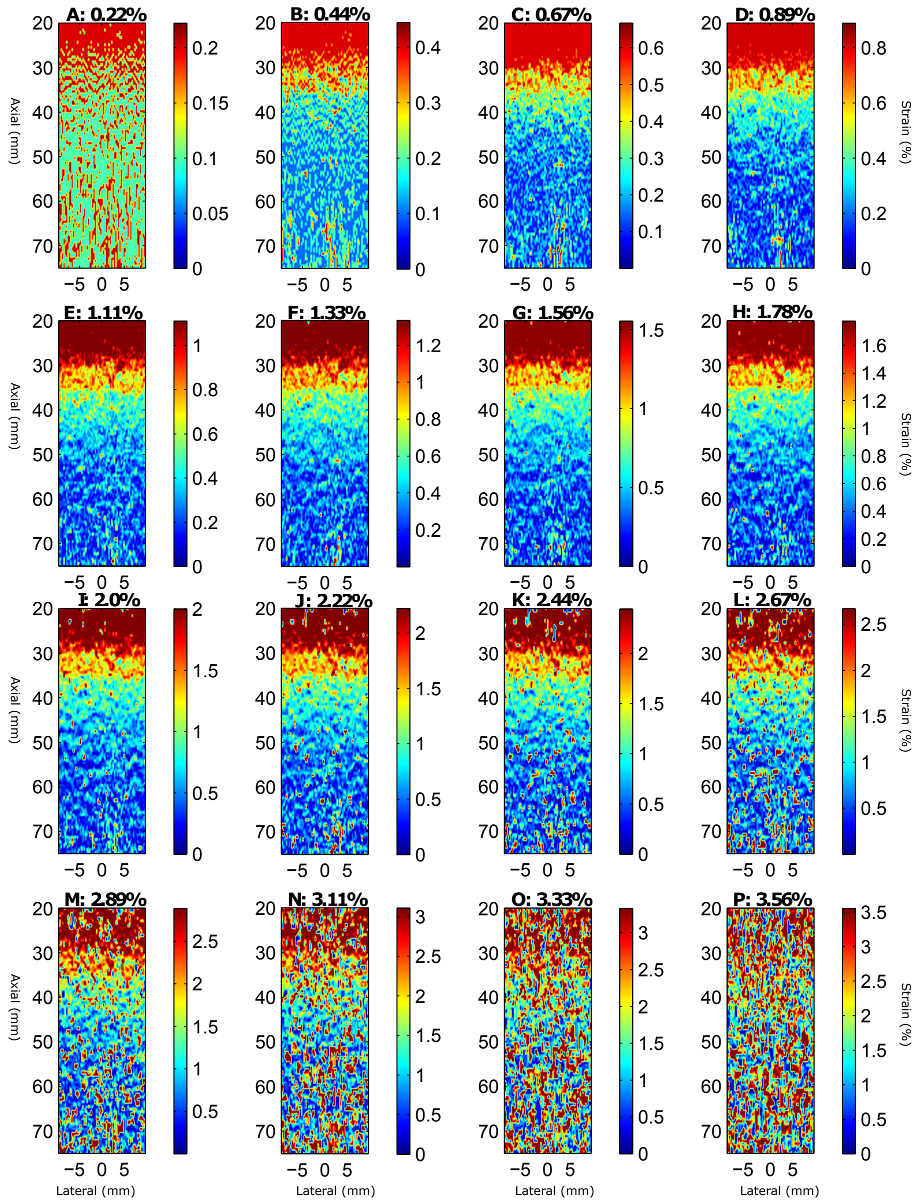

Figure 2.5: Homogeneous phantom strain images with their respective applied strain values indicated at top of each image. The colourbar scale indicates strain values in percentage notation. It can be observed that, for applied strain values between 0.67 and 2.67 percentage (D to L) are relatively of good quality with higher smoother area and quality is degraded at lower and higher strain values, specifically 0.22% (A), 0.44% (B), 2.89% (M), 3.11% (N), 3.33% (O), and 3.56% (P) strain images. The key parameters are centre frequency (f_c) = 5.5 MHz, bandwidth = 5 MHz, correlation window length = 4 mm and correlation window separation (ΔT) = 0.5 mm.

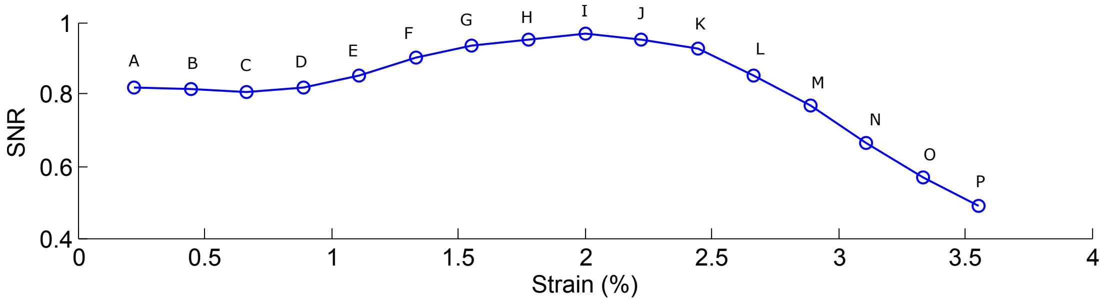

Figure 2.6: Normalised SNR values calculated for all applied strains. The SNR achieves highest value at 2.22% applied strain. The strain SNR plot follows bandpass filter shape which is according to the strain imaging theory. The key parameters are Centre frequency (f_c) = 5.5 MHz, Bandwidth (B) = 5 MHz, correlation window length = 4 mm and correlation window separation (ΔT) = 0.5 mm.

compressions, as low and high compression images are noisy while medium level compressions (C to J images) produced relatively smoother strain values inside and outside inclusion and also preserved good contrast and shape of the inclusion. Subjectively analysing, eight strain images from C to J possess better quality in terms smoothness (variance) and contrast, while the images B, K, and L are moderately noisy and images A, M, N, O, and P are highly noisy in terms of strain CNR, therefore inclusion can not be seen. Observing the inclusion and background strain values in the images from C to J, it can be noticed that, inclusion strain values are about three times lower than the background strain values, which confirms the successful reconstruction of the phantom inclusion contrast.

The measured diameter of the inclusion in the strain images is 9.70 mm which is close to the true diameter with slight compromise on sharpness, this inclusion reconstruction performance can be attributed to using axial window kernel length (4 mm) which is 40% lower than the axial dimension (10 mm) of the inclusion. In lateral direction, spatial resolution of strain estimation is determined by the width of the scan line, which is equal to the width (0.31 mm) of the transducer element.

To determine quality of these images in a quantitative way and select a relatively accurate image, normalised CNR and NMA percentage metrics were calculated for all sixteen strain images using ROIs, and were presented in Fig. 2.9. A 5 mm square box ROIs were selected to calculate CNR values, one was placed inside the inclusion, while other outside the inclusion at the same depth. In the Fig. 2.9a, it can be observed that CNR values follow the characteristic band-pass shape, where boundaries of the strain dynamic range are drawn using -3 dB threshold, denoted by the dashed straight line at 0.7 value of the peak normalised CNR. The strain values within the -3 dB dynamic range indicate first increasing and then decreasing CNR trend. Conventionally higher CNR value is regarded as higher performance strain image, which can be misleading due to various bias sources. According to the proposed idea, to quantify the quality of the estimation in a robust way, NMA percentage metric is computed and summarised in the Fig. 2.9b. It can be observed that, images for strain values between 0.67% and 0.22% fall within the -3 dB dynamic range of the peak CNR values. In the second step using NMA values, it can be noticed that, 0.67% strain image (D) has the lowest NMA which indicates the noisy portion, therefore this image is selected as relatively reliable strain image among all sixteen multiple deformation images.

Observing the NMA percentage plots for applied strain values, it can be concluded that, the loss of coherence (decorrelation) is a linear function of the applied strain within the dynamic range and is non-linear outside the dynamic range window. The loss of coherence is dominated by the lateral, elevational decorrelation and slightly impacted by axial motion due to imperfect temporal stretching operation. As the optimal selected image contains some strain pixels whose correlation coefficient falls below the 0.7. In pursuit to know comprehensive accuracy of the strain image, the optimal strain image pixels of poor correlation coefficient values are masked by the grey colour to visualise the pixels of poor estimation. The noised-masked optimal image for the 10 mm inclusion is shown in the Fig. 2.7a.

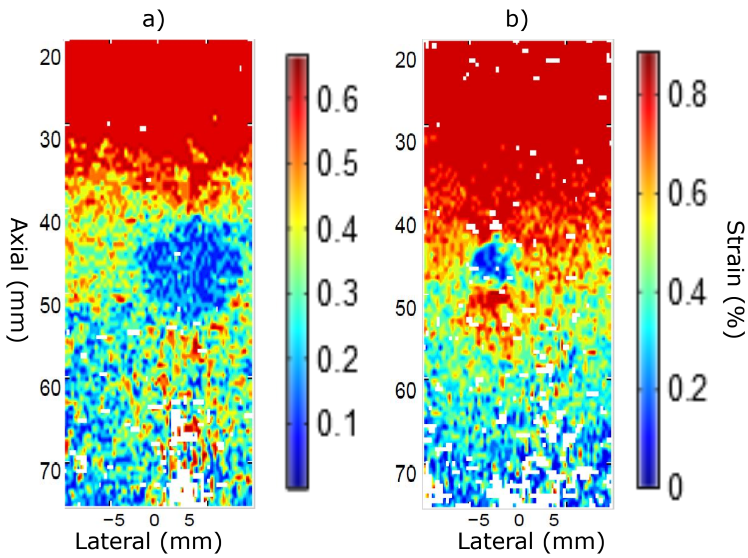

Figure 2.7: The optimal images pixels with correlation coefficient less than 0.7 are masked by the grey colour to indicate poor estimation pixels. a) The noise-maksed optimal image for the 10 mm inclusion. b) The noise-masked optimal image for the 5 mm inclusion.

Heterogeneous phantom study II results

The strain images are produced for all the applied deformations and are presented in the Fig. 2.10. The quality of strain images follow the similar trend and images for strain between lower and higher amplitudes produce good quality in terms of contrast. For the 5 mm inclusion, visually analysing, the six strain images with strains from 0.67% to 2.0% (D to J) are able to visualise the inclusion clearly. The images quality with strain 0.22% (A), 0.44% (B) and equal to and greater than 2.2% (K to P) deteriorates in terms of strain variance and the inclusion can not be visualised. The size of the inclusion is lower than the actual size, and this can be attributed to higher size of the axial window kernel (4 mm) in comparison to inclusion size (5 mm), eventually axial window length is 80% of the size of the inclusion, which is significantly higher. The underestimation of the size of the inclusion was also experienced in the early strain imaging study by (Doyley *et al.*, 2001)

To quantitatively determine the quality of strain images, CNR and NMA

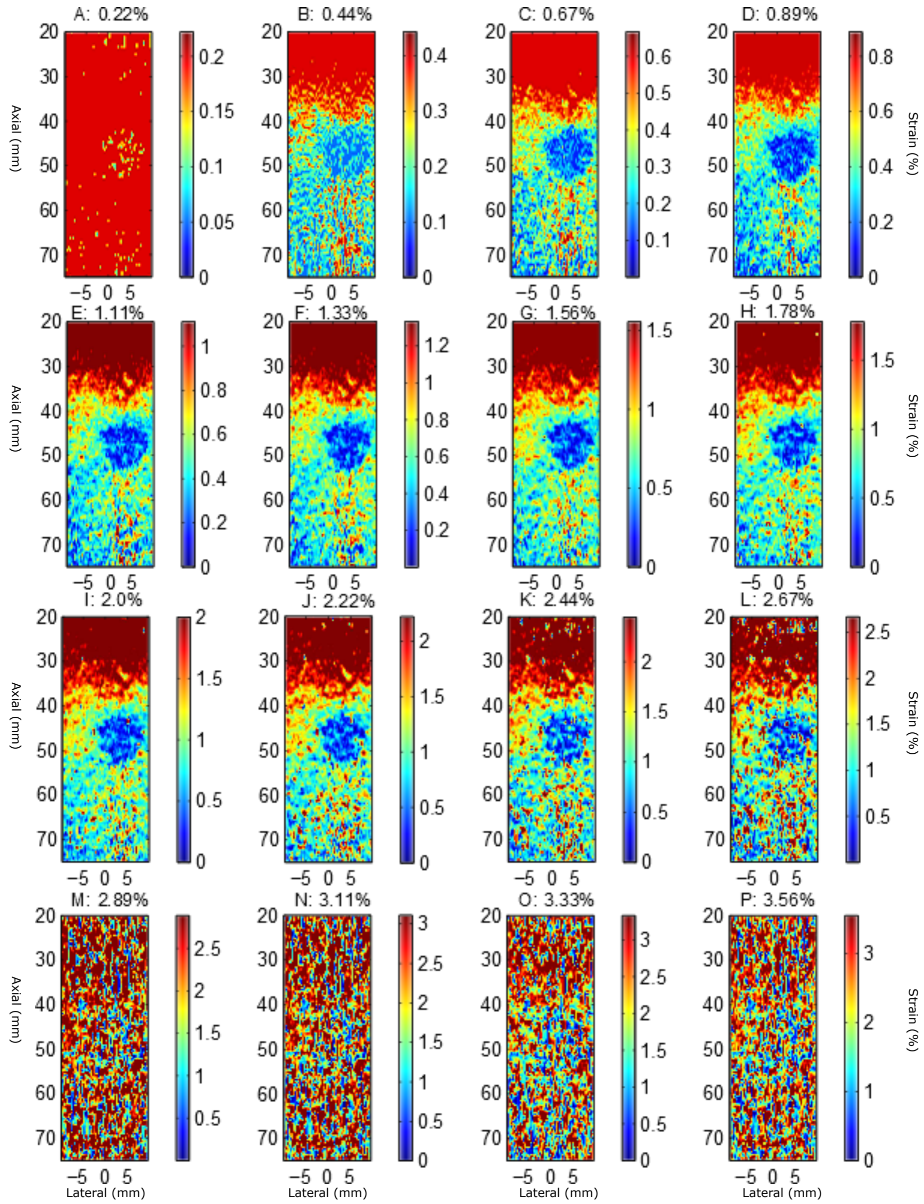

Figure 2.8: Elastograms for the phantom with 10 mm inclusion. The images for the sixteen strain values are in the ascending order from left to right and top to bottom where each elastogram is labeled by corresponding applied strain value. The images from C to J are found within the -3 dB threshold of maximum contrast. Out of these 8 strain images, 0.67% (C) strain image which has least noisy portion is selected as the optimal strain image. The key parameters are centre frequency (f_c) = 5.5 MHz, Bandwidth (B) = 5 MHz, correlation window length = 4 mm and correlation window separation (ΔT) = 0.5 mm.

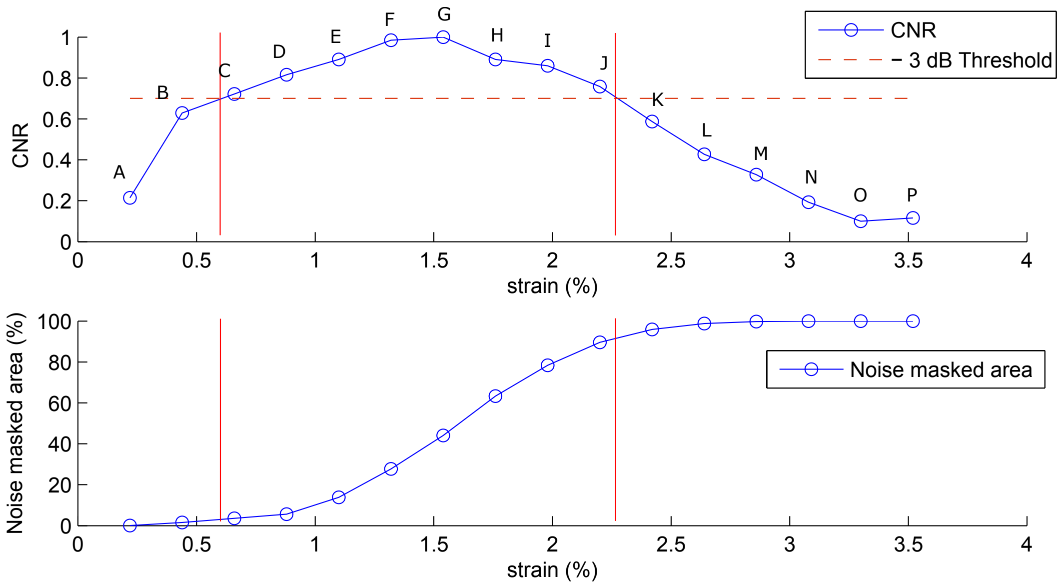

Figure 2.9: Normalized CNR and noise masked area (NMA) percentage plots of the tissue mimicking phantom with 10 mm lesion. The marker positions indicate CNR values and dashed red line indicates -3 dB (0.7) of the peak normalized CNR. There are 8 strain CNR values falling within the -3 dB strain dynamic range. In the second row, NMA metric indicate that strain image of 0.67% has least noisy portion and is relatively optimal image in terms of accuracy.. The key parameters are Centre frequency (f_c) = 5.5 MHz, Bandwidth (B) = 5 MHz, correlation window length = 4 mm and correlation window separation (ΔT) = 0.5 mm.

metrics are calculated in the same way as in the 10 mm inclusion study, with only the difference of ROI size which was selected as 3 mm square boxes inside and outside the inclusion as shown in the Fig. 2.4c. The quality metrics strain CNR and NMA percentage are presented in the Fig. 2.11. It can be noticed that, there is similar bandpass shape response for the CNR values against applied strain values, whereas dynamic range and sensitivity of the strain is lower than the 10 mm inclusion phantom study. Looking at the Fig. 2.11 CNR plot, between strain of 0.89% and 1.78%, contrast falls within -3 dB dynamic range (denoted by the dashed red line), while for strain values out of the dynamic range window, reconstructed images are noisy as CNR falls below the 70% of the peak value. There are five strain images (D to H) above the CNR threshold line, to find the relative optimal elastogram among these five images, corresponding NMA percentage is calculated and plotted for all the strains. Looking at the NMA percentage plot (see Fig. 2.11), the 0.89% (D) strain image has the least noisy area among these five images, therefore this image can be selected as the reliable strain image among other sixteen multiple deformation images. The dynamic range of the strain filter for 5 mm inclusion is narrow and sensitivity is less than the 10 mm inclusion phantom study. This implies that, lower size inclusions detection is more challenging than the bigger inclusions.

Finally, the optimal strain image pixels of poor correlation coefficient values are masked by the grey colour to visualise the pixels of poor estimation. The noised-masked optimal image for the 5 mm inclusion is shown in the Fig. 2.7b.

2.4 Discussion

Quality metric such as SNR is a global quality matrics which is used to measure uniformity of strain estimation within the uniform tissue types such as inside inclusion and background. CNR measures amount of variation in strain estimation between inclusion and background (Bilgen & Insana, 1997b; Varghese & Ophir, 1997b). These metrics fail to quantify matching or coherence of the signals which are used for the strain measurement. Another method proposed by the Cambridge group used amplitude of the ultrasound signals to identify noisy estimation pixels and red-masked noisy areas, correspndingly (Chen *et al.*, 2010;

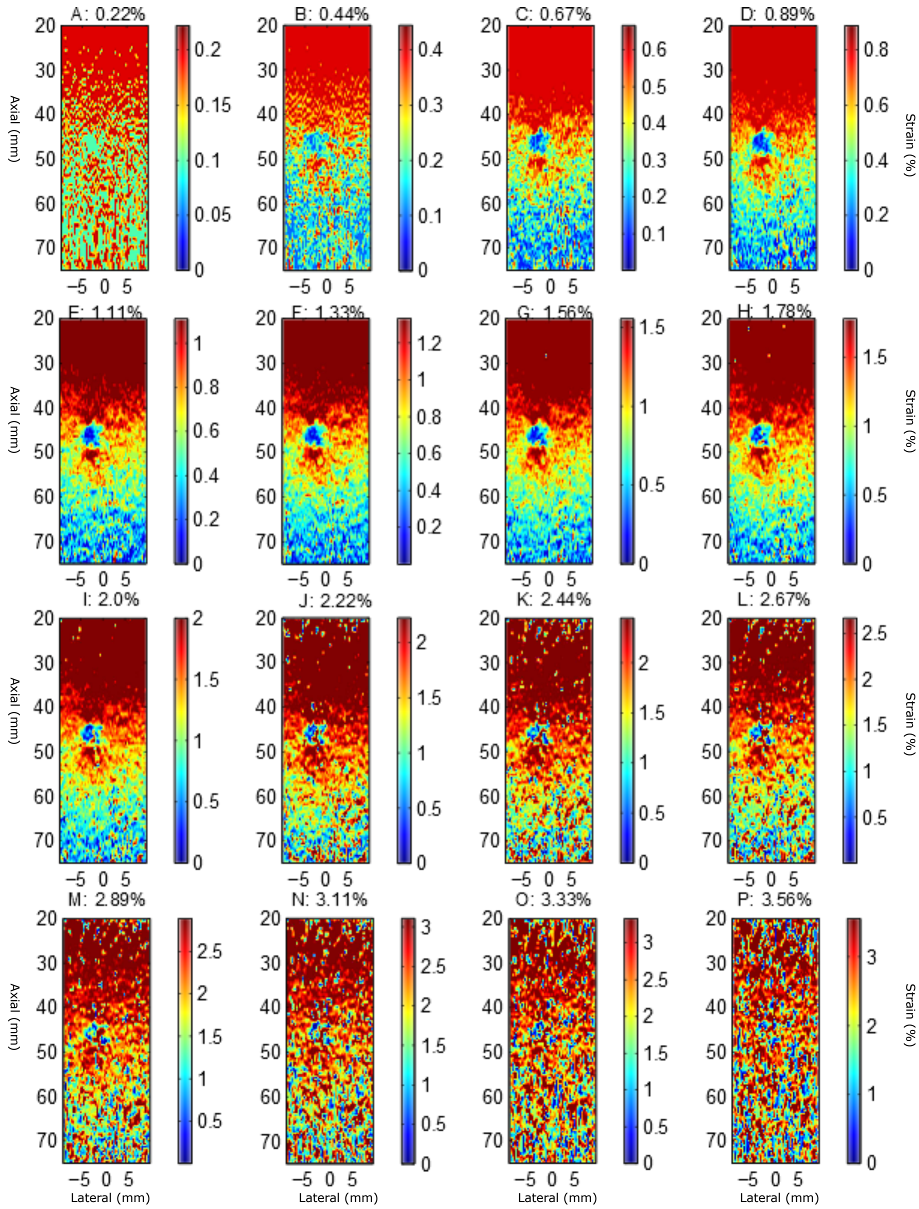

Figure 2.10: Elastograms for the phantom with 5 mm inclusion. The images for the all sixteen strain values are in the ascending order from left to right and top to bottom where each elastogram is labelled by corresponding applied strain value. The images from D to H are found within the -3 dB threshold of maximum contrast. Out of these 5 strain images, 0.89% (D) strain image which has least noisy portion is selected as the optimal strain image. The key parameters are centre frequency (f_c) = 5.5 MHz, Bandwidth (B) = 5 MHz, correlation window length = 4 mm and correlation window separation (ΔT) = 0.5 mm.

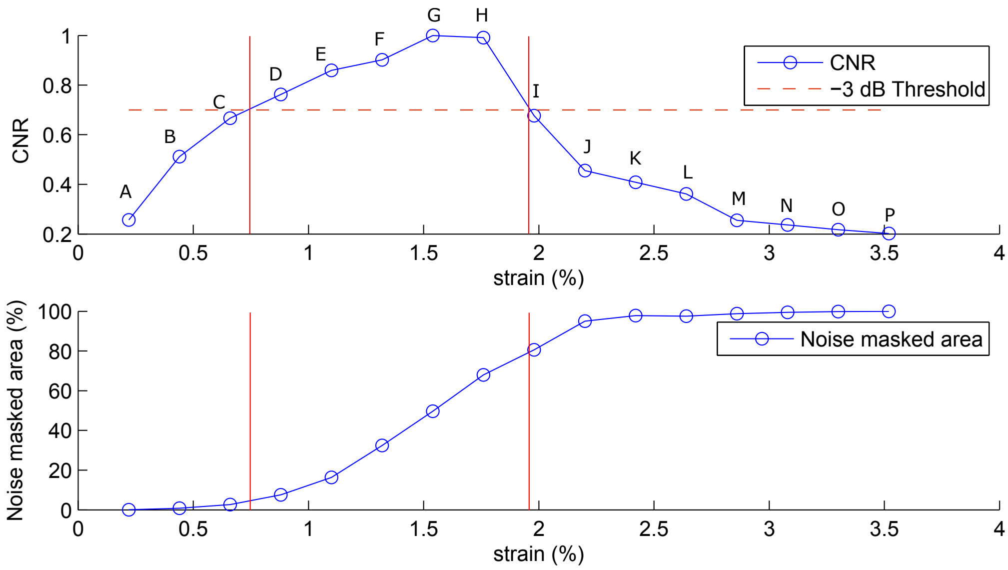

Figure 2.11: Normalized CNR and noise masked area (NMA) percentage plots of the tissue mimicking phantom with 5 mm lesion. The marker positions indicate CNR values and dashed red line indicates -3 dB (0.7) of the peak normalized CNR. There are 5 strain CNR values falling within the -3 dB strain dynamic range. In the second row, NMA metric indicate that strain image of 0.89% has least noisy portion and is relatively optimal image in terms of accuracy.. The key parameters are Centre frequency (f_c) = 5.5 MHz, Bandwidth (B) = 5 MHz, correlation window length = 4 mm and correlation window separation (ΔT) = 0.5 mm.

Lindop *et al.*, 2008). Ultrasound signal amplitude of the signals or SNR is one factor among many factors which contributes to the quality of strain measurement. Proposed two way quality estimation method addressed these limitation by using a novel quality metric called noise masked area which is based on correlation coeffiient along with the CNR. Both metrics ensured the final selected have adaquate contrast and the least noisy estimation pixels among multiple images.

In the 10 mm phantom study, the diameter reconstruction of inclusion was equal to 9.70 mm, while in the 5 mm phantom, the size of the inclusion (3.2 mm) underestimated due to the large kernel length used for the correlation analysis. A slight underestimation can also be confirmed in the previous study by (Doyley *et al.*, 2001). However, static nature of the tissue excitation enables to use multiple events of acquisitions of a single speckle state, therefore, this limitation can be removed by using noise reduction techniques such as ultrasonic averaging, and multi-compression averaging (MA). Accuracy of elastograms produced in this study can be further improved by summing multi-deformation images as used in the clinical study by the (Hiltawsky *et al.*, 2001).

In future studies, a weighted averaging will be performed in contrast to conventional averaging, where each image within the -3 dB CNR dynamic range can be assigned a weight (quality score) based on CNR and NMA values before applying summation operation. A limitation of this study is that, during experiments, the controlled compression was applied using motion control device, which is not possibe in clinical free-hand strain elastography. However, free-hand usage of the probe needs a proper training because slight change in the orientation of probe during experiment may change results drastically. For strain elastography, the European federation of societies for ultrasound in medicine and biology (EFSUMB) recommended that (Cosgrove *et al.*, 2013), a sequence of strain images should be acquired and stored as cine loop images. For final diagnosis, a strain image with reproducible characteristics should be selected. In this perspective of guidelines, this quality estimation method will be useful to select a high quality strain image in a quantitative way.

2.5 Conclusions

The proposed two-way approach combined both contrast and correlation coefficient to select strain image to select final image having both good contrast and estimation accuracy to address limitations of previous quality tracking methods (Bilgen & Insana, 1997b; Chen *et al.*, 2010; Lindop *et al.*, 2008; Varghese & Ophir, 1997b). The proposed method was tested for two inclusion based phantoms and selected accurate strain image. This method can provide a significant basis for optimization for both free-hand and motion controlled strain imaging in research and also guide clinicians to select best possible quality strain image. For precise diagnosis, final image is presented with noisy estimated pixels masked by grey colour, indicating image pixels with poor accuracy.

Chapter 3

Implementation of shear wave elastography

3.1 Introduction

UARP I was used for strain elastography experiments in the Chapter 2 while the system limited in various technical aspects such as ability to store RF data samples from all channels for long duration. This limited ultrasound machine to be used for shear wave elastography. Elastography based on acoustic radiation force requires highly efficient ultrasound system to enable shear wave generation and tracking at high frame-rate along with storage capacity high enough to save and transfer upto 300 RF data frames. Ultrasound Group, University of Leeds, updated UARP I and improved the capacity to conduct shear wave elastography, conventional B-mode imaging, and blood flow research, and called UARP II or second generation UARP.

3.2 UARP II hardware overview

The UARP II ultrasound is a 128 channel modular system consisting of set of rack of 8 cards, where each card is responsible for handling 16 transmit (TX) and receive (RX) channels and each channel is individually accessible from the computer. Each card consists of a TX/RX and a Stratix V FPGA (field programmable gate array) board. Each channel have a high voltage TX Pulse generator with an integrated receive pathway which is connected to Analog to Digital Converter (ADC). A given channel of the UARP is therefore shared between TX and RX.

3.2.1 UARP II transmitters

For transmission, the UARP II uses Quad 5-Level High-Voltage pulse generators which have an integrated switch for selecting between transmit and receive mode. The pulse drivers are rated for up to 105 V, and load currents of up to 2A. For 5-Level High-Voltage pulse, as an example set of voltages would be: 100 V, 60 V and 0 V. The drive current can be selected to be limited to 0.5A, 1A, 1.5A, or 2A.

3.2.2 UARP II ADC

There are two ADCs on the TX/RX board, each clocked for a sampling rate of 80 MHz and 12-bit resolution. Each channel of the ADC chip has internal Low Noise Amplifier (LNA), Programmable Grain Amplifier (PGA) and a 40dB variable gain Time Gain Compensation (TGC) attenuator. Each channel also utilises a 3rd order Low Pass Filter (LPF) with a selectable cut-off frequency of 10MHz, 15MHz, 20MHz or 30MHz.

3.2.3 UARP II transmit controller

In UARP II, the transmit (TX) controller handles all the aspects of waveform generation, trigger generation, waveform transmission, and transmit beamforming, and is configured using Matlab based scripts. It also manages clock generation and synchronisation of clocks and triggers between multiple cards. When a trigger occurs, it causes the transmit controller to start generating waveforms for all TX channels. Transmit waveforms such as shear wave generation tone burst and B-mode imaging pulse are then fed out to the TX pulse chips when the individual channel is triggered. Beamforming delays are automatically changed during a sequence of triggers allowing the beamforming pattern to be automatically sequenced. For maximum configurability, all TX waveforms and beamforming delays are actually produced using a MATLAB utility. These waveforms are then uploaded to the FPGA card to be sent out by the TX controller.

3.2.4 UARP II receive controller

The receive (RX) controller is the part of the firmware which handles control of the ADCs, data acquisition, receive beamforming and data storage. The ADC front end of this module runs at 80MHz, while the sample processing and data storage side run at a much faster internal clock speed of 200MHz. The primary function of the receive controller is the acquisition of data from the ADCs. Samples from the ADC are transferred to the FPGA using serial interface (LVDS).

3.2.5 UARP II ADC sample storage

To allow for data capture at the highest possible speed, each UARP II card contains 1GiB (Gibibit) of DDR3 (Double Data Rate 3) memory. This memory is used for temporary storage of data from the ADCs and will also be used for any on-FPGA image processing. In the current design, the largest sample depth for a single firing is 32768 samples per channel, which equates to a round trip ultrasound depth in water of approximately 61 cm.

3.3 Shear wave elastography sequences

The shear wave elastography implementation was divided into two stages. In the first stage, transmit sequences for shear wave generation and tracking were designed and then algorithms were written to estimate shear wave induced tissue motion, perform directional filtering and shear wave speed measurement. In this section, transmit sequence design related details are presented while signal processing flow is explained in the progressing chapters.

3.3.1 Push transmit excitation mode

There are two key parts of push beam design on UARP II. First, push beam transmit waveform is designed using Harmonic Reduction Pulse Width Modu-

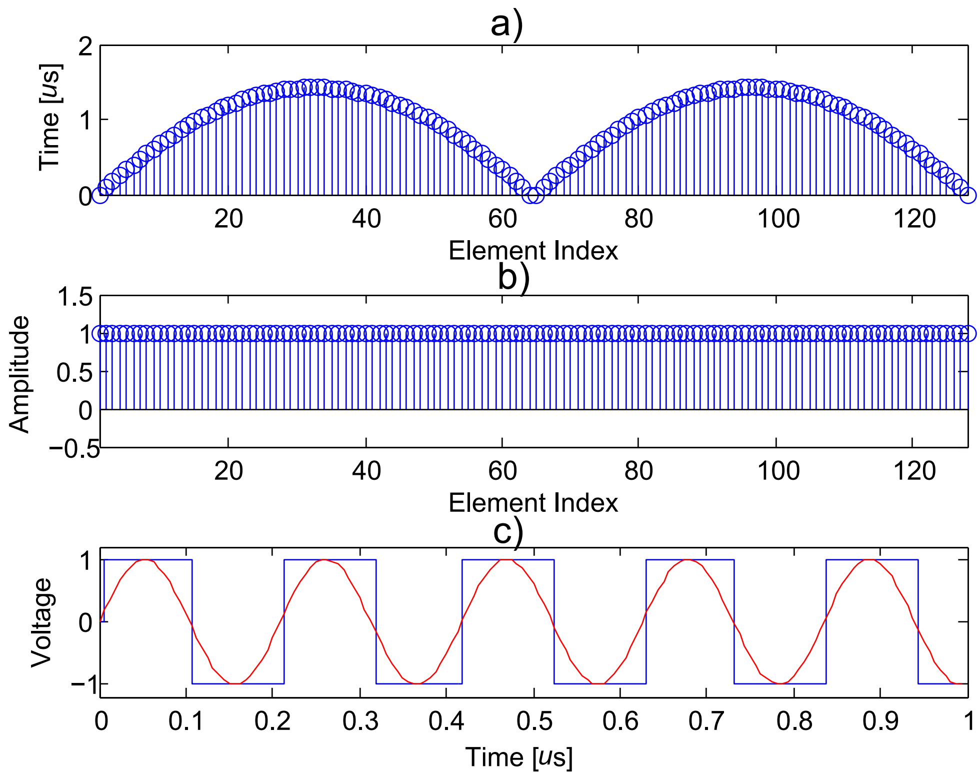

Figure 3.1: a) A sample of transmit sequence diagrams for the proposed technique dual push beam shear wave elastography. a) A sample of phase delay profile for dual push beam technique showing two transmit beams focused at 40 mm. b) A sample of apodisation profile for the dual push beam technique, where amplitude '1' indicates transducer elements that are used during transmission. c) A 1 μs sample of push beam tone burst waveform (with blue color) showing also pulse width modulation (with red color) generated waveform.

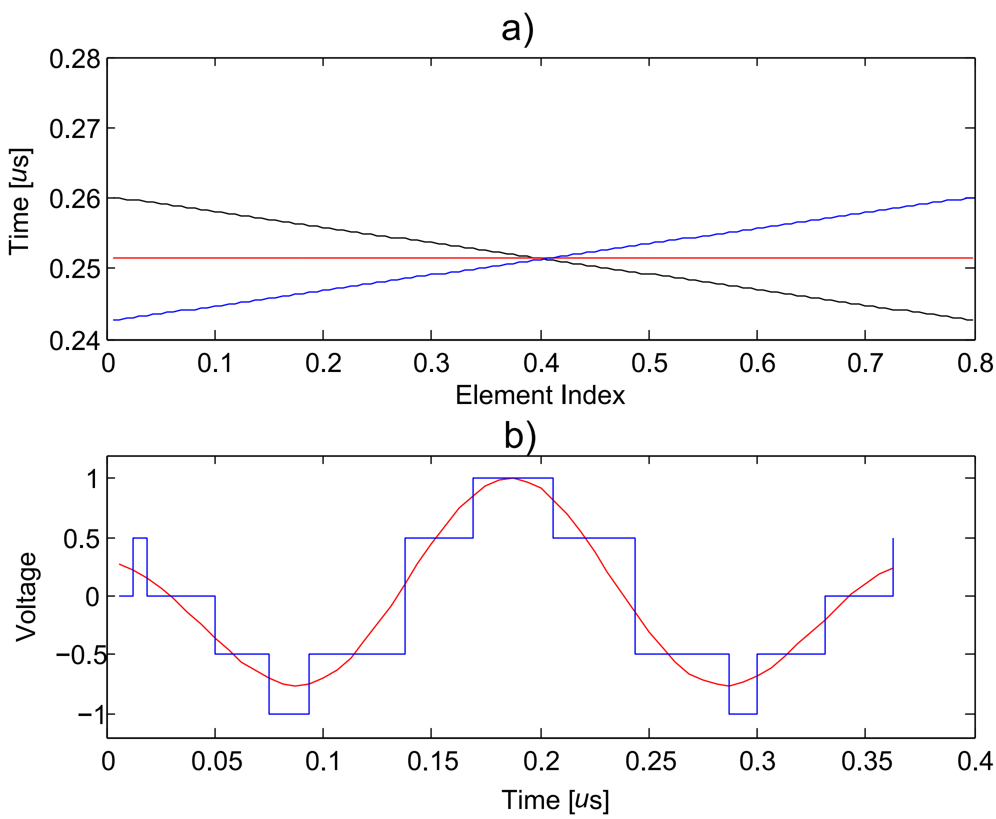

Figure 3.2: a) A sample of three angle steered (-4°, 0°, +4°) delay profiles for tracking beams. b) A sample of 5-level tracking beam waveform signal generated using pulse width modulation along with the desired signal.

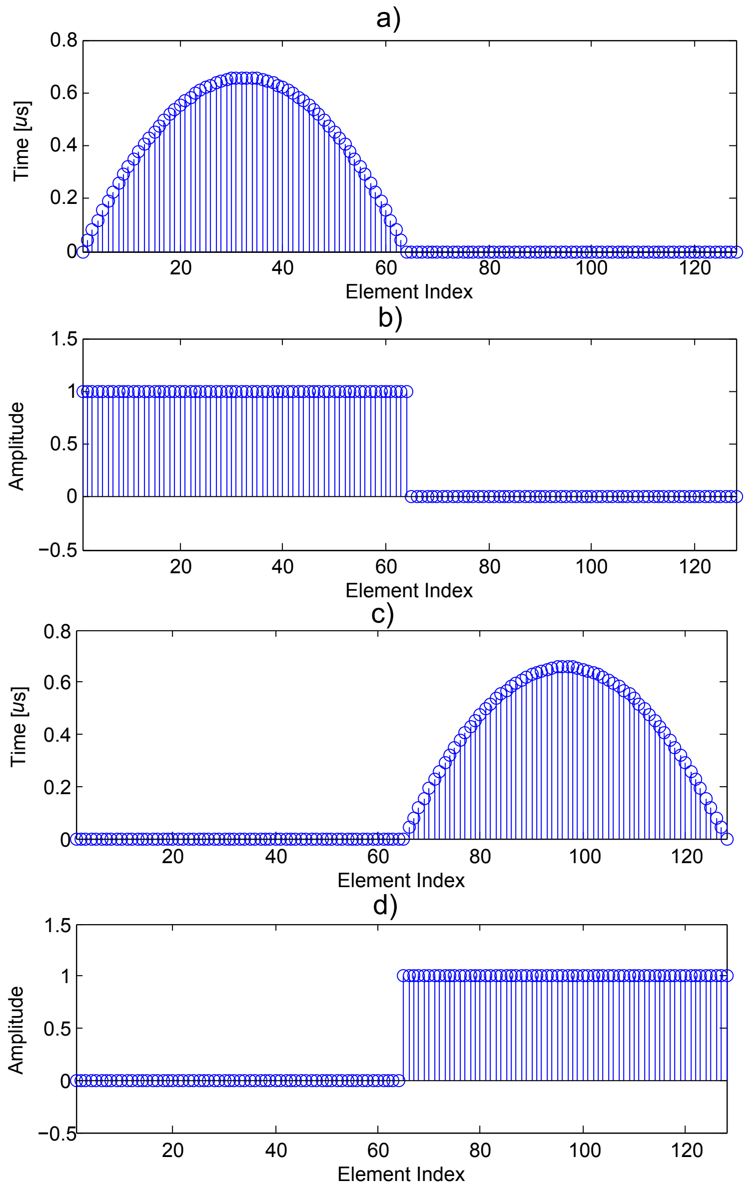

Figure 3.3: A sample of transmit sequence diagrams for supersonic shear imaging elastography containing both left and right push beam sequences. Phase delay profile for left (a) and right (c) shear wave beams are plotted here. A sample of apodisation profile for both left (b) and (d) right push beam, where amplitude '1' indicates transducer elements that are used during transmission.

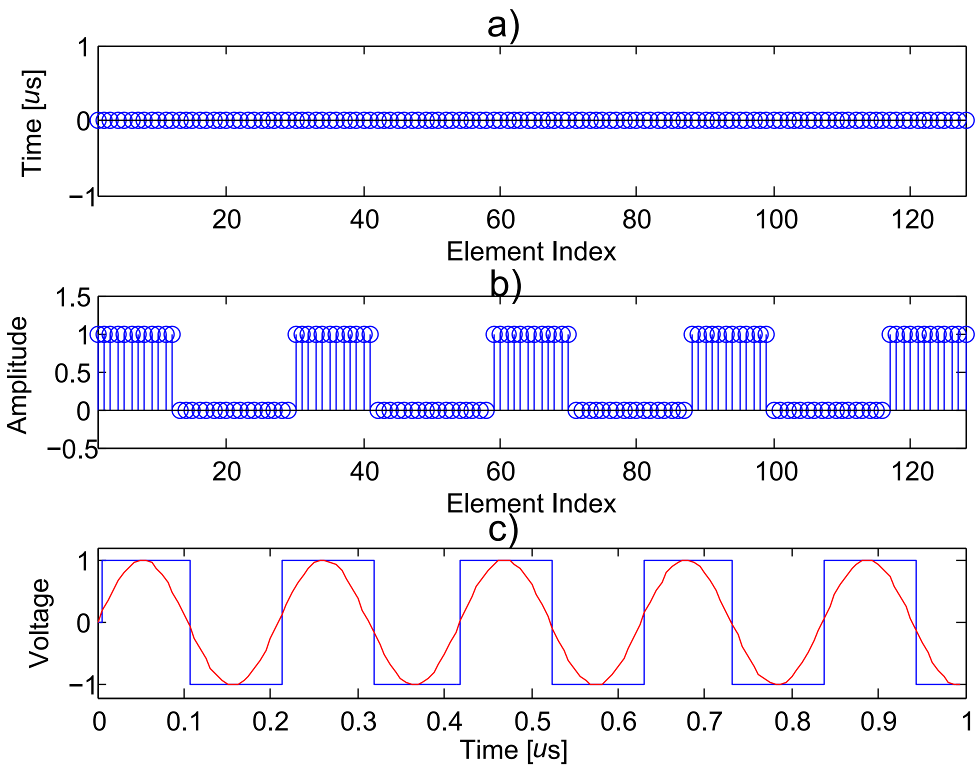

Figure 3.4: A sample of transmit sequence diagrams for comb-push shear wave elastography containing. a) No transmission delays as unfocused push beams are used for this technique. Apodisation profile indicates that transducer array is divided into five sub-aperture to generate five push beams. c) 1 μs sample of tracking tone burst signal which is used during shear wave tracking, showing both desired (red) and pulse width modulated (blue) signals.

lation (HRPWM) algorithm (Cowell *et al.*, 2014; Smith *et al.*, 2013) which uses switched excitations at 5-level amplitude discrete positions to approximate desired signal. Amplitude levels of ± 1, ± 0.5 and 0 in excitation pulse correspond to ± 100 V, ± 50 V and 0 V for power supply voltages. A sample of the push beam generated excitation signal is presented in Fig. 3.4. All the transmit waveforms are sampled at 160 MHz.

The frequency of the push beam excitation was selected equal to the centre frequency of the transducer to maximise transmission efficiency, while in some applications lower frequencies can be used to reduce frequency dependent ultrasound attention and increase penetration depth. For L7-4 linear array transducer, push beam centre frequency was set to 4.79 MHz, which is the centre frequency of the transducer. The designed push beam excitation waveform and corresponding parameters are defined in the TX Matlab structure and uploaded to the FPGA card later to be used for excitation. The waveforms for each excitation are stored separately to enable different kinds of waveforms to be used for each excitation.

The amplitude and duration of the push beam excitation waveform is usually selected keeping ultrasound exposure and transducer heating into consideration. Shear wave tissue displacement (alternatively shear wave SNR) is proportional to radiation force which is effectively function of push beam excitation voltage and duration. When selecting high excitation voltages for long duration, it is possible that, system power supply experience drop in the excitation voltage and exerted radiation force intensity decreases at the end of push beam duration. Typically, ± 100 V and ± 50 V with duration of 600 μs are used for shear wave elastography experiments for linear array transducers.

Second, the push beam aperture is determined by designing an aperture, delay, and apodisation profiles. Aperture profile enables to excite only certain combination of elements and leave other elements unused during shear wave generation, which depends upon the type of shear wave elastography methods. Whereas, the delay profile sets the focal pattern of transmission as some elastography methods used focused transmission beams such as SSI, while U-CUSE employs unfocused plane transmission. Rectangular apodisation is typically used for shear wave beams, therefore, aperture profile acts also as an apodisation profile. For typical 600 μs duration push beam and pulse repetition interval (PRI) of 100 μs, six aperture and delay profiles are designed and stored for each push beam excitation frame.

3.3.2 Track transmit excitation mode

The tracking beam was designed in the similar pattern as used for push beam. First for tracking sequence design, a short excitation pulse with duration of typically few cycles with centre frequency equal to centre frequency of transducer is designed using HRPWM algorithm, as presented in Fig. 3.4a. A lower tracking beam frequency can be selected for harmonic shear wave tracking (Song *et al.*, 2013b) for improved displacement estimation. In shear wave detection, all the elements are excited simultaneously and no transmission focus is used, however, to improve tracking quality, typically three insonification steered angles are used. The steering profiles are designed by applying increasing or decreasing delays at each transducer element. The tracking excitation voltage is set to ± 100 V to use maximum supply voltage, as lack of transmission focus may limit tracking SNR.

3.3.3 Transmit and receive sequence

The receive (RX) controller is part of the firmware and manages control of ADCs, data acquisition, receive beamforming, receive beamforming and data storage. For a typical shear wave elastography experiment, the PRI is set to 100 μs, alternatively, a frame rate equal to 10 kHz, which is adequate to capture backscattered data up to 6 cm (time of flight $\sim$ 60 μs) for typical acoustic speed soft tissue. For the first 10 frames, backscattered data using tracking beam configuration is captured, then, push beam excitation for 6 frames is used, and finally the UARP II transmission switches back to tracking mode for typically 200-250 frames. The received RF data is sampled at 80 MHz with 12-bit resolution which is approximately 16 times of the centre frequency and captured at all elements simultaneously and stored in the local memory. Later, RF data is transferred to computer storage for post-processing. The beamforming operations are performed on the raw RF in the post-processing period to produce beamformed images. After the RF data is obtained, six push beam duration frames and one frame following the push six beam frames are discarded as it contains reverberations and strong reflections from previous excitations.

Chapter 4

Dual Push Beam Shear Wave Elastography

4.1 Introduction

Acoustic radiation force based shear wave elastography methods are explained in detail in Chapter 1 with challenges faced by each technique and resolved by the subsequently proposed methods. ARF based techniques such as SWEI, ARFI shear wave imaging, and SSI methods faced two common problems, first inability to produce shear wave speed in push beam regions and second reduction of shear wave SNR at high rate when shear waves propagate away from the source region.

Lack of shear wave field at the location where push beams are placed leads to a problem called 'blind area' or 'dead zone' artefact. Shear wave field 'blind area' artefact is demonstrated in Fig. 4.1a, with the help of schematic diagram of SSI push beams placed at successive depths, and corresponding elasticity map is superimposed onto B-mode image as shown in Fig. 4.1b. Shear waves generated using radiation force has bi-polar directivity pattern and waves travel along the transverse (lateral) direction away from each other after generation is ceased as indicated by arrows. The shear motion vector at push beam location is low and buried in the noise (Bercoff *et al.*, 2004b; Sarvazyan *et al.*, 1998), therefore no shear elasticity information can be extracted in that location. The artefact at the push beam location can be observed in Fig. 4.1b, where reconstructed values are highly noisy and not related to the true local elasticity. To address this issue, data acquisitions were repeated multiple times, and for each acquisition event, shear wave beams were placed at different lateral locations to achieve shear elasticity in the ‘blind area’ (Tanter *et al.*, 2008). Along with solving the problem, using multiple data acquisition events eventually reduced the effective frame rate, increased processing load for producing a single elasticity map, and increased acquisition time limits utility of the method for tissues in motion due to physiologically moving parts.

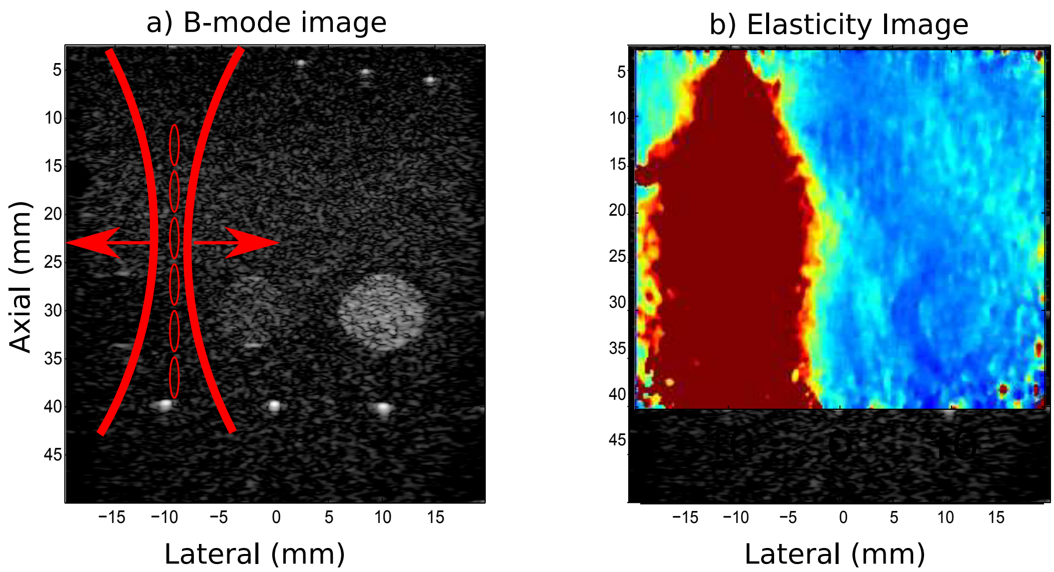

Figure 4.1: A schematic diagram generated using UARPII ultrasound machine showing ARF-based SSI shear wave generation beam locations with the help of B-mode image and corresponding elasticity map. (a) Shear wave beam focal depths are indicated using red dots at successive depths. After generation is ceased, shear wave field travels laterally away from each other, indicated by the arrows. The corresponding elasticity map superimposed onto the B-mode image is presented in (b). A ‘blind area’ artefact can be seen on left of the elasticity map in the region where shear wave beams are placed.

Another issue faced by SSI and ARFI imaging techniques is shear wave field attenuation along the lateral direction. This issue arises from the fact that in ARFI and SSI, all the push beams are placed at the single lateral location and wave field amplitude attenuates as the wave travels along the lateral direction. This effect is demonstrated in Fig. 4.2. The elasticity map for a single event

SSI is shown in Fig. 4.2a, and a lateral line at a depth of 20 mm is selected to measure corresponding shear wave SNR along the lateral line. Peak displacement generated by shear waves, which indicates shear wave SNR is presented in Fig. 4.2b. The peak displacement plot indicates that, amplitude of the shear wave field reduces along the lateral dimension, and wave field attenuates. In result due to attenuation, amplitude the wave field at another side of the FOV can decrease below the significant level where accuracy of elasticity estimation is compromised. An attempt to increase the shear wave SNR is key to improve elasticity estimation accuracy.

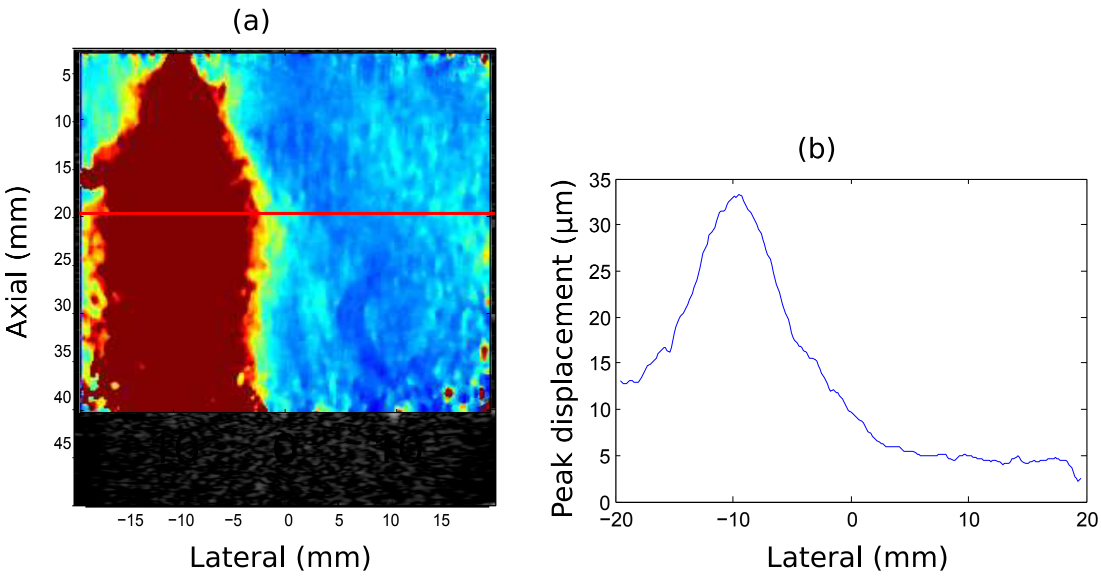

Figure 4.2: Attenuation experienced by shear wave field using conventional SSI based shear wave generation is demonstrated using elasticity map generated by the UARPII machine. (a) Elasticity image with a lateral line at a depth of 20 mm is shown where peak displacements in units of μm are computed for all acquisition time. (b) The plot indicates that shear wave field attenuates as the wave propagates along the lateral direction, and shear wave SNR is reduced to a very low level at another end of the FOV, while peak in the displacement profile indicates the lateral position where shear wave beam is applied. Reduction in the shear wave field amplitude or SNR is directly related to the level of elasticity estimation accuracy.

Another limitation which is discussed and a possible solution is presented in this chapter is related to CUSE techniques, which is penetration depth of the shear wave field generated by CUSE is limited due to small apertures used for these techniques. The CUSE based techniques such as U-CUSE and F-CUSE use multiple small sub-aperture beams to generate shear waves to optimise the distribution of shear wave field energy in the lateral direction, and this limits the acoustic energy penetration along the depth and subsequently imaging depth of the reconstructed elasticity maps. Penetration depth improvement is required for imaging conditions where targets are very deep from the skin, such as liver and abdomen imaging in obese conditions as a conservative example.

To address the above detailed challenges, a new shear wave generation method is proposed, where aperture array is divided into two sub-apertures as shown by Fig. 4.3, and the technique is named as Dual Push Beam (DPB) shear wave elastography. Using two parallel push beams attempts to enable shear wave field at every pixel in the imaging region and covering the push beam locations areas with shear wave field. The DPB addresses the first challenge without employing multiple push and detect events. Using two push beams at different lateral locations along the FOV produces two shear wave sources and improves overall shear wave SNR. As DPB uses two simultaneous and parallel beams to generate shear waves, therefore the whole transducer array can be divided into two large sub-apertures to insonify deeper targets with shear waves. It is important to note that dividing the ultrasound array (typically 128 elements) into multiple small sub-apertures leads to poor access along the depth in terms of acoustic radiation force, as used by the U-CUSE (5 beams, 12 elements sub-aperture each) and F-CUSE (4 beams, 32 elements sub-aperture each). The proposed method attempts to increase penetration depth, and also shear wave SNR can be enhanced by using tighter focal profiles at shallow depths. In summarised way, the proposed method uses two simultanous push beams along the FOV enables producing 2D elasticity map in a single push detect event, which effectively removes shear wave 'blind area' artefact, offers overall improved SNR of shear wave field along the both lateral and depth dimensions, and increases the axial range of shear wave generation.

In this study, various experiments are conducted using commercial phantom and the ultrasound system, custom developed by the Ultrasound Group, University of Leeds. Four different sub-aperture configurations are explored for the purpose to optimise DPB technique for different imaging depth applications. These configurations are named as DPB aperture 1 (DPB-AP1), DPB aperture 2 (DPB-AP2), DPB aperture 3 (DPB-AP3) and, DPB aperture 4 (DPB-AP4), where each configuration differs from each other in terms of sub-aperture size. The shear wave field from two sources interact with each and produce complex shear wave patterns due to interference. To separate right-to-left (RL) travelling waves from left-to-right (LR) travelling waves, a directional filter was used Deffieux *et al.* (2011). Shear wave speed maps were produced for both RL and LR shear wave fields using time-of-flight cross-correlation based method and RL and LR elasticity maps were combined to produce full FOV elasticity map.

The structure of the chapters follows as; Section 4.2 explains principles of the DPB for shear wave generation, high frame-rate plane wave imaging features for shear wave tracking, shear wave motion estimation, directional filtering and methods used for local Young's modulus estimation using shear wave speed calculation. Section 4.3 presents homogeneous, inclusion based, and imaging depth investigation experiments and results. The final Section 4.4 summarises the results and presents the conclusion of the study.

4.2 Materials and methods

4.2.1 The principles of technique

DPB shear wave generation technique divides the transducer array into two sub-apertures, allocates each sub-aperture for each push beam, where each aperture uses separate delay profile. The generic schematic diagram of the DPB method is shown in Fig. 4.3. At same lateral location push beams are placed using focused acoustic beams indicated by the dots. Four sub-apertures DPB-AP1, DPB-AP2, DPB-AP3 and DPB-AP4 with an aperture size of 16, 32, 48, and 64 elements for each push beam, respectively. The purpose of testing four different sub-apertures is to investigate the performance of each configuration at shallow and deep regions and to find compromises and advantages among different aperture sizes. Between two lateral push beams, a sub-aperture gap is required to significantly separate shear waves from each source (Song *et al.*, 2012), therefore an aperture gap of

24 and 16 elements was allocated for DPB-AP1 and DPB-AP2, respectively. For DPB-AP3 and DPB-AP4 configuration, there was no aperture gap, because the lateral centre of the beams is significantly separated due to a large aperture and beam convergence. Apodization profile for all four configurations is shown in Fig. 4.4. The '1' and '0' in the y-axis indicate the used elements (sub-aperture used for shear wave generation) and un-used elements during shear wave generation mode, respectively. In Fig. 4.4, it can be observed that, as the aperture size is increasing the lateral central axis of the push beams is also getting further away from each other, which allows not to use any aperture gaps for DPB-AP3 and DPB-AP4 configurations. The lateral locations of the push beams can also be clearly visualised in Fig. 4.5, where samples of the delay profiles for each configuration are plotted. The peaks of the profiles getting further apart from each other, as the aperture size for push beam is increasing.

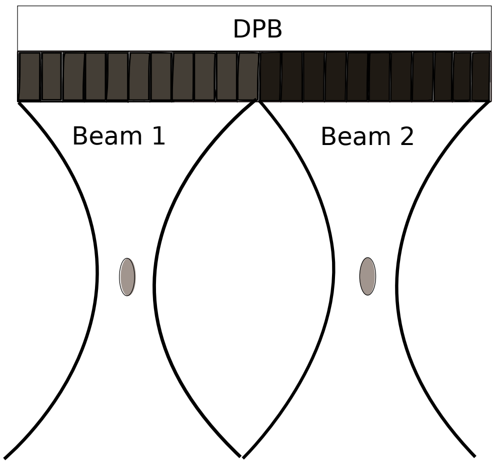

Figure 4.3: A generic schematic diagram of the DPB shear wave generation method, where two parallel and concurrent shear wave sources (left and right) are placed to enable shear displacement data at both push beam locations. Both focused push beams at depths as indicated by dots are placed, where focal depth is selected appropriately to application. In this study, four types of DPB configurations with varying aperture size are tested.

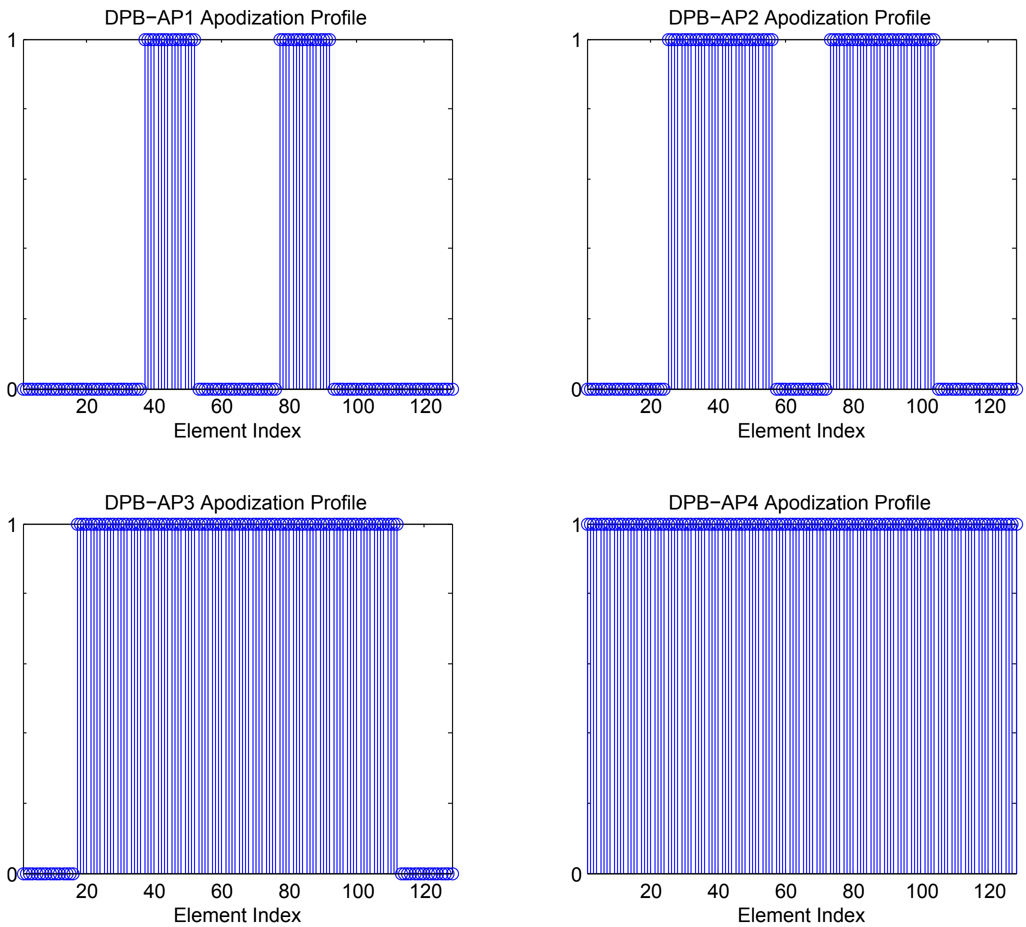

Figure 4.4: Push beam aperture apodization profiles for all four DPB configurations, titled with their respective names. All the '1's amplitude indicates to elements used for shear wave generation and '0's indicate to elements that are turned off. The x-axis indicates transducer element index, spans from 1 to 128 elements. It can be seen that, the aperture size varied from 16, 32, 48 to 64 for each push beam, from DPB-AP1 to DPB-AP4 configurations. The aperture gap of 24 elements and 16 elements was placed between parallel push beams for DPB-AP1 and DPB-AP2, respectively, to place a significant spatial gap between co-located push beams.

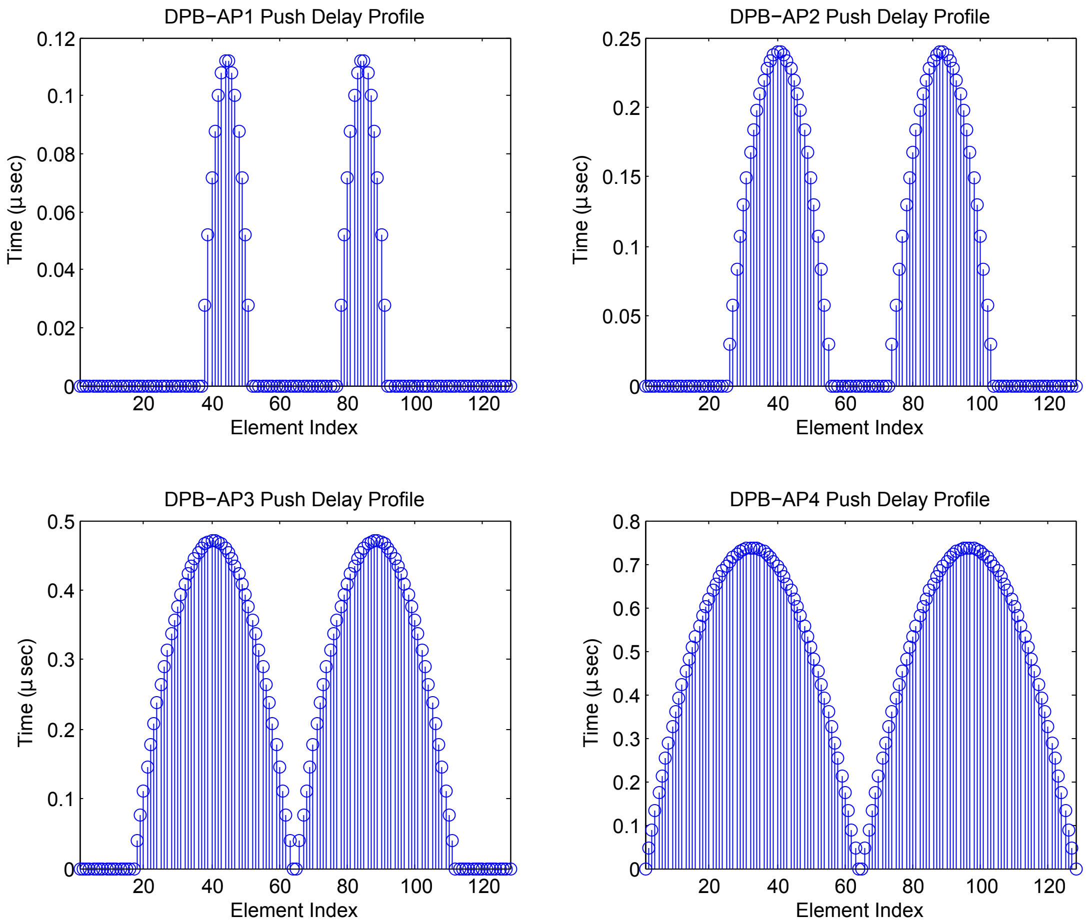

Figure 4.5: Sample delay profiles for focused beams for each DPB configuration. The focal depths used for calculating delay profiles are 15 mm, 30 mm, 40 mm and 45 mm axial locations for all four configurations in the order of configuration names. The delay profiles also indicate the aperture size and lateral locations of push beams. It can be clearly observed that lateral beam centres are getting further away as aperture size is increasing, therefore no aperture gap was used for DPB-AP3 and DPB-AP4 configurations.

Ultrasound system

The proposed shear wave elastography technique DPB, and existing techniques such as SSI, U-CUSE and F-CUSE are implemented on UARP II. The scanner is developed by the Ultrasound Group, University of Leeds, specifically for research (Smith *et al.*, 2012, 2013). The 128 channel ultrasound system is capable of high frame rate plane wave imaging and storing all the backscattered RF data into the primary memory of the system. A linear array medical ultrasound probe (Prosonic L3-8/40EP) with 128 elements is used for all the experiments in this study. The UARP II system and transducer array specifications are listed in Table. 4.1.

Table 4.1: Linear array transducer and UARP II parameters

Parameter	Value
Transducer Name	Prosonic L3-8/40EP
Transducer Elements	128
Transducer Centre Frequency (-6 dB)	4.79 MHz
Transducer Fractional Bandwidth (-6 dB)	57.261 %
Transducer Element Pitch	0.3048 mm
Transducer Elevation Focus	20 mm
Transducer Elevation Aperture Size	6 mm
Transducer Field of View	38.71 mm
UARP II Transmit Frequency	160 MHz
UARP II Receive Frequency	80 MHz

RF data acquisition sequence

The data acquisition procedure for all shear wave elastography experiments conducted in this chapter is divided into three parts. First, a reference equilibrium speckle patterns are achieved using coherent B-mode plane wave imaging, then ultrasound switches to shear wave generation mode, and finally again returns back to coherent plane wave imaging mode to track tissue motion generated by induced shear waves by radiation force. For simplicity, these stages are named as 'pre-push', 'shear wave generation', and 'post-push' modes, respectively. For pre-push and post-push modes, three angle coherent plane wave imaging is used with angles (-4°, 0°, +4°) to improve speckle tracking accuracy.

For pre- and post-push speckle tracking, the transducer array was excited using -30 dB Gaussian-modulated sinusoidal pulse with centre frequency of 4.79 MHz, same as the transducer array centre frequency to maximise acoustic transmission efficiency. In shear wave generation mode for each lateral location, a 570 μs sinusoidal tone burst (6 push beams at same depths, 95 μs each), with the centre frequency equal to transducer centre frequency was used for all the experiments. When shear wave generation is ceased, the ultrasound machine switches back to plane wave imaging mode to track shear wave motion using ultrasound speckle tracking methods. The frame rate of the ultrasound machine for all experiments is set to 10 kHz (excitation trigger period = 100 μs). The total duration of data acquisition is 25 ms, with 1 ms for pre-push mode, 0.6 ms for the shear wave generation mode, and 23.3 ms for post-push shear wave tracking. The first post-push frame was discarded because it contained strong acoustic reflections coming from shear wave generation mode transmissions. Imaging depth for all RF data frames were set to 6 cm for a total of 250 frames during acquisition.

4.2.2 B-mode image formation

The high frame rate imaging is crucial for tracking shear wave induced motion simultaneously along the lateral direction, which was actualised by performing transmission and reception at all elements at the same time. High frame rate imaging used single plane wave insonification in the transmission mode and B-mode image was formed using conventional delay and sum beamforming method in the receive mode (Alomari *et al.*, 2014; Montaldo *et al.*, 2009) using off-line processing. During pre- and post-push speckle tracking, the medium was insonified by the -30 dB Gaussian-modulated sinusoidal pulse using width modulated waveform generation method (Smith *et al.*, 2013). To improve shear wave motion estimation accuracy, coherent plane wave compounding with three different steering angles (-4°, 0°, +4°) were used, suggested by (Montaldo *et al.*, 2009) for shear wave elastography. At each pixel location, three spans moving average filter was used in the slow time direction to average three consecutive frames. Axial pixel resolution of B-mode image is equal to the spatial sampling period ($\sim$ 9.25 μm, assuming acoustic speed = 1540 m/s), while lateral resolution (lateral pixel) was set to one-half of the ultrasound wavelength ($\lambda/2 \sim 152.4$ μm) during beamforming and temporal resolution of the RF data was set equal to 100 μs, governed by the 10 kHz frame rate configured for all shear wave experiments in this study.

4.2.3 Shear wave motion estimation

Shear wave motion is tracked using cross correlation based speckle tracking algorithms. A shear wave is a type of transverse mechanical wave, therefore application of acoustic radiation force in elastic material generates shear waves travelling (carrying the energy) in the lateral direction while generating speckle motion in the axial direction. The axial motion induced by shear waves is estimated by calculating the axial component of displacement using speckle tracking between two subsequent RF three-angle compounded frames. There are various methods to track shear waves used in elastography literature mainly categorised as time-based and phase-based estimators, as detailed in comparative study is done by (Viola & Walker, 2003). Shear wave tracking by the Professor Greenleaf group (which developed CUSE) was achieved the by 2D autocorrelation method which is a phased-based estimation, inspired from a blood flow estimation method (Kasai *et al.*, 1985; Loupas *et al.*, 1995a,b), while SSI elastography group used normalised cross correlation (NCC), which is a time-based technique (Bercoff *et al.*, 2004b; Montaldo *et al.*, 2009; Tanter *et al.*, 2008). For ultrasound speckle tracking, NCC was suggested as superior to other methods (Viola & Walker, 2003), although 2D autocorrelation is faster than NCC. The drawback of 2D autocorrelation is poor performance in low SNR conditions.

For all studies in this chapter, the axial displacement was calculated using one-dimensional NCC. The shear wave motion was estimated by using a 6λ kernel in depth and with a kernel shift of $\lambda/2$ between two neighbouring kernels. To achieve sub-sample displacement estimation, the beamformed RF data was interpolated 30 times using spline interpolation before speckle tracking; this improves displacement estimation resolution/precision from approximately 9 μm to 0.3 μm. After displacement estimation, a 2 x 2 pixel (λ x λ) spatial median filter was applied on each displacement frame to remove local outliers. A sample of displacement images for all the configurations of the shear wave generation is presented in Fig. 4.6. A peak axial displacement at beam locations up to 10 μm for DPB-AP1 and DPB-AP2 configurations, while up to 30 μm and 40 μm for DPB-AP3 and DPB-AP4 can be observed in Fig.4.6 as last two configurations use bigger sub-apertures.

4.2.4 Directional filtering

Each lateral beam places shear wave sources at increasing depths, which produces two shear waves travelling in the transverse direction and motion along axial direction. When two shear wave sources are placed using DPB configurations, waves start travelling in directions away from and opposite to each other, and this interaction of waves generates complex shear wave interference patterns. The waves travelling from left to right of the transducer are called LR while right to left propagating waves are called RL shear waves. There is need to spatially filter and separate each direction shear waves to avoid shear wave speed estimation artefacts. The shear wave displacement dataset produced after the shear wave motion estimation stage has three dimensions, two dimensions in space (axial and lateral) and one dimension in time (slow time). A 2D slice of image signal containing lateral and slow time dimension at each depth is selected and transformed into frequency domain using the 2D Fourier Transform (FT) method. In the frequency domain, lateral slice dimension is transformed into spatial frequency (m^{-1}) and slow time dimension is transformed into temporal frequency (Hz). Interestingly in the FT transformed image, The LR shear wavefield energy lies in the first and third quadrant while RL shear wavefield energy occupies the

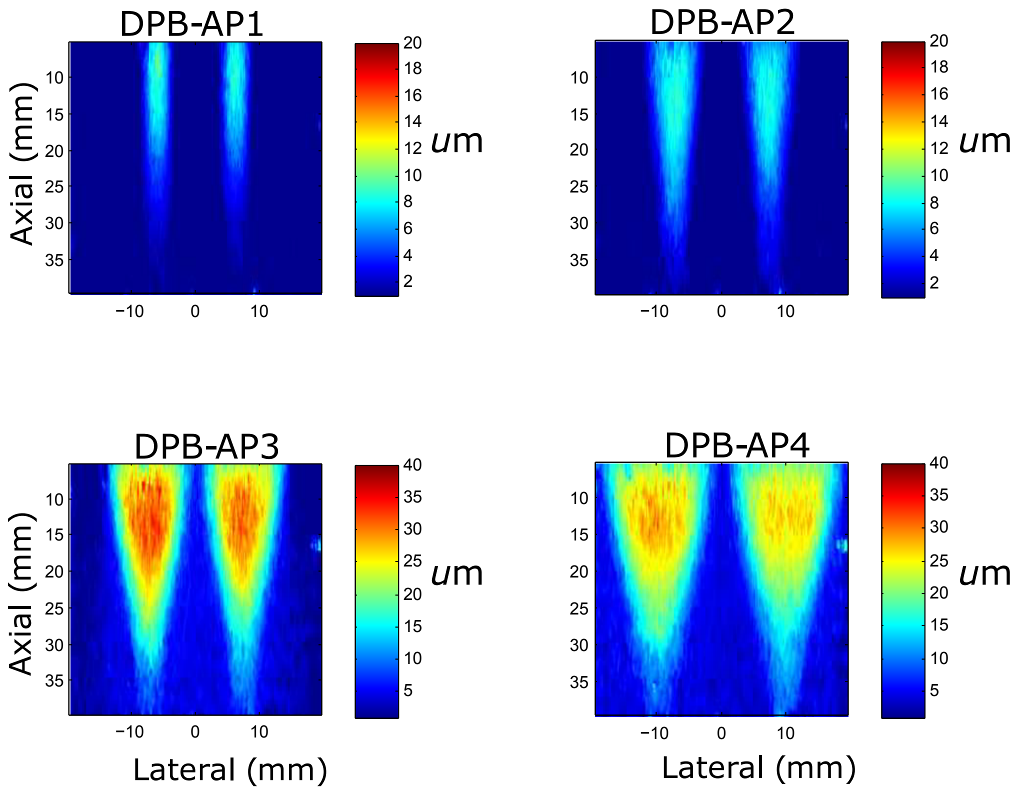

Figure 4.6: A sample of axial displacement images at time instant equal to 0.2 ms after shear wave generation (or at 1.8 ms after data acquisition is started) is ceased for all four DPB configurations. The colour bar scale indicates displacement and is in the units of μm. All the images are labelled according to corresponding shear wave generation configurations. It can be observed that, as sub-aperture used for push beam generation is increasing from DPB-AP1 to DPB-AP4, the produced axial displacement image is also improved, and eventually improving overall shear wave SNR of acquired dataset.

second and fourth quadrant. A binary mask is designed to separate the signal of the first and third quadrant from the second and fourth quadrant in order to separate RL and LR shear wave field. Further, to avoid artefacts due to Gibbs oscillations, the edges of the binary mask are apodized, as proposed by (Deffieux *et al.*, 2011; Manduca *et al.*, 2003; Song *et al.*, 2012).

Before and after directionally filtered and separated LR and RL shear wave-field images are presented in Fig. 4.7, calculated for depth of a 15 mm. The DPB shear wave generation generates two shear wave energy sources, which enable shear waves in the lateral direction for a time before shear wave energy is damped completely as can be seen in Fig. 4.7a. This shear wave sources originate at where the shear wave beam centres are located (around -7.5 mm and +7.5 mm) and travel in both directions. It can be observed that shear wave energy reduces as the slow time increases and displacement amplitude is significantly reduced around 15 ms slow time. In Fig. 4.7b and Fig. 4.7c, it can be seen that RL and LR shear wave fields are separated, respectively. The RL and LR wave field image indicate that, RL shear wave is travelling towards left of the image and LR is travelling towards right of the image.

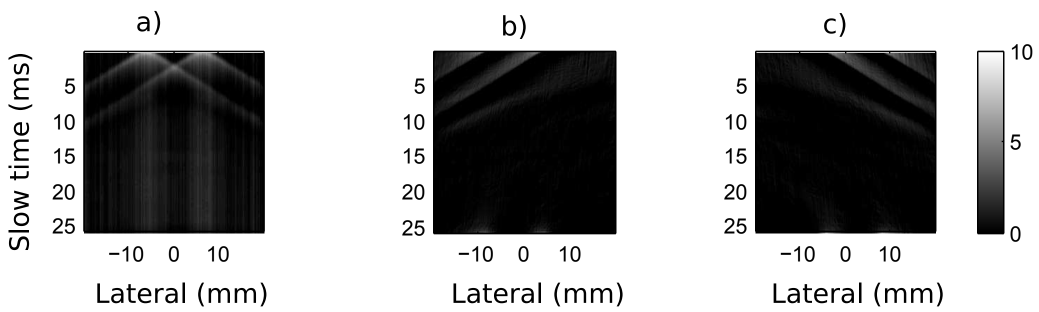

Figure 4.7: Shear wave field images along all slow time and lateral dimension at a depth of 15 mm before and after applying the directional filter. (a) The complex shear waves field with interference patterns before directional filtering. (b) The RL travelling only shear wave field separated from the complex shear wave field using 2D FFT. (c) The LR travelling only extracted shear waves. The colourbar scale displacement and is in the units of displacement μm.

4.2.5 Local Young's modulus reconstruction

Shear wavefront arrival time (also called time of flight) estimation method was used for estimating shear wave speed. After calculating shear wave speed for all pixels in the image, the Young's modulus map is calculated by using the relationship between shear wave speed and Young's modulus, expressed using Equation 1.9.

Arrival-time estimation algorithm

The left and right travelling (LR and RL) 3D shear wave field dataset are produced, after separating complex shear wavefields using a directional filter. For each dataset, the shear wave propagation speed map was calculated using arrival time algorithm proposed by (McLaughlin & Renzi, 2006). Arrival time delay (time of flight) between two lateral locations was calculated by cross correlating the temporal shear wave motion profiles between two lateral locations separated by 16 lateral pixels (Lateral kernel $\sim$ 2.4 mm) at the same depth. Before performing normalised cross correlation, each time profile data is bandpass filtered (Bandwidth $\sim$ 10 to 500 Hz). For sub-frame delay estimation, each time profile data is interpolated by ten times using spline interpolation, eventually increasing frame rate up to 100 kHz. Finally, to improve estimation accuracy , data is Tukey windowed (ratio of tapered section to constant section is 0.1) to smooth edges of the motion data. After calculating arrival time delay between two lateral locations, the shear wave speed was calculated by the calculating ratio of lateral kernel over arrival time delay. Each dataset (RL and LR) produces shear wave speed estimation covering half of the FOV, therefore the final image is obtained by concatenating LR and RL elasticity images and sharp boundary edges are smoothed by median filter.

4.3 Experiments and results

In this section, all the experiments and corresponding results and discussion are presented. It includes experiments conducted using the homogeneous scenario,

Table 4.2: Signal processing parameters

Parameter	Value
Displacement estimation window	2 mm
Displacement estimation window separation	$\lambda/2$
Axial up-sampling	30 times
Shear wave speed estimation window	8λ
Shear wave speed estimation window separation	$\lambda/2$
Temporal up-sampling	10 times
Elasticity image median filtering	2λ x 2λ

a heterogeneous scenario with low elasticity inclusion and high elasticity inclusion. Also, an experimental and simulation study was conducted to investigate effects of shear wave generation depth improvements using large aperture DPB configurations.

4.3.1 Homogeneous phantom study

The purpose of this study is to test if placing two lateral shear wave sources can achieve 2D elasticity map covering full field of view of transducer, without using multiple acquisitions. Further, the quality of the produced elasticity maps is measured using mean and standard deviation (std.) and compared with two-acquisition based SSI elasticity maps and reference phantom measurements. It is important to know that, mean parameter indicates estimation bias and mean value of the proposed method is compared with the SSI calculated mean and nominal (reference) elasticity value of the phantom, while standard deviation measures jitter or precision of elasticity measurement. Shear wave generation using DPB investigates four different sub-apertures [16, 32, 48, 64] for each lateral source, the purpose is to use different sub-aperture for different imaging depth. In contrast to U-CUSE and F-CUSE where single sub-apertures are investigated and fixed, while here four different DPB configurations are investigated to increase flexibility.

Imaging meduim

A commercial multi-purpose, multi-tissue Zerdine gel based ultrasound phantom (Model 040GSE, CIRS Inc., Norfolk, VA, USA) was used for all the experiments in this study. The phantom is multi-purpose, therefore, it has both B-mode imaging and elasticity targets. The schematic diagram and corresponding ultrasound image of the phantom provided by the manufacturer are shown in Fig. 4.8. The imaging medium background nominal (calibrated and provided by the manufacturer) elasticity is 22 ±5 kPa, and two sets of three inclusions targets have elasticity of 10 ±3 kPa (Inclusion I), 40 ±5 kPa (Inclusion II) and 60 ±6 kPa (Inclusion III). Acoustic attenuation, acoustic speed, and mass density of the imaging parts of the phantom are 0.5 dB/cm-MHz, 1050 kg/m^3 and 1540 m/s, respectively. These acoustic and mechanical properties of the phantom are listed in Table. 4.3.

It was found that, there was a discrepancy between elastic modulus measurements acquired from three shear wave elastography systems and values provided by the manufacturer. (Oudry *et al.*, 2014) conducted a study to investigate elastic measurement variability for Zerdine gel phantom samples among four different techniques and found inter-system bias up to 34%. The author associated the source of bias with the different measurement sample size, and shape requirements and protocols used for different testing machines, thus result in boundary condition related bias among different measurement methods. Also, measurement bias among four methods increased from soft to stiff sample measurements due to diffraction effects, also observed by (Sandrin *et al.*, 2003) for transient elastography method. This study concluded that, there is lack of gold standard for elasticity measurements and recommended cautious approach for using manufacturer's provided values as reference for ultrasound elastography experiments. As ultrasound based shear wave elastography is more close to the proposed method being tested in terms of governing laws and measurement protocols, therefore, ultrasound elastography obtained values are used as reference for this study. Observing the elasticity maps achieved by SSI shear wave elastography enabled system (Aixplorer, SuperSonic Imagine, France) in Fig. 4.9 and LOGIQ E9 (GE Healthcare, UK) ultrasound elastography system in 4.10, elasticity values for background, Inclusion I, Inclusion II, and Inclusion III were measured approximately as 22 kPa, 10 kPa, 27 kPa, and 40 kPa, respectively. To keep the schematic diagram original as provided by the manufacturer, values inside diagrams are not changed, as presented in Fig. 4.8, Fig. 4.11, Fig. 4.15 and Fig. 4.17.

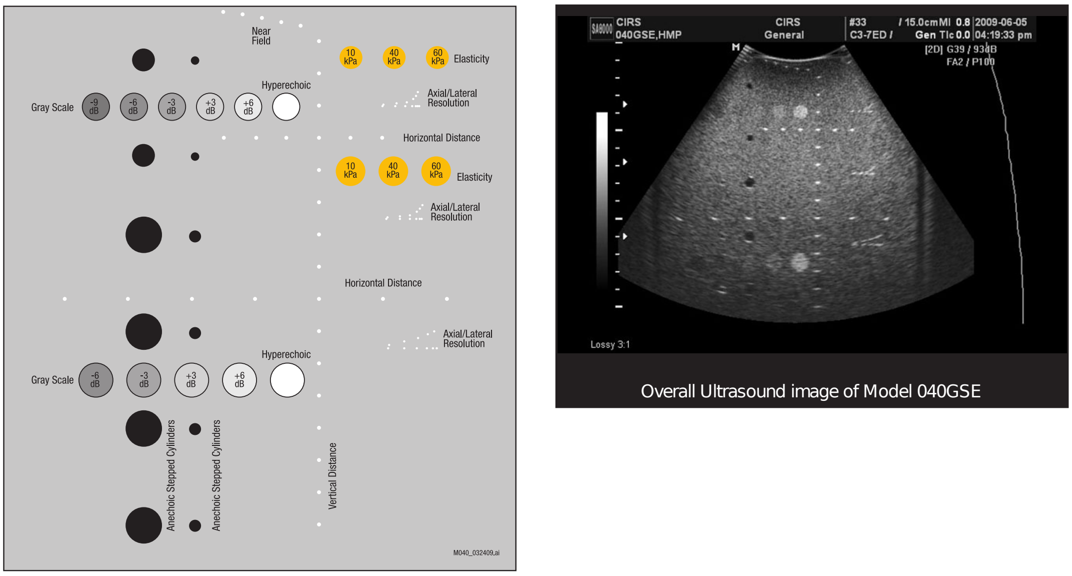

Figure 4.8: The schematic diagram of the CIRS Multi-Purpose, Multi-Tissue ultrasound phantom and corresponding B-mode image provided by the manufacturer. Left) The phantom schematic shows targets like wire, cysts, hyper-echoic, hypoechoic, and elasticity targets, suitable for various ultrasound applications. For elastography, only elasticity targets (orange colored circles) and background tissue phantom are used. There are two groups of elasticity targets, one centred at 15 mm (shallow) while the second group at 50 mm (deep) depth of the surface of the transducer, and shallow group targets have a diameter of 6 mm while deep inclusion diameter is 8 mm. In each group, there are three cylindrical inclusions, 10 kPa, 40 kPa, and 60 kPa. Right) The corresponding B-mode image indicates all the B-mode targets while elasticity inclusions can not be shown. The diagram and B-mode image reproduction here is credited to the manufacturer (CIRS Inc., Norfolk, VA, USA).

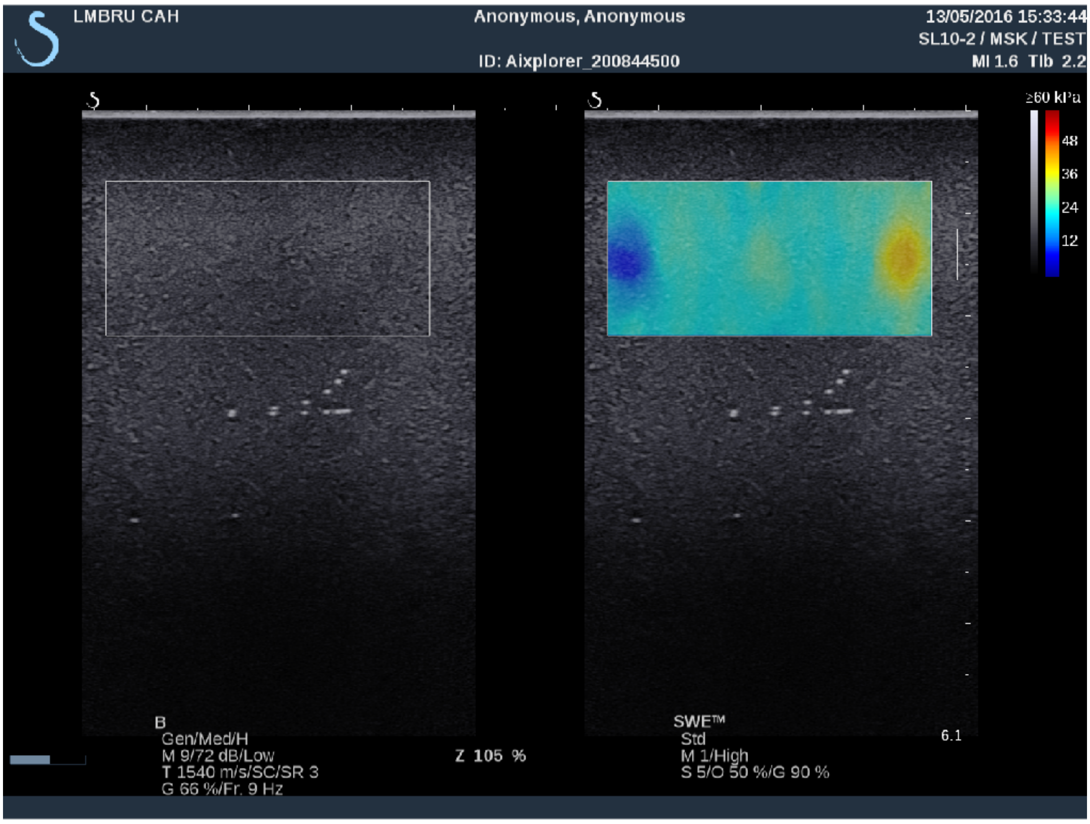

Figure 4.9: A sample of B-mode and elasticity map of the ROI indicated by the rectagular box acquired using SSI shear wave elastography enabled ultrasound system. It can be observed that, Inclusion I (left) elasticity is approximately 10 kPa, Inclusion II (centre) can not be clearly detected as elasticity is close to background elasticity, while Inclusion III (right) is detected as approximately 40 kPa, while background elasticity is around 22 kPa. Courtesy of Chapel Allterton Hospital, Leeds, UK for access to ultrasound system.

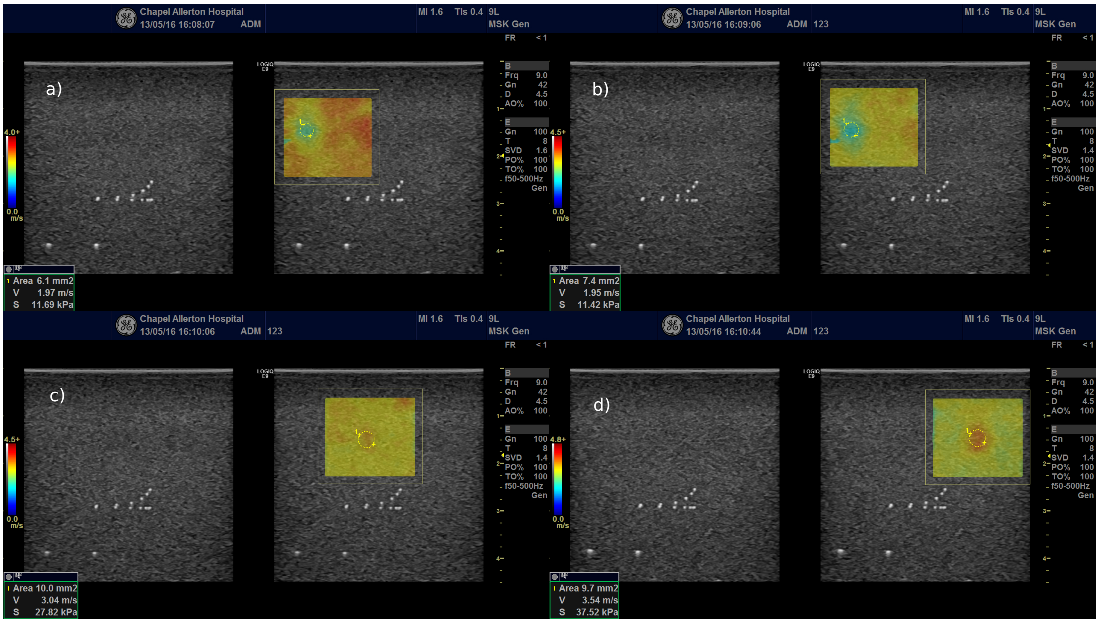

Figure 4.10: A sample of B-mode and elasticity maps acquired using GE LOGIQ E9 shear wave elastography machine. It can be observed that, Inclusion I (a and b) elasticity is approximately 11.50 kPa, Inclusion II (c) is detected as stiffness of 28 kPa which is close to background elasticity of approximately 22 kPa, while Inclusion III (d) is detected as approximately 38 kPa. Courtesy of Chapel Allterton Hospital, Leeds, UK for access to ultrasound system.

Table 4.3: CIRS phantom properties provided by the manufacturer

Name	Value
Model	040GSE
Material	Zerdine
Acoustic Speed	1540 m/s
Density	1020 to 1080 kg/m^3
Acoustic Attenuation	0.5 dB/cm-MHz
Background Elastic Modulus	22 $\pm$5 kPa
Inclusions Elastic Modulus	10 $\pm$3, 40 $\pm$5 and 60 $\pm$6 kPa

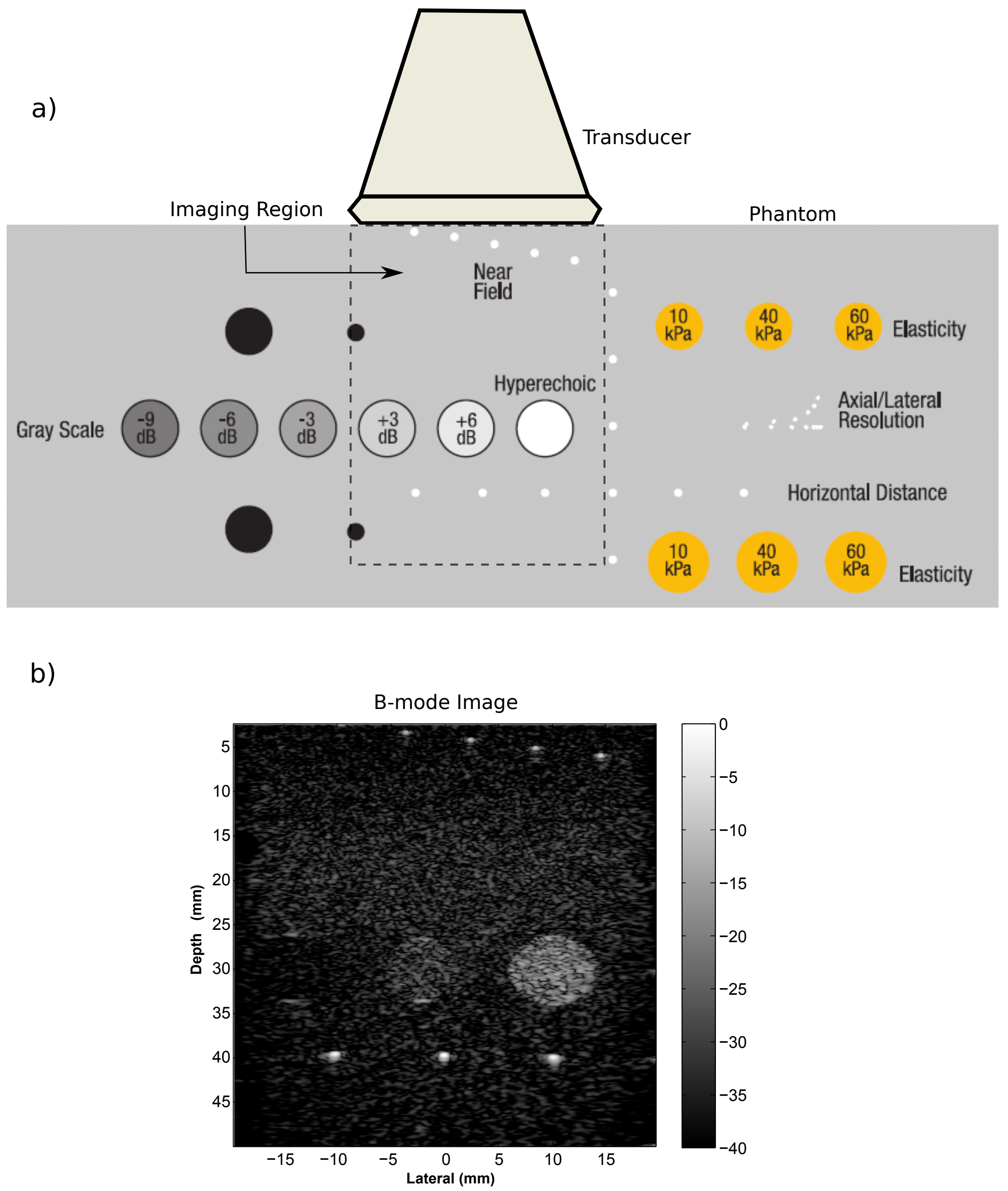

Figure 4.11: Experimental set up indicating the phantom diagram with the imaging region and the corresponding B-mode image for the homogeneous study. (a) Linear array transducer placed close to the surface of the phantom, slightly touching the phantom surface to ensure there is no air gap between transducer and phantom surface and also to ensure the transducer is not applying high stress which may alter the elasticity of the phantom. Degassed and de-ionised water was used as an impedance matching layer in order to avoid air gap between the transducer and phantom surface. The imaging region is indicated by the dotted rectangular box. (b) B-mode image produced by three angle compound plane wave imaging are able to visualise the wire and echo targets.

Experimental Setup

A linear array transducer was placed close to the surface of the phantom, slightly touching the surface of the phantom avoiding any applied stress by the transducer onto the phantom. Degassed and de-ionised water was used as an acoustic impedance matching layer between the transducer and the phantom surface, the water was contained using a water well (provided by the manufacturer). A 50 mm depth and 38.71 mm lateral imaging region with only homogeneous elastic phantom part was selected for the experiment for RF data acquisition indicated by dotted rectangular box in Fig. 4.11a using dotted lines. The corresponding B-mode image is shown in Fig. 4.11b, where near field, horizontal distance wire targets and hyperechoic, +6 dB, and +3 dB acoustic inclusion targets can be seen. In this experiment, all four DPB configurations are tested. As a reference technique, an experiment was also conducted for conventional two acquisition SSI technique. For the DPB configurations, shear wave generation beams were focused at [15 30 40 45] mm for AP1 to AP4, respectively. For SSI, to acquire a single 2D elasticity image, two acquisitions were obtained, called left (SSI-Left) and right (SSI-Right) acquisitions. For each acquisition, push beams are placed at successive depths, which are [35 37 39 41 43 45] mm.

The focal configuration details for AP1 to AP4, SSI-Left and SSI-Right schemes are summarised in Table. 4.4. For DPB configurations AP1 to AP4, F/numbers are set in the decreasing (5.12, 4.10, 3.07, 2.30 and 2.30) order. This is designed considering depth dependent attenuation reduces radiation force at increasing depths, therefore narrower beams are selected at increasing depths to allow compensation of attenuation. Final elasticity image depth dimensions are curtailed according to an imaging depth of the shear wave generation.

Table 4.4: Aperture and focal depth parameters for homogeneous phantom experiment study. From AP1 to AP4, transmit focal profiles become tighter, considering depth dependent attenuation reduces radiation force at increasing depths, therefore narrower beams are selected at increasing depths to allow compensation of attenuation.

Name	Aperture size	Focal depths
DPB-AP1	4.88 mm (16 Elements)	[15 15 15 15 15 15] mm
DPB-AP2	9.75 mm (32 Elements)	[30 30 30 30 30 30] mm
DPB-AP3	14.63 mm (48 Elements)	[40 40 40 40 40 40] mm
DPB-AP4	19.50 mm (64 Elements)	[45 45 45 45 45 45] mm
SSI-Left	19.50 mm (64 Elements)	[35 37 39 41 43 45] mm
SSI-Right	19.50 mm (64 Elements)	[35 37 39 41 43 45] mm

Homogeneous phantom study results

Elasticity maps are produced for all the four DPB configurations and two-acquisition SSI and presented in Fig. 4.12. The size of elasticity maps for DPB-AP1 and DPB-AP2 is 3 mm to 25 mm in axial direction, and -18.2 mm to +18.2 mm laterally. The axial length of other elasticity maps is 3 mm to 40 mm, while FOV is same. The elasticity data values are used starting from 3 mm depth as in near field region elasticity estimation were noisy near the transducer and backscattered echo RF data is received once high amplitude vibrations are attenuated. For the DPB-AP1 and DPB-AP2 configurations, push beam focal depths are selected as 15 mm and 30 mm respectively. To avoid temperature raising inside the phantom, ±50 V was used for shear wave generation. For other all configurations, full power supply voltage ±100 V was applied. Low voltage excitation pulse reduces the peak displacement and eventually shear wave SNR. The displacement images produced in this study are shown in Fig. 4.6, it can be observed that DPB-AP1 and DPB-AP2 displacement maps have lower peak displacement as compared to DPB-AP3 and DPB-AP4.

A region-of-interest (ROI) was selected to calculate the mean and standard deviation of the estimated Young's modulus as used by the previous studies (Song *et al.*, 2012, 2013a, 2014). The mean and standard deviation values are plotted using errorbar plot in Fig. 4.13. Size of the ROI is 3 mm to 25 mm in the axial and 36.4 mm in the lateral direction for all the elasticity maps. The pixel resolution of the final Young's modulus maps is 152.4 μm ($\lambda/2$) in both axial and lateral directions. For local shear wave speed calculation, displacement time profiles were selected with a lateral spacing of 16 lateral pixels ($8\lambda = 2.44$ mm). To remove estimation outliers, a 2λ x 2λ spatial window median filter was applied.

Statistical parameters of elasticity measurements (Fig. 4.13) have indicated good agreement among all the DPB configurations and SSI. There is less than 2 kPa difference in mean values between all DPB and SSI configuration and the standard deviation is less than 1 kPa for each DPB method. All the proposed configuration results are comparable and better in some cases relative the SSI estimation results. The bias (when compared with nominal value) for all DPB methods is within 5 kPa range. The overestimation observed in the shallow regions, is possibly due to diverging beams at shallow depths when large apertures and deep axial focal points are used. The beam divergence increases away from the focal point and also widens when tighter focal beams are used. As F/numbers are decreasing from DPB-AP1 to SSI, beams are getting more diverged close to the transducer and result in the overestimation artefacts. The bias due to beam divergence (large aperture size and depth away from the focal point) also had been observed in the shear wave elastography by (Zhao *et al.*, 2011b).

Shear wave generation SNR images in terms of peak shear wave displacement are presented in Fig. 4.14 for DPB-AP4, SSI-left, SSI-right, and added image of SSI-left and SSI-right. It can be observed that, AP4 configuration produces good SNR in both left and right parts of the image, greater than the individual left and right SSI peak displacement maps, while combined SSI-left and SSI-right produces higher over SNR than the AP4 configuration. The possible reason is AP4 uses all the 128 elements simultaneously in contrast to SSI single acquisition which uses 64 elements, placing high load on the power supply. For numerical comparison, peak displacement values are summed for each image, where AP4 has produced 1.46, and 1.55 times higher SNR than SSI-left and SSI-right while combined SSI map produces 1.33 times higher SNR than the AP4 map.

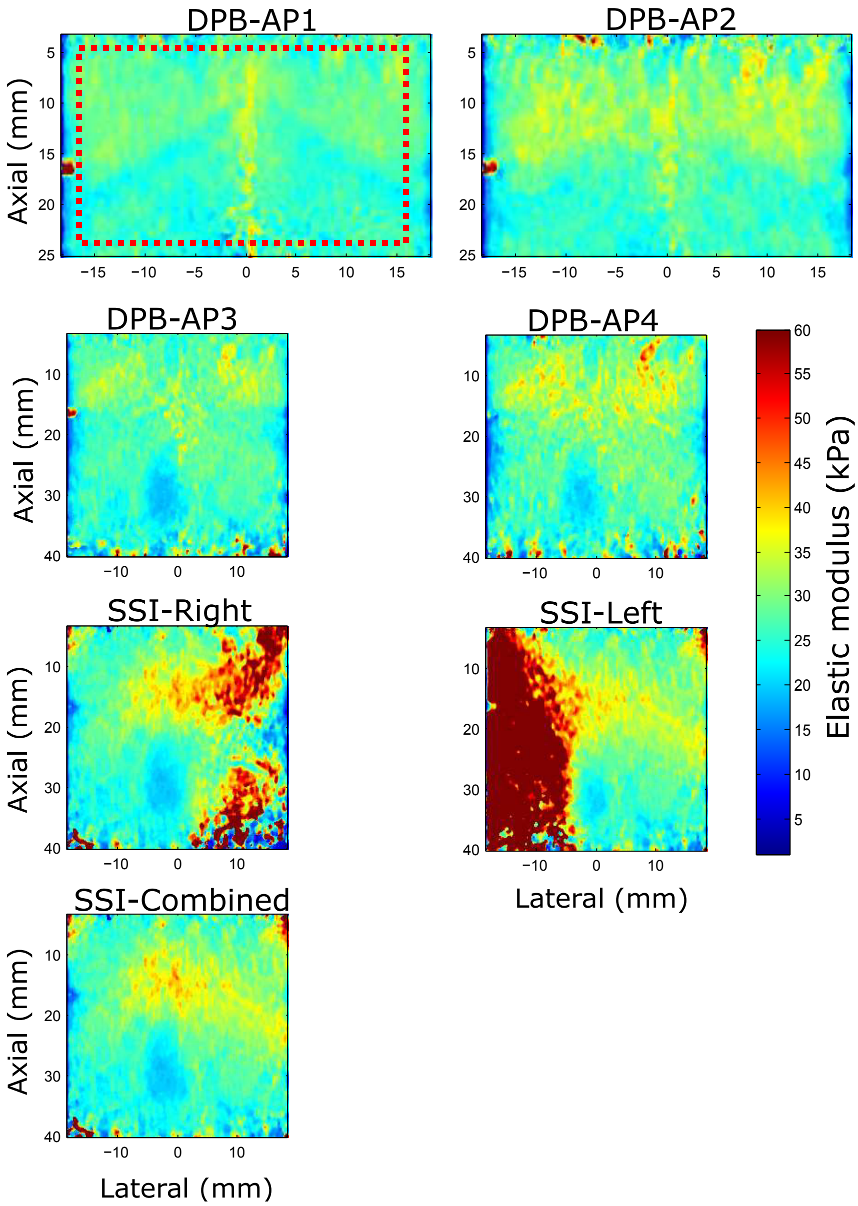

Figure 4.12: Elastic modulus maps for all the DPB configurations, and SSI for the homogeneous phantom experiment. The colourbar scales are same for all the maps and indicate Young's modulus ranging from 1 to 60 kPa. Shear wave generation configuration for each map is indicated by the labels at the top of each map. All the four configurations are able to produce 2D elasticity maps without any artefact in a single push-detect acquisition, while for the conventional SSI technique two push-detect events named as SSI-Right and SSI-Left produce full 2D map named SSI-Combined. The ‘dead zone’ artefact can be observed in SSI-Left and SSI-Right images.

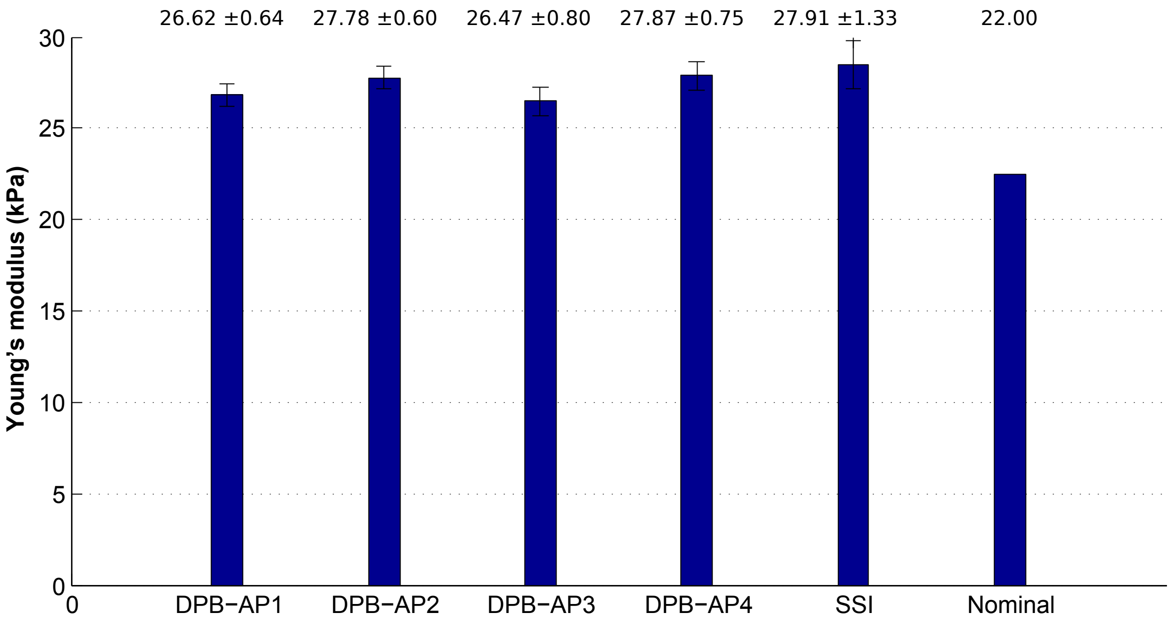

Figure 4.13: Errorbar plots for the homogeneous experimental results in the ROI, showing Young's modulus mean and standard deviation values for four DPB, SSI and nominal value. Bias (compared with the nominal value) for all DPB methods is within 5 kPa range and standard deviation is less than 1 kPa, while for SSI bias and standard deviation is slightly increased. All the proposed methods perform comaprabe and better in some cases than the two-acquisition SSI.

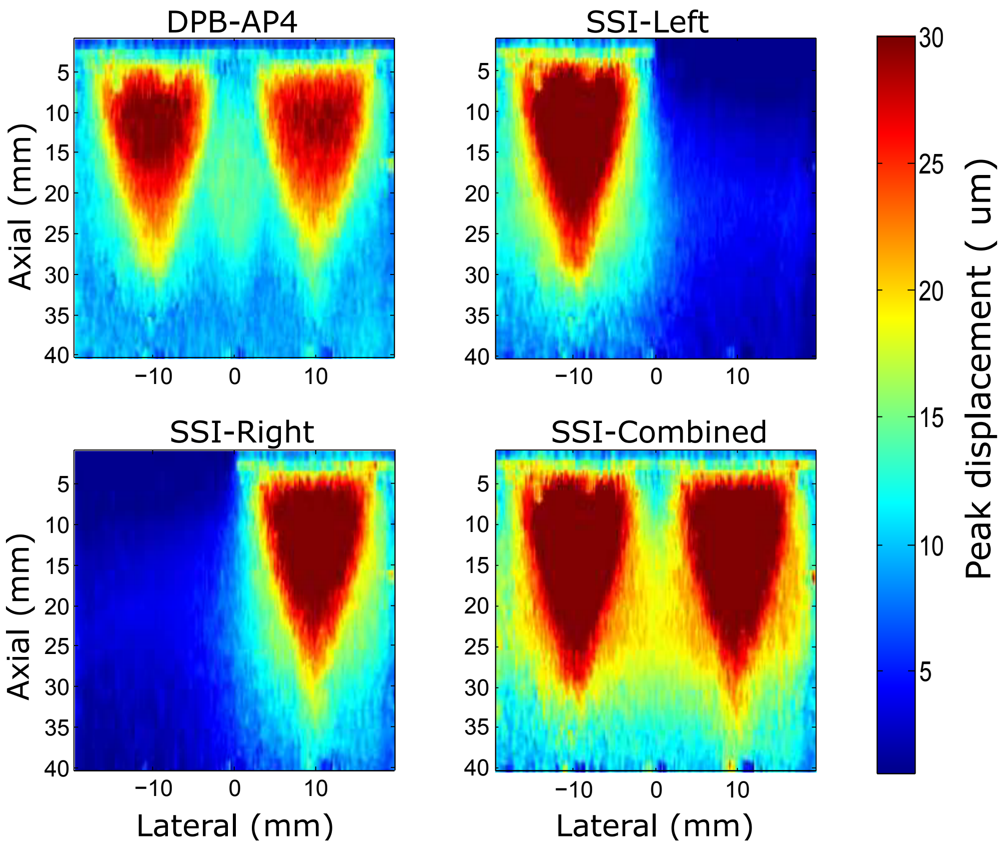

Figure 4.14: A sample of peak axial displacement images for DPB-AP4 and SSI configurations are presented for comparative SNR analysis between the proposed method and SSI. It can be observed that, AP4 configuration produces good SNR in both left and right parts of the image, and greater than individual left and right SSI peak displacement maps, while combined SSI-left and SSI-right produces higher overall SNR than the AP4 configuration. For numerical comparison, peak displacement values are summed for each image, where AP4 has produced 1.46, and 1.55 times higher SNR than SSI-left and SSI-right while combined SSI map produces 1.33 times higher SNR than the AP4 map.

Images and quality parameters indicate that it is possible to produce a 2D elasticity map with full FOV without using multiple acquisitions and compromising elasticity estimation accuracy, as mean and standard deviation values of all four DPB configurations are comparable with the SSI value. In terms of shear wave SNR, DPB-AP4 produces higher values than the single acquisition SSI, and it can be concluded that the proposed method has improved SNR.

4.3.2 Inclusion phantom study

The objective of the inclusion based phantom study is to evaluate the capacity of the proposed technique to detect elasticity targets. For this purpose, two independent studies each with low and high elasticity inclusions are performed and results are discussed. Moreover, the quality of inclusion detectability is measured by calculating elastic modulus mean and standard deviation inside the inclusion and background and values are compared with the U-CUSE produced elasticity map.

Low elasticity inclusion experiment

The CIRS phantom as used in the previous study was used for the inclusion based experiments. The reference value for the inclusion elasticity is 10 kPa and the centre of the inclusion is located at 15 mm beneath the surface of the phantom. The size of the inclusion is 6 mm and the stiffness is about 2.2 times lower than the background elasticity. Details of the experimental sequence and parameters are the same as used in the homogeneous study experiment. A schematic diagram indicating imaging region and corresponding B-mode image is shown in Fig. 4.15, where B-mode visualises hyperechoic and wire targets with quality adequate for shear wave elastography signal processing.

For statistical analysis, ROIs were selected to measure performance metrics for the inclusion-based phantom experiments (Fig. 4.16). A square box with dimensions of 4.5 mm axially and laterally was placed at the centre of the inclusion to calculate parameters while four similar size ROIs were placed around the

Table 4.5: Elastic modulus mean and standard deviation measurements of inclusion and background from four DPB and U-CUSE configurations for low elasticity inclusion experiment

Name	Background (kPa) mean ± std.	Inclusion (kPa) mean ± std.	Back./Incl.
DPB-AP1	26.58 ± 0.78	14.40 ± 0.32	1.84
DPB-AP2	27.50 ± 0.71	16.50 ± 0.47	1.66
DPB-AP3	28.02 ± 0.81	17.26 ± 0.34	1.62
DPB-AP4	29.06 ± 0.86	19.47 ± 0.44	1.49
U-CUSE	24.29 ± 0.65	13.33 ± 0.27	1.82

inclusion to calculate background elasticity parameters. The mean, standardised deviation (std.) and background to inclusion (Back./Inc.) elasticity ratio parameters are calculated and summarised in Table. 4.5.

The elasticity maps produced indicate that all four DPB configurations are able to detect inclusion with varying estimation quality and contrast. The DPB-AP1, DPB-AP2, and DPB-AP3 are able to visualise the low elasticity target with good contrast and sharp boundaries. The DPB-AP4 performance is poor in shallow regions as also observed in the homogeneous study, therefore, inclusion contrast is not well reconstructed. In the quantitative aspect, inclusion mean detection bias is the least in the DPB-AP1 and slightly higher than the U-CUSE which is used as comparative reference (see Table. 4.5). For other DPB techniques, bias increases from DPB-AP2 to DPB-AP4 configurations. In terms of background ROIs, the performance pattern the same. The standard deviation is less than 1 kPa in all background and inclusion measurements.

High elasticity inclusion experiment

The same CIRS phantom as used in the previous study was used for this study targeting the stiffer inclusion part of the phantom. The schematic diagram indicating the imaging region and the produced B-mode image are shown in Fig.

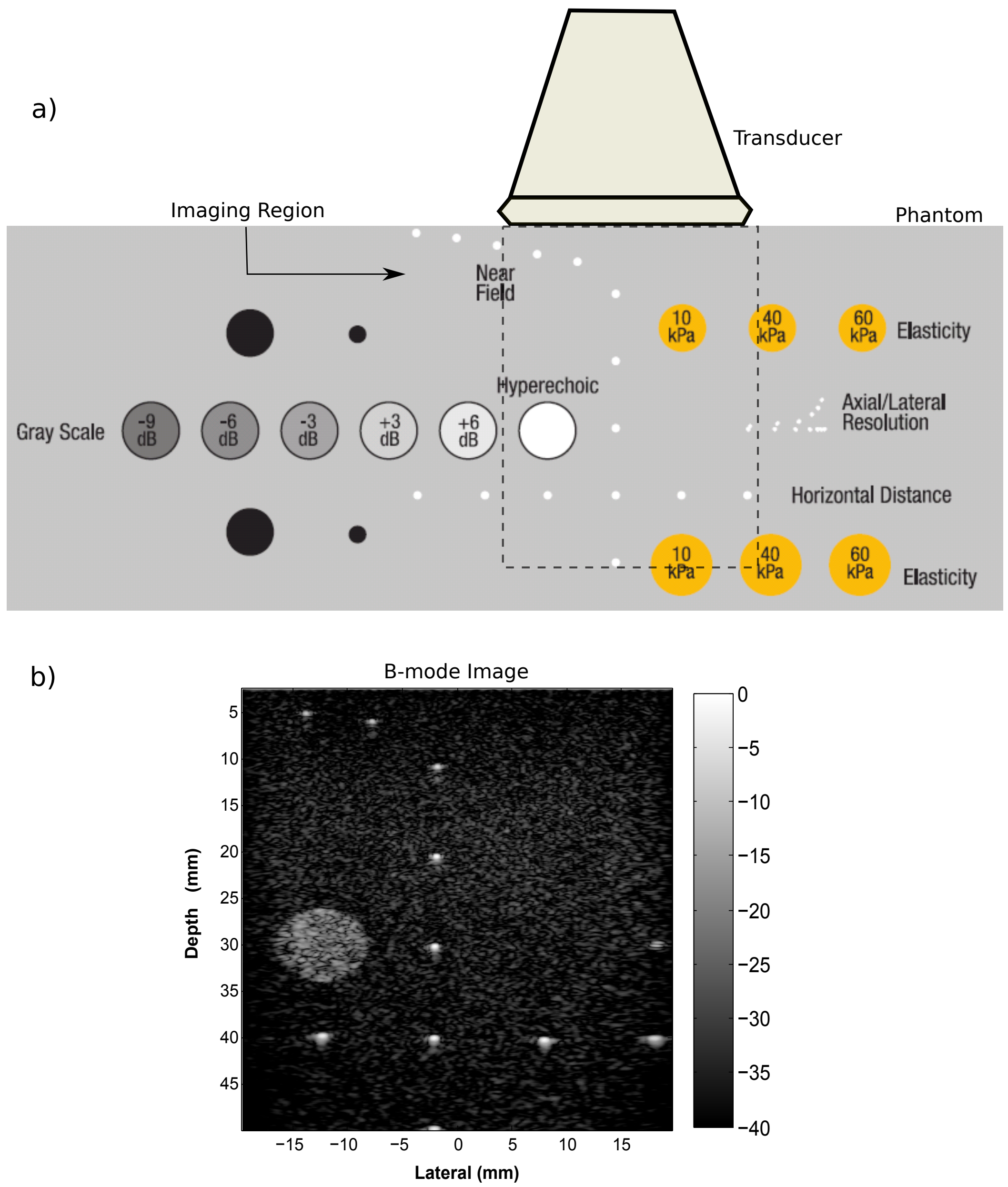

Figure 4.15: Experimental set up and corresponding B-mode image for low elasticity inclusion study. (a) The linear array transducer placed close to the surface of the phantom, slightly touching the phantom surface to ensure there is no air gap between transducer and phantom surface and also to ensure transducer is not applying stress on the phantom. The degassed and de-ionised water was used as an impedance matching layer in order to avoid air between the transducer and phantom surface. The imaging region is indicated by the dotted rectangular box. (b) B-mode image produced by three angles compounded plane wave imaging is presented, shows wire and echo targets.

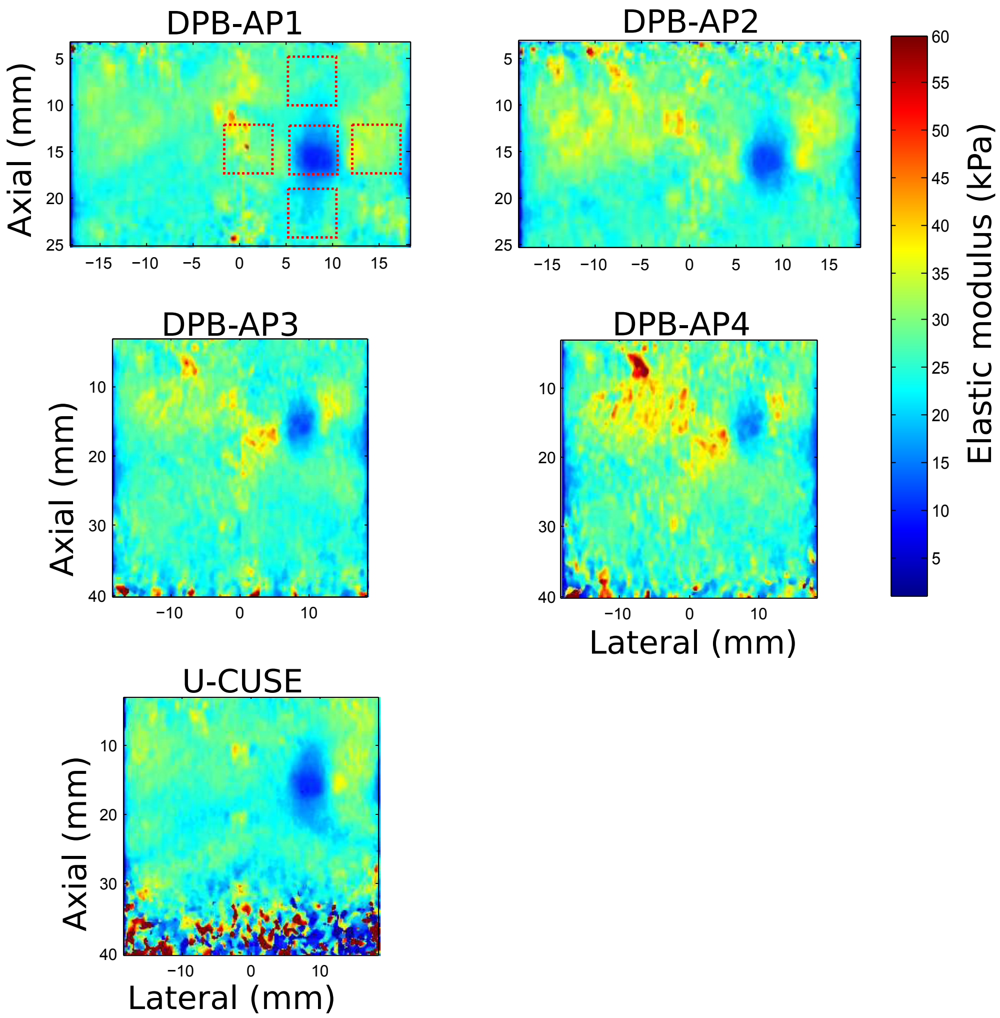

Figure 4.16: Elastic modulus maps for all the DPB configurations for low elasticity phantom experiment. The colourbar scales are same for all the maps and indicate Young's modulus ranging from 10 to 60 kPa. The push beam shear wave generation configuration for each map is indicated by the labels at top of the each map. Elasticity maps indicate that all four DPB configurations are able to detect inclusion with varying estimation quality and contrast. The DPB-AP1, DPB-AP2, and DPB-AP3 are able to visualise the low elasticity target with good contrast and sharp boundaries. The DPB-AP4 performance is poor in shallow regions due to highly diverged beams close to the transducer. DPB-AP1 elasticity shows the red rectangular boxes used for statistical values calculation for inclusion and background. The DPB-AP1 and DPB-AP2 configurations are designed for shallow imaging, therefore imaging depth is up to 25 mm, while for DPB-AP3 and DPB-AP4 imaging depth is increases up to 40 mm.

4.17, where axial/lateral wire targets are visualised with good quality. All experimental parameters are same as used in the homogeneous phantom study. The reference elastic modulus of the inclusion is 40 kPa and is located at 15 mm beneath the surface. The size of the inclusion is 6 mm and the inclusion stiffness is about 1.77 times higher than the background elasticity, calculated as the ratio of 40 kPa to 22 kPa.

For statistical measurements used for performance calculation, ROIs were selected to measure performance metrics for the inclusion-based phantom experiments (Fig. 4.18). A square box with dimensions of 4 mm axially and laterally was placed at the centre of the inclusion to calculate parameters while four similar size ROIs were placed around the inclusion to calculate background elasticity parameters. The mean, standardised deviation and inclusion to background (Inc./Back.) elasticity ratio parameters are calculated and summarised in Table. 4.6.

Elasticity maps (see Fig. 4.18) indicate that all four DPB configurations are able to detect inclusion with varying estimation quality and contrast. The DPB-AP1 elasticity image reconstructed inclusion with good contrast (see Table. 4.6) comparable with the U-CUSE performance. In DPB-AP2, and DPB-AP3 images, background part above the inclusion generated overestimated values and blurred the contrast, while in the DPB-AP4 image, above and to left of the inclusion are overestimated, deteriorated overall contrast. This overestimation in shallow regions is possibly related with the highly diverged shear wave beams in the shallow regions, and same pattern has been observed in all three studies. The inclusion boundaries are sharper in the DPB-AP1 as compared to the other three schemes of DPB due to narrow push beam used.

In the quantitative aspect, inclusion mean detection bias is negligible and significant variance in the DPB-AP1, DPB-AP2, and DPB-AP3 compared with nominal inclusion value, while U-CUSE underestimated the inclusion (see Table. 4.6). The DPB-AP4 has poor performance in terms of both elasticity bias and variance. In the inclusion background estimation, mean values are overestimated with negligible variance for all three DPB configurations while U-CUSE also resulted in overestimation.

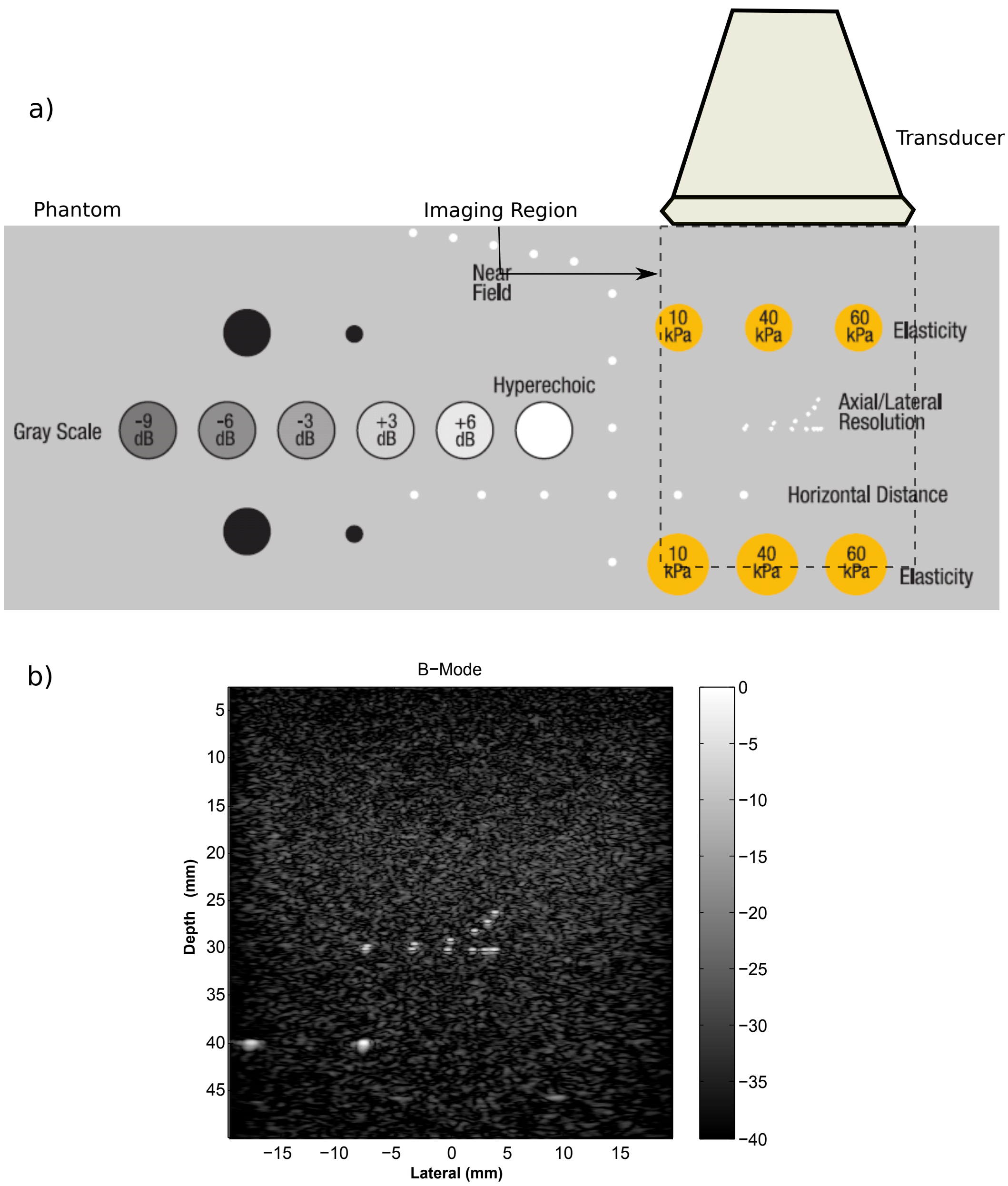

Figure 4.17: Experimental set up and corresponding B-mode image for high elasticity inclusion study. (a) The linear array transducer placed close to the surface of the phantom, slightly touching the phantom surface to ensure there is no air gap between transducer and phantom surface and also to ensure transducer is not applying stress on the phantom. The degassed and de-ionised water was used as an impedance matching layer in order to avoid air between the transducer and phantom surface. The imaging region is indicated by the dotted rectangular box. (b) B-mode image produced by three angles compounded plane wave imaging is presented, shows wire and echo targets.

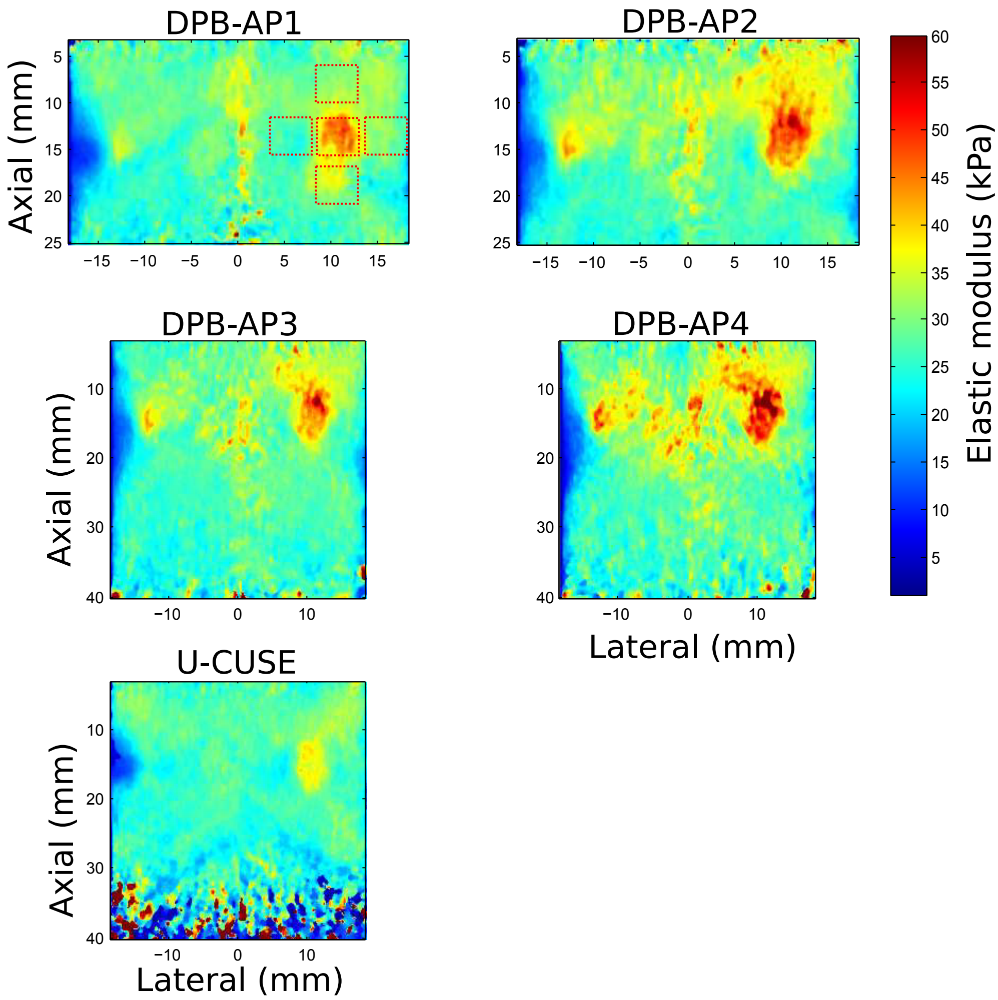

Figure 4.18: Elastic modulus maps for all DPB configurations for high elasticity phantom experiment. The colourbar scales are same for all the maps and indicate Young's modulus ranging from 1 to 60 kPa. The shear wave generation configuration for each map is indicated by the labels at top of the each map. All four DPB configurations are able to detect inclusion with varying estimation quality and contrast. The DPB-AP1 image reconstructed inclusion with good contrast and comparable with the U-CUSE image. In DPB-AP2, and DPB-AP3 images, background part above the inclusion generated overestimated values and blurred the contrast, while in DPB-AP4 image, above and left side of inclusion background are overestimated, deteriorated overall contrast. The DPB-AP1 elasticity shows the red rectangular boxes used for statistical values calculation for inclusion and background. The DPB-AP1 and DPB-AP2 configurations are designed for shallow imaging, therefore imaging depth is up to 25 mm, while for DPB-AP3 and DPB-AP4 imaging depth is increases up to 40 mm. A minor portion of the 10 kPa inclusion which is part of the imaging region can be seen at the left in all elasticity maps.

Table 4.6: Elastic modulus mean and standard deviation measurements of inclusion and background from four DPB and U-CUSE configurations for high elasticity inclusion experiment

Name	Background (kPa) mean ± std.	Inclusion (kPa) mean ± std.	Incl./Back.
DPB-AP1	30.28 ± 0.43	42.82 ± 2.26	1.41
DPB-AP2	32.45 ± 0.70	41.71 ± 4.00	1.28
DPB-AP3	32.05 ± 0.72	41.10 ± 4.20	1.28
DPB-AP4	33.82 ± 1.34	31.59 ± 4.63	0.93
U-CUSE	28.77 ± 0.57	35.96 ± 0.26	1.25

4.3.3 Deep shear wave generation study

In this study, various experiments are conducted to investigate if using the proposed DPB method elasticity imaging depth can be improved relative to U-CUSE and F-CUSE.

Shear wave generation depth test experiment I

The objective of this experiment is to investigate the penetration depth improvement by using large apertures such as used by DPB-AP2, DPB-AP3, and DPB-AP4 configurations. Penetration depth improvement is compared with U-CUSE and F-CUSE. The push beam focal depths are 40 mm, 50 mm, 60 mm, and 40 mm for DPB-AP2, DPB-AP3, DPB-AP4, and F-CUSE, respectively. In this experiment, due to deep focal depths chosen specifically to evaluate maximum shear wave penetration depth that can be achieved using the proposed technique, therefore shallow region overestimation artefacts are expected in the images. The F/numbers for three configurations are used in decreasing order so that depth dependent intensity attenuation can be compensated. Experimental sequence and signal processing parameters remain the same as used in the previous experiments. Elasticity image axial range is 3 mm to 45 mm, while lateral width is similar to transducer FOV. The shear wave generation voltage for all these experiments was set to ±100 V.

U-CUSE uses five unfocused beams each with 12 elements, while F-CUSE employs four beams with 32 elements for each beam, as proposed by (Song *et al.*, 2012, 2013a). The DPB-AP2 beam aperture size is the same as F-CUSE, the DPB-AP3 aperture size is 1.5 times larger, while the DPB-AP4 beam aperture size is 2 times larger than the F-CUSE. The larger aperture has ability to produce tighter focal profiles, which increases acoustic intensity generation at the focal point. Moreover, larger apertures can reach to deeper regions of tissues, compared to smaller apertures.

An experiment was conducted using the homogeneous part of the similar phantom as used in previous studies. The experimental setup and the produced B-mode image is shown in Fig. 4.19. For three DPB apertures, U-CUSE and F-CUSE experiments 2D elasticity maps are produced and shown in Fig. 4.20. Looking at the elasticity maps it can be observed that, the imaging depth of all three DPB configurations and F-CUSE is between 40 mm and 42 mm, while U-CUSE has slightly less which is between 32 mm to 35 mm. According to the results, all three DPB configurations reached up to 42 mm, which is equal to the F-CUSE penetration depth and relatively better than the U-CUSE imaging depth. The DPB-AP3 and DPB-AP4 results are in contrast to expected results.

Possible reasons for little difference in imaging depth improvement for moving from the DPB-AP1 (16 elements) to DPB-AP4 (64 elements) configuration can be related to the transducer and/or ultrasound power supply. First possible reason is power supply voltage drop due to high current demand of the shear wave generation. To investigate this, an experiment was conducted and is explained in Subsection. 4.3.3. Another possible reason is related to the transducer array. In this study for all experiments, a linear array transducer is used, which is optimised for shallow tissue imaging such as breast and thyroid and therefore the elevational focus is fixed at 20 mm. The fixed elevational focus at shallow depths optimises acoustic intensity generation efficiency and 3D beam profile at the elevational focus, therefore selecting axial focal depth away from the elevational focus results in poor acoustic intensity generation at deeper regions. This is explained by the simulation study in Subsection. 4.3.3.

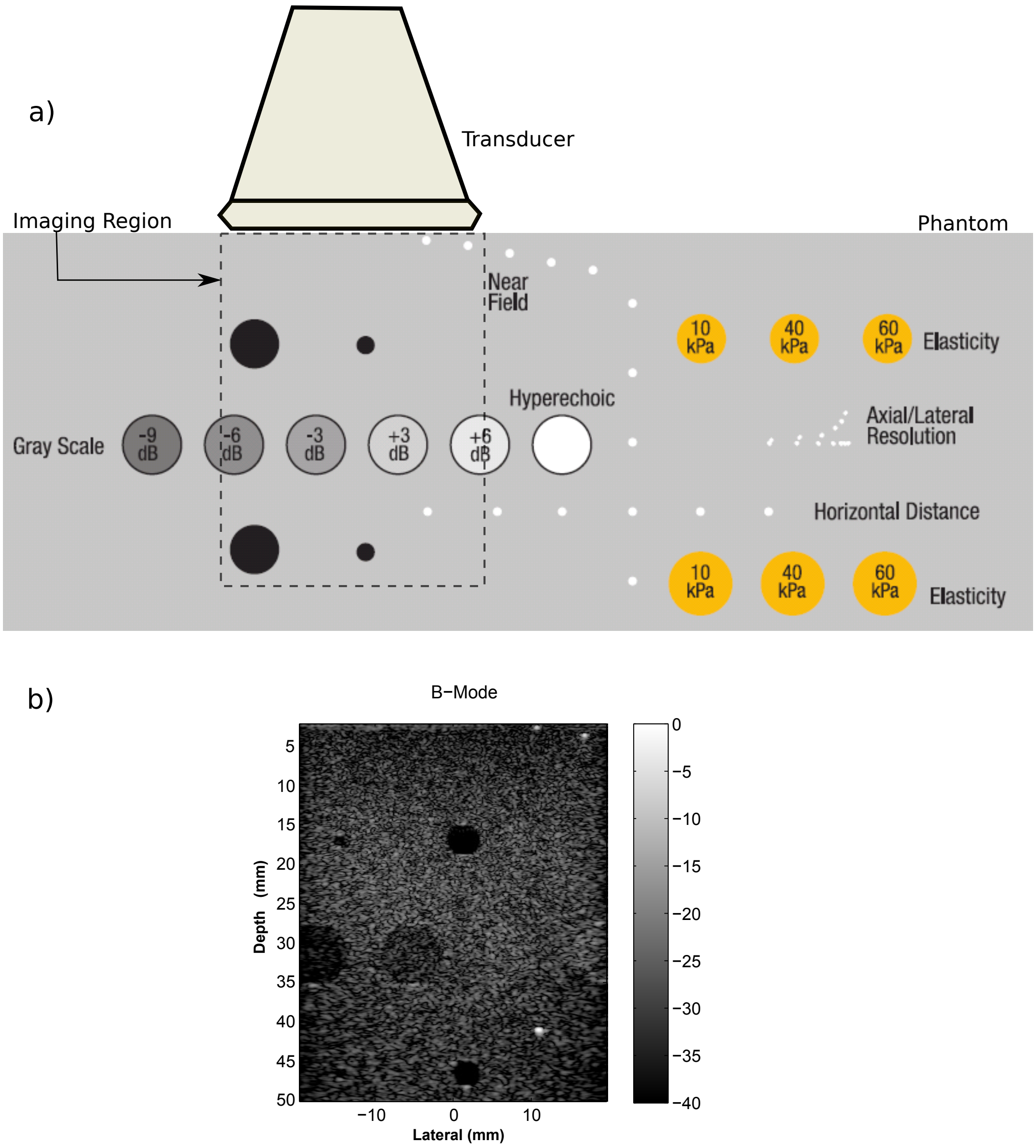

Figure 4.19: Experimental setup and corresponding B-mode image for depth of penetration experimental phantom study a) The linear array transducer placed close to the surface of the phantom, slightly touching the phantom surface to make certain there is no air gap between transducer and phantom surface and also there is no stress from the transducer. Degassed and de-ionised water was used in order to avoid any air between the transducer and phantom surface. The imaging region is indicated by the rectangular box. b) B-mode image produced by three angles compounded plane wave imaging is presented, shows wire and echo targets.

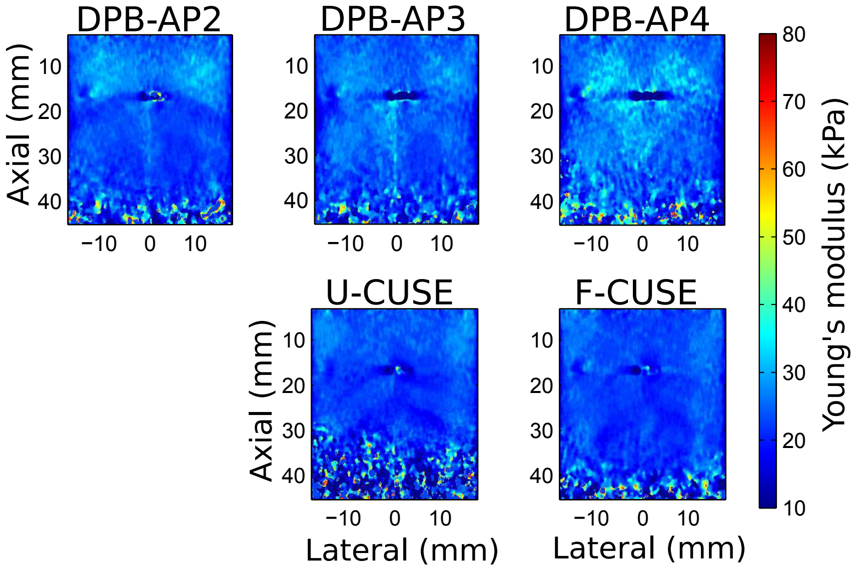

Figure 4.20: Young's modulus maps for three DPB configurations, U-CUSE and F-CUSE for the homogeneous phantom experiment. Colorbar scales are same for all the maps and indicate Young's modulus ranging from 10 to 80 kPa. The push beam shear wave generation configuration for each map is indicated by the labels at top of the each map. The low elasticity value (dip in elasticity) at the centre of the each map can be seen, that resulted from the anechoic target within the imaging region.

UARP II power supply voltage drop test

The objective of this experiment is to measure if the required voltage supply and current are maintained to the transducer for the duration of the experiment. UARP II pulse drivers are rated for ±105 V and are able to drive load currents of up to 2A. To maintain the hardware safety, the power supply is used within ±100 V and 1.8 A limits. The set of applied voltage levels for a unit amplitude 5-level PWM generated waveforms are: ±100 V, ±50 V, and 0 V. Due to long duration tone burst and high voltage requirements for shear wave generation, the power supply voltage drops as the transmission sequences increases, which eventually impacts the shear wave generation and tracking efficiency.

To measure the amount of voltage drop, an experiment was conducted using similar excitation sequences, as used in the above experiments. Reviver channel/01 of a mixed signal oscilloscope (MSOS104A, Keysight technologies., Santa Rosa, USA) was connected to the UARP II channel/01, and an oscilloscope was synchronised with the ultrasound system excitations using the clock trigger from UARP II. Full excitation voltage ±100 V as used in previous experiment (Section 4.3.3) are used and applied voltage on transducer was captured at UARP II channel/01 using the oscilloscope. The measured applied voltage levels for all four DPB configurations are shown in Figs. 4.21 and 4.22, and corresponding tone burst final few cycles (indicated using black rectangle box) are shown on the right side. The shear wave sequence spans from 1 ms to 1.6 ms, while pre-push and post-push imaging pulses can be seen in the plots.

DPB-AP1 excitation voltage falls from 100 V to about 80 V, which is 20% of the maximum initial applied voltage. The voltage drop for the DPB-AP2, DPB-AP3, and DPB-AP3 is about 25%, 30%, and 40%, respectively. As the aperture size increases from DPB-AP1 to DPB-AP4, therefore current demand also increases, eventually dropping the voltage at a higher rate. The reduced excitation voltage reduces the radiation force generation and shear wave SNR, which is the important parameter for shear wave speed estimation accuracy. The reduced voltage also affects imaging/tracking pulse amplitude and eventually tracking accuracy. It needs to be noted here that the voltage drop effect is equally impacting DPB-AP4 and F-CUSE configurations because both use all transducer elements at the same time for shear wave generation, but DPB-AP3 is less affected (30% voltage drop) than these two techniques. It can be concluded that, given power supply maintains the required current, the penetration depth can be improved.

Acoustic intensity comparative study using Field II simulations

To investigate the impact of fixed elevational focus of linear array transducer on acoustic radiation force penetration depth, two different elevational focus transducers (20 mm and 60 mm) were simulated. A Field II simulation tool was used and Peak Negative Pressure (PNP) distribution for all DPB configurations was calculated. The linear array transducer (L3-8/40EP) was simulated using parameters listed in Table. 4.1. Imaging medium parameters were set to CIRS phantom, as given in Table. 4.3, to make sure attenuation and acoustic speeds are similar to previous experimental studies. Pressure 2D fields were calculated in the region of 80 mm axially, and 40 mm laterally, with a resolution of 0.1 mm in both directions. The transmission sampling frequency was set to 160 MHz during simulation, keeping same of UARP II system. The duration of the tone burst excitation was set to 10 μs.

Focal depths were used same as used in the deep shear wave generation experiment (Subsection. 4.3.3). The PNP 2D images for elevational focus 20 mm and 60 mm are produced and presented in Figs. 4.23 and 4.24, respectively. By comparing pressure amplitude images, it can be observed that for DPB-AP1 (axial focal depth = 30 mm), where the axial focal point is close to the elevational focus, the higher pressure amplitudes are generated as compared to 60 mm elevational focus. For DPB-AP2 (axial focal depth = 40 mm), for 20 mm elevational focus, most of the acoustic energy is concentrated around 20 mm and therefore amplitude at 40 mm is lower than the 60 mm elevational focus images. The similar observation has been achieved for DPB-AP3 and DPB-AP4 configurations.

Simulation results indicate that elevational focus close to the transducer array enables concentration of acoustic energy within shallow imaging regions up to 40 mm and limits at deeper regions, while placing elevational focus at deep regions such as 6 cm, the acoustic energy can be translated towards deep regions. In future, these configurations will be tested using transducers with deeper elevational

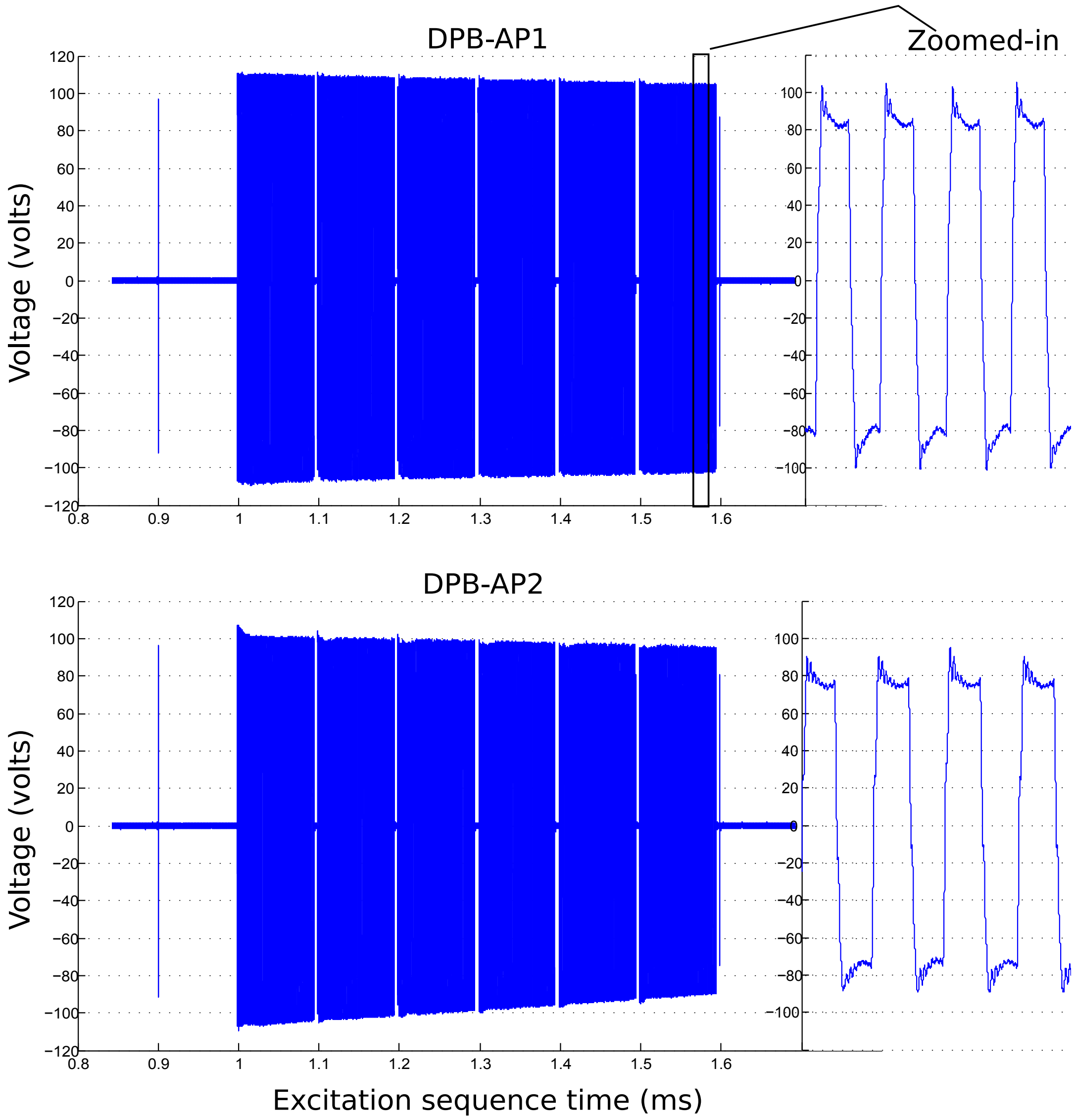

Figure 4.21: Excitation voltage measured at UARP II channel/01 using an oscilloscope for DPB-AP1 and DPB-AP2 configurations, while on the right final time segment of the shear wave excitation is zoomed in to clearly observe the voltages, as indicated the black box. The shear wave generation excitation spans from 1 ms to 1.6 ms and an imaging excitation pulse at 0.9 ms can also be seen. The voltage drop for DPB-AP1 within the excitation duration is from 100 V to 80 V, about 20% drop from the initial voltage, while for DPB-AP2 the voltage falls about 25%.

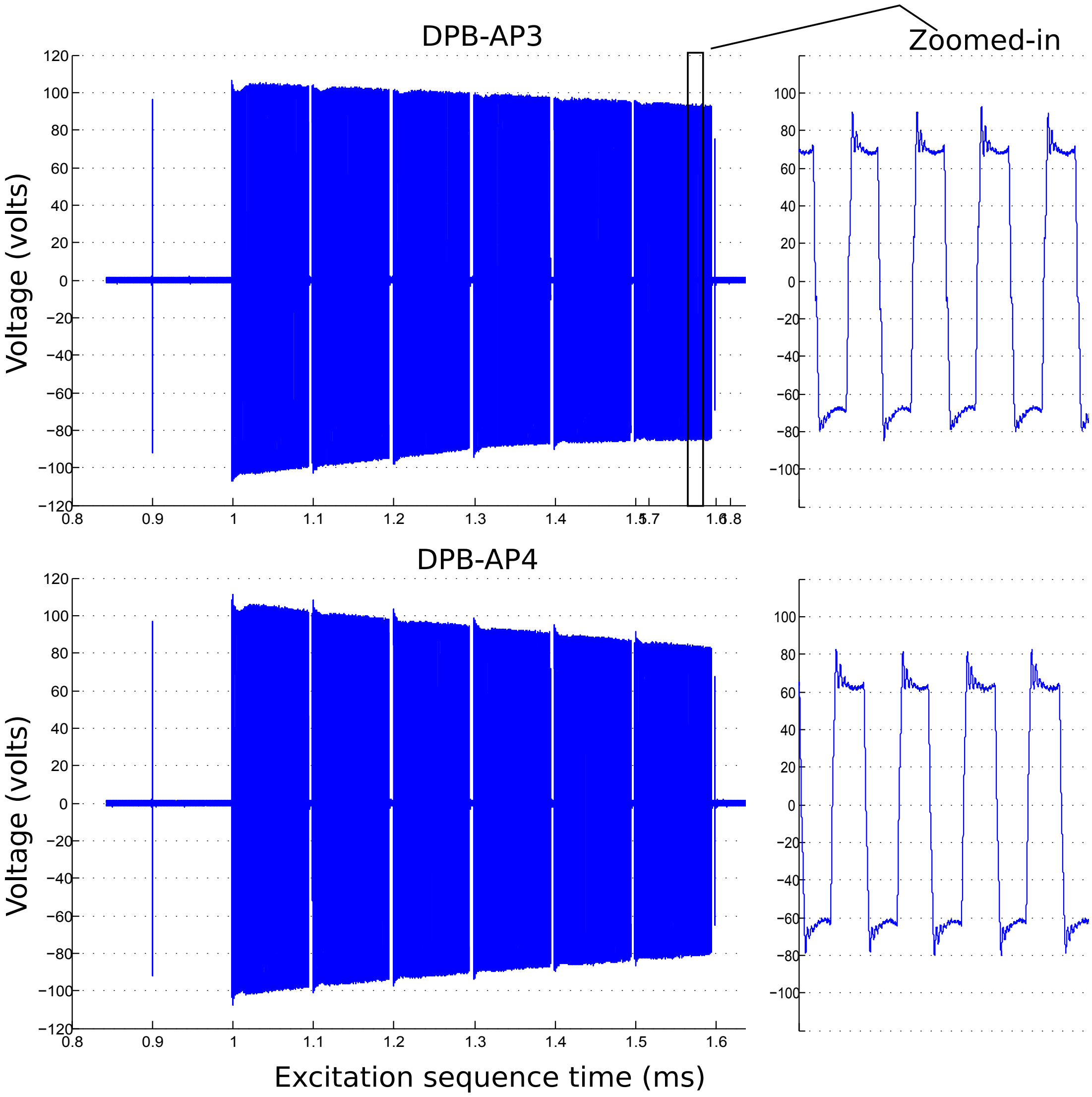

Figure 4.22: Excitation voltage measured at UARP II channel/01 using an oscilloscope for DPB-AP3 and DPB-AP4 configurations, while on the right final time segment of the shear wave excitation is zoomed in to clearly observe the voltages, as indicated the black box. The shear wave generation excitation spans from 1 ms to 1.6 ms and an imaging excitation pulse at 0.9 ms can also be seen. The voltage drop for DPB-AP3 within the excitation duration is from 100 V to 70 V, about 30% drop from the initial voltage, while for DPB-AP4 the voltage falls about 40%.

focuses such as C4-2 convex array transducer (Philips Healthcare, Andover, MA, USA).

Shear wave generation depth test experiment II

This experiment was conducted to test if using lower power supply voltages place less load on the power supply and penetration depth improvement can be achieved using DPB-AP4 relative to F-CUSE. Excitation voltage of ±50 V, that is half of the rated power supply voltage, is used for experiment. The DPB-AP4 uses 64 elements for each push beam whereas F-CUSE 32 elements for each push beams. The Focal depth for both configurations is selected 30 mm, while other experimental and signal processing parameters are similar to previous experiments. The elasticity map for both configurations is produced and presented in Fig. 4.25.

It can be observed that, DPB-AP4 is able to generate shear waves deeper than the F-CUSE. There is no quantitative method to measure imaging depth therefore visual observations are used here. Looking at elasticity maps, an improvement between 7 mm to 10 mm can be noticed. Moreover, it is important to note that, there are overestimation artefacts are produced at shallow regions, which are possibly induced due to widened shear wave beams closer to the transducer. Results indicate that, proposed method has potential to improve penetration depth of elasticity imaging relative to CUSE techniques.

4.4 Discussion

Homogeneous phantom experiments

A slight depth dependent bias in the estimation values has been observed and it increases when higher apertures and deeper focused beams are used. The shear wave beam profile dependent bias and transducer elevational focus oriented shear wave speed estimation errors has been observed in previous shear wave elastography studies and possible solutions were proposed by Zhao *et al.* (2011b). According to the study, possible reasons can be multiple intensity peaks generated in the beams due to a mismatch between elevational and axial focus and also a high lateral divergence of the beams at shallow regions. Moreover, the phantom

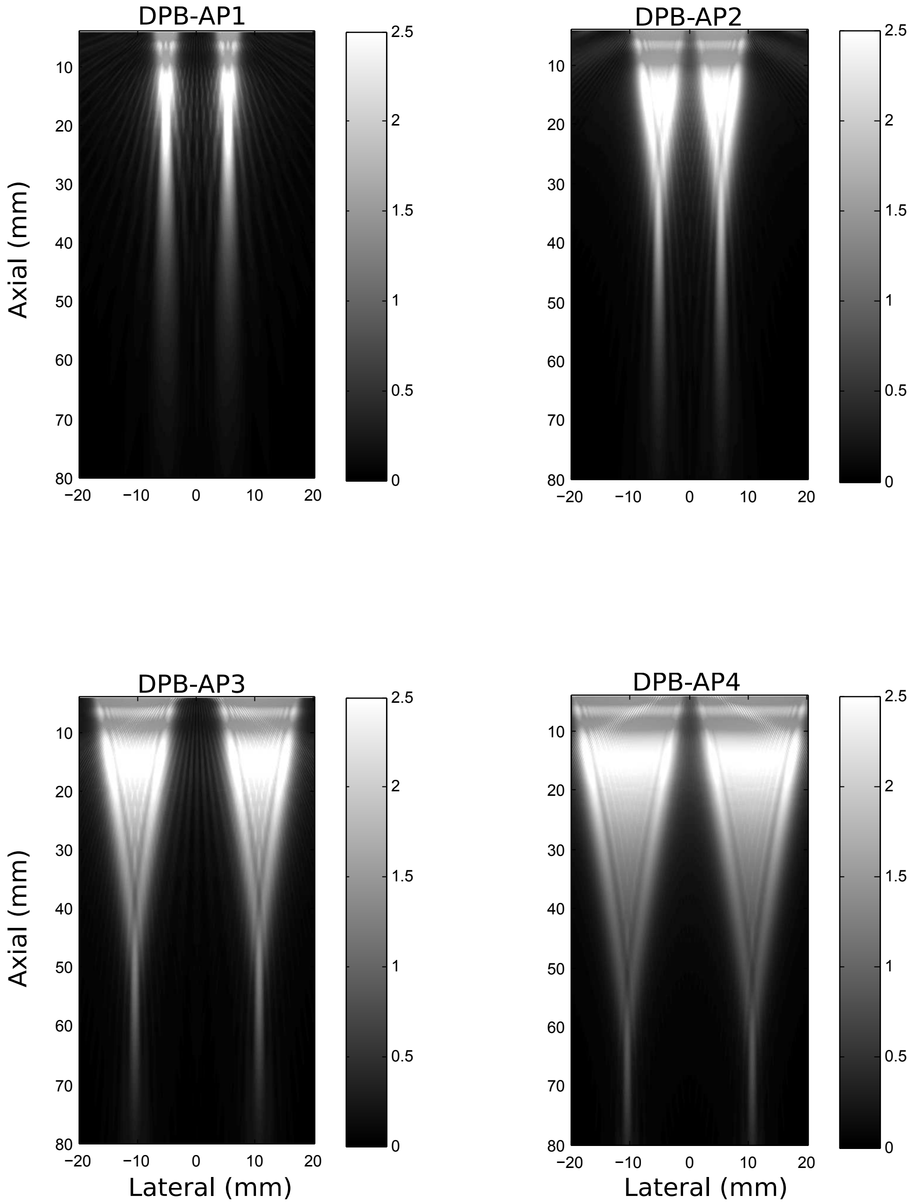

Figure 4.23: Field II acoustic pressure images for all the DPB configurations. The linear array transducer and CIRS phantom parameters are simulated and elevational focus is set to 20 mm, that is the original elevational focus of the L7-4 transducer used in the experimental study. The colourbar scale indicates simulated pressure amplitudes in the arbitrary units. The push beams are focused at 30 mm, 40 mm, 50 mm, and 60 mm for AP1 to AP4 configurations, respectively. It can be observed that, when axial focus is away from the elevational focus, the pressures values at deeper focal depths are highly attenuated, instead of larger apertures are used.

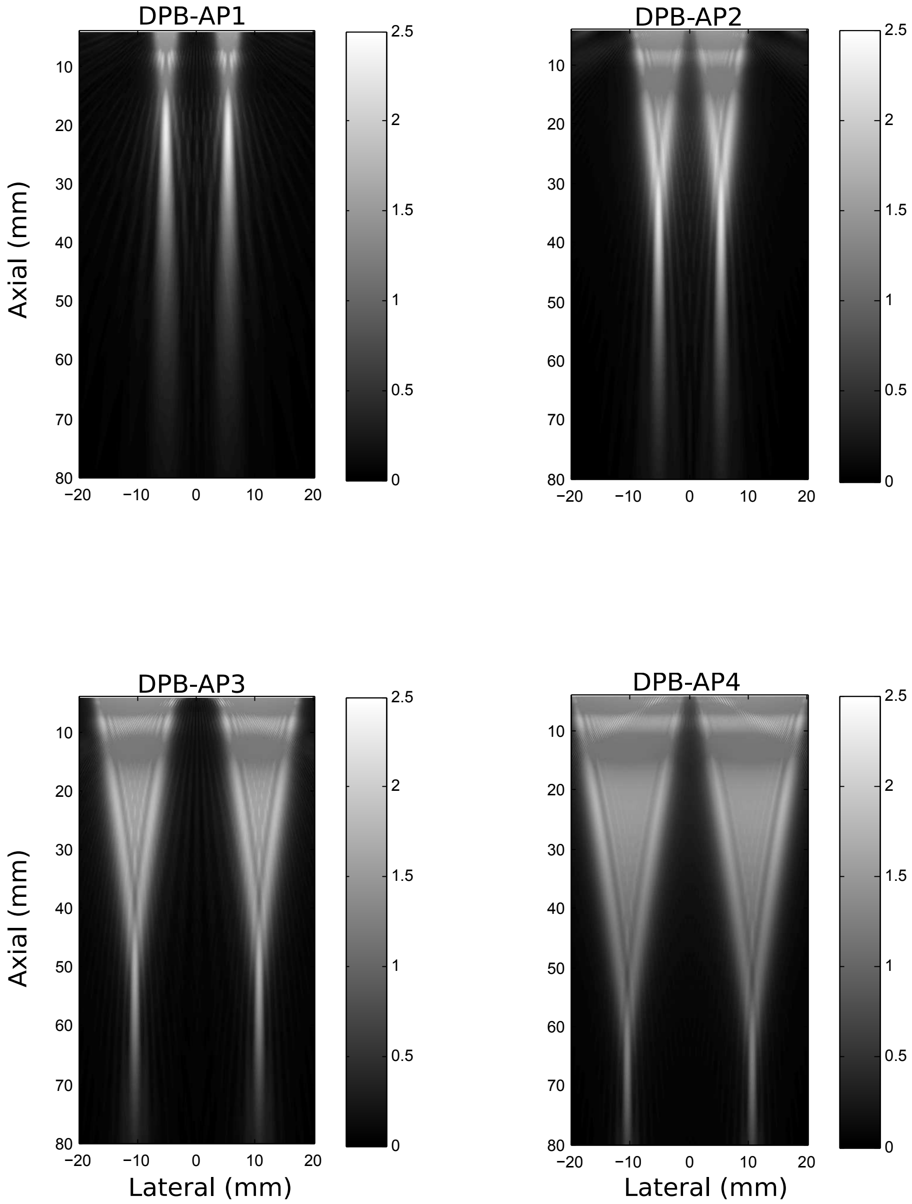

Figure 4.24: Field II acoustic pressure images for all the DPB configurations. The linear array transducer and CIRS phantom parameters are simulated and elevational focus is set to 60 mm while other parameters are maintained similar to L7-4 transducer. The colourbar scale indicates simulated pressure amplitudes in the arbitrary units. The push beams are focused at 30 mm, 40 mm, 50 mm, and 60 mm for AP1 to AP4 configurations, respectively. It can be observed that, when axial focus is close to the elevational focus, the pressures values at deeper focal depths are translated in an efficient way compared to shallow elevational focus simulation.

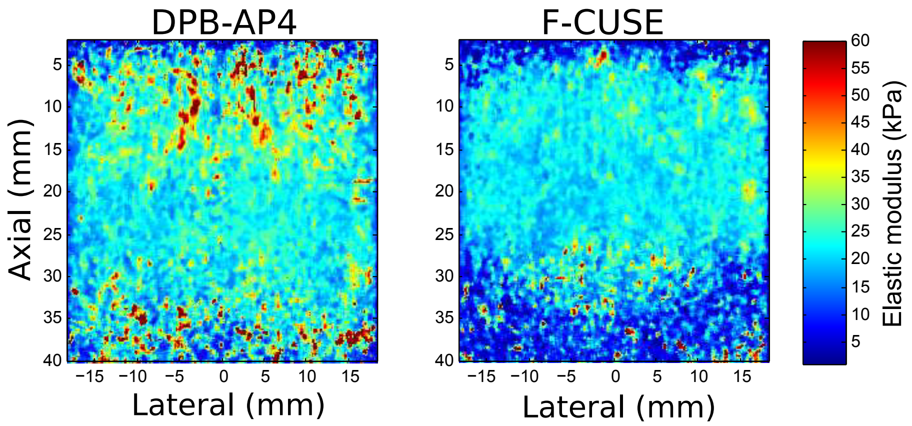

Figure 4.25: Young's modulus maps for DPB-AP4 and F-CUSE. Colorbar scales are same for all the maps and indicate Young's modulus ranging from 10 to 60 kPa. The push beam shear wave generation configuration for each map is indicated by the labels at top of the each map. Improvement in axial extention can be observed in the DPB-AP4 relative to the F-CUSE.

used in the studies is not pure elastically homogeneous, it contains hyperechoic, hypoechoic and wire targets, there is a potential of shear wave reflection and refraction from these targets into the scan plane, or changing the direction of wave field within the scan plane. These may cause overestimation of elasticity because shear wave speed algorithm assumes that all shear wave sources are in the scan plane and wave propagating is at 0 angle to the lateral direction.

It is suggested that, by placing axial focal points close to the elevational focal point and 2D shear wave speed estimation methods, the bias can be reduced. Also, 3D directional filters can be used to remove any reflection and refraction from out the plane sources and boundaries. These suggestions will be investigated in the future to reduce the bias. To achieve comprehensive insight into the issue, the Finite Element Modelling (FEM), and calibrated phantom studies across different ultrasound systems is required.

Inclusion phantom experiments

The DPB-AP3 (focused at 40 mm) and DPB-AP4 (focused at 45 mm) resulted in elasticity overestimation in the shallow imaging regions because shear wave beams were designed for achieving maximum imaging depth (Table. 4.5 and

4.6), while shallow overestimation artifact is less in the DPB-AP1 and DPB-AP2 configurations and these artefacts are consistent among all experiments. One of the solution to resolve this issue is to optimise shear wave beams for shallow and deeper regions separately and then combine both images to form a final elasticity map with uniform accuracy across the whole image. However, this solution reduces the effective frame rate by half because it requires two data acquisitions to produce final image. Nevertheless, since two acquistions take less than 40 ms, which is shorter than the breathing, pulstile and cardiac cycle motion to induce artifacts between two acquisitions (Song *et al.*, 2015).

The measured size of the inclusion is slightly reduced that is 4.5 mm for low elasticity inclusion, and 4 mm for high-elasticity inclusion, while nominal size is 6 mm. The shape of the cylindrical inclusion is well-preserved in the low elasticity inclusion, while the reconstructed shape of the high elasticity inclusion is elliptical. Possible reason for the slight discrepancy in inclusion size and shape is shear wave speed measurement window kernel ($8\lambda = 2.4$ mm) length with reference to the size of the inclusion (6 mm). There is a trade-off for selection of the lateral window kernel, larger windows produce robust estimations while narrow kernels offer better spatial in the lateral direction McLaughlin & Renzi (2006). In a similar way, the kernel size along the axial direction ($6\lambda \sim= 2$ mm) affects the axial resolution of elasticity estimation in the axial direction. The axial and lateral window kernels are used to optimise robustness of estimation.

Deep shear wave generation study

In this chapter, it is demonstrated that the proposed technique has a potential to increase penetration depth for shear wave field generation. It is important to know that, power supply limitation and suitable transducer findings are part of the research study and included in the thesis as problem diagnosis contribution during shear wave implementation of DPB on UARP II ultrasound machine. The solution to this problem is beyond the scope of the research and is included in the future directions. These hardware limitation do not produce unreliable results, however, it limited to experimentally test maximum achievable penetration depth using DPB-3 and DPB-4 configurations. Although, the experimental study in

Subsection 4.3.3 uses 50 V, reducing affects of power supply voltage drop, verifies that DPB-3 and DPB-4 configurations are able to improve penetration depth compared to the U-CUSE and F-CUSE techniques. Further, penetration depth improvement using proposed method was also verified uisng simulation study as presented in Subsection 4.3.3. Deep shear wave generation study experiments provided the evidences that two hardware modifications which include increasing power supply capacitance and using curved linear aaray transducer will be helpful to further improve penetaration depth capacity of the proposed method.

Future directions

In the future, studies need to be conducted to investigate the full potential of the proposed technique. First, to enable utility of the technique in the clinical conditions, it is important to calibrate the excitation voltage and duration and corresponding intensity and temperature to keep MI less than 1.9 and TI less than 1 degree Celsius below the FDA recommendations (Hoskins *et al.*, 2010). Second, an experimental study is required to ensure that DPB is able to detect the elasticity targets independent of the lateral locations. This can be achieved by translating the transducer along the lateral direction to place the inclusion at various locations with reference to the lateral dimension of the transducer. In future, the technique needs to be explored for different size and contrast inclusion targets, to measure the spatial resolution and contrast features of the proposed technique. Finally, a detailed study is required to understand the true reasons and correct depth-dependant and aperture-dependant shear wave elasticity biases, to enable correct 2D full FOV elasticity maps.

4.5 Conclusions

Phantom experimental studies conducted and presented in this chapter indicate that a 2D elasticity maps can be produced using all four DPB configurations using single data acquisition event in contrast to multiple events of experiments were used in previous technique. This enables to capture elasticity snapshot of soft tissues in less than 20 ms. The lower aperture DPB configurations, DPB-AP1 and

DPB-AP2 are designed to measure elasticity for shallow tissues such as breast, thyroid, and skeletal muscles. The larger aperture DPB techniques including DPB-AP3 and DPB-AP4 are suitable to be used for deep tissue imaging such as liver, kidney, spleen, and heart. This technique will also help to recover elasticity in difficult imaging conditions such as obese patients and high attenuation tissues. Implementation of shear wave elastography on research-based ultrasound system UARP II gave immense control on designing shear wave generation and tracking configurations and this builds the shear wave elastography platform for future research.

Chapter 5

Improved Methods for Steered Shear Wave Motion Tracking

5.1 Introduction

The shear compounding approach presented in this chapter aims to address the challenges involved with the current compounded Shear Wave Elastography (SWE) techniques. The ultimate objective of shear wave elastography is to measure the underlying tissue stiffness accurately and to reconstruct elastic inhomogeneities precisely. One of the concept to improve elastic reconstruction quality, shear compounding technique was proposed by both SSI and CUSE research groups. The shear compounding concept actually originated from B-mode spatial compounding, which aimed to improve image quality by reducing random electronic and speckle noise (Jespersen *et al.*, 1998; Montaldo *et al.*, 2009; Tanter *et al.*, 2002). The idea was to average beamformed backscattered signals obtained using differently angled ultrasound field transmissions. The illumination of the scattering function from different directions offers scattering function information from different directions, and averaging the information from various directions reduces random noise and improves the resolution and the contrast of B-mode images.

A similar concept was employed for shear wave elastography to improve inclusion reconstruction geometry and accuracy and named as shear compounding. In the shear compounding SWE, tissue is illuminated by shear waves from different directions, and all differently angled reconstructed maps are averaged. It should be noted that, the B-mode spatial plane wave compound imaging is used in the imaging or shear wave tracking mode and uses longitudinal waves, while shear compounding uses shear waves, and used in the shear wave generation mode. The shear compounding was first introduced by the SSI research group (Bercoff *et al.*, 2004b), where differently angled shear wave field were generated using various supersonic regimes. Another shear compounding technique was proposed by the CUSE group, where multiple angle shear waves were produced using curved sub-apertures of the curvilinear transducer array. In both studies, the results promised reduction in the standard deviation of the measurements and improved inclusion boundary reconstruction.

According to shear wave theory, the shear waves are transverse waves, where particle motion is perpendicular to the direction of propagation. When zero angle shear waves are generated, the waves propagate laterally (parallel to the transducer elements) while the corresponding motion vector is orthogonal to the propagation direction that is along the axial direction. If plane zero angle transmit beams are used, then both tissue displacement vector direction and beams are aligned to each other. In this scenario, speckle motion is in the direction of the imaging beam axis and shear wave motion is tracked accurately without any artefact. The challenge arises when steered shear waves are used and the direction of speckle motion is tilted with respect to the axial dimension, creating both axial and lateral components of the motion. The SSI technique calculated the displacement along the direction of the ultrasound beam regardless of the shear wave steering angle, while (Song *et al.*, 2014) used a curvilinear array to produce and track shear waves. When speckle motion is not aligned with the imaging beam axis, there is a need to tilt the tracking beams to accurately track the tilted speckle motion, and avoid displacement estimation artefacts. This issue is also shared by blood flow estimation research, where angle between transmit beam and blood flow limits velocity vector estimation accurately. To address this issue, (Jensen, 2003; Jensen & Bjerngaard, 2003) proposed directional beamforming concept where transmit beams are aligned with the blood flow angle in the recieving mode using post-processing of the RF data. This chapter addresses the similar problem by spatially aligning tracking beams with the shear wave beams.

5.2 Materials and methods

This section presents details about the principles of the conventional and the proposed shear wave tracking methods. Further subsections explain the ultrasound system used for experiments and shear wave elastography signal processing flow. The signal processing flow is presented in the order as RF data is processed, from acquiring data to producing final 2D elasticity maps.

5.2.1 Generation and tracking of angled shear waves

The shear wave elastography generates shear waves and tracks the corresponding motion of the waves using an ultrasound transducer. In the conventional shear wave tracking method, three-angle plane-wave based coherent compounded tracking is used. In the compounded displacement tracking method, the central angle is always zero while the other two are selected by adding and subtracting 2° or 4° from the central angle, as used by (Montaldo *et al.*, 2009; Song *et al.*, 2012). This method was used for both the conventional shear wave elastography schemes such as SSI, and CUSE, but also used for SSI and CUSE based shear compounding experiments, where steered shear waves are generated (Bercoff *et al.*, 2004b; Song, 2014). For these techniques, in the shear wave tracking phase, three different steering angles centred around zero (-4°, 0° +4°) were used, which resulted in the mis-alignment between shear waves and tracking beams. This method of tracking steered shear waves is named as conventional or mis-aligned tracking and explained using schematic diagram, as shown in Fig. 5.1, where there is no angular alignment between push and tracking beams. In contrast to the conventional way, the proposed method enables tracking beam (insonification) angles adjusted to the push beam angles (shear wave beam) so that tracking beam is aligned with the tissue motion, as shown in Fig. 5.1. The proposed method is tested for five different push beam angles. For tracking, a similar three-angle compounded plane-wave imaging is used in order to improve tracking accuracy. Three compounding angles are selected as the central angle is parallel to the push beam angle while the other two angles are calculated by adding and subtracting 2° from the push beam angle. For this chapter, aligned tracking terminology is used for the proposed method while conventional tracking term is used for fixed angle tracking beams.

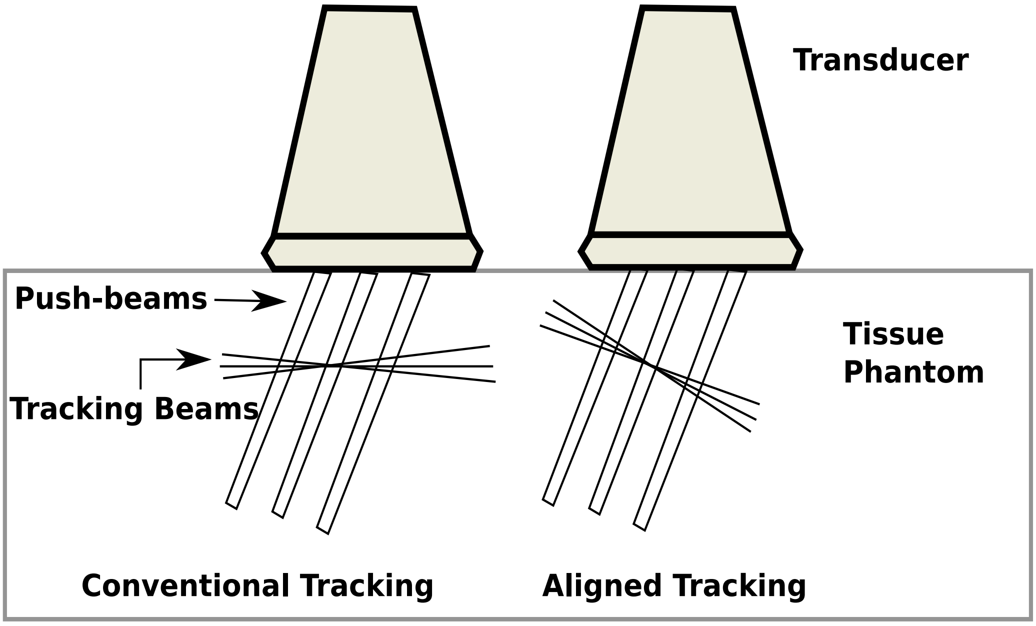

Figure 5.1: The schematic diagram of the aligned and conventional shear wave tracking using push beam and tracking beam locations with respect to the transducer and tissue medium. (left) In the conventional tracking, tracking beams are fixed, independant of the push beam angles and are selected around the zero or plane angle. In this method, tracking beam angles are not aligned with the push beam angles. (right) In aligned tracking beams, three compounded tracking beams are adjusted and placed around push beam angles to enable accurate angled shear wave motion estimation.

The Ultrasound array research platform II (UARP II), developed by the Ultrasound Group, University of Leeds was used for the RF data acquisition (Smith *et al.*, 2012, 2013). The 128 element L3-8/40EP (Prosonic Co., Ltd, Korea) medical probe with centre frequency of 4.79 MHz was used for shear wave generation and tracking. Five push beam angles were tested for both aligned and conventional tracking schemes and are listed as (-15°, -10°, 0°, +10°, +15°). For shear wave generation, three focused (focal depth 30 mm) push beams, 16 elements each were used, with tone burst of 570 μs. After shear wave generation, for aligned tracking scheme, the corresponding imaging compounding angles used were (-17°,

-15°, -13°), (-12°, -10°, -8°) , (-2°, 0° +2°) , (+12°, +10°, +8°) , and (+17°, +15°, +13°), for (-15°, -10°, 0° , +10° , +15°) push beam angles, respectively. In conventional tracking scheme, compounding angles were fixed to (-2°, 0°, +2°) for all the push beam angles. During beamforming process, the lateral width was set to $\lambda/2$.

For all the studies in this chapter, the axial displacement was calculated using one-dimensional NCC. The shear wave motion was estimated by using 6λ kernel in space (depth) and with a kernel shift of $\lambda/2$ between two neighbouring kernels. To achieve sub-sample displacement estimation, the beamformed RF data was interpolated 30 times using spline interpolation before speckle tracking; this enables displacement estimation precision of approximately 0.3 μm. After estimation, a 2 x 2 pixel spatial median filter was applied to each displacement frame to remove local outliers, replacing median of values equal to size of median filter. The axial and lateral resolution of the displacement maps is $\lambda/2$.

5.2.2 Directional filtering

The directional filters are applied and complex shear wave 3D dataset is decomposed into LR and RL 3D shear wave dataset. Each dataset is separately used for shear wave speed calculation and then both LR and RL maps are concatenated to produce a single full FOV shear wave speed map (Deffieux *et al.*, 2011).

5.2.3 Robust 2D shear wave speed calculation

In the plane shear wave elastography techniques, the shear waves propagate in the direction parallel to the lateral dimension of the transducer, assuming there are no refraction during the propagation due to medium inhomogeneities. Following the shear wave polarization angle, the 1D time-of-flight (TOF) methods estimate shear wave speed by cross correlating shear wave time profiles at two lateral locations at the same depth, which are separated by the specified window size, as shown in Fig. 5.2a. The shear wave motion signal at lateral position **a** denoted by the $S(m - w/2, n, t)$ and **b** denoted by the $S(m + w/2, n, t)$ are correlated and arrival time delay Δt from **a** to **b** is measured. The shear wave speed C_s is calculated using ratio of the distance **ab** to the time Δt that is $ab/\Delta t$. Normalised cross-correlation is calculated using following expression (Pinton *et al.*, 2006);

$$CC(j) = \frac{\sum_{-M/2}^{M/2} [S(m-w/2,n,i) - S(m-w/2,n,i)]}{\sqrt{\sum_{-M/2}^{M/2} [S(m-w/2,n,i) - S(m-w/2,n,i)]^2}} \times \frac{[S(m+w/2,n,i+j) - S(m+w/2,n,i)]}{\sqrt{\sum_{-M/2}^{M/2} [S(m+w/2,n,i+j) - S(m+w/2,n,i)]}} \tag{5.1}$$

where CC is the normalised cross correlation output M is the number of shear wave signal data points along the slow time direction, m is the lateral dimension, n is the axial dimension, t is the slow time dimension, and w is the lateral kernal or window size. The argument where the cross-correlation peak is located determines the time delay between two lateral shear wave time profiles $S(m-w/2,n,t)$ and $S(m+w/2,n,t)$ in terms of frames, and is further converted into seconds using the pulse repetition frequency (PRF) of the imaging mode;

$$\Delta t = \frac{\text{argmax } CC(j)}{PRF} \tag{5.2}$$

The final shear wave speed C_s at location (m,n) which is at the centre of the shear wave time profile lateral locations used for the calculation, is ratio of the distance between lateral locations and time delay (Δt). The distance between two lateral locations is the product of the number of lateral scan lines (w) and width of the each lateral line (Δx). The expression is given as;

$$C_s(m,n) = \frac{w \ . \ \Delta x}{\Delta t} \tag{5.3}$$

In the final stage, the shear modulus (G) is calculated using the following expression, where ρ is the density of the medium;

$$G = \rho \, C_s^2 \tag{5.4}$$

The shear modulus is related to the Young's modulus (E) using the expression;

$$E = 3 \, G \tag{5.5}$$

For shear compounding elastography, the shear waves are generated at various angles relative to the lateral dimension of the transducer, and shear wave polarization is no more in the true lateral dimension, as shown in Fig. 5.2b. In this angled shear wave propagation phenomenon, the 1D shear wave speed estimation methods are not accurate, and results in overestimated elasticity values (Song *et al.*, 2014). In the case of angled shear waves, the actual shear wave front path is **ab** while using 1D estimation estimation, the wave front path **ac** is selected, which is higher in length than the true path, which eventually results in the biased (overestimated) shear wave speed (Song *et al.*, 2014). The shear wave propagation direction assumed in the 1D method is violated when shear wave motion is angled (see Fig. 5.2b).

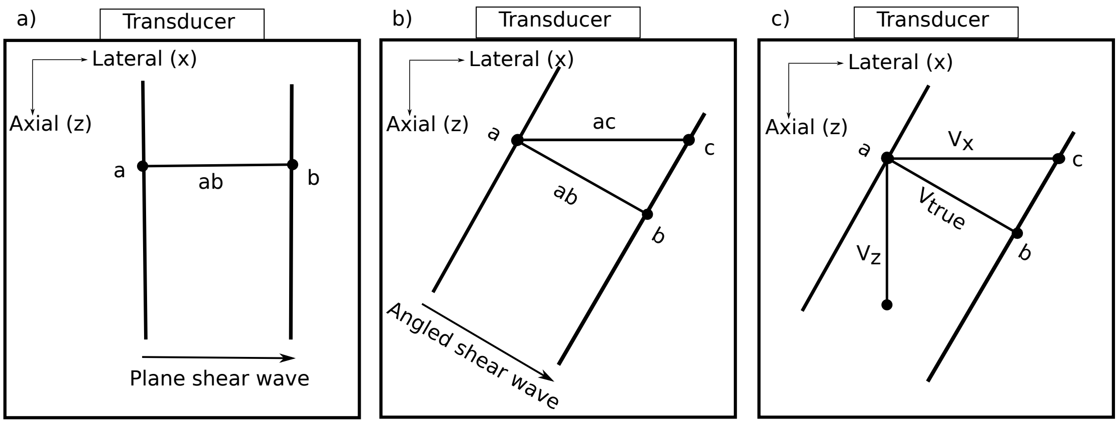

Figure 5.2: 2D shear wave speed estimation for angled shear waves propagation. (a) The diagram of the plane zero angle shear wave front propagation, where from lateral point **a** to lateral point **b**, wave front arrival time is calculated. The propagation direction of the shear waves is along the true lateral direction. (b) The diagram for the angled shear wave propagation, where calculating shear wave front arrival time overestimates the shear wave speed because assumed distance **ab** is higher than the true distance **ac** travelled by the wave front. (c) The diagram for the calculation of the true shear wave speed (V_{true}) using both lateral (V_X) and axial (V_Z) components of the true shear wave speed.

For the true shear wave speed calculation, a 2D window based method was proposed (Song, 2014). In this method, the shear wave speed is calculated along both lateral (x) and axial (z) directions and the true shear wave speed V_{true} (C_s) is calculated by calculating both V_{x}, and V_{z} (see Fig. 5.2c) and then combining both in the following mathematical relationship;

$$V_{\text{true}} = \frac{V_{\text{x}} V_{\text{z}}}{\sqrt{V_{\text{x}}^2 + V_{\text{z}}^2}} \tag{5.6}$$

To increases the robustness of the shear wave speed estimation at each pixel, four different estimations are used using four different kernals with a width of 5λ, 6λ, 7λ, and 8λ each (Song, 2014). In contrast to 1D methods, where 1D window is used to average four estimations, here a 2D distance weighted window is used to calculate shear wave speed at each pixel location. The 2D weighted window gives higher weight to the estimated values which are near to centre of the 2D window as explained in detail by (Song, 2014). Before performing cross-correlation, each time profile data is bandpass filtered (Bandwidth $\sim$ 10 to 500 Hz). For sub-frame delay estimation, each time profile data is interpolated by ten times using spline interpolation, eventually increasing the frame rate up to 100 kHz. Finally, to improve shear wave speed estimation accuracy, data is Tukey windowed (ratio of tapered section to constant section is 0.1) to smooth the edges of the motion data. Signal processing parameters are summarised in Table. 5.1.

5.2.4 Compounding of multiple angle elasticity maps

In this part, all five elasticity maps are compounded using threshold averaging. In threshold averaging, at each pixel in the 2D elasticity map, only Young's modulus values contribute to the averaging which have values restricted below the upper threshold. The upper threshold is selected considering nominal elasticity of the phantom. In this study, the upper threshold is set to 50 kPa, where all the greater values are considered outliers and are not used.

Table 5.1: Signal processing parameters

Parameter	Value
Displacement estimation window	2 mm
Displacement estimation window separation	$\lambda/2$
Axial up-sampling	30 times
2D shear wave speed estimation window	8λ x 8λ
Shear wave speed estimation window separation	$\lambda/2$
Temporal up-sampling	10 times

5.2.5 Single inclusion phantom study

This experiment aims to test the idea of angle aligned shear wave generated displacement estimation. A softer inclusion than the background centred at the imaging region is used. Moreover, it is also evaluated if improvement in the steered shear wave tracking can be translated into improving shear wave elasticity reconstruction. This section includes details of the phantom used, experimental setup, and the corresponding displacement and elastic modulus image results.

Imaging meduim

The imaging medium used for this experiment was similar to imaging medium used in Chapter 4, a detailed discussion is given in Section. 4.3.1.

Experimental Setup

The experimental setup of the single inclusion study is presented with help of schematic diagram, as shown in Fig. 5.3a. The imaging region is indicated by the dashed lines, where 10 kPa inclusion is at the centre, indicated by the yellow circles. The imaging region also indicates 40 kPa inclusion which is ignored due to reasons discussed in Chapter 4 and Section 4.3.1. Linear array transducer was placed at the phantom surface, slightly touching the phantom surface to avoid any significant stress as elasticity changes when force is applied to the elastic medium. De-gassed, de-ionised water was used to avoid any air gap between transducer and surface of the phantom.

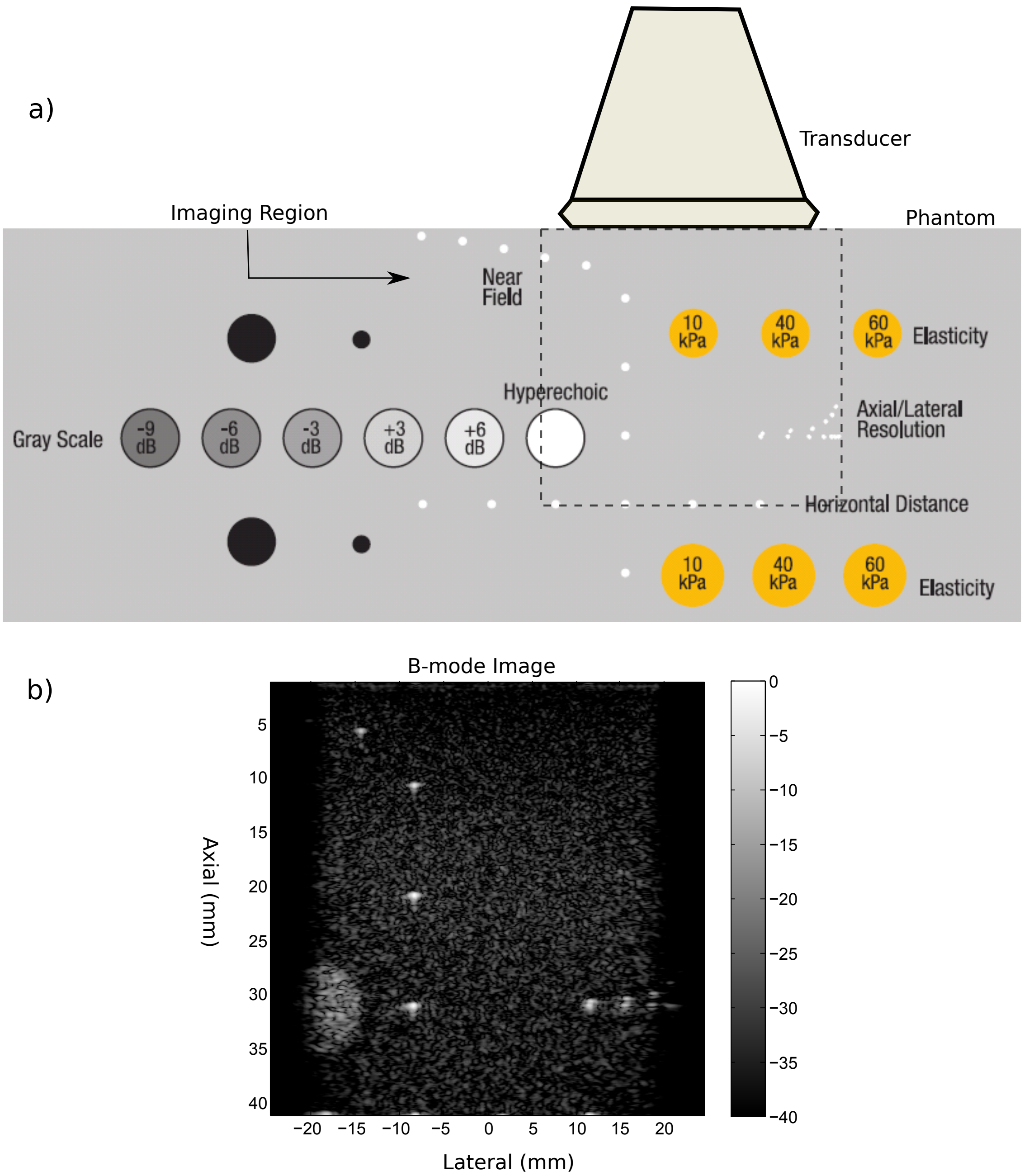

Figure 5.3: The schematic diagram of the single inclusion experimental setup including CIRS phantom and imaging region. (a) The imaging region is of 40 mm in the axial and 49 mm in the lateral direction. The imaging region is selected in a way that the 10 kPa inclusion is at the centre of transducer. The ultrasound transducer is placed slightly touching the phantom surface to avoid any stress on the phantom. To avoid air contents between transducer and phantom surface, the degassed and de-ionised water was used as a acoustic impedance matching medium. (b) In the B-mode image, all the wire targets within the transducer aperture width region are visulised with good quality.

The RF data is acquired using UARP II and then processed off-line on a general desktop PC with Intel(R) Core(TM) i5-2500 CPU at 3 GHz with 8 GB RAM. All the post-processing is achieved using Matlab (The Mathworks, Natick, MA, USA). The signal processing flow is explained in Section. 5.2. Three angle compounded plane wave image is produced with an elongated FOV and presented in Fig. 5.3b. The axial and lateral scatterers and hyperechoic target partially can be observed. There is no B-mode data outside the original FOV of the transducer, these elongated FOV are filled with the data in the steered tracking beam B-mode images. The elongated FOV has dimensions of -25 mm to 25 mm, while axial dimension spans from 2 mm to 40 mm.

5.2.6 Multiple inclusion phantom study

The objective of this study is to test the proposed idea in a relative complex imaging conditions which uses two elasticity targets with stiffer and softer inclusions than the background. This experiment also evaluates the reproducibility of the results both at displacement estimation and elasticity reconstruction stage. This section presents experimental setup, imaging medium, and corresponding results.

Experimental setup and parameters

The experimental set-up is similar to the used in Chapter 4 and details are discussed in Section. 4.3.2. The B-mode is produced using three-angle plane-wave compounded imaging (see Fig. 5.4b). In the B-mode image, the axial/lateral B-mode targets can be visuliased, indicating the quality is satisfactory for the further processing of the b-mode RF data. If the B-mode image results are not satisfactory, then the RF data does not qualify for the further shear wave elastography signal processing and is discarded and experiment is repeated. The experimental setup conditions are same as explained in the previous experiment.

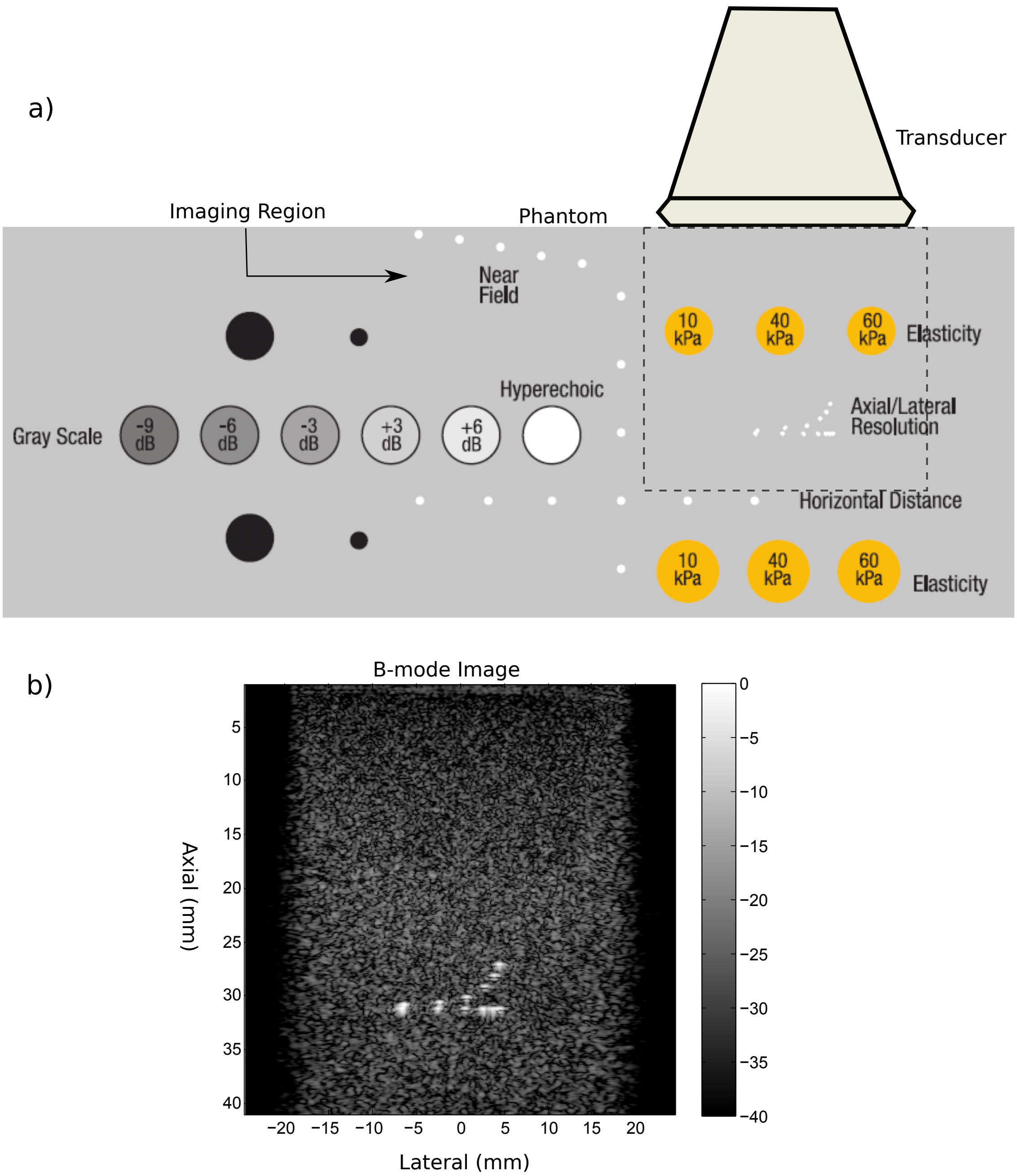

Figure 5.4: Schematic diagram of the multiple inclusion experimental setup. (a) The imaging region is of 40 mm axial by 49 mm lateral and is selected to include both 10 kPa and 40 kPa inclusions are part of the imaging. The transducer slightly touches the phantom surface to avoid any stress on the phantom and degassed, de-ionised water used as an impedance matching meduim. (b) The B-mode image shows axial/lateral resolution targets with good spatial resolution.

5.3 Results

Single inclusion study results

Shear wave displacement maps for all experiments are produced at time 0.1 ms after shear wave generation is ceased, and are presented for all steered angles in Fig. 5.5. The conventional tracking maps are shown in Figs. 5.5a, 5.5b, 5.5c, 5.5d. In the conventional tracking maps, it can be observed that tilted shear wave tracking using plane wave (zero) angles produced artefacts (pointed by the arrows) which falsely reconstructs the direction of the push beam angle as zero angle push beam, while true push beam angles are (-15°, -10°, +10°, +15°). When tracking beams were switched to aligned tracking (Figs. 5.5f, 5.5g, 5.5h, 5.5i), the artefacts were successfully suppressed and the true push beam direction was estimated, and overlapping between two push beams was also reduced. The peak artefact amplitude is up to 5 μm, where peak amplitude of the shear wave produced displacement ranges from 25 μm 30 μm, this indicates that artefact level was from -15.5 dB to -14 dB, when calculated relative to peak displacement level. The artefact amplitude in the aligned tracked maps, when compared at the same location is reduced to more than half the amplitude of conventional tracking. The reduction in the artefact peak when aligning the push beam and tracking angles by one half relative to conventional tracking is equal to 6 dB improvement in the decibels expressions.

These results can be observed in another perspective where the same displacement images are produced using 0 μm to 25 μm dynamic range, and are presented for the conventional method in Fig. 5.6 and for the aligned tracking method in Fig. 5.7. Improvements in the push beam displacement artefact suppression can also be observed for all four steering angles. The zero push beam angle magnitude is the same for both conventional and aligned tracking methods, because even in a conventional tracking method, the tracking beams are angularly aligned with the push beams. Ideally, there should be zero amplitude displacement outside the push beam regions, the possible reason for this (see Fig. 5.5) is that, all the tracking compounding angles are not exactly same as the push beam angle, but three angles are chosen as; the first tracking angle is same as the push beam angle, while other two angles are 2 degrees surrounding the central angle. Therefore,

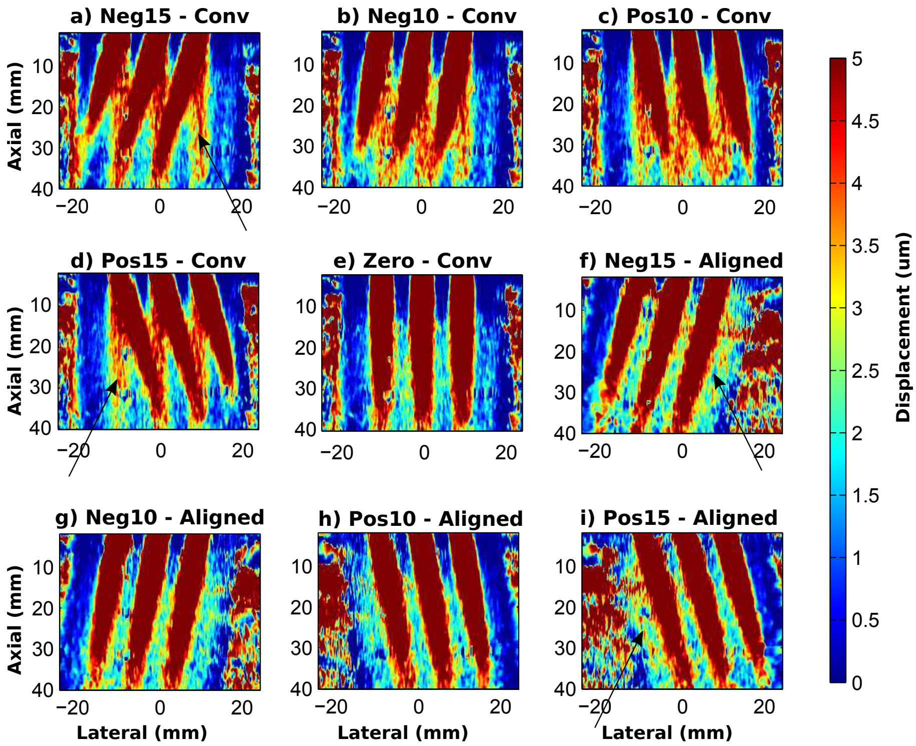

Figure 5.5: The displacement maps for aligned and conventional tracking beams used for listed (-15°, -10°, 0°, +10°, +15°) push beam angles at time instant of 0.1 ms after ultrasound switches to imaging mode. The labels on each displacement map indicate the push beam and associated tracking angle. All conventional tracking beams are fixed to (-2°, 0°, +2°), while aligned tracking beams are adjusted to the push beam angle. Color bar scale is in the units of μm. The false push beam angle direction artefact are produced by the conventional tracked maps pointed by arrows (map a and d) while in aligned tracked maps, the push beam wave-front angle are truly reconstructed (map f and i).

this minor mis-alignment between push beam angles and tracking angles can be a reason of displacement artifacts outside the push beam locations.

Another improvement achieved by the aligned tracking is the improved displacement estimation amplitude. It can be observed in Fig. 5.6 and Fig. 5.7 subjectively, and in Fig. 5.8 it is presented in quantitative way. The comparison plots of displacement amplitude difference for -15° are produced (see Fig. 5.8), where displacement amplitudes are averaged for a axial region spanning from 10 mm to 15 mm (indicated by the red rectangular box) along the whole field of view. Displacement images for -15° using conventional and aligned tracking method are presented in Fig. 5.8a and Fig. 5.8b, respectively. Fig. 5.8c and Fig. 5.8d are the averaged displacement amplitudes calculated using displacement maps for conventional and aligned methods, respectively. The displacement amplitude estimation enhancement can be observed in all three beams, where peak displacement improvement was observed in the rightmost push beam, which is equal to 4.5 μm. In the decibel expressions, the peak displacement improvement is 2.21 dB. Peak amplitude difference varies among all three beam and also among different steering angles, therefore the average improvement will remain close to the numbers calculated.

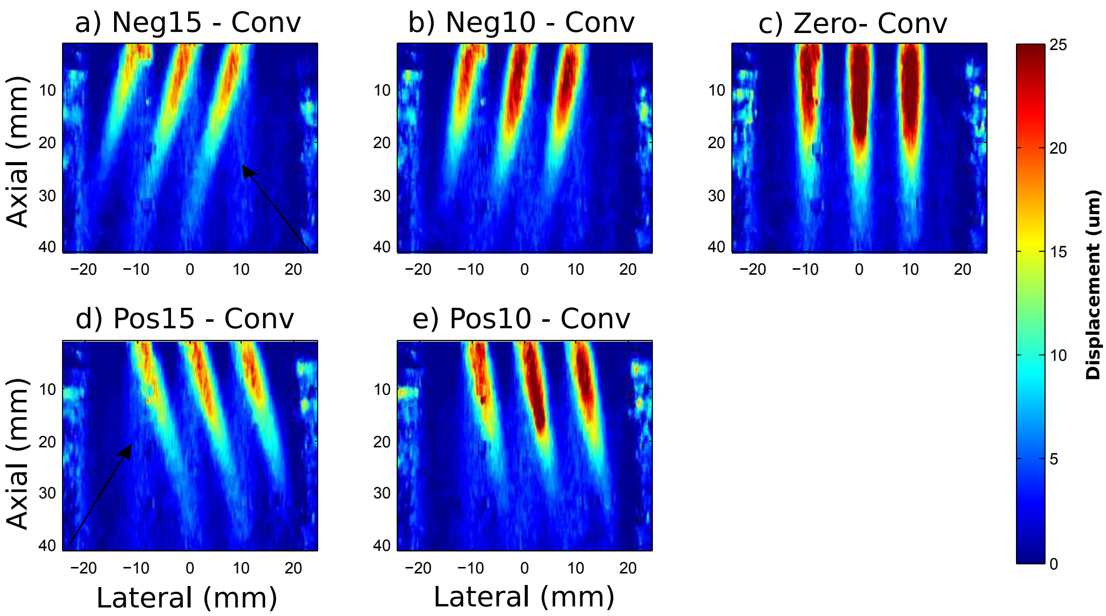

Figure 5.6: Displacement maps for conventional tracking beams used for listed (-15°, -10°, 0°, +10°, +15°) push beam angles at time instant of 0.1 ms after ultrasound switches to imaging mode. Labels on each displacement map indicate the push beam angles. In all maps, conventional tracking beams are fixed to (-2°, 0°, +2°). Colorbar scale is in the units of μm. The false push beam angle direction artefact are produced by the conventional tracked maps as pointed by arrows in the -15°, -10°, +10°, +15° displacement maps. The artefacts amplitude is up to 4.5 μm and is same for all steered push beam angles.

Further, some observations are made using these maps. First the displacement generated by each push beam within a single displacement map is not uniform, generally but not necessarily the rightmost beam generates the highest amplitude while the leftmost beam has the least amplitude. Second, the peak amplitude generation is not uniform for all push beam steering angles, as zero push beam angle map has the highest displacements. It can be noticed that, the higher the steering angle, the lesser the peak displacement generation. This non-uniformity possibly indicates that the radiation force generation efficiency is affected by the steering angle of the insonification. Moreover, it is possible that all the transducer elements are not equally efficient in radiation force generation.

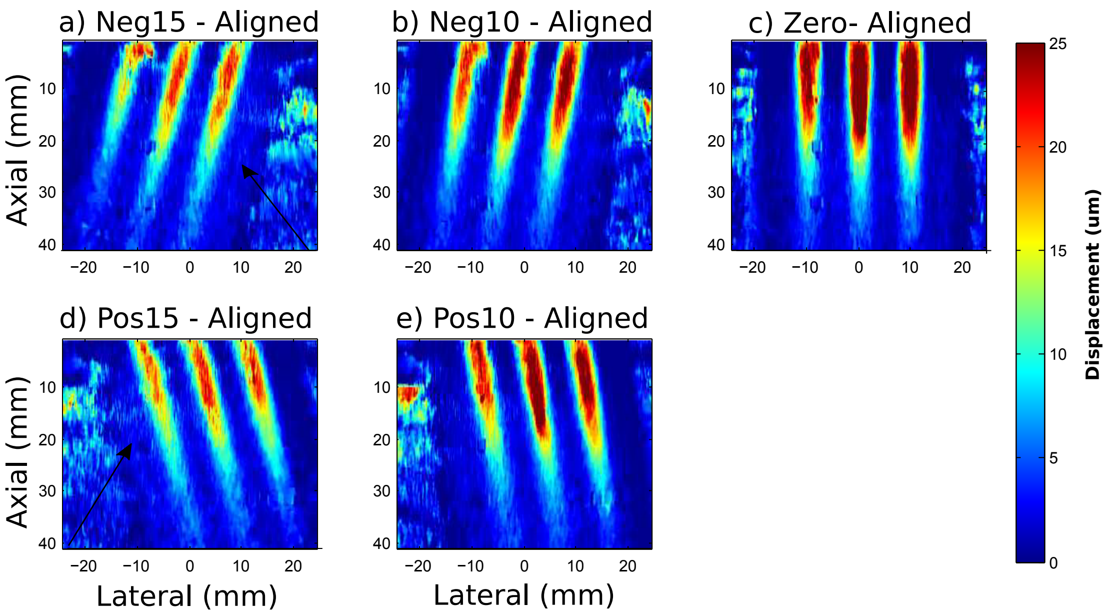

Figure 5.7: Displacement maps for angle-aligned tracking beams used for listed (-15°, -10°, 0°, +10°, +15°) push beam angles at time instant of 0.1 ms after ultrasound switches to imaging mode. Labels on each displacement map indicate the push beam angles. In each map, tracking beam angles used are adjusted and aligned to the push beam angles. Colorbar scale is in the units of μm. False push beam angle direction artefacts are suppressed and displacement amplitudes are increased using angled tracking. Locations where artefacts are reduced are pointed by arrows in the -15°, -10°, +10°, +15° displacement maps.

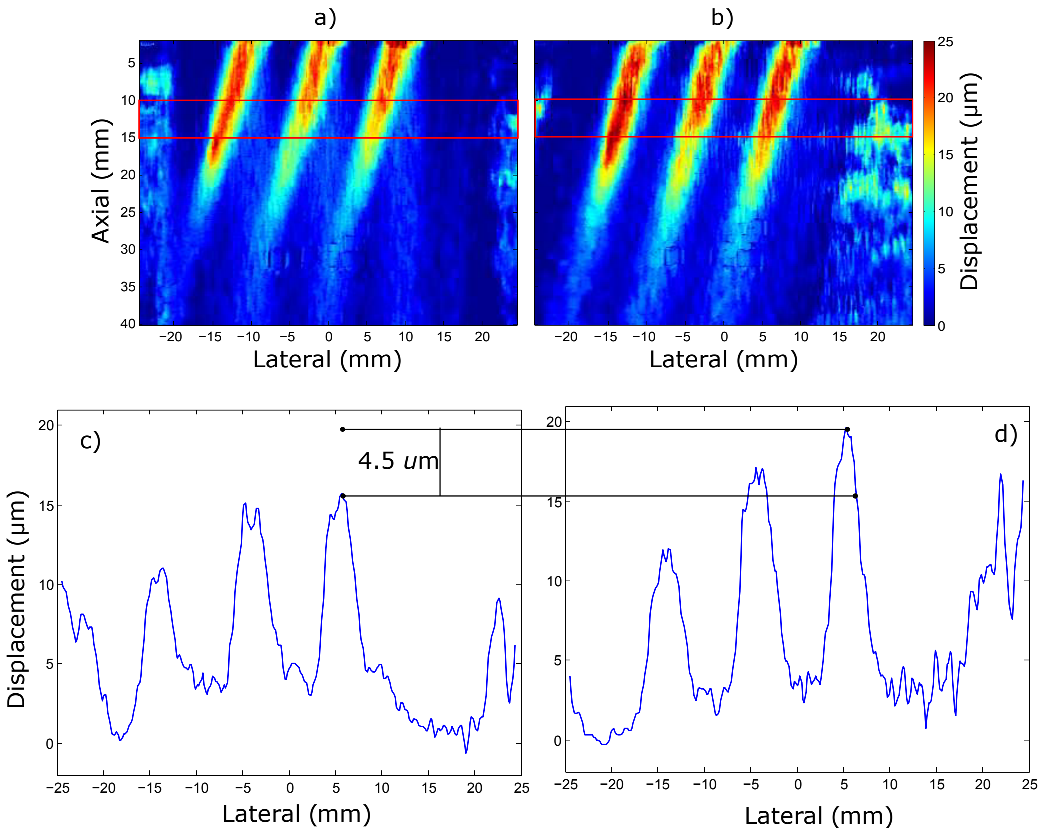

Figure 5.8: Displacement improvement maps and plots using aligned tracking when compared with the conventional tracking. (a) Displacement map generated using -15° push beam angle, where displacement artefacts can be observed. (b) Aligned tracked displacement map for the -15° push beam angle, whereas displacement amplitude is increased and artefacts are also suppressed. The displacement data in the red rectangular box is selected and averaged along the depth, and plotted for both maps. (d) Estimated angled displacement amplitude is improved up to 4.5 μm by in the aligned map, compared to the conventional (c) map.

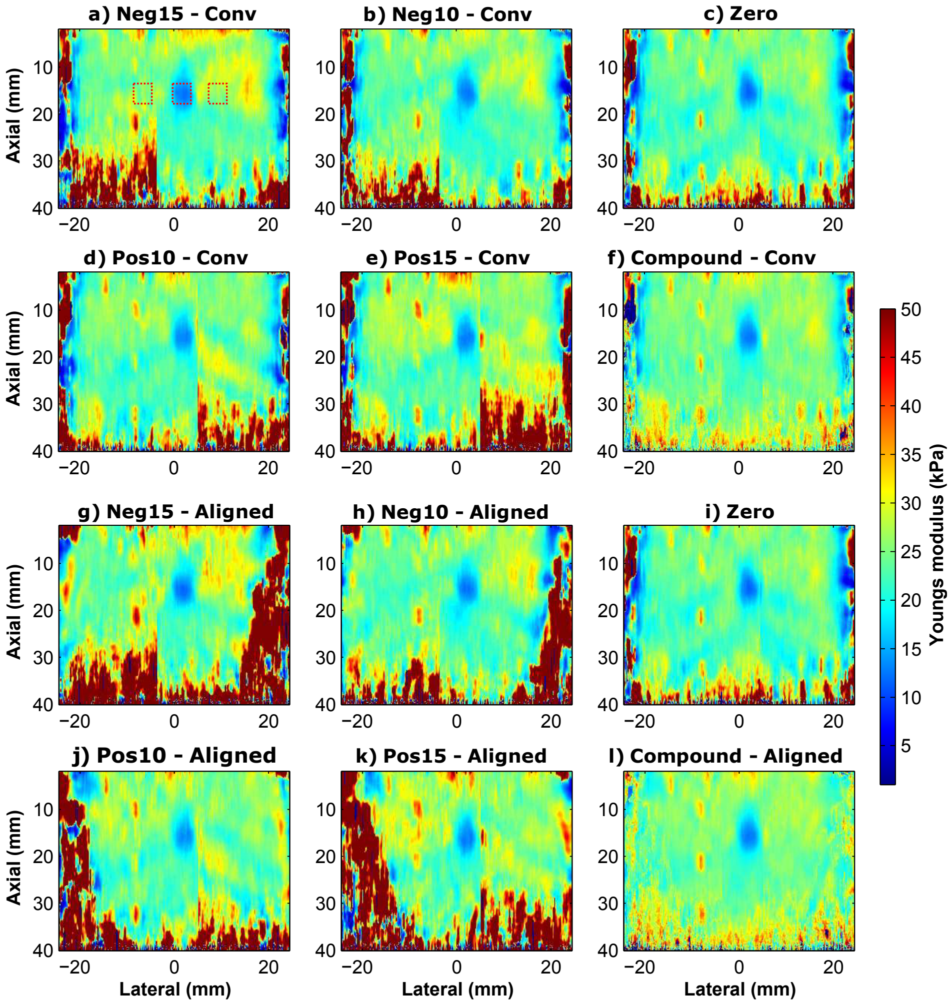

Figure 5.9: Elasticity maps for all the five shear wave steered angles including compounded map for both conventional and proposed technique method are presented. In elasticity measurements, -15°, -10° and +15° aligned tracked shear wave maps (Maps. g, h, and j) slightly sharp reconstruction of inclusion geometry can be observed contrast to conventional tracked maps (Maps. a, b, and d), while in +10° maps (Maps. e, and k), no difference is observed and results are comparable. In the final compounded elasticity maps, the boundaries of the inclusion in the map produced by the aligned technique (Map. l) are relatively sharper than the reconstructed inclusion in the conventional map (Map. f). Also, aligned tracked compounded elasticity map has wider lateral extension than the conventional compounded map.

Elasticity maps for all five shear wave steered angles including compounded map for both conventional and proposed technique method are produced and presented in Fig. 5.9. In elasticity measurements, -15°, -10° and +15° aligned tracked shear wave maps (Figs. 5.9g, 5.9h, and 5.9j) produced slightly sharp reconstruction of inclusion geometry contrast to the conventional tracked maps (Figs. 5.9a, 5.9b, and 5.9d), while in +10° maps (Figs. 5.9e, and 5.9k), no difference was observed and results are comparable. In the final compounded elasticity maps, it can be subjectively observed that, the boundaries of the inclusion in the map produced by the aligned technique (Fig. 5.9l) are relatively sharper than the reconstructed inclusion in the conventional map (Fig. 5.9f).

For statistical measurements, mean and standard deviation for elasticity values for inclusion and background are calculated. A region of interest (ROI) with size of 4.5 x 4.5 mm axial and laterally was placed at the centre of the inclusion for target calculations. For background, mean and standard deviation values are achieved by placing two ROIs on right and left of the inclusion and final values are averaged of both measurements. The statistical calculations for target and background using conventional and aligned tracking methods are listed in Table. 5.2. In terms of quantitative analysis, there were no consistent indications of improvement and performance in terms of bias and variance were found comparable for both the conventional and aligned tracking schemes in both inclusion and surrounding. The statistical Student's t-test was used and data between conventional background was tested for both inclusion and background. The values for both background and inclusion (p-value = 0.21 and p-value = 0.35) indicated no statistically significant difference was observed between conventional and proposed method.

Multiple inclusion phantom study results

Displacement and elasticity maps are produced for all the five steered angles, including the final shear compounded elasticity map for both the aligned and conventional tracking technique. In these displacement maps, it can be observed that the improvement in displacement angle and amplitude estimation for aligned

Table 5.2: Young's modulus mean and standard deviation measurements for background and inclusion using conventional and aligned tracking for 10 kPa inclusion

	Background		Inclusion	
Angle	Conventional (Mean ±std.)	Aligned (Mean ±std.)	Conventional (Mean ±std.)	Aligned (Mean ±std.)
- 15	26.34 ±0.63	28.65 ±0.96	14.51 ±0.39	14.26 ±0.30
- 10	23.54 ±0.46	25.27 ±0.59	14.64 ±0.41	14.33 ±0.26
0	23.79 ±0.53	23.79 ±0.52	13.70 ±0.40	13.70 ±0.41
+ 10	23.33 ±0.60	23.61 ±0.73	15.20 ±0.25	15.61 ±0.42
+ 15	26.77 ±0.72	27.12 ±1.36	15.34 ±0.34	15.93 ±1.08
Compounded	24.76 ±0.40	25.70 ±0.38	14.70 ±0.27	14.78 ±0.35

tracked displacement maps is repeated and is consistent. The conventional tracking maps are shown in Figs. 5.10a, 5.10b, 5.10c, 5.10d, where artefacts can be clearly seen (indicated by the arrows) with an amplitude of up to 5 μm for both positive and negative push beam angles, as observed in Fig. 5.5a and Fig. 5.8. Looking at the zero angle displacement map (see Fig. 5.10e), the amplitude of displacement in between the shear wave beams is small relative to angled conventional displacement maps, while aligned maps indicate results similar to zero angle map in terms of noise between the beams. As in the zero angle maps, shear wave generation and tracking angles are aligned, therefore small artefacts are observed. The similarity between aligned tracked maps and zero angle maps point to aligned tracking as an optimal angle shear wave detection method. The displacement estimation improvements in terms of amplitude and artefact reduction are similar to the previous experiment (see Section 5.2.5) and reproducibility can be confirmed.

Elasticity maps for all five shear wave steered angles including compounded map for both conventional and proposed technique method are presented in Fig. 5.11. For elasticity measurements, no difference between aligned and conventional tracked maps for individual angle maps was observed in terms reconstructing the inclusion geometry. Statistical test values for background, 10 kPa inclusion and 40 kPa inclusion (p-value = 0.61, p-value = 0.16 and p-value = 0.22) measured using data in Table. 5.3 and Table. 5.4 indicated no statistically significant difference between conventional and proposed method.

In the final compounded elasticity maps, it can be subjectively observed for the 40 kPa inclusion, the boundaries are relatively sharper and elasticity estimation is uniform for maps produced by the proposed method (Fig. 5.11l) compared to the conventional technique maps (Fig. 5.11f). For the 10 kPa inclusion, overall boundary of the inclusion is delineated in better way than the contemporary conventionally tracked map, and this helpful to measure inclusion geometry. Moreover, lateral dimensions of the compounded elasticity maps are wider and edges have smooth estimation regions.

For statistical measurements, mean and standard deviation for elasticity values for both 10 kPa and 40 kPa inclusion and background are calculated. A region of interest (ROI) with size of 4.5 x 4.5 mm axial and laterally was placed at the centre of the inclusion for target calculations. For background, mean and standard deviation values are achieved by placing two ROIs on right and left of the inclusion and final values are averaged of both measurements. Statistical calculations for 10 kPa and 40 kPa target and background using conventional and aligned tracking methods are listed in Table. 5.3 and Table. 5.4, respectively. For $+10°$ and $+15°$ 10 kPa inclusion, measurements are outliers because the target was not part of imaging region for these tracking angles, as can be observed in Fig. 5.11j and Fig. 5.11k. In terms of quantitative analysis, there were no consistent indications of improvement and performance in terms of bias and variance were found comparable for both the conventional and aligned tracking schemes in both inclusion and surrounding.

5.4 Discussion

Ideally, shear compounding approach aims to cover the inclusion with the shear waves from all the directions, whereas practically using ultrasound-based shear wave generation techniques, the medium can only be illuminated from limited angles and push beam angles are further limited by the linear array probe. The higher steering angles in the linear probe results in widened beam-width, reduced sensitivity, and grating lobe artefacts, therefore higher steering angles may not

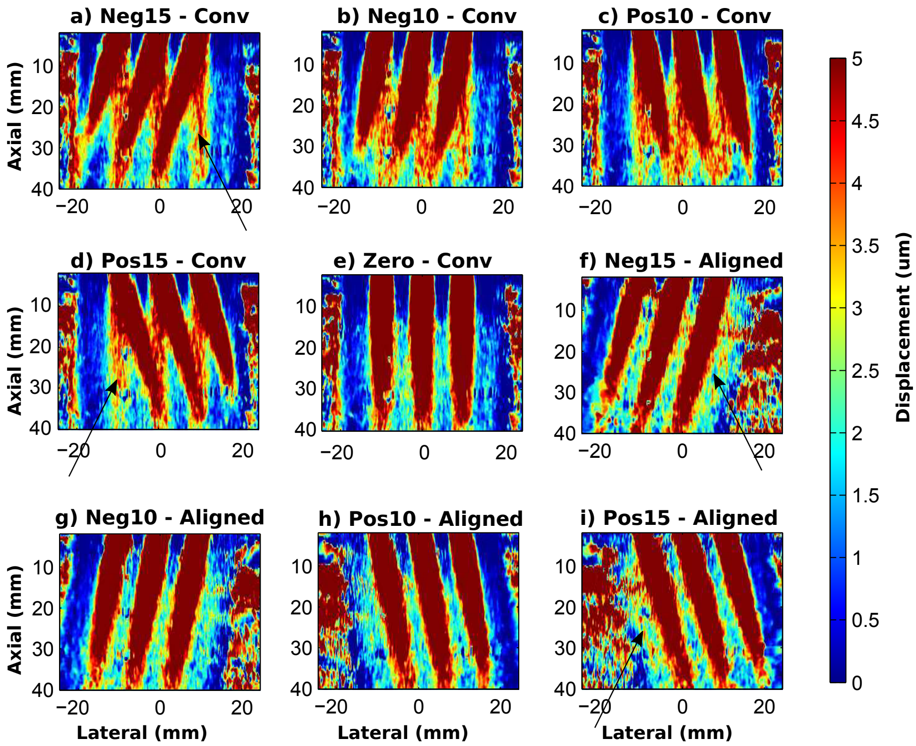

Figure 5.10: The displacement maps for aligned and conventional tracking beams used for listed (-15°, -10°, 0°, +10°, +15°) push beam angles at time instant of 0.1 ms after ultrasound switches to imaging mode. The labels on each displacement map indicate the push beam and associated tracking angle. All conventional tracking beams are fixed to (-2°, 0°, +2°), while aligned tracking beams are adjusted to the push beam angle. Colorbar scale is in the units of μm. The false push beam angle direction artefact are produced by the conventional tracked maps pointed by arrows (map a and d) while in aligned tracked maps, the push beam wave-front angle are truly reconstructed (map f and i).

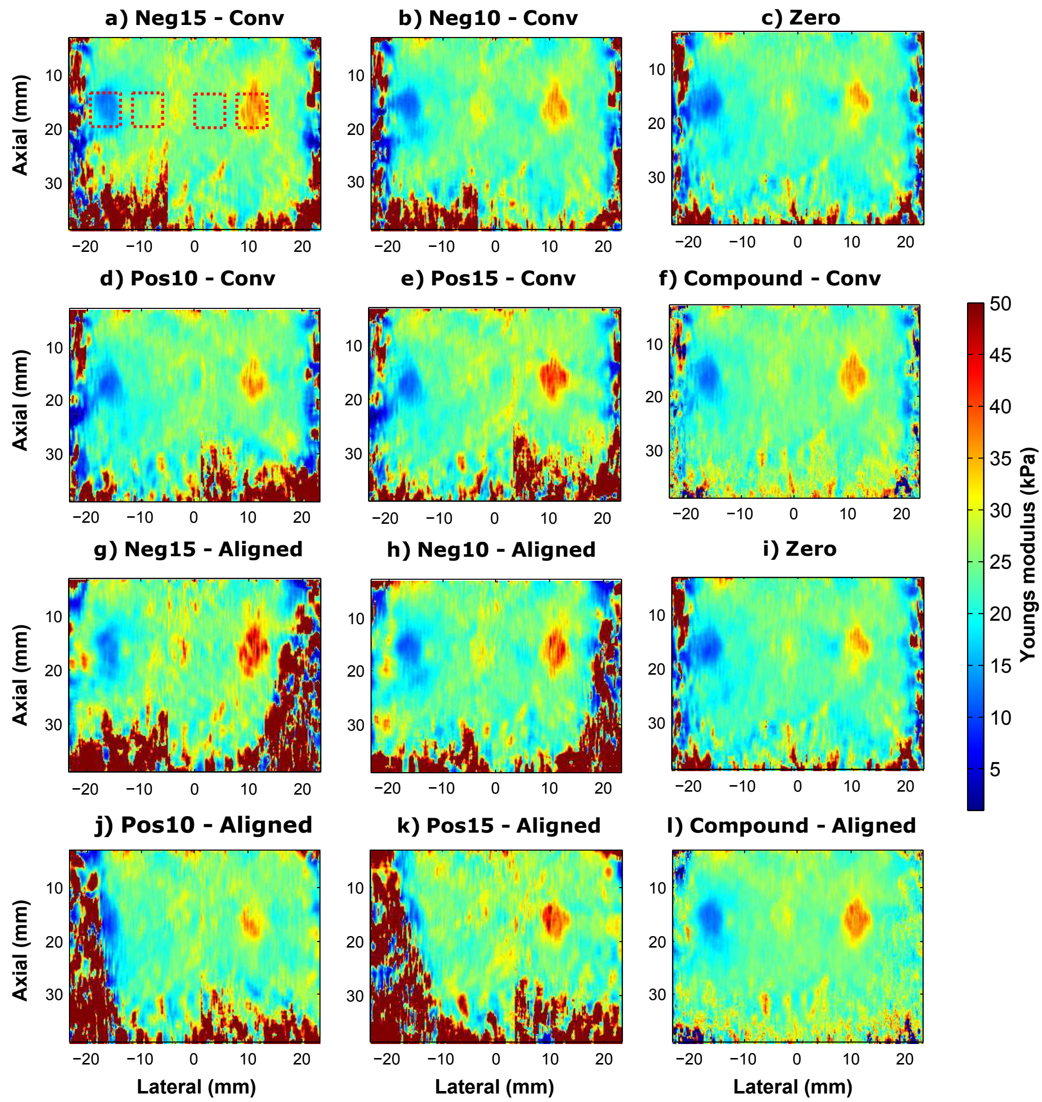

Figure 5.11: Elasticity maps for five push beam angles and corresponding compounded maps for aligned and conventional tracking methods. Colorbar scale is in units of Youngs modulus (kPa). In the final compounded elasticity maps, it can be subjectively observed for 40 kPa, the boundaries of the inclusion in the map produced by the aligned technique (Map. l) are relatively sharp and smooth estimation inside the inclusion than the reconstructed inclusion in the conventional map (Map. f). For 10 kPa inclusion, overall boundary of the inclusion is delineated in better way than the contemporary conventionally tracked map. Lateral dimensions of the compounded elasticity maps are wider and edges have smooth estimation regions.

Table 5.3: Young's modulus mean and standard deviation measurements for background and inclusion using conventional and aligned tracking for 10 kPa inclusion

	Background		Inclusion	
Angle	Conventional	Aligned	Conventional	Aligned
	(Mean ±std.)	(Mean ±std.)	(Mean ±std.)	(Mean ±std.)
- 15	25.47 ±0.57	27.20 ±0.86	14.72 ±0.58	15.49 ±0.89
- 10	24.47 ±0.53	26.07 ±0.47	14.11 ±0.67	13.79 ±0.75
0	24.37 ±0.48	24.37 ±0.48	13.17 ±0.31	13.17 ±0.31
+ 10	25.13 ±0.36	24.69 ±0.40	14.15 ±0.54	55.20 ±75.1
+ 15	25.62 ±0.40	25.54 ±0.52	15.00 ±0.59	101.3 ±125
Compounded	25.01 ±0.43	25.57 ±0.30	14.24 ±0.28	14.18 ±0.39

Table 5.4: Young's modulus mean and standard deviation measurements for background and inclusion using conventional and aligned tracking for 40 kPa inclusion

Angle	Conventional	Aligned
	Inclusion (Mean ±std.)	Inclusion (Mean ±std.)
- 15	34.60 ±0.92	39.35 ±1.62
- 10	33.60 ±0.83	36.70 ±1.37
0	31.61 ±0.83	31.61 ±0.83
+ 10	33.11 ±0.76	31.73 ±0.96
+ 15	38.07 ±1.24	37.23 ±0.94
Compounded	34.20 ±0.82	35.23 ±0.85

improve the results using linear array transducer (Hoskins *et al.*, 2010). The phased array transducers allow to steer the ultrasound field using higher angles, therefore the proposed method needs to be evaluated using higher angles. In the higher angle shear wave generation, the improvements can be expected manyfold better than the current results, because in this study maximum angle was 15 degree, which is not significantly greater than the zero degree. In the alternative way, the shear compounding angles can be further increased if mechanical sources are used for shear wave generation as used by (Zhao *et al.*, 2014).

Previously, shear compounding has been investigated by only two studies

(Bercoff *et al.*, 2004b; Song *et al.*, 2014) and both are different in many aspects in contrast to the proposed shear compounding approach. The SSI based shear compounding method used multiple supersonic Mach numbers to steer shear waves, where steering angle is the function of medium elasticity, which is unknown parameter during the experiment, therefore shear waves with required angles can not be generated. The second shear compounding approach used curved linear probe where different array locations offer different beam angles, therefore the steering angles are fixed according the curvature and size of the transducer. In both methods, there is a weak flexibility and control over selection of the push beam steering angles. The proposed method used linear array transducer combined with the electronic delay profiles to steer both push beams and tracking beams in the specified angles. The ultrasound beam steering angle capability of the linear array probe is limited to lower angles, while phased array transducers are suitable to generate higher ultrasound insonifications angles.

The CUSE based shear compounding technique (Song *et al.*, 2014) acquired a five shear wave angle dataset in 44 ms, which was used to generate a single compounded elasticity map. The current technique used 15 ms duration for each shear wave angle dataset, while 45 ms for all five angles to produce a final compounded elasticity map. The duration of the RF data acquisition are equal in the fast shear compounding approach and in the current study, and therefore in terms of vulnerability to the physiological motions, both techniques are equal. The advantage of the current technique over previous both techniques is improved angled displacement estimation and more flexible control over the generation of differently angled shear waves.

Another important aspect of the study is the generation of shear waves in different directions using linear array transducer by using electronic steering. In the first two studies, multiple angle shear wave field was produced either using a supersonic concept or using curved linear array. In the SSI based shear wave generation, it is challenging to produce required shear wave angle because the produced shear wave angle is a function of underlying tissue shear modulus, which can not be known priori. In the later case, the differently angled shear waves were created at different portions of the array exploiting curved geometry of the array.

The curved arrays offer different angles at different elements, and can not produce a single angle at the whole aperture. There is a disadvantage using curved arrays for the high attenuating tissue clinical conditions, because angled shear waves created from rightmost sub-aperture can travel only up to neighbouring sub-aperture but can not propagate in whole medium and this limits shear compounding based on two or three angles. The current study also addresses both challenges of SSI and CUSE based shear compounding techniques.

Shear wave speed estimation is a three step process once B-mode image is formed. In the first stage, tissue motion spatio-temporal profile induced by the shear waves is calculated and then using directional filtering shear wave reflections are filtered out and left and right travelling waves are separated. In the third step, using spatio-temporal data, shear wave speed is estimated. It is important to note that, the proposed method assumes that shear wave induced motion is always in the direction of pushing beam axis either plane or tilted, however tissue inhomogenuities in *in-vivo* conditions lead to wave refraction and diffraction and change the wave propagation direction. Due to this phenomenon, there will be a mis-alignment between shear wave motion and tracking beam direction and eventually leads to errors in the shear wave induced motion estimation. Shear wave refraction and diffraction can lead to underestimation in the displacement amplitude and error in the displacement direction. To resolve this issue, 2D speckle tracking methods was proposed by (Tanter *et al.*, 2002) and should be implemented in the future work. However, this experimental study in this chapter uses 2D shear wave speed estimation method that is third step in the signal processing flow, which ensures that shear wave independent of direction can be estimated accurately.

Limitations and future directions

One of the limitations of this study is the inability to use higher push beam angles such as 45, 30, 15, and 0 degrees for shear compounding as only a linear array transducer was available in the ultrasound lab at the time of the experimental study. In future studies, effect of using the proposed method of shear wave tracking for higher angles using phased array probe should be investigated. Another limitation of the study is that only phantom based experiments are conducted, while *in-vivo* clinical scenarios can be far more complex in terms of tissue elastic homogeneity, inclusion geometry, acoustic speed aberration, and shear wave attenuation. In the future studies, the experiments should be conducted using *in-vivo* and *ex-vivo* scenarios. Further, there is need to investigate existing angled tissue motion methods used in the blood flow velocity such as directional velocity estimation using focusing along the flow direction (Jensen *et al.*, 2016; Jensen, 2003; Jensen & Bjerngaard, 2003). In these studies, the imaging beams are focused along the blood flow motion direction using beamforming in the receive mode to accurate estimate angled motion without steering beams in the transmit mode. For shear compounding using this method, angled tissue motion can be estimated without steering the beam angles and avoiding generation of the grating lobes, which effect the shear wave tracking quality. This study used three parallel simultaneously generated focused push beams to illuminate the medium with the differently angles shear waves, further experiments will be to conducted to realise proposed tracking method for other shear wave elastography methods.

5.5 Conclusions

In this experimental work, the effect of spatially aligning tracking beams with shear wave polarisation angles is investigated and compared with the conventional method. The results conclude that, angled displacement values are estimated with correct push beam direction and improved displacement amplitude using the proposed method while conventional tracking underestimated the displacement amplitude and produced artefacts. In the final elasticity maps, aligned tracking improved inclusion reconstruction geometry and maintained contrast equal to conventional method. The results suggest that, angularly aligning shear wave tracking beams with the shear wave generation beams improve angled speckle motion amplitude and direction estimation. In contrast to existing shear compounding techniques, the current study offers more control over the selection of the shear wave generation angles and improved shear wave tracking accuracy. This technique promises a great potential to design shear wave tracking methods suitable to polarisation of shear waves, and improve the quality of shear wave tracking.

Chapter 6

Bias and Variability Observations for Different Shear Wave Elastography Methods

6.1 Introduction

Shear wave elastography provides non-invasive and quantitative measurements of soft tissue stiffness, which are useful as a clinical biomarker for various pathological conditions for liver and breast elasticity imaging. The variability of shear wave speed among different locations and measurement depths can potentially change the diagnosis in clinical conditions and limit the reliability of shear wave elastography methods. Ideally, shear wave elastography needs to produce a elasticity map with known and uniform accuracy along the depth and lateral direction to enable reliable diagnosis. In this respect, (Zhao *et al.*, 2011b) observed that shear wave speed estimation using focused beams is not uniform along the lateral and axial direction and significantly changes as the measurement location is changed. Author (Zhao *et al.*, 2011b) also noticed the significant difference of shear wave speed between linear array and curvilinear transducers and also using different push beam apertures. The limitation of study conducted by (Zhao *et al.*, 2011b) was that, it only used single push beam and shear wave speed measurements taken at focal depth, whereas, practically, shear wave configuration and corresponding propagation are more complicated. Also, clinically, shear wave speed measurements are needed not only at focal depth but also in the areas surrounding the focal depth of the push beam.

Later on, the Quantitative Imaging Biomarker Alliance (QIBA) conducted a systematic inter-system shear wave speed variability study using calibrated viscoelastic healthy and fibrous liver mimicking phantoms. The results demonstrated variability among different ultrasound systems at different depths and values followed the same pattern among three different phantoms (Hall *et al.*, 2013; Palmeri *et al.*, 2015). Following this, (Dillman *et al.*, 2015) compared SSI (Aixplorer, SuperSonic Imagine, France) and ARFI (ACUSON S3000, Siemens Healthcare, Germany) elastography methods using commercial machines. They also found that shear wave speeds were significantly different when measured at different depths and also using different machines. Another study by (Shin *et al.*, 2016) also investigated inter-system variability among three different shear wave elastography systems for liver diagnosis using different transducers and different measurements depths. The study found that there was considerable difference in mean shear wave speed depending on different ultrasound systems, transducers, and measurement depths and cautious approach was suggested when considering elasticity values for liver fibrosis diagnosis. These last three studies focused on inter-system and inter-transducer variability with little attention to the shear wave configurations fundamental parameters such as push beam aperture, the number of push beams and push beam focal depth dependent variability. Currently, there is no study which compares different shear wave configurations in terms of investigating variability along depth and lateral directions and penetration depth capacity.

This study addresses above mentioned limitations of previous studies and in this respect set of experiments were designed, implemented on ultrasound system UARP II and conducted on the commercial phantom. This study investigates shear wave speed variability using different shear wave configurations, push beam focal depths, measurement depths, and lateral measurement locations. Further, a repeatability study was also conducted.

6.2 Materials and methods

This section explains methods used for the experiment and final statistical analysis. It includes details about shear wave generation configurations and parameters used, ultrasound system, shear wave tracking, elasticity estimation algorithm, and statistical tools.

6.2.1 Shear wave configurations

In this study, seven different shear wave configurations were designed, where each configuration differs from the others in terms of aperture size, number of push beams, and whether beams used are focused or unfocused. The configurations also include existing shear wave configurations such as U-CUSE, F-CUSE, and DPB-AP4 as proposed in the previous chapter. Each configuration is illustrated in Fig. 6.1 using corresponding phased delay profiles. There are six different focused beam and one unfocused beam based configuration. The unfocused (US) configuration uses plane wave transmissions for shear wave generation therefore delay profiles are zero at each element. All other configurations are focused radiation force beam methods. These delay profiles are plots for 20 mm focused beams, therefore, it can be observed that, as transmit aperture is decreasing, peak phase delay (in μs) is decreasing.

It is important to note that, 4-Beam focused and 5-Beam unfocused configurations (see Fig. 6.1) are equivalent to F-CUSE and U-CUSE shear wave generation techniques. It can be observed that, push beam transmit aperture for Beam-2 (F2) focused, Beam-3 (F3) focused, Beam-4 (F4) focused, Beam-5 (F5) focused, Beam-6 (F6) focused, Beam-7 (F7) focused and Beam-5 (US) unfocused are 64, 42, 32, 24, 12, 12, and 12 elements, respectively. The F4, F7 and US unfocused cases use a 12 element transmit aperture, however, F6 and F7 differ in terms of number of push beams, while F5 used unfocused push beams. F2 to F4 configurations do not have any aperture gap between two push beams, while F5, F6, F7, and US unfocused used 2, 11, 7, and 17 elements gap, respectively. For each focused configuration, five different focal push beam locations were investigated (20, 25, 30, 35, and 40 mm away from the transducer surface). The focal depths were chosen near to the transducer surface due to shallow fixed elevational focus ($\sim$ 20 mm) of transducer and also considering typical measurement depth expected for linear high-frequency transducers. For each combination of experimental parameters, three repeated RF data acquisitions were obtained without moving the transducer. Therefore, total of 105 measurements were conducted in this study ($\sim$ seven configurations by six focal depths by three repetitions).

6.2.2 Experimental set-up and signal processing

The experimental set-up (Section 4.3.1), RF data acquisition parameters (Sections 4.2.1 and 4.2.1) and shear wave speed estimation signal processing flow and parameters (Sections 4.2.3, 4.2.4, and 4.2.5) are similar to the used in Chapter 4. To achieve improved shear wave speed estimation, displacement data was averaged over two wavelengths in both axial and lateral directions, eventually resulting in pixel resolution of λ in both directions.

6.3 Results

Repeatability measurement test

For each experimental setup combination, three repeated measurements were taken to investigate the repeatability of shear wave speed measurements. For six focused shear wave configurations, and five different push focal depths for each configuration were used and three repeated measurements for each combination, which results a total of 15 acquisitions for each configuration. For unfocused configuration (US), 15 repeated measurements were achieved to ensure same sample size for all configurations. There were total of 105 ultrasound shear wave data acquisitions. The ROI with size of 20 mm^2 square box was selected for all measurements which spanned from in axial = 5 mm $\sim$ 25 mm and lateral = -10 mm $\sim$ +10 mm direction. Average shear wave speed inside the ROI was calculated for all 105 measurements and then average standard deviation among 15 acquisitions for each configuration was calculated. In the final calculations, average standard deviation for F2, F3, F4, F5, F6, F7, and US were measured as 0.004, 0.003, 0.007, 0.003, 0.017, 0.027 m/s. The results indicate that, there is a significant

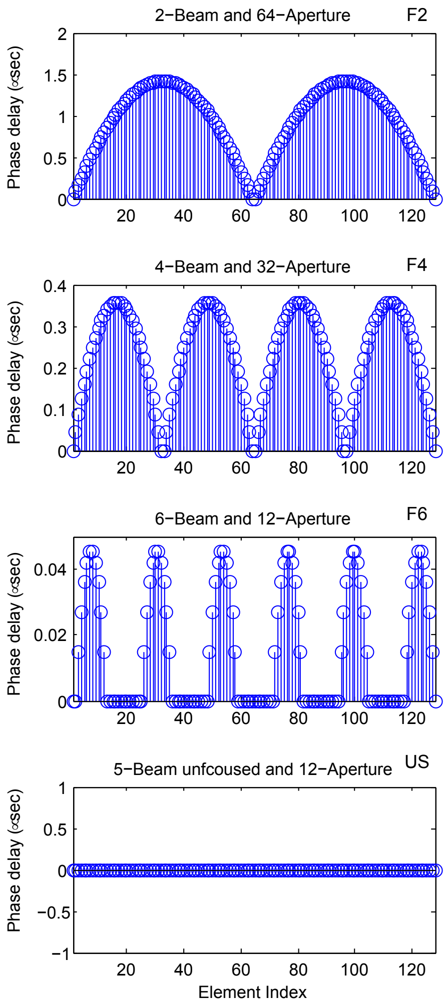

Figure 6.1: Various shear wave generation configurations are presented in terms of corresponding delay profiles. The titles on each subplot indicate number of beams, and transmit aperture used for each beam. The US configuration uses plane wave transmissions for shear wave generation therefore delay profiles are zero at each element. All other configurations except the final unfocused are focused radiation force beam methods. These delay profiles are plots for 20 mm focused beams, therefore, it can be observed that, as aperture is dcreasing, peak phase delay (in μs) is also decreasing. It is important to note that, 4-Beam focused and 5-Beam unfocused configurations are equivalent to F-CUSE and U-CUSE shear wave generation techniques.

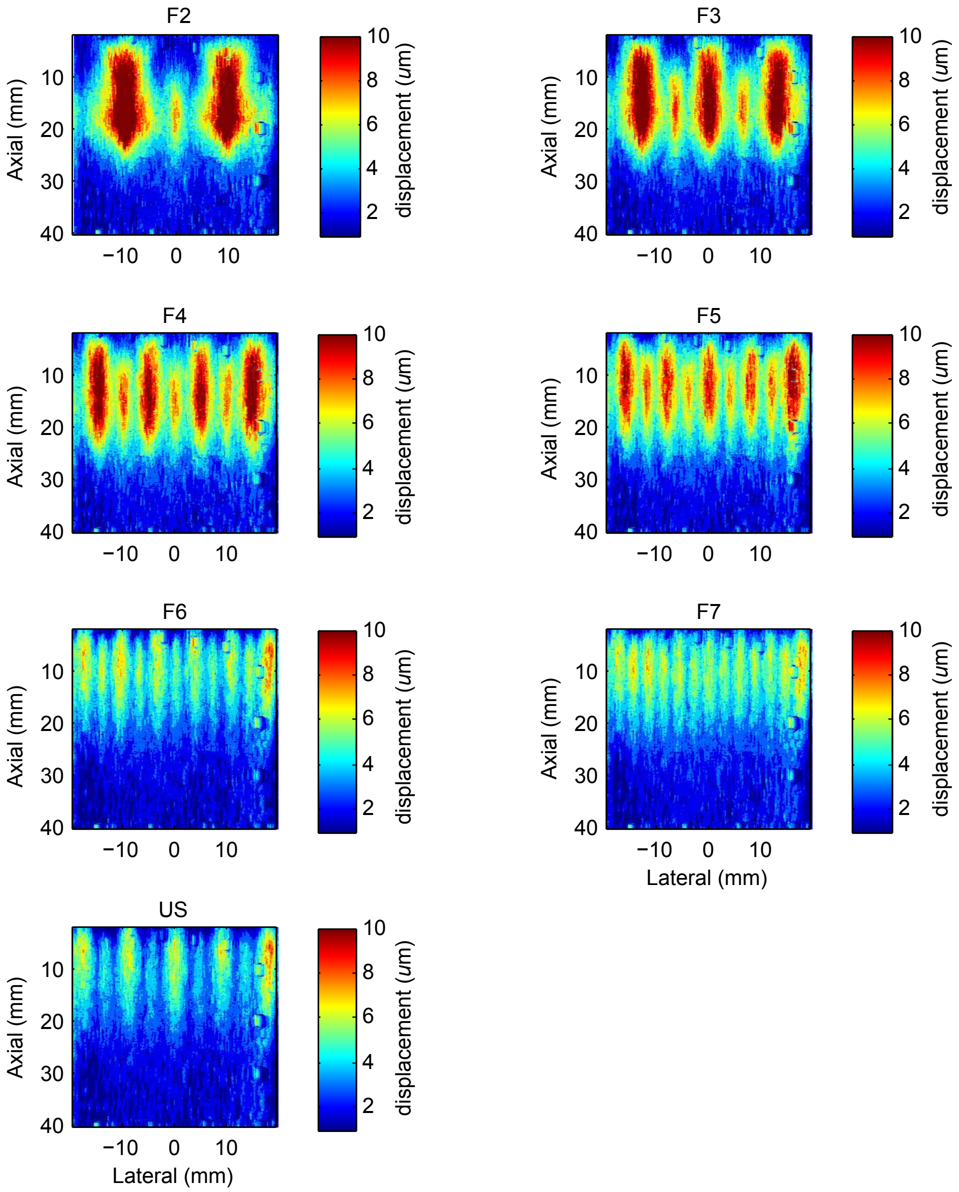

Figure 6.2: Peak displacement maps for all seven kinds of push beam generation methods. The colourbar scale indicates axial displacement in units of μm. It can be observed that, larger aperture shear wave generation methods (F2, F3, F4, F5) are able to produce higher peak displacement at beam locations compared to the low aperture beam (F6, F7, US) methods. It can be observed that, larger apertures are suitable for generating higher displacements, while distribution of displacement peaks along the FOV is not uniform, which is better when number of shear wave beams are increased along the lateral dimension.

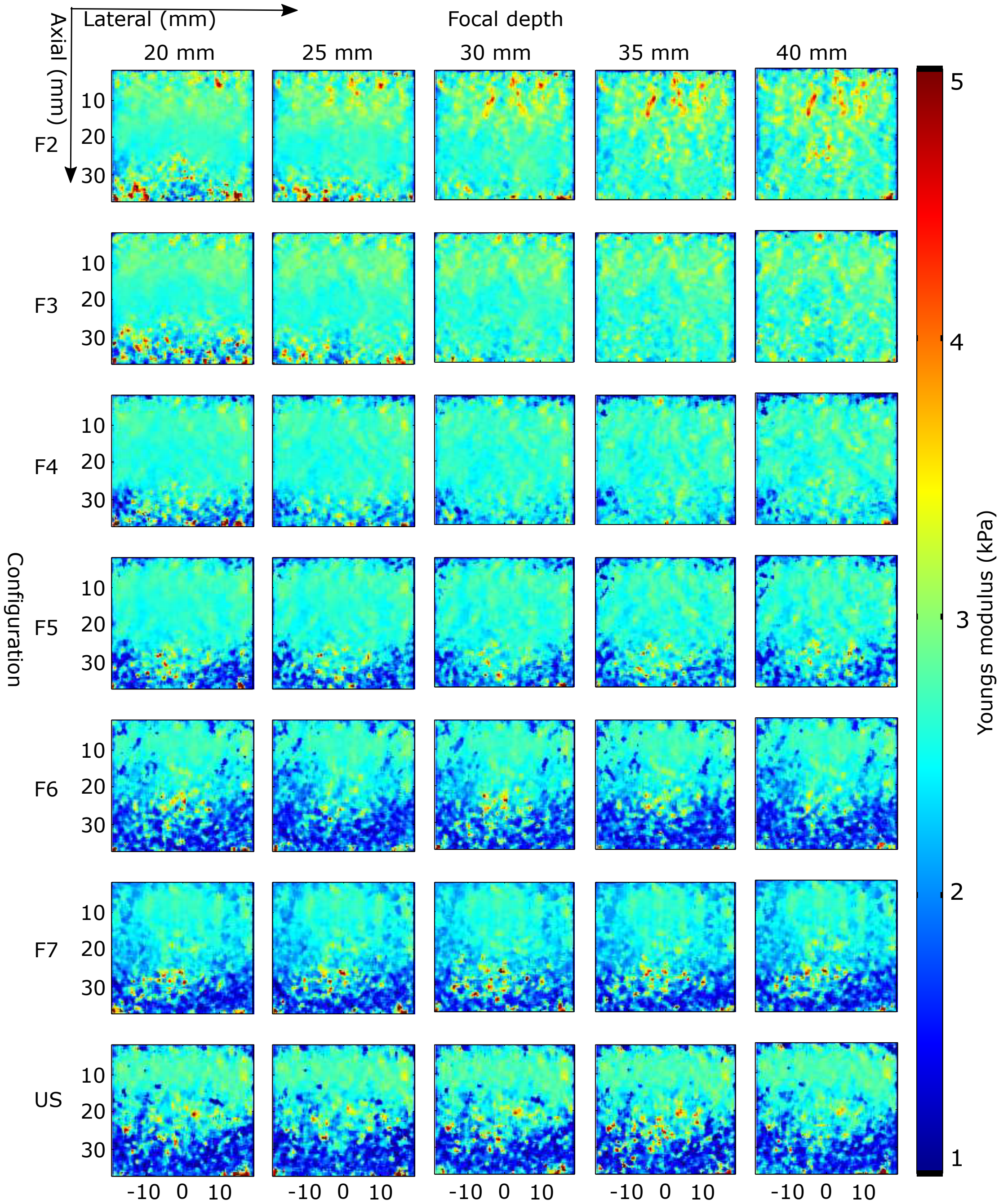

Figure 6.3: Shear wave speed maps for all sevan and five different configurations are displayed here. Shear wave configurations are indicated by respective labels on each row and push beam focal depths are labelled at top of each column. In each shear wave speed map, horizontal axis shows lateral and vertical axis shows axial dimension. Colourbar colours indicate shear wave speed in the units of m/s.

repeatability and have small variation among multiple acquisitions. For instance, taking maximum variation which is 0.027 m/s, it results in a difference of 0.0023 kPa in the expression of elastic modulus, which is negligible in comparison to the order of ones and tens of kPa of soft tissues biological elasticity.

Configuration dependent variability

The inter-configuration variability was investigated among seven shear wave configurations detailed in the previous section. For each configuration, push focal depths which include 20, 25, 30, 35, and 40 mm datasets were acquired, therefore total of 35 different measurement combinations were used. For each combination, shear wave speed mean and standard deviation was calculated and displayed using bar plots as shown in Fig. 6.4. The results indicate that, shear wave speed inside ROI decreases from F2 to US shear wave configuration, alternatively, as push beam aperture decreases, mean shear wave speed also decreases. It can be observed that for F4, F5 and US configurations, measured shear wave speed is comparable with the nominal (N) values, F2, and F3 resulted in overestimated while F6 and F7 resulted in underestimated speed values, when compared with the nominal shear wave speed. These results are consistent for all four push beam focal depths. In terms of variance within the ROI, F2, F6, F7, and US have relatively higher standard deviation relative to the F3, F4 and F5. The standard deviation for F2 is dominated in the shallow regions due to overestimated values, while for F6, F7, and US, deeper parts of ROI resulted in densely underestimated and scattered overestimated values and causing higher standard deviation. The Student's t-test (Zhao *et al.*, 2011b) values for all shear wave configurations pairing all focal depths were calculated and p-values indicate that, estimations are statistically significantly different between all configurations except few as listed in Table. 6.1. Another quality factor of shear wave generation techniques is shear wave penetration depth with adequate SNR. In the performance perspective, it can be observed in the shear wave speed images presented in Fig. 6.4 that, using higher aperture along with higher focal depths helps to reconstruct shear wave speed in deeper regions. Also, as the aperture was decreased from F2 to F6, penetration depth also decreased significantly.

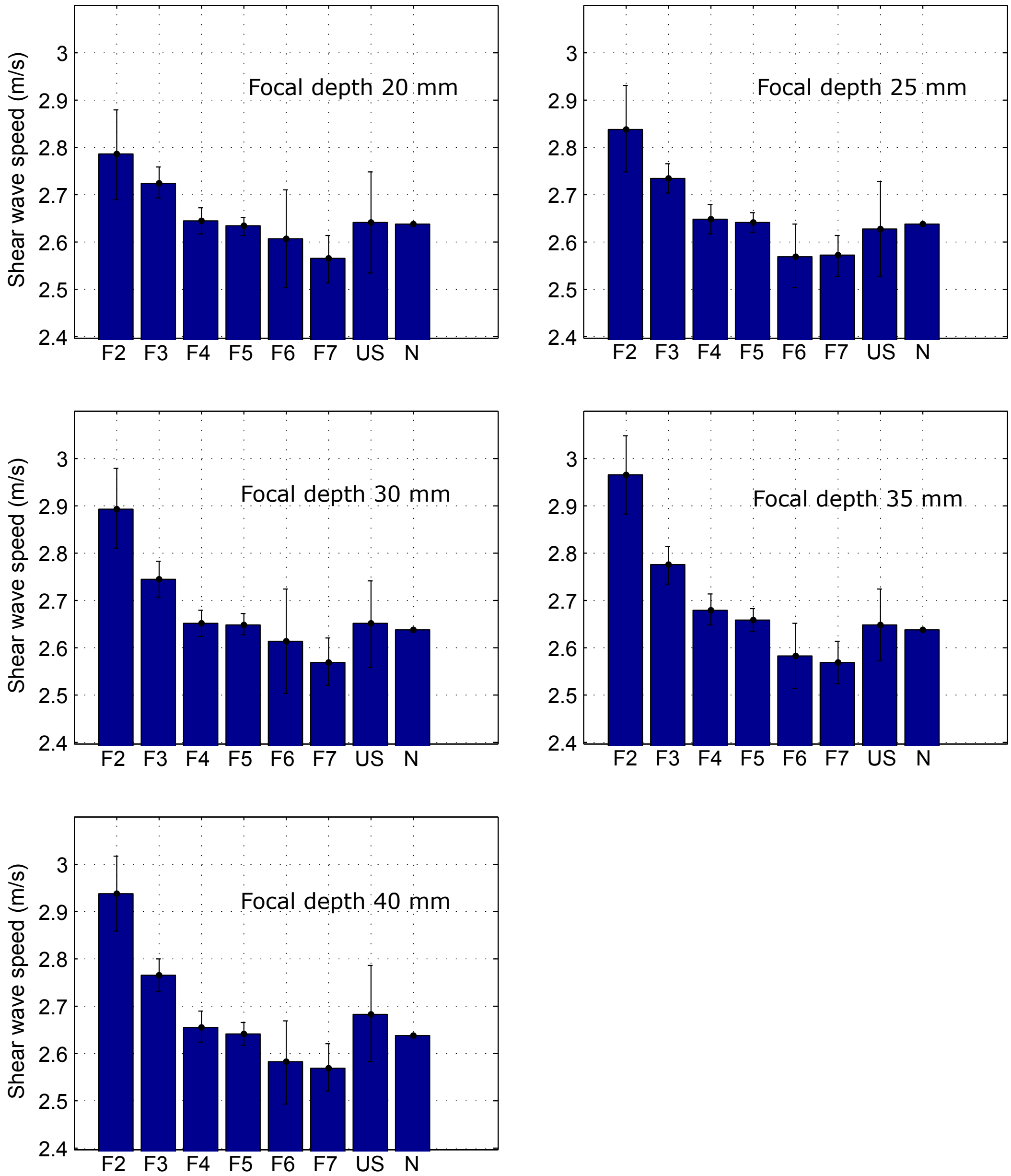

Figure 6.4: Shear wave speed mean and standard deviation measurements in the ROI for seven different shear wave generation configurations along with nominal (N) phantom value. The ROI is axial = 5 mm ∼ 25 mm and lateral = -10 mm ∼ +10 mm. Shear wave speed measurements for push beam focal depth 20, 25, and 30 mm are displayed here.

Table 6.1: Student's t-test values for shear wave beam configuration dependent variability experiment. The p-values are calculated for all shear wave configuration combinations. The bold values indicate statistically significantly different p results.

	F2	F3	F4	F5	F6	F7	US
F2		< 0.01	< 0.01	< 0.01	< 0.01	< 0.01	< 0.01
F3	< 0.01		< 0.01	< 0.01	< 0.01	< 0.01	< 0.01
F4	< 0.01	< 0.01		< 0.01	< 0.01	< 0.01	**0.1175**
F5	< 0.01	< 0.01	**0.04**		< 0.01	< 0.01	< 0.01
F6	< 0.01	< 0.01	< 0.01	< 0.01		**0.06**	**0.0015**
F7	< 0.01	< 0.01	< 0.01	< 0.01	**0.06**		< 0.01
US	< 0.01	< 0.01	**0.11**	**0.02**	**0.02**	< 0.01	

Focal depth dependent variability

In order to investigate if shear wave speed measurement values vary for different push beam focal depths, five push beam focal locations which include 20, 25, 30, 35 and 40 mm, and six different configurations which include from F2 to F7, were used for comparative study. The ROI was selected for mean and standard deviation calculations, which spanned from 5 mm $\sim$ 25 mm in the axial and -10 mm $\sim$ +10 mm in the lateral direction, with size of 20 mm^2 square box. All the measured values are displayed using bar plots and presented in Fig. 6.5. It can be observed that, as the push beam focal depth is increasing from 20 mm to 40 mm with increment of 5 mm, shear wave speed inside ROI is also increasing, where this overestimation in shear wave speed as a function of focal depth is high for F2 and F3, F4 and little effect was observed for and F5 configurations. Along with consistency in F4 and F5 as a function of increasing focal depths, measured shear wave speed values are comparable with the nominal shear wave speed. In F6 and F7, no consistent difference was observed among different push beam focal depths and results were underestimated relative to the nominal values. In terms of estimation variance, F2, F6, and F7 resulted in higher standard deviation relative to the F3, F4, and F5. The Student's t-test (Zhao *et al.*, 2011b) values for all focal depths pairing all shear wave configurations were calculated and p-values indicate that, estimations are not statistically significantly different between all focal depths few as listed in Table. 6.2.

Table 6.2: Student's t-test values for focal depth dependent variability experiment. The bold values indicate statistically significantly different p results.

	20	25	30	35	40
20		**0.8800**	**0.5959**	**0.6033**	**0.5065**
25	**0.8800**		**0.7136**	**0.7063**	**0.6018**
30	**0.5959**	**0.7136**		**0.9640**	**0.8439**
35	**0.6033**	**0.7063**	**0.9640**		**0.8871**
40	**0.5065**	**0.6018**	**0.8439**	**0.8871**	

Measurement depth dependent variability

The purpose of this study is to understand if shear wave speed measurements vary at different measurement depths along the shear wave beam axial axis. For this study, four configurations F2, F3, F4 and F5 are investigated for five push beam focal locations 20, 25, 30, 35 and 40 mm. For each, measurements are achieved for near depth ROI called D1 which spans from 5 mm $\sim$ 15 mm and far depth ROI called D2 which spans from 15 mm $\sim$ 25 mm in the axial while -10 mm $\sim$ +10 mm in the lateral direction for ROIs. For each combination, mean and standard deviation values are calculated and displayed in Fig. 6.6. Looking at the bar plots, it can be observed that, shallow ROI (D1) have higher shear wave speed values relative to the deep ROI (D2) shear wave speed measurements, and it is consistent for all four configurations and all five focal depths. Further, it is important to note that, variability between two measurement depths is higher for F2 and F3 and very low for F4 and F5 configurations. Along with high variability between two measurement depths for F2 and F3, an overestimation can be

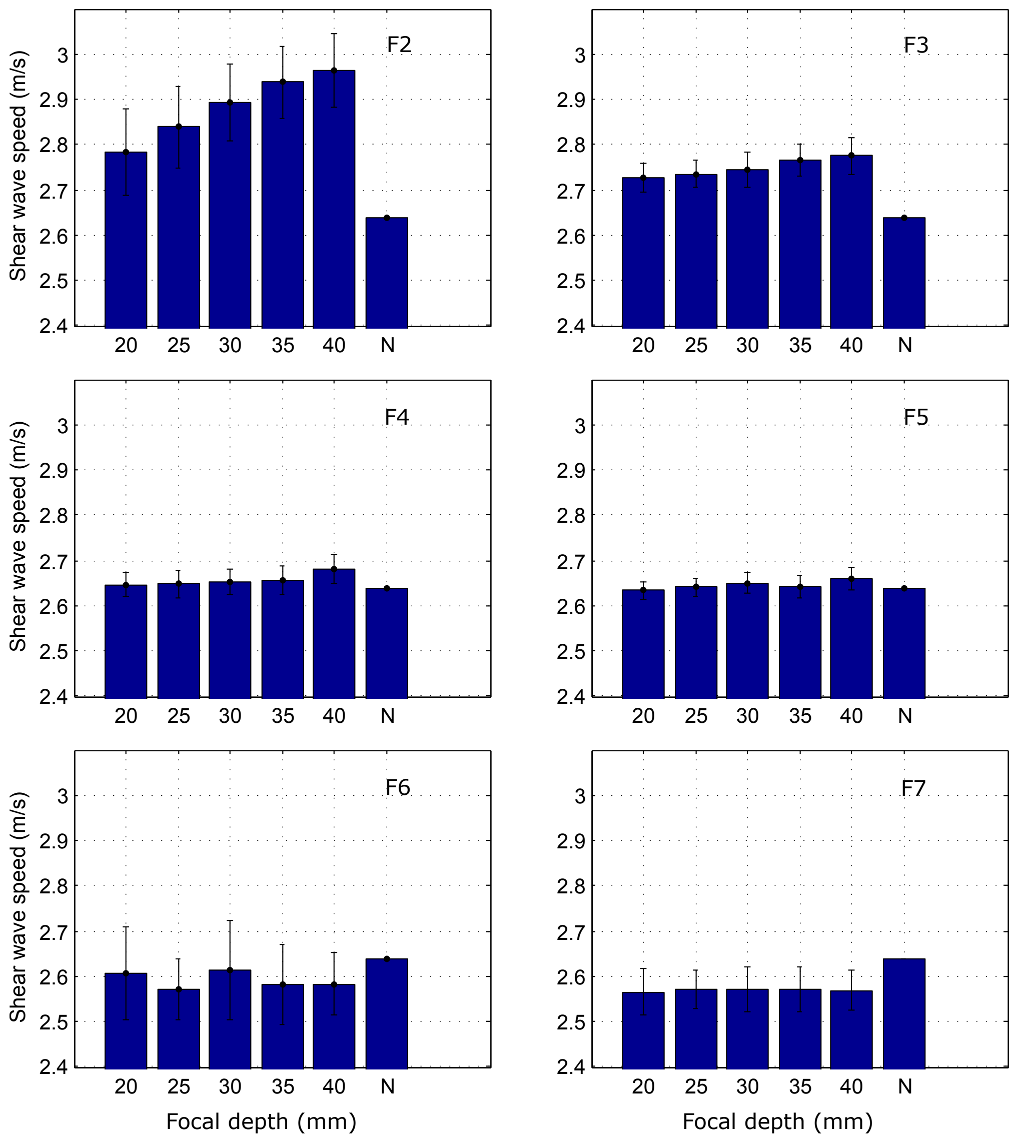

Figure 6.5: Shear wave speed mean and standard deviation measurements in the ROI for seven different shear wave generation configurations along with nominal (N) phantom value. The ROI is axial = 5 mm $\sim$ 25 mm and lateral = -10 mm $\sim$ +10 mm. Shear wave speed measurements for push beam focal depth 20, 25, and 30 mm are displayed here. Shear wave speed measurements for push beam focal depth 35 and 40 mm are displayed here.

observed for both depths, while F4 and F5 values are comparable to the nominal values. The Student's t-test was applied between D1 and D2 elasticity estimation data as presented in Fig. 6.6, and measured value (p-value $= \mathbf{0.012}$) indicate that estimation difference between two measurements depths is not statistically significant.

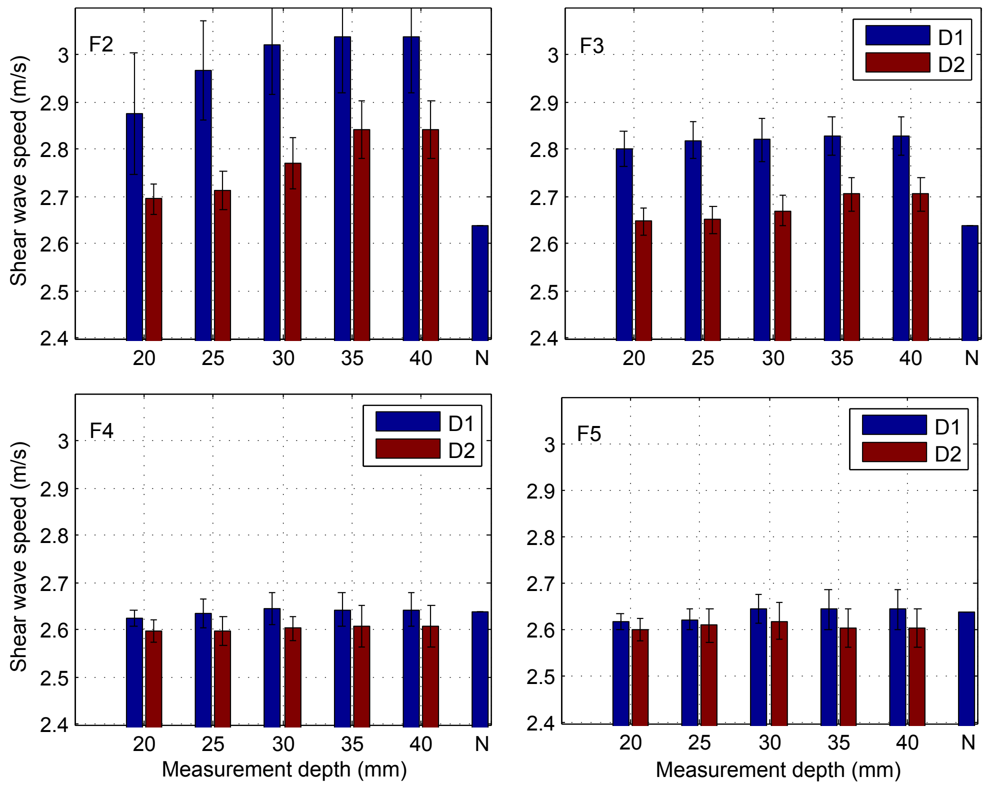

Figure 6.6: Shear wave speed mean and standard deviation parameters are displayed for two different depths (D1, D2) for F2, F3, F4 and F5 configurations and 20, 25, 30, 35, and 40 mm push focal depths. The ROI for D1, and D2 is 5 mm $\sim$ 15 mm, and 15 mm $\sim$ 25 mm axially while -10 mm $\sim$ +10 mm in the lateral direction. The results indicate that, shear wave speed values decrease as the measurement depth increases (away from transducer) for all combinations.

Lateral location dependent variability

To investigate the variability of shear wave speed estimation at different lateral locations, three different ROIs (called L1, L2, L3), placed at three lateral locations were used for four configurations which include F2, F3, F4, and F5 and five push beam focal locations 20, 25, 30, 35 and 40 mm. The ROI for L1, L2, and L3 is -15 mm $\sim$ -5 mm, -5 mm $\sim$ +5 mm, and +5 mm $\sim$ +15 mm respectively in the lateral direction while 5 mm $\sim$ 25 mm in the axial direction for all three lateral ROIs. For each combination, mean and standard deviation values are calculated and displayed in Fig. 6.7. A small variability of shear wave speed can be observed among three different lateral locations for all combinations where the variability decreased as from configuration F2 to F5. The Student's t-test was also applied between L1 and L2 (p-value = **0.34**), between L1 (p-value ¡ 0.01) L3 and between L2 and L3 (p-value = **0.016**) elasticity estimation data as presented in Fig. 6.7, and measured p-value indicate that estimations are not statistically significantly different between L1 and L2, L2 and L3, while significant difference was observed between L1 and L3.

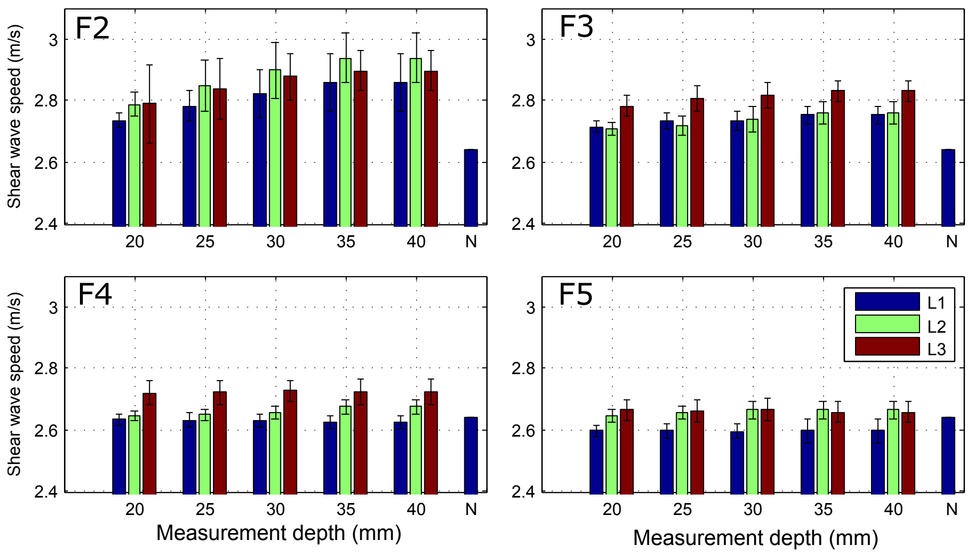

Figure 6.7: Shear wave speed mean and standard deviation parameters are displayed for three different lateral locations (L1, L2, L3) for F2, F3, F4, and F5 configurations and 20, 25, 30, 35, and 40 mm push focal depths. The ROI for L1, L2, and L3 is -15 mm $\sim$ -5 mm, -5 mm $\sim$ +5 mm, and +5 mm $\sim$ +15 mm respectively in the lateral direction while 5 mm $\sim$ 25 mm in the axial direction for all three lateral ROIs. A small variability of shear wave speed can be observed among three different lateral locations for all combinations.

6.4 Discussion

Repeatability test Observing the results, it can be inferred that, there is a good repeatability for all seven configurations and amount of deviation is negligible in compare to the elasticity values of biological tissues, which are on the order of tens and hundreds of kPa. This indicates that, shear wave motion dataset has adequate SNR both in generation and tracking within the ROI used for measurements. It is also important to notice that, US have the poor repeatability among all configurations and it is related with poor shear wave SNR, can be observed in the peak shear wave displacement (see Fig. 6.2) images.

Configuration dependent variability The results indicate that (see Fig. 6.4), higher aperture shear wave configurations resulted in overestimated values while low-aperture beams F6 and F7 produced underestimated shear wave speed values and F4, F5, and US produced results comparable with the nominal shear wave speed of the phantom in the ROI. These results were consistent for five push beam focal depths which include 20, 25, 30, 35, and 40 mm. In terms of variance, F3, F4 and F5 resulted in the lowest standard deviation. It can be inferred that, in terms of bias and standard deviation, F4 and F5 performed better than all other shear wave configurations for measurement depth from 5 to 25 mm. Statistical test also observed significant difference in elasticity estimation when different shear wave configurations are used. Moreover, it can be noticed that, higher aperture beams resulted in overestimation possibly due to wide and diverged geometry of the push beams generated. Large apertures generate tighter focal lateral profile at the focus and increasingly diverging away from the focal point. The overestimation possibly arises from the fact that, when higher aperture beams are used, shear wave source have a complicated shape rather than the plane shape (Hoskins *et al.*, 2010), which is ideal for 1D shear wave speed estimation methods. This curved shape shear wave source steers the shear waves higher than the zero angle, depends upon the degree of curvature. Time of flight based shear wave estimation assumes shear wave travelling along lateral direction at zero angle and this error in propagation direction is possibly adding some errors.

Focal depth dependent variability The results indicate that (see Fig. 6.5), for high aperture F2 and F3 configurations, shear wave speed increased as the focal depth increased from 20 to 40 mm up to 1.5 m/s (7 kPa) and 0.5 m/s (0.8 kPa), respectively. For F5, F6, F7 configuration, a minor change (less than 0.2 m/s or 0.13 kPa) in the shear wave speed was observed. This points to that, configurations with high aperture are sensitive to selection of push beam locations, as the aperture decreases, the effect of changing push beam focal point is very little. Further, F6 and F7 resulted in the underestimated values, and and F5 produced values comparable to the nominal shear wave speed value of phantom. Statistical test values resulted in statistically no significant difference when push beam focal depths are changed. The possible reason is this study used only five focal depths which is a small sample size to achieve accurate statistical test. In future studies, experiments should be conducted with small steps in the focal depths. As focal point is placed away from transducer, beam spatial profile along the lateral dimension diverges more in the ROI (5 to 25 mm), and this produces the same effect as increasing push beam aperture size. A study by (Zhao *et al.*, 2011b) also observed variability by changing focal depth and pointed the possible reason as; shear waves generated out of the axial-lateral scan plane due to multiple intensity peaks in the elevational plane, and shear waves travel less distance than the assumed distance thus resulting in over-estimation. Although, no experimental evidence was provided to validate the reason.

Measurement depth dependent variability The results indicate (see Fig. 6.6) that, shallow depth ROI (5 to 15 mm) have higher shear wave speed values relative to the deep ROI (15 to 25 mm) shear wave speed measurements for all configurations, while for and F5 demonstrated little variability compared to F2, and F3. The difference was up to 2 m/s for F2, up to 1.5 m/s for F3 and less than 0.5 m/s for and F5. This indicates that, shear wave speed measurement depth variability is less sensitive to small aperture configurations than large aperture configurations.

Lateral location dependent variability The results (Fig. 6.7) found small variability (less than 0.5 m/s) of shear wave speed among three different lateral locations for all combinations. Results indicate that, F2 configuration benefited in terms of shear wave penetration depth and shear wave SNR across the FOV, but also resulted in overestimation bias in shallow regions, and overestimation increased when focal depths were moved away from the transducer. The shallow region overestimation was found less in the F3 than F2 and negligible in the and F5 configurations. Also, push beam focal depth, measurement depth, and lateral location dependent variability was also negligible for and configurations. For the imaging depth up to 25 mm, and F5 performed superior in terms bias and variance, and possibly imaging depth can be increased up to 40 mm using higher excitation voltages. For imaging depth higher than the 40 mm, F2 and F3 are suitable. Finite element based simulations can be used to understand and correct push beam geometry related bias. An interesting insight can be achieved if an effect of shear wave source geometry (beam shape) on shear wave speed propagation and its speed estimation can be observed. The previous study by the (Zhao *et al.*, 2011b) also observed that, varying aperture size for push beam changed shear wave speed significantly for the L7-4 transducer, though, measurements were made at focal depth only and beam geometry away from focal depth was ignored. The same study pointed that, placing axial focal depths away from the elevational focus is possibly reason of overestimation bias, but current study results suggest that, the difference between axial and elevational focus only generated different shear wave speeds in large apertures, and no significant difference was observed for small apertures. This indicates that, overestimation is not related with the elevational and axial focus difference, but the geometry of lateral profile of push beams because higher aperture tends to have wider lateral profiles away from the focal depth. It is also important to investigate the effect of push beam geometry on shear wave spectrum contents as dispersion due to viscosity enable different shear wave speed at different frequencies.

According to the guidelines issued for clinical use of ultrasound elastography for liver diagnosis by World Federation for Ultrasound in Medicine and Biology (WFUMB) (Ferraioli *et al.*, 2015), Young's modulus cut-off values were proposed for different stages of liver fibrosis. In this guideline, liver stiffness values between 2.5 and 7 kPa points to likely no or mild fibrosis (F0-F1) and 7 to 9 kPa likely indicate significant fibrosis (F2), 9.5 to 12.5 kPa likely indicate severe fibrosis, whereas for values from 12.5 up to 75 kPa, cirrhosis is highly likely, given certain conditions of patient. As there is a minimum of 2 kPa difference between two liver diseases stages, therefore elasticity bias as low as 1 kPa may also change the diagnosis outcome. In clinical ultrasound systems, shear wave configuration and push beam focal depth are usually fixed for a certain clinical application. Therefore, this suggests that, more detailed studies needed to be conducted to measure bias for a certain shear wave configuration and focal depth and measurements need to be corrected before final diagnosis.

For breast elastography, WFUMB suggested that (Barr *et al.*, 2015), elastography image along with the Breast Imaging-Reporting and Data System (BI-RADS) score acquired using B-mode image should be used to improve sensitivity and specificity of diagnosis. The cut-off values of elasticity were classified as BI-RADS II ($<$ 20 KPa), BIRADS III (20 to 60 KPa), BIRADS IV (60 to 80 kPa) and BIRADS V ($>$ 80 KPa). Also, generally imaging depths required for breast imaging are up to 40 mm, therefore, and F5 can be better suited for this clinical application. However, for obese patients, F2 and F3 have potential to look into deeper abnormalities, as there is large difference in elasticity ($\sim$ 20 kPa) between two neighbouring cut-off values therefore small variabilities along depth and lateral direction may not effect the diagnosis results as severely as for liver fibrosis diagnosis.

Limitations and future directions

This study was conducted using linear array transducer which is clinically used for shallow tissue imaging such as breast, and thyroid. For liver diagnosis, usually elasticity values from 20 to 60 mm away from transducer surface are required, and curvilinear array transducer with deep elevational focus is used to translate ultrasound energy at deeper regions for both shear wave generation and tracking. In future, a similar study will be realised for curvilinear array transducer. In future work, spectrum contents of shear waves at each pixel for all configurations will be investigated to understand if push beam geometry (beam width) alters shear wave spectrum significantly. This will guide us to understand and correct viscosity or dispersion induced errors.

As, large aperture push beams do not produce plane shear wave sources, while shapes are curved and change for changing aperture and focal depth. These curved sources steer the shear waves at different angles with respect to lateral dimension, therefore, in future studies, 2D shear wave speed estimation methods will be investigated to address this problem (Song *et al.*, 2014). In future, this study will be conducted using maximum possible and safe voltage excitations and the configurations with poor shear wave SNR such as F6, F7, and US performance will be evaluated. Homogeneous phantom studies are useful for diffuse disease examination such as liver fibrosis, while for mass developing pathologies such as breast lesion, target detection performance of imaging technique is also required. In the future work, shear wave schemes designed and studied in this study will be used to assess efficiency for target detectability in terms of spatial resolution and elastic contrast reconstruction.

6.5 Conclusions

Shear wave speed values are not consistent when push beam aperture, focal depth are changed and also shear waves speed values are not uniform along depth and lateral direction for same configuration and focal depth. Large aperture configurations are able to generate large displacements at deeper regions with high shear wave SNR, but had disadvantage of adding bias and resulted in non-uniform accuracy along the map. For medium size aperture, bias was minimum and elasticity reconstruction was uniform across the map. Low aperture beam schemes were not able to generate shear waves enough to fill whole field of view, however, it was observed that, small apertures may enable more accurate and uniform elasticity reconstruction in shallow imaging conditions given shear wave SNR is improved using high excitation voltages. This study suggests that, shear wave configuration can be customised for each clinical application requirement in terms of imaging depth, tissue stiffness and required accuracy.

Chapter 7

Discussion of the Thesis

7.1 Discussion

Research study conducted in this thesis aimed to address challenges discussed in the introductory chapter. The aim of the thesis was divided among five objectives and each objective resolved the limitations discussed in the detail in corresponding chapters. The first objective was achieved by designing, and implementing transmit, receive, and signal processing flow for strain and shear wave elastography techniques. The other four objectives are using four separate studies discussed in the following sections.

7.2 Two-way Approach for Quality Evaluation of Elastograms

This study implemented strain elastography method on ultrasound system UARP I and proposed a novel quantity evaluation method to address the limitation of existing quality measurement techniques. This method will be helpful in clinical utilisation of strain elastography because currently there is no accuracy tracking scheme which ensures that signals used for strain estimation have adequate coherence. Existing quality metric such as SNR and CNR are global quality matrices which are used to measure only uniformity of strain estimation within the uniform tissue types such as inside inclusion and background (Bilgen & Insana, 1997b; Varghese & Ophir, 1997b). The method proposed by the Cambridge group used amplitude of the ultrasound signals to identify noisy estimation pixels and red-masked noisy areas, correspondingly (Chen *et al.*, 2010; Lindop *et al.*, 2008). Ultrasound signal amplitude of the signals or SNR is one factor among many factors which contributes to the quality of strain measurement. Proposed method used a novel quality metric NMA which is based on correlation coefficient along with the CNR. Both metrics ensure that the final selected image have adequate contrast and the least noisy estimation pixels among multiple images.

The study that inclusion diameters were underestimated than the original size, also observed in the previous study by (Doyley *et al.*, 2001). To resolve this, some research should be directed towards improving RF data SNR and adaptive estimation windows. Also, static nature of the tissue excitation enables to use multiple events of acquisitions of a single speckle state, therefore, this limitation can be removed by using noise reduction techniques such as ultrasonic averaging, and multi-compression averaging (MA). n future studies, further experiments using calibrated elasticity phantoms should be conducted to further validate the idea for different tissue conditions. Also in future studies, quality-score weighted averaging of multiple good quality strain images should be performed to improve the accuracy of strain estimation.

7.3 Dual Push Beam Shear Wave Elastography

The Dual Push beam shear wave elastography method produced elasticity image using a single RF data acquisition event where existing technique SSI uses three different events to form a single elasticity image. Few problems were encountered during studies regarding ultrasound machine power supply which should be solved in the future studies. It was observed that, there is depth dependent bias in the estimation values which increases when higher apertures and deeper focused beams are used, similarly observed in the previous study Zhao *et al.* (2011b). Possible reasons can be multiple intensity peaks generated in the beams due to a mismatch between elevational and axial focus and also a high lateral divergence of the beams at shallow regions. Moreover, the phantom used in the studies is not pure elastically homogeneous, it contains hyperechoic, hypoechoic and wire targets, there is a potential of shear wave reflection and refraction from these targets into the scan plane, or changing the direction of wave field within the scan plane. These may cause overestimation of elasticity because shear wave speed algorithm assumes that all shear wave sources are in the scan plane and wave propagating is at 0 angle to the lateral direction.

It is suggested that, by placing axial focal points close to the elevational focal point and 2D shear wave speed estimation methods, the bias can be reduced. Also, 3D directional filters can be used to remove any reflection and refraction from out the plane sources and boundaries. These suggestions will be investigated in the future to reduce the bias. To achieve comprehensive insight into the issue, the finite element modelling (FEM), and calibrated phantom studies across different ultrasound systems is required. Future studies in this direction will be conducted using the curvilinear transducer to investigate further potential with respect to penetration depth, and also calibrating excitation voltages to maintain the safe ultrasound exposure.

7.4 Improved Methods for Steered Shear Wave Motion Tracking

Shear wave elastography schemes use steered shear wave to form multi-angle compounded elasticity image to improve elasticity estimation quality. It was observed that, steered shear wave displacement tracking by the un-steered tracking beams result in the displacement direction artifacts and underestimated displacement amplitude. To address this problem, a novel method was introduced for shear wave tracking and improved steered shear wave displacement SNR and reduced artifacts by aligning push beam and tracking angles. In the final elasticity maps, aligned tracking improved inclusion reconstruction geometry and maintained contrast equal to the conventional method. In contrast to existing shear compounding techniques, the current study offers more control over the selection of shear wave generation angles and improved shear wave tracking accuracy.

This research study also demonstrated that there is need to pay adequate research attention to shear wave tracking as given to shear wave generation and optimised detection methods based on various shear wave propagation directions need to be developed. In this research perspective, aligned tracking method will be realised on phased array transducer that allows using higher steering angles, that will enable to investigate full potential of the aligned tracking method. In other direction of this study, an external vibrations will be tested to employ wider steered angles than which can be generated by the transducer and respective steered shear waves can be tracked using proposed tracking method. In future, studies also will be conducted to understand the relationship between shear wave displacement SNR and shear wave speed estimation accuracy to maintain adequate SNR to achieve accurate elasticity reconstruction.

7.5 Bias and Variability Observations for Different Shear Wave Elastography Methods

Another limitation of existing shear wave elastography methods is that there is a technique, ultrasound system, transducer, and measurement depth dependent inconsistency, therefore it is highly challenging to set a standard cut-off values for diagnostic and staging liver and breast diseases. According to the study, shear wave speed values are not consistent when push beam aperture, focal depth are changed and also shear waves speed values are not uniform along depth and lateral direction for same configuration and focal depth. It was observed that, small apertures may enable more accurate and uniform elasticity reconstruction given shear wave SNR is improved using high excitation voltages and compensating low aperture push beam limitation.

This study suggests that, shear wave configuration can be customised for each clinical application requirement in terms of imaging depth, tissue stiffness and required accuracy. This is a preliminary study to investigate effects of push beam parameters on shear wave speed bias and variability and its impact on clinical diagnosis accuracy. Further, in future studies, this study should be realised for curvilinear transducer array to access tissue depths used for liver fibrosis staging. Also, future research should be directed to develop variability corrections and also understanding of physical phenomena which cause changes of elasticity estimation variability among different experimental and measurement conditions.

7.6 Publications

7.6.1 Journal Publications (In Process)

Following papers cover the research work presented in the Chapter 4, and Chapter 6, respectively.

1. Hyder, Safeer, Sevan Harput, David MJ Cowell, and Steven Freear. "Dual push beam (DPB) Shear Wave Elastography", *Ultrasound in Medicine & Biology, 2017.*

2. Hyder, Safeer, Sevan Harput, David MJ Cowell, and Steven Freear. "Bias and Variability Observations for Different Shear Wave Elastography Methods", *Ultrasound in Medicine & Biology, 2017.*

7.6.2 Conference Publications

Following papers cover the research work presented in the Chapter 2, and Chapter 5, respectively.

1. Hyder, Safeer, Sevan Harput, Zainab Alomari, and Steven Freear. "Two-way Quality Assessment Approach for Tumour Detection using Free-hand Strain Imaging", *In Ultrasonics Symposium (IUS), 2014 IEEE International, pp. 1853-1856. IEEE, 2014.*

2. Hyder, Safeer, Sevan Harput, Zainab Alomari, David MJ Cowell, James McLaughlan, and Steven Freear. "Improved Shear Wave-front Reconstruction Method by Aligning Imaging Beam Angles with Shear-wave Polarization: Applied for shear compounding application.," *In Ultrasonics Symposium (IUS), 2016 IEEE International, pp. 1-4. IEEE, 2016.*

7.6.3 Co-authored Conference Publications

1. Alomari, Zainab, Sevan Harput, Safeer Hyder, and Steven Freear. “Selecting the Number and Values of the CPWI Steering Angles and the Effect of that on Imaging Quality.,” *In Ultrasonics Symposium (IUS), 2014 IEEE International, pp. 1191-1194. IEEE, 2014.*

2. Alomari, Zainab, Sevan Harput, Safeer Hyder, and Steven Freear. “The Effect of the Transducer Parameters on Spatial Resolution in Plane-wave Imaging.,” *In Ultrasonics Symposium (IUS), 2015 IEEE International, pp. 1-4. IEEE, 2015.*

References

ALAM, S.K. & OPHIR, J. (1997). Reduction of Signal Decorrelation from Mechanical Compression of Tissues by Temporal Stretching: Applications to Elastography. *Ultrasound in Medicine & Biology*, **23**, 95–105. 15

ALAM, S.K., OPHIR, J. & KONOFAGOU, E.E. (1998). An Adaptive Strain Estimator for Elastography. *IEEE Transactions on Ultrasonics, Ferroelectrics, and Frequency Control*, **45**, 461–472. 12, 14, 36, 37

ALBRECHT, T., BLOMLEY, M., BOLONDI, L., CLAUDON, M., COSGROVE, D., PISCAGLIA, F., NOLSOE, C., DIETRICH, C., CHOI, B., AVERKIOU, M. *et al.* (2017). EFSUMB Guidelines and Recommendations on the Clinical Use of Liver Ultrasound Elastography, update 2017 (long and short version). *Ultraschall in der Medizin-European Journal of Ultrasound*, **38**, 327–329. 32

ALOMARI, Z., HARPUT, S., HYDER, S. & FREEAR, S. (2014). Selecting the Number and Values of the CPWI Steering Angles and the Effect of that on Imaging Quality. In *Ultrasonics Symposium (IUS), 2014 IEEE International*, 1191–1194, IEEE. 78

AMADOR, C., URBAN, M.W., CHEN, S. & GREENLEAF, J.F. (2011). Shearwave Dispersion Ultrasound Vibrometry (SDUV) on Swine Kidney—. *IEEE Transactions on Ultrasonics, Ferroelectrics, and Frequency Control*, **58**. 26

ATHANASIOU, A., TARDIVON, A., TANTER, M., SIGAL-ZAFRANI, B., BERCOFF, J., DEFFIEUX, T., GENNISSON, J.L., FINK, M. & NEUENSCHWANDER, S. (2010b). Breast Lesions: Quantitative Elastography with Supersonic Shear ImagingPreliminary Results. *Radiology*, **256**, 297–303. 31

Athanasiou, A., Tardivon, A., Tanter, M., Sigal-Zafrani, B., Bercoff, J., Deffieux, T., Gennisson, J.L., Fink, M. & Neuenschwander, S. (2010a). Breast Lesions: Quantitative Elastography with Supersonic Shear ImagingPreliminary Results 1. *Radiology*, **256**, 297–303. 4

Barr, R.G., Nakashima, K., Amy, D., Cosgrove, D., Farrokh, A., Schafer, F., Bamber, J.C., Castera, L., Choi, B.I., Chou, Y.H. *et al.* (2015). EFSUMB Guidelines and Recommendations for Clinical Use of Ultrasound Elastography: Part 2: Breast. *Ultrasound in Medicine & Biology*, **41**, 1148–1160. 4, 164

Bavu, É., Gennisson, J.L., Couade, M., Bercoff, J., Mallet, V., Fink, M., Badel, A., Vallet-Pichard, A., Nalpas, B., Tanter, M. *et al.* (2011). Noninvasive in Vivo Liver Fibrosis Evaluation Using Supersonic Shear Imaging: A Clinical Study on 113 Hepatitis C Virus Patients. *Ultrasound in Medicine & Biology*, **37**, 1361–1373. 32

Bercoff, J., Tanter, M., Chaffai, S. & Fink, M. (2002). Ultrafast Imaging of Beamformed Shear Waves Induced by the Acoustic Radiation Force. Application to Transient Elastography. In *Proceedings of the 2002 IEEE Ultrasonics Symposium*, vol. 2, 1899–1902. 27

Bercoff, J., Tanter, M. & Fink, M. (2004a). Sonic Boom in Soft Materials: The Elastic Cerenkov Effect. *Applied Physics Letters*, **84**, 2202–2204. 27

Bercoff, J., Tanter, M. & Fink, M. (2004b). Supersonic Shear Imaging: A New Technique for Soft Tissue Elasticity Mapping. *IEEE Transactions on Ultrasonics, Ferroelectrics, and Frequency Control*, **51**, 396–409. 19, 24, 26, 27, 28, 69, 79, 119, 120, 143

Berg, W.A., Cosgrove, D.O., Doré, C.J., Schäfer, F.K., Svensson, W.E., Hooley, R.J., Ohlinger, R., Mendelson, E.B., Balu-Maestro, C., Locatelli, M. *et al.* (2012). Shear-wave Elastography Improves the Specificity of Breast US: The BE1 Multinational Study of 939 Masses. *Radiology*, **262**, 435–449. 31

Bilgen, M. (1999). Target Detectability in Acoustic Elastography. *IEEE Transactions on Ultrasonics, Ferroelectrics, and Frequency Control*, **46**, 1128–1133. 37

Bilgen, M. & Insana, M. (1997a). Predicting Target Detectability in Acoustic Elastography. In *Ultrasonics Symposium, 1997. Proceedings., 1997 IEEE*, vol. 2, 1427–1430, IEEE.

Bilgen, M. & Insana, M. (1997b). Predicting Target Detectability in Acoustic Elastography. In *Ultrasonics Symposium, 1997. Proceedings., 1997 IEEE*, vol. 2, 1427–1430, IEEE. 54, 58, 166

Brstad, T.K. (2011). *Intraoperative Ultrasound Strain Imaging of Brain Tumors*. Master's thesis, Norwegian University of Science and Technology. 1

Callister, W.D. & Rethwisch, D.G. (2011). *Materials Science and Engineering*, vol. 5. John Wiley & Sons NY. 4, 5, 6

Cassinotto, C., Lapuyade, B., Mouries, A., Hiriart, J.B., Vergniol, J., Gaye, D., Castain, C., Le Bail, B., Chermak, F., Foucher, J. *et al.* (2014). Non-invasive Assessment of Liver Fibrosis with Impulse Elastography: Comparison of Supersonic Shear Imaging with ARFI and FibroScan®. *Journal of Hepatology*, **61**, 550–557. 32

Castéra, L., Vergniol, J., Foucher, J., Le Bail, B., Chanteloup, E., Haaser, M., Darriet, M., Couzigou, P. & de Lédinghen, V. (2005). Prospective Comparison of Transient Elastography, Fibrotest, APRI, and Liver Biopsy for the Assessment of Fibrosis in Chronic Hepatitis C. *Gastroenterology*, **128**, 343–350. 26

Céspedes, I. & Ophir, J. (1993). Reduction of Image Noise in Elastography. *Ultrasonic Imaging*, **15**, 89–102. 12

Chang, J.M., Moon, W.K., Cho, N. & Kim, S.J. (2011). Breast Mass Evaluation: Factors Influencing the Quality of US Elastography. *Radiology*, **259**, 59–64. 31

Chaturvedi, P., Insana, M.F. & Hall, T.J. (1998). 2-D Companding for Noise Reduction in Strain Imaging. *IEEE Transactions on Ultrasonics, Ferroelectrics, and Frequency Control*, **45**, 179–191. 15

Chen, L., Freeman, S., Gee, A., Housden, R., Prager, R., Sinnatamby, R. & Treece, G. (2010). Initial Clinical Experience of an Ultrasonic Strain Imaging System with Novel Noise-masking Capability. *The British Journal of Radiology*, **83**, 702–706. 37, 54, 58, 167

Chen, L., Freeman, S., Gee, A., Housden, R., Prager, R., Sinnatamby, R. & Treece, G. (2014). Initial Clinical Experience of an Ultrasonic Strain Imaging System with Novel Noise-masking Capability. *The British Journal of Radiology*. 9

Chen, S., Fatemi, M. & Greenleaf, J.F. (2004). Quantifying Elasticity and Viscosity from Measurement of Shear Wave Speed Dispersion. *The Journal of the Acoustical Society of America*, **115**, 2781–2785. 26

Chen, S., Urban, M.W., Pislaru, C., Kinnick, R., Zheng, Y., Yao, A. & Greenleaf, J.F. (2009). Shearwave Dispersion Ultrasound Vibrometry (SDUV) for Measuring Tissue Elasticity and Viscosity. *IEEE Transactions on Ultrasonics, Ferroelectrics, and Frequency Control*, **56**, 55–62. 7, 26

Chen, S., Zhao, H., Song, P., Urban, M.W. & Greenleaf, J.F. (2011). Shear Wave Speed Measurement Using an Unfocused Ultrasound Push Beam. In *Ultrasonics Symposium (IUS), 2011 IEEE International*, 1171–1174, IEEE. 29

Cho, N., Lim, J. & Moon, W.K. (2014). Usefulness of Ultrasound Elastography in Reducing the Number of Breast Imaging Reporting and Data System Category 3 Lesions on Ultrasonography. *Ultrasonography*, **33**, 98–104. 4

Cobbold, R.S. (2006). *Foundations of Biomedical Ultrasound*. Oxford University Press. 2

COSGROVE, D., PISCAGLIA, F., BAMBER, J., BOJUNGA, J., CORREAS, J.M., GILJA, O., KLAUSER, A., SPOREA, I., CALLIADA, F., CANTISANI, V. *et al.* (2013). EFSUMB Guidelines and Recommendations on the Clinical Use of Ultrasound Elastography. Part 2: Clinical Applications. *Ultraschall in der Medizin-European Journal of Ultrasound*, **34**, 238–253. 57

COWELL, D., SMITH, P., HARPUT, S., MCLAUGHLAN, J. & FREEAR, S. (2014). Non-linear Harmonic Reduction Pulse Width Modulation (HRPWM) for the Arbitrary Control of Transducer-integrated Switched Excitation Electronics. In *Ultrasonics Symposium (IUS), 2014 IEEE International*, 807–810, IEEE. 66

DEFFIEUX, T., GENNISSON, J.L., BERCOFF, J. & TANTER, M. (2011). On the Effects of Reflected Waves in Transient Shear Wave Elastography. *IEEE Transactions on Ultrasonics, Ferroelectrics, and Frequency Control*, **58**, 2032–2035. 29, 73, 82, 122

DENIS, M., BAYAT, M., MEHRMOHAMMADI, M., GREGORY, A., SONG, P., WHALEY, D.H., PRUTHI, S., CHEN, S., FATEMI, M. & ALIZAD, A. (2015a). Update on Breast Cancer Detection Using Comb-push Ultrasound Shear Elastography. *IEEE Transactions on Ultrasonics, Ferroelectrics, and Frequency Control*, **62**, 1644–1650. 31

DENIS, M., MEHRMOHAMMADI, M., SONG, P., MEIXNER, D.D., FAZZIO, R.T., PRUTHI, S., WHALEY, D.H., CHEN, S., FATEMI, M. & ALIZAD, A. (2015b). Comb-push Ultrasound Shear Elastography of Breast Masses: Initial Results Show Promise. *IEEE Transactions on Ultrasonics, Ferroelectrics, and Frequency Control*, **10**, e0119398. 4, 31

DILLMAN, J.R., CHEN, S., DAVENPORT, M.S., ZHAO, H., URBAN, M.W., SONG, P., WATCHAROTONE, K. & CARSON, P.L. (2015). Superficial Ultrasound Shear Wave Speed Measurements in Soft and Hard Elasticity Phantoms: Pepeatability and Reproducibility Using Two Ultrasound Systems. *Pediatric Radiology*, **45**, 376–385. 32, 148

DOYLEY, M.M., BAMBER, J.C., FUECHSEL, F. & BUSH, N.L. (2001). A Freehand Elastographic Imaging Approach for Clinical Breast Imaging: System Development and Performance Evaluation. *Ultrasound in Medicine & Biology*, **27**, 1347–1357. 51, 57, 167

DUCK, F.A. (2013). *Physical Properties of Tissues: A Comprehensive Reference Book*. Academic Press. 6

FERLAY J, E.M.D.R.E.S.M.C.R.M.P.D.F.D.B., SOERJOMATARAM I (2014). Cancer Incidence and Mortality Worldwide: IARC CancerBase No. 11. Lyon, France: International Agency for Research on Cancer;. 30

FERRAIOLI, G., FILICE, C., CASTERA, L., CHOI, B.I., SPOREA, I., WILSON, S.R., COSGROVE, D., DIETRICH, C.F., AMY, D., BAMBER, J.C. *et al.* (2015). EFSUMB Guidelines and Recommendations for Clinical Use of Ultrasound Elastography: Part 3: Liver. *Ultrasound in Medicine & Biology*, **41**, 1161–1179. 4, 32, 163

FOUCHER, J., CHANTELOUP, E., VERGNIOL, J., CASTERA, L., LE BAIL, B., ADHOUTE, X., BERTET, J., COUZIGOU, P. & DE LEDINGHEN, V. (2006). Diagnosis of Cirrhosis by Transient Elastography (FibroScan): A Prospective Study. *Gut*, **55**, 403–408. 26

FRAQUELLI, M., RIGAMONTI, C., CASAZZA, G., CONTE, D., DONATO, M.F., RONCHI, G. & COLOMBO, M. (2007). Reproducibility of Transient Elastography in the Evaluation of Liver Fibrosis in Patients with Chronic Liver Disease. *Gut*, **56**, 968–973. 26

FRIEDRICH-RUST, M., ONG, M.F., MARTENS, S., SARRAZIN, C., BOJUNGA, J., ZEUZEM, S. & HERRMANN, E. (2008). Performance of Transient Elastography for the Staging of Liver Fibrosis: A Meta-analysis. *Gastroenterology*, **134**, 960–974. 26

GENNISSON, J.L., DEFFIEUX, T., MACÉ, E., MONTALDO, G., FINK, M. & TANTER, M. (2010). Viscoelastic and Anisotropic Mechanical Properties of In Vivo Muscle Tissue Assessed by Supersonic Shear Imaging. *Ultrasound in Medicine & Biology*, **36**, 789–801. 7

GREENLEAF, J.F., FATEMI, M. & INSANA, M. (2003). Selected Methods for Imaging Elastic Properties of Biological Tissues. *Annual Review of Biomedical Engineering*, **5**, 57–78. 3

HALL, T.J., MILKOWSKI, A., GARRA, B., CARSON, P., PALMERI, M., NIGHTINGALE, K., LYNCH, T., ALTURKI, A., ANDRE, M., AUDIERE, S. *et al.* (2013). RSNA/QIBA: Shear Wave Speed as a Biomarker for Liver Fibrosis Staging. In *Ultrasonics Symposium (IUS), 2013 IEEE International*, 397–400, IEEE. 32, 148

HILTAWSKY, K.M., KRÜGER, M., STARKE, C., HEUSER, L., ERMERT, H. & JENSEN, A. (2001). Freehand Ultrasound Elastography of Breast Lesions: Clinical Results. *Ultrasound in Medicine & Biology*, **27**, 1461–1469. 57

HIPPOCRATES (2009). *The Book of Prognostics*. 3

HOSKINS, P.R., MARTIN, K. & THRUSH, A. (2010). *Diagnostic Ultrasound: Physics and Equipment*. Cambridge University Press. 2, 4, 5, 6, 7, 116, 142, 161

HYDER, S., HARPUT, S., ALOMARI, Z. & FREEAR, S. (2014). Two-way Quality Assessment Approach for Tumour Detection Using Free-hand Strain Imaging. In *Ultrasonics Symposium (IUS), 2014 IEEE International*, 1853–1856, IEEE. i

HYDER, S., HARPUT, S., ALOMARI, Z., COWELL, D.M., MCLAUGHLAN, J. & FREEAR, S. (2016). Improved Shear Wave-front Reconstruction Method by Aligning Imaging Beam Angles with Shear-wave Polarization: Applied for Shear Compounding Application. In *Ultrasonics Symposium (IUS), 2016 IEEE International*, 1–4, IEEE. i

JENSEN, J., HOYOS, C.A.V., STUART, M.B., EWERTSEN, C., NIELSEN, M.B. & JENSEN, J.A. (2016). In Vivo High Frame Rate Vector Flow Imaging Using Plane Waves and Directional Beamforming. In *Ultrasonics Symposium (IUS), 2016 IEEE International*, 1–4, IEEE. 145

JENSEN, J.A. (2003). Directional Velocity Estimation Using Focusing Along the Flow Direction. I: Theory and Simulation. *IEEE Transactions on Ultrasonics, Ferroelectrics, and Frequency Control*, **50**, 857–872. 119, 145

JENSEN, J.A. & BJERNGAARD, R. (2003). Directional Velocity Estimation Using Focusing Along the Flow Direction. II: Experimental Investigation. *IEEE Transactions on Ultrasonics, Ferroelectrics, and Frequency Control*, **50**, 873–880. 119, 145

JESPERSEN, S.K., WILHJELM, J.E. & SILLESEN, H. (1998). Multi-angle Compound Imaging. *Ultrasonic Imaging*, **20**, 81–102. 118

KALLEL, F., OPHIR, J., MAGEE, K. & KROUSKOP, T. (1998). Elastographic Imaging of Low-Contrast Elastic Modulus Distributions in Tissue. *Ultrasound in Medicine & Biology*, **24**, 409–425. 8

KANAI, H. (2005). Propagation of Spontaneously Actuated Pulsive Vibration in Human Heart Wall and in Vivo Viscoelasticity Estimation. *IEEE Transactions on Ultrasonics, Ferroelectrics, and Frequency Control*, **52**, 1931–1942. 22

KANAI, H. (2009). Propagation of Vibration Caused by Electrical Excitation in the Normal Human Heart. *Ultrasound in Medicine & Biology*, **35**, 936–948. 22

KASAI, C., NAMEKAWA, K., KOYANO, A., OMOTO, R. *et al.* (1985). Real-time Two-dimensional Blood Flow Imaging Using an Autocorrelation Technique. *IEEE Trans. Sonics Ultrason*, **32**, 458–464. 79

KONOFAGOU, E., LEE, W.N., LUO, J., PROVOST, J. & VAPPOU, J. (2011). Physiologic Cardiovascular Strain and Intrinsic Wave Imaging. *Annual Review of Biomedical Engineering*, **13**, 477–505. 22

LINDOP, J.E., TREECE, G.M., GEE, A.H. & PRAGER, R.W. (2008). An Intelligent Interface for Freehand Strain Imaging. *Ultrasound in Medicine & Biology*, **34**, 1117–1128. 37, 57, 58, 167

Loupas, T., Peterson, R. & Gill, R.W. (1995a). Experimental Evaluation of Velocity and Power Estimation for Ultrasound Blood Flow Imaging, by means of a Two-dimensional Autocorrelation Approach. *IEEE Transactions on Ultrasonics, Ferroelectrics, and Frequency Control*, **42**, 689–699. 79

Loupas, T., Powers, J. & Gill, R.W. (1995b). An Axial Velocity Estimator for Ultrasound Blood Flow Imaging, Based on a Full Evaluation of the Doppler Equation by Means of a Two-dimensional Autocorrelation Approach. *IEEE Transactions on Ultrasonics, Ferroelectrics, and Frequency Control*, **42**, 672–688. 79

Madsen, E.L., Hobson, M.A., Shi, H., Varghese, T. & Frank, G.R. (2005). Tissue-mimicking Agar/Gelatin Materials for Use in Heterogeneous Elastography Phantoms. *Physics in Medicine and Biology*, **50**, 5597. 38

Manduca, A., Oliphant, T.E., Dresner, M., Mahowald, J., Kruse, S.A., Amromin, E., Felmlee, J.P., Greenleaf, J.F. & Ehman, R.L. (2001). Magnetic Resonance Elastography: Non-invasive Mapping of Tissue Elasticity. *Medical Image Analysis*, **5**, 237–254. 18, 19

Manduca, A., Lake, D.S., Kruse, S.A. & Ehman, R.L. (2003). Spatio-temporal Directional Filtering for Improved Inversion of MR Elastography Images. *Medical Image Analysis*, **7**, 465–473. 82

Mariappan, Y.K., Glaser, K.J. & Ehman, R.L. (2010). Magnetic Resonance Elastography: A Review. *Clinical Anatomy*, **23**, 497–511. 2

McAleavey, S., Menon, M. & Elegbe, E. (2009). Shear Modulus Imaging with Spatially-modulated Ultrasound Radiation Force. *Ultrasonic Imaging*, **31**, 217–234. 27

McAleavey, S.A., Menon, M. & Orszulak, J. (2007). Shear-modulus Estimation by Application of Spatially-modulated Impulsive Acoustic Radiation Force. *Ultrasonic Imaging*, **29**, 87–104. 27

McLaughlin, J. & Renzi, D. (2006). Shear Wave Speed Recovery in Transient Elastography and Supersonic Imaging Using Propagating Fronts. *Inverse Problems*, **22**, 681. 21, 83, 115

Melodelima, D., Bamber, J.C., Duck, F.A. & Shipley, J.A. (2007). Transient Elastography Using Impulsive Ultrasound Radiation Force: A Preliminary Comparison with Surface Palpation Elastography. *Ultrasound in Medicine & Biology*, **33**, 959–969. 24

Mohammed, H.A.A., Yang, J.D., Giama, N.H., Choi, J., Ali, H.M., Mara, K.C., Harmsen, W.S., Wiesner, R.H., Leise, M.D., Therneau, T.M. *et al.* (2017). Factors Influencing Surveillance for Hepatocellular Carcinoma in Patients with Liver Cirrhosis. *Liver Cancer*, **6**, 126–136. 32

Montaldo, G., Tanter, M., Bercoff, J., Benech, N. & Fink, M. (2009). Coherent Plane-wave Compounding for Very High Frame Rate Ultrasonography and Transient Elastography. *IEEE Transactions on Ultrasonics, Ferroelectrics, and Frequency Control*, **56**, 489–506. 2, 78, 79, 118, 120

Muller, M., Gennisson, J.L., Deffieux, T., Tanter, M. & Fink, M. (2009). Quantitative Viscoelasticity Mapping of Human Liver Using Supersonic Shear Imaging: Preliminary in Vivo Feasability Study. *Ultrasound in Medicine & Biology*, **35**, 219–229. 28, 32

Muthupillai, R., Rossman, P.J., Lomas, D.J., Greenleaf, J.F., Riederer, S.J. & Ehman, R.L. (1996). Magnetic Resonance Imaging of Transverse Acoustic Strain Waves. *Magnetic Resonance in Medicine*, **36**, 266–274. 22

Nabavizadeh, A., Song, P., Chen, S., Greenleaf, J.F. & Urban, M.W. (2014). Shear Wave Generation with Steered Ultrasound Push Beams. In *Ultrasonics Symposium (IUS), 2014 IEEE International*, 647–650, IEEE. 30

Nabavizadeh, A., Song, P., Chen, S., Greenleaf, J.F. & Urban, M.W. (2015). Multi-source and Multi-directional Shear Wave Generation with Intersecting Steered Ultrasound Push Beams. *IEEE Transactions on Ultrasonics, Ferroelectrics, and Frequency Control*, **62**, 647–662. 30

NAUMOVA, A.V., MODO, M., MOORE, A., MURRY, C.E. & FRANK, J.A. (2014). Clinical Imaging in Regenerative Medicine. *Nature Biotechnology*, **32**, 804–818. 1

NHS (2016). Diagnostic Imaging Dataset 2015-16 Data. Tech. rep., NHS, England, https://www.england.nhs.uk/statistics/statistical-work-areas/diagnostic-imaging-dataset/diagnostic-imaging-dataset-2015-16-data/. 1

NIGHTINGALE, K., MCALEAVEY, S. & TRAHEY, G. (2003). Shear-wave Generation Using Acoustic Radiation Force: In Vivo and Ex Vivo Results. *Ultrasound in Medicine & Biology*, **29**, 1715–1723. 26

NIGHTINGALE, K.R., PALMERI, M.L., NIGHTINGALE, R.W. & TRAHEY, G.E. (2001). On the Feasibility of Remote Palpation Using Acoustic Radiation Force. *The Journal of the Acoustical Society of America*, **110**, 625–634. 24

O'DONNELL, M., SKOVORODA, A.R., SHAPO, B.M. & EMELIANOV, S.Y. (1994). Internal Displacement and Strain Imaging Using Ultrasonic Speckle Tracking. *IEEE Transactions on Ultrasonics, Ferroelectrics, and Frequency Control*, **41**, 314–325. 8

OLIPHANT, T.E., MANDUCA, A., EHMAN, R.L. & GREENLEAF, J.F. (2001). Complex-valued Stiffness Reconstruction for Magnetic Resonance Elastography by Algebraic Inversion of the Differential Equation. *Magnetic Resonance in Medicine*, **45**, 299–310. 19

OPHIR, J., CESPEDES, I., PONNEKANTI, H., YAZDI, Y. & LI, X. (1991). Elastography: A Quantitative Method for Imaging the Elasticity of Biological Tissues. *Ultrasonic Imaging*, **13**, 111–134. v, vi, 8, 10, 11, 12, 24, 46

OUDRY, J., LYNCH, T., VAPPOU, J., SANDRIN, L. & MIETTE, V. (2014). Comparison of four different techniques to evaluate the elastic properties of phantom in elastography: Is there a gold standard? *Physics in Medicine and Biology*, **59**, 5775. 85

Palmeri, M., Nightingale, K., Fielding, S., Rouze, N., Deng, Y., Lynch, T., Chen, S., Song, P., Urban, M., Xie, H. *et al.* (2015). RSNA QIBA Ultrasound Shear Wave Speed Phase II Phantom Study in Viscoelastic Media. In *Ultrasonics Symposium (IUS), 2015 IEEE International*, 1–4, IEEE. 32, 148

Palmeri, M.L. & Nightingale, K.R. (2004). On the Thermal Effects Associated with Radiation Force Imaging of Soft Tissue. *IEEE Transactions on Ultrasonics, Ferroelectrics, and Frequency Control*, **51**, 551–565. 24

Pellicoro, A., Ramachandran, P., Iredale, J.P. & Fallowfield, J.A. (2014). Liver Fibrosis and Repair: Immune Regulation of Wound Healing in a Solid Organ. *Nature Reviews. Immunology*, **14**, 181. 32

Pernot, M., Fujikura, K., Fung-Kee-Fung, S.D. & Konofagou, E.E. (2007). ECG-gated, Mechanical and Electromechanical Wave Imaging of Cardiovascular Tissues in Vivo. *Ultrasound in Medicine & Biology*, **33**, 1075–1085. 22

Pinton, G.F., Dahl, J.J. & Trahey, G.E. (2006). Rapid Tracking of Small Displacements with Ultrasound. *IEEE Transactions on Ultrasonics, Ferroelectrics, and Frequency Control*, **53**, 1103–1117. 12, 21, 123

Piscaglia, F., Salvatore, V., Mulazzani, L., Cantisani, V. & Schiavone, C. (2016). Ultrasound Shear Wave Elastography for Liver Disease. A Critical Appraisal of the Many Actors on the Stage. *Ultraschall in der Medizin-European Journal of Ultrasound*, **37**, 1–5. 32

Provost, J., Gurev, V., Trayanova, N. & Konofagou, E.E. (2011a). Mapping of Cardiac Electrical Activation with Electromechanical Wave Imaging: An in silico–in Vivo Reciprocity Study. *Heart Rhythm*, **8**, 752–759. 22

Provost, J., Lee, W.N., Fujikura, K. & Konofagou, E.E. (2011b). Imaging the Electromechanical Activity of the Heart in Vivo. *Proceedings of the National Academy of Sciences*, **108**, 8565–8570. 22

RADDIN, J.B. (1964). Magic and Medical Science in Ancient Egypt. *Archives of Internal Medicine*, **113**, 925–925. 3

SACK, I., BUNTKOWSKY, G., BERNARDING, J., BRAUN, J. *et al.* (2001). Magnetic Resonance Elastography: A Method for the Noninvasive and Spatially Resolved Observation of Phase Transitions in Gels. *Journal of the American Chemical Society*, **123**, 11087–11088. 22

SANDRIN, L., FOURQUET, B., HASQUENOPH, J.M., YON, S., FOURNIER, C., MAL, F., CHRISTIDIS, C., ZIOL, M., POULET, B., KAZEMI, F. *et al.* (2003). Transient Elastography: A New Noninvasive Method for Assessment of Hepatic Fibrosis. *Ultrasound in Medicine & Biology*, **29**, 1705–1713. 26, 85

SARVAZYAN, A., PASECHNIK, V. & SHNOL, S. (1968). Low Velocity of Sound in Gels and Protoplasmic Structures. Possible Biological Implication of this Phenomenon. *Biophysics*, **13**, 587–594. 18

SARVAZYAN, A., HALL, T., URBAN, M., FATEMI, M., AGLYAMOV, S. & GARRA, B. (2011). Elasticity Imaging-an Emerging Branch of Medical Imaging. *An Overview. Curr Med Imaging Rev*, **7**, 255–282. 4

SARVAZYAN, A.P., RUDENKO, O.V., SWANSON, S.D., FOWLKES, J.B. & EMELIANOV, S.Y. (1998). Shear Wave Elasticity Imaging: A New Ultrasonic Technology of Medical Diagnostics. *Ultrasound in Medicine & Biology*, **24**, 1419–1435. 7, 18, 24, 69

SARVAZYAN, A.P., URBAN, M.W. & GREENLEAF, J.F. (2013). Acoustic Waves in Medical Imaging and Diagnostics. *Ultrasound in Medicine & Biology*, **39**, 1133–1146. 5, 6, 7, 18

SHIN, H.J., KIM, M.J., KIM, H.Y., ROH, Y.H. & LEE, M.J. (2016). Comparison of Shear Wave Velocities on Ultrasound Elastography Between Different Machines, Transducers, and Acquisition Depths: a Phantom Study. *European Radiology*, **26**, 3361–3367. 32, 148

SINKUS, R., LORENZEN, J., SCHRADER, D., LORENZEN, M., DARGATZ, M. & HOLZ, D. (2000). High-resolution Tensor MR Elastography for Breast Tumour Detection. *Physics in Medicine and Biology*, **45**, 1649. 22

SMITH, P.R., COWELL, D.M., RAITON, B., KY, C.V. & FREEAR, S. (2012). Ultrasound Array Transmitter Architecture with High Timing Resolution Using Embedded Phase-locked Loops. *IEEE Transactions on Ultrasonics, Ferroelectrics, and Frequency Control*, **59**. 40, 77, 121

SMITH, P.R., COWELL, D.M. & FREEAR, S. (2013). Width-modulated Square-wave Pulses for Ultrasound Applications. *IEEE Transactions on Ultrasonics, Ferroelectrics, and Frequency Control*, **60**, 2244–2256. 66, 77, 79, 121

SONG, P. (2014). *Innovations in Ultrasound Shear Wave Elastography*. Ph.D. thesis, Faculty of Mayo Clinic College of Medicine Mayo Graduate School. 3, 4, 18, 19, 20, 21, 120, 124, 125

SONG, P., MANDUCA, A., LI, Z., ZHAO, H., URBAN, M.W., GREENLEAF, J.F. & CHEN, S. (2011). Two-dimensional Shear Elasticity Imaging Using Comb-push Acoustic Radiation Force and Algebraic Direct Inversion of the Motion Differential Equation. *The Journal of the Acoustical Society of America*, **130**, 2424–2424. 19

SONG, P., ZHAO, H., MANDUCA, A., URBAN, M.W., GREENLEAF, J.F. & CHEN, S. (2012). Comb-push Ultrasound Shear Elastography (CUSE): A Novel Method for Two-dimensional Shear Elasticity Imaging of Soft Tissues. *IEEE Transactions on Medical Imaging*, **31**, 1821–1832. 19, 29, 73, 82, 92, 104, 120

SONG, P., URBAN, M.W., MANDUCA, A., ZHAO, H., GREENLEAF, J.F. & CHEN, S. (2013a). Comb-push Ultrasound Shear Elastography (CUSE) with Various Ultrasound Push Beams. *IEEE Transactions on Medical Imaging*, **32**, 1435–1447. 19, 30, 92, 104

SONG, P., ZHAO, H., URBAN, M.W., MANDUCA, A., PISLARU, S.V., KINNICK, R.R., PISLARU, C., GREENLEAF, J.F. & CHEN, S. (2013b). Improved Shear Wave Motion Detection Using Pulse-inversion Harmonic Imaging with a Phased Array Transducer. *IEEE Transactions on Ultrasonics, Ferroelectrics, and Frequency Control*, **32**, 2299–2310. 67

Song, P., Manduca, A., Zhao, H., Urban, M.W., Greenleaf, J.F. & Chen, S. (2014). Fast Shear Compounding Using Robust 2-D Shear Wave Speed Calculation and Multi-directional Filtering. *Ultrasound in Medicine & Biology*, **40**, 1343–1355. 19, 30, 92, 119, 124, 143, 165

Song, P., Macdonald, M.C., Behler, R.H., Lanning, J.D., Wang, M.H., Urban, M.W., Manduca, A., Zhao, H., Callstrom, M.R., Alizad, A. *et al.* (2015). Two-dimensional Shear-wave Elastography on Conventional Ultrasound Scanners with Time-Aligned Sequential Tracking (TAST) and Comb-push Ultrasound Shear Elastography (CUSE). *IEEE Transactions on Ultrasonics, Ferroelectrics, and Frequency Control*, **62**, 290–302. 115

Srinivasan, S., Kallel, F. & Ophir, J. (2002). Estimating the Elastographic Signal-to-Noise Ratio Using Correlation Coefficients. *Ultrasound in Medicine & Biology*, **28**, 359–368. 15, 37

Szabo, T.L. (2004). *Diagnostic Ultrasound Imaging: Inside Out*. Academic Press. 1

Szabo, T.L. (2014). *Diagnostic Ultrasound Imaging: Inside Out*. Academic Press. 2

Tanter, M., Bercoff, J., Sandrin, L. & Fink, M. (2002). Ultrafast Compound Imaging for 2-D Motion Vector Estimation: Application to Transient Elastography. *IEEE Transactions on Ultrasonics, Ferroelectrics, and Frequency Control*, **49**, 1363–1374. 118, 144

Tanter, M., Bercoff, J., Athanasiou, A., Deffieux, T., Gennisson, J.L., Montaldo, G., Muller, M., Tardivon, A. & Fink (2008). Quantitative Assessment of Breast Lesion Viscoelasticity: Initial Clinical Results Using Supersonic Shear Imaging. *Ultrasound in Medicine & Biology*, **34**, 1373–1386. 21, 28, 31, 70, 79

Vappou, J., Luo, J. & Konofagou, E.E. (2010). Pulse Wave Imaging for Noninvasive and Quantitative Measurement of Arterial Stiffness in Vivo. *American Journal of Hypertension*, **23**, 393–398. 22

Varghese, T. & Ophir, J. (1996). Estimating Tissue Strain from Signal Decorrelation Using the Correlation Coefficient. *Ultrasound in Medicine & Biology*, **22**, 1249–1254. 12

Varghese, T. & Ophir, J. (1997a). Enhancement of Echo-signal Correlation in Elastography Using Temporal Stretching. *IEEE Transactions on Ultrasonics, Ferroelectrics, and Frequency Control*, **44**, 173–180. 36

Varghese, T. & Ophir, J. (1997b). A Theoretical Framework for Performance Characterization of Elastography: The Strain Filter. *IEEE Transactions on Medical Imaging*, **44**, 164–172. 42, 46, 54, 58, 167

Varghese, T., Ophir, J. & Cespedes, I. (1996). Noise Reduction in Elastograms Using Temporal Stretching with Multicompression Averaging. *Ultrasound in Medicine & Biology*, **22**, 1043–1052. 12, 14

Viola, F. & Walker, W.F. (2003). A Comparison of the Performance of Time-delay Estimators in Medical Ultrasound. *IEEE Transactions on Ultrasonics, Ferroelectrics, and Frequency Control*, **50**, 392–401. 12, 79

Weaver, J.B., Pattison, A.J., McGarry, M.D., Perreard, I.M., Swienckowski, J.G., Eskey, C.J., Lollis, S.S. & Paulsen, K.D. (2012). Brain Mechanical Property Measurement Using MRE with Intrinsic Activation. *Physics in Medicine and Biology*, **57**, 7275. 22

Wells, P.N. & Liang, H.D. (2011). Medical Ultrasound: Imaging of Soft Tissue Strain and Elasticity. *Journal of the Royal Society Interface*, **8**, 1521–1549. 3, 5, 6, 15

World Cancer Research Fund, A.I.f.C.R. (2017). Food, Nutrition, Physical Activity, and the Prevention of Cancer: a Global Perspective. Tech. rep. 31

Wu, Z., Taylor, L.S., Rubens, D.J. & Parker, K.J. (2004). Sonoelastographic Imaging of Interference Patterns for Estimation of the Shear Velocity of Homogeneous Biomaterials. *Physics in Medicine and Biology*, **49**, 911. 22

Wu, Z., Hoyt, K., Rubens, D.J. & Parker, K.J. (2006). Sonoelastographic Imaging of Interference Patterns for Estimation of Shear Velocity Distribution in Biomaterials. *The Journal of the Acoustical Society of America*, **120**, 535–545. 22

Yin, M., Woollard, J., Wang, X., Torres, V.E., Harris, P.C., Ward, C.J., Glaser, K.J., Manduca, A. & Ehman, R.L. (2007). Quantitative Assessment of Hepatic Fibrosis in an Animal Model with Magnetic Resonance Elastography. *Magnetic Resonance in Medicine*, **58**, 346–353. 22

Zhao, H., Song, P., Urban, M.W., Greenleaf, J.F. & Chen, S. (2011a). Robust Shear Wave Speed Measurement Using Comb-push Ultrasound Radiation Force. In *Ultrasonics Symposium (IUS), 2011 IEEE International*, 1270–1273, IEEE. 29

Zhao, H., Song, P., Urban, M.W., Kinnick, R.R., Yin, M., Greenleaf, J.F. & Chen, S. (2011b). Bias Observed in Time-of-light Shear Wave Speed Measurements Using Radiation Force of a Focused Ultrasound Beam. *Ultrasound in Medicine & Biology*, **37**, 1884–1892. 29, 32, 92, 111, 147, 154, 157, 162, 163, 167

Zhao, H., Song, P., Urban, M.W., Greenleaf, J.F. & Chen, S. (2012). Shear Wave Speed Measurement Using an Unfocused Ultrasound Beam. *Ultrasound in Medicine & Biology*, **38**, 1646–1655. 29

Zhao, H., Song, P., Meixner, D.D., Kinnick, R.R., Callstrom, M.R., Sanchez, W., Urban, M.W., Manduca, A., Greenleaf, J.F. & Chen, S. (2014). External Vibration Multi-Directional Ultrasound Shearwave Elastography (EVMUSE): Application in Liver Fibrosis Staging. *IEEE Transactions on Medical Imaging*, **33**, 2140–2148. 142